



National Library
of Canada

Bibliothèque nationale
du Canada

Canadian Theses Service

Service des thèses canadiennes

Ottawa, Canada
K1A 0N4

NOTICE

The quality of this microform is heavily dependent upon the quality of the original thesis submitted for microfilming. Every effort has been made to ensure the highest quality of reproduction possible.

If pages are missing, contact the university which granted the degree.

Some pages may have indistinct print especially if the original pages were typed with a poor typewriter ribbon or if the university sent us an inferior photocopy.

Reproduction in full or in part of this microform is governed by the Canadian Copyright Act, R.S.C. 1970, c. C-30, and subsequent amendments.

AVIS

La qualité de cette microforme dépend grandement de la qualité de la thèse soumise au microfilmage. Nous avons tout fait pour assurer une qualité supérieure de reproduction.

S'il manque des pages, veuillez communiquer avec l'université qui a conféré le grade.

La qualité d'impression de certaines pages peut laisser à désirer, surtout si les pages originales ont été dactylographiées à l'aide d'un ruban usé ou si l'université nous a fait parvenir une photocopie de qualité inférieure.

La reproduction, même partielle, de cette microforme est soumise à la Loi canadienne sur le droit d'auteur, SRC 1970, c. C-30, et ses amendements subséquents.

**INVESTIGATION OF ELECTRODEPOSITED CuInSe_2 FILMS
FOR PHOTOVOLTAIC CELLS**

by

C. X. Qiu

**A Thesis Submitted to the
Faculty of Graduate Studies and Research
In Partial Fulfillment of the Requirements
For the Degree of Doctor of Philosophy**

**Department of Electrical Engineering
McGill University
Montreal, Canada
June, 1991**



National Library
of Canada

Bibliothèque nationale
du Canada

Canadian Theses Service Service des thèses canadiennes

Ottawa, Canada
K1A 0N4

The author has granted an irrevocable non-exclusive licence allowing the National Library of Canada to reproduce, loan, distribute or sell copies of his/her thesis by any means and in any form or format, making this thesis available to interested persons.

L'auteur a accordé une licence irrévocable et non exclusive permettant à la Bibliothèque nationale du Canada de reproduire, prêter, distribuer ou vendre des copies de sa thèse de quelque manière et sous quelque forme que ce soit pour mettre des exemplaires de cette thèse à la disposition des personnes intéressées.

The author retains ownership of the copyright in his/her thesis. Neither the thesis nor substantial extracts from it may be printed or otherwise reproduced without his/her permission.

L'auteur conserve la propriété du droit d'auteur qui protège sa thèse. Ni la thèse ni des extraits substantiels de celle-ci ne doivent être imprimés ou autrement reproduits sans son autorisation.

ISBN 0-315-72007-7

ABSTRACT

Uniform polycrystalline p-type CuInSe_2 films, thicknesses ranging from 1 to 4 μm , were deposited by a stable electrodeposition process developed in our laboratory. A (112) preferred orientation was found for the films. Vacuum annealing experiment results showed an improvement in the crystalline quality of the films after the annealing. The metal ratio of the films was not altered significantly by the annealing process. Al/CuInSe_2 Schottky junctions fabricated on p-type CuInSe_2 films showed that the current transport mechanism in the intermediate voltage region was governed by a recombination component. A dispersion effect of the capacitance-voltage curves with frequency, observed on the Schottky junctions suggested the presence of either enhanced interface states or deep levels in the depletion region. Solar cells of CdS/CuInSe_2 were fabricated by vacuum evaporating low resistivity n-type CdS layers on the electrodeposited p-type CuInSe_2 films. The highest AM1 active area conversion efficiency, for the 0.9 cm^2 cells, was 5.2% after an air heat treatment at 200°C. The efficiency value was increased to 5.6% in small area devices fabricated using a similar procedure. The air heat treatment was found to reduce the apparent carrier concentration in the CuInSe_2 films. Current-voltage (I-V) characteristics of the cells showed a definite relationship between the short circuit current and the indium to copper ratio in the CuInSe_2 films. Temperature dependent I-V curves revealed a dominant recombina-

tion current component for the heterojunction cells. The value of barrier height for a cell was estimated to be 0.64 eV. It was found that the differential capacitance values depended on measurement frequencies, resulting in frequency-dependent voltage intercepts. The C^{-2} -V curves were also observed to shift to more negative voltages under illumination. Interface states were believed to be responsible for all these effects. The density of the charged interface states under AM1 illumination condition for a cell with efficiency of 5.2% was estimated to be $5 \times 10^{12} \text{ cm}^{-2}$. Admittance spectroscopy results showed that there was a relation between the composition of the CuInSe_2 films and the activation energy of the deep levels. For the films with an indium/copper ratio of 1.1, the activation energy was about 50 meV. The trap states were much deeper (160 meV) for the films with an In/Cu ratio of 1.25.

RÉSUMÉ

On a déposé des couches minces homogènes de 1 à 4 μm d'épaisseur de CuInSe_2 polycristallin de type p par un procédé d'électrodéposition développé dans notre laboratoire. On a trouvé que les films déposés avaient une orientation préférentielle (112). Des expériences de recuit sous vide ont résulté en une amélioration de la qualité cristalline des films. Le rapport indium/cuivre n'a pas subi de changement significatif durant le recuit. Des jonctions Schottky du type Al/CuInSe_2 fabriquées à partir des films électrodéposés ont montré que le transport du courant dans la zone des tensions intermédiaires était gouverné par un mécanisme de recombinaison. On a observé une dispersion des courbes capacité-tension mesurées à différentes fréquences des jonctions Schottky, ce qui suggère la présence d'états d'interface activés ou de niveaux profonds dans la zone d'appauvrissement. On a fabriqué des cellules solaires du type CdS/CuInSe_2 en évaporant sous vide des couches de CdS de type n de faible résistivité sur les films électrodéposés de CuInSe_2 de type p. La plus haute efficacité de conversion sous illumination AM1 était de 5.2% après traitement thermique à 200°C dans l'air pour des surfaces actives de 0.9 cm^2 . L'efficacité augmentait jusqu'à 5.6% pour des dispositifs de petites surfaces fabriqués de façon similaire. On a constaté que le traitement thermique dans l'air réduisait la concentration apparente de porteurs dans les films de CuInSe_2 . Les caractéristiques courant-tension (I-V) des cellules ont montré une relation

certaine entre le courant de court-circuit des cellules et le rapport indium/cuivre dans les films de CuInSe_2 . Les courbes I-V mesurées à différentes températures ont révélé que la recombinaison était le mécanisme dominant de transport du courant dans ces hétérojonctions. La hauteur de barrière d'une cellule a été estimée à 0.64 eV. On a trouvé que les valeurs de capacité différentielle dépendaient de la fréquence de mesure. On a aussi observé un décalage des courbes C^2 -V vers les tensions négatives lorsque les cellules étaient sous illumination. On croit que des états d'interface sont responsable de tous ces effets. On a estimé à $5 \times 10^{12} \text{ cm}^{-2}$ la densité d'états d'interface chargés d'une des cellules d'efficacité 5.2% sous illumination AM1. Des mesures de spectroscopie par admittance ont montré une relation entre la composition des films de CuInSe_2 et l'énergie d'activation des niveaux profonds. Pour les films ayant un rapport indium/cuivre de 1.1, l'énergie d'activation était d'environ 50 meV. Les niveaux de piège étaient beaucoup plus profonds (160 meV) pour les films ayant un rapport In/Cu de 1.25.

ACKNOWLEDGEMENTS

It is the author's privilege to express her gratitude to her supervisor, Prof. I. Shih for his invaluable guidance during this study. The author is thankful to Prof. C. H. Champness for reading the thesis and to L. Isnard for translating the abstract into French.

The author would like to acknowledge the technical assistance from Mr. Y. Kwon, Mr. G. Rhodrigue and the electrical and mechanical shops in the department. Special thanks are due to Mr. C.N. Qiu for performing the X-ray diffraction measurements. The financial assistance from the Natural Sciences and Engineering Research Council of Canada is greatly acknowledged.

The author is grateful to her parents for their continuing love and support throughout her entire life. The author would like to express her special appreciation to her brother, Chunong, for his assistance during the last five years. Special thanks are also due to the author's daughter, Julia, for making the life so enjoyable.

TABLE OF CONTENTS

<u>Table</u>	<u>Page</u>
ABSTRACT	i
RÉSUMÉ	iii
ACKNOWLEDGMENTS	v
TABLE OF CONTENTS	vi
Chapter 1 INTRODUCTION	1
Chapter 2 THEORY OF SOLAR CELLS	8
2.1 PN Junction Solar Cells	8
2.2 Absorption Coefficient and Spectral Response ...	8
2.3 Equivalent Circuit and I-V Characteristics	10
2.4 Heterojunction Solar Cells	12
2.5 Thin Film Cells	13
Chapter 3 DEPOSITION AND CHARACTERIZATION OF CuInSe ₂ THIN FILMS	21
3.1 Introduction	21
3.2 Film Deposition	22
3.3 Adhesion of the CuInSe ₂ Films to the Substrates	25
3.4 Film Characterization	25
3.4.1 SEM Photographs	
3.4.2 X-ray Diffraction (XRD)	
3.4.3 Electron Probe Micro Analysis (EPMA)	
3.4.4 Secondary Ion Mass Spectroscopy (SIMS)	
3.4.5 Hot Probe	
3.5 Conclusions	31

Chapter 4	HEAT TREATMENT EFFECTS OF CuInSe ₂ FILMS	45
4.1	Introduction	45
4.2	Heat Treatment Experiments	45
4.3	Effect of Heat Treatment on Composition	47
4.4	Effect of Heat Treatment on Crystalline Quality	49
4.5	Conclusions	51
Chapter 5	Al/CuInSe ₂ SCHOTTKY JUNCTIONS FABRICATED USING P-TYPE CuInSe ₂ FILMS	64
5.1	Introduction	64
5.2	Theory of Schottky Junctions	65
5.3	Schottky Junction Fabrication	67
5.4	Current-voltage Characteristics	67
5.5	Differential Capacitance Measurements	69
5.6	Conclusions	72
Chapter 6	FABRICATION OF CdS/CuInSe ₂ PHOTOVOLTAIC CELLS	88
6.1	Introduction	88
6.2	Deposition Process of low Resistivity CdS Films	89
6.3	Examination of CdS Films.....	91
6.4	Al Contact Deposition	94
6.5	AR Coating Deposition	95
6.6	Conclusions	96
Chapter 7	CHARACTERIZATION OF THE CdS/CuInSe ₂ SOLAR CELLS	109
7.1	Introduction	109

7.2	Current-voltage Characteristics	110
7.2.1	Effects of Post-fabrication Air Heat Treatments	
7.2.1.1	Cells fabricated on the Mo plate substrates	
7.2.1.2	Cells on the Mo/glass substrates	
7.2.2	Compositional Effects on The I-V Characteristics	
7.2.3	Anti-reflection (AR) Coatings	
7.2.4	Series Resistance Effect	
7.2.5	Temperature-dependent I-V Characteristics	
7.2.6	Fitting Results of the Cells	
7.3	Differential Capacitance-voltage Measurements...	118
7.3.1	Dark C-V Results	
7.3.2	Effect of Heat Treatment	
7.3.3	Illuminated C-V Results	
7.3.4	Effect of Series Resistance on the C^{-2} -V Curve	
7.4	Spectral Response	126
7.5	I_{sc} - V_{oc} Relationship	127
7.6	Conversion Efficiency	127
7.7	Small Area Cells	128
7.8	Energy Band Diagram	130
7.9	Conclusions	130
Chapter 8	ADMITTANCE SPECTROSCOPY FOR THE STUDY OF DEEP LEVELS IN THE ELECTRODEPOSITED $CuInSe_2$ FILMS	163
8.1	Introduction	163
8.2	Theory of Admittance Spectroscopy	164
8.3	Measurement Results	167
8.4	Conclusions	171
Chapter 9	DISCUSSION AND CONCLUSIONS	185
REFERENCES	194

Chapter 1 INTRODUCTION

Results of environmental research in recent years have raised public awareness of the green house effect. This effect was mainly caused by the increased amount of carbon dioxide released into the atmosphere from fossil fuel combustion. Analysis of air samples showed that carbon dioxide in the atmosphere has increased by about 25% since the beginning of the industrial revolution in 1800^{1.1}. In order to prevent further increase of the concentration of carbon dioxide in atmosphere and to avoid the global warming, besides efficient use of energy, it is required to develop carbon free energy resources such as solar, wind, geothermal and other renewable sources.

In addition to the environmental problems (including air pollution) caused by the conventional energy sources, energy resources on the earth are also limited and will be exhausted in the near future. On the contrary, the life of the sun is so enormous that developing technologies for the use of solar energy is very attractive. Among all of the solar energy technologies, photovoltaic (PV) devices (or solar cells) which convert the solar energy directly into electricity appear to be the most attractive ones.

Since the first demonstration of the photovoltaic effect in a solid state system in 1877^{1.2}, more than a century has passed. Since then, the world has witnessed enormous progress in the

photovoltaic area, including the demonstration of the first modern silicon solar cells in 1954^{1,3}, the use of photovoltaic arrays to supply electricity to space ships and space stations, and countless demonstration PV power panels. Photovoltaic cells also play an important role in telecommunications, navigational aids, remote area power supply, water pumping and consumer electronics. Following the increase in the efficiency for single and tandem cells and the maturing of the thin film technologies, the following concept is generally accepted by people: In the near future, photovoltaic cells will supply electricity on a large scale as part of a grid network and it will meet part of the electricity demand.

To compete with the conventional large scale generation economically, it is essential to lower the cost of electricity generated by the PV cells. This requirement can be achieved in two directions: to increase the cell efficiency and to decrease the manufacturing cost of the PV cells. Figure 1.1 plots the required module cost as a function of efficiency for flat plate modules^{1,2}. The vertical line gives the cost efficiency combination required to compete with conventional electricity generation systems.

To reduce the manufacturing cost, cells in a thin film form are required. At the present, there are three thin film semiconductor materials which are considered to be the best candidates for high efficiency thin film cells. They are polycrystalline CdTe, CuInSe₂ (also CuInGaSe₂) and amorphous Si. Among them, the semiconductor CuInSe₂ is well known for its thermal stability

and high optical absorption coefficient. Nearly 99% of the incident above-bandgap light is absorbed within the first half micron of the material. The semiconductor CuInSe_2 has a tetragonal structure with the lattice constant, a , equal to $5.78 \text{ \AA}^{1.4}$. It is a direct bandgap material with E_g equal to 1.01 eV. CuInSe_2 forms a good heterojunction with CdS, since the lattice mismatch between (112) plane of CuInSe_2 and (001) plane of CdS is only about 1.12%^{1.5} and the electron affinities of the two materials are very close. The properties of CuInSe_2 are listed in table 1.1. Parameters of the semiconductor CdS are also given in the table for comparison. Photovoltaic cells based on CuInSe_2 thin films with a conversion efficiency over 14% have been successfully fabricated^{1.6}. In addition to the high efficiency required for low cost applications, the semiconductor CuInSe_2 is also an ideal small bandgap cell in a high efficiency tandem structure. Recently, Gale and coworkers have reported an AMO efficiency of 23.1% on a tandem structure fabricated by mechanically stacking a GaAs thin film top cell and a CdZnS/CuInSe_2 bottom cell^{1.7}.

Up to the present time, most of the CuInSe_2 films used for the high efficiency solar cells are deposited using the three-source evaporation method^{1.8, 1.9, 1.10, 1.11}. This method provides the greatest degree of control over the stoichiometry of the films. During the evaporation, sensors installed in the chamber are used for precise control of the individual deposition rate for each boat and the substrates are heated to a temperature in the range of 350-450°C. Sputtering methods, including dc, rf and reactive sputtering, have been used for the preparation of

CuInSe₂ thin films^{1.12, 1.13, 1.14}. In the reactive sputtering method, Cu and In are simultaneously sputtered in an atmosphere containing Ar and H₂Se. The substrates are held at 400°C during the sputtering. The highest conversion efficiency obtained by this method is 6%^{1.15}. A two-step method involving selenization of metal layers has also been used for the deposition of CuInSe₂ films^{1.16, 1.17}. In this method, Cu and In layers are first deposited either by evaporation or by electrodeposition. The metal films are then converted into CuInSe₂ films by carrying out a selenization process in the presence of H₂Se. This process is performed at a temperature in the range of 380-450°C for a time period of 2-3 hours. A high conversion efficiency of 10.8% has been obtained by using this process^{1.18}. However, the adhesion of the metal films to the substrate remains a problem for this method.

All of deposition methods mentioned above often require expensive equipment and high energy consumption and therefore are not ideal for future industrial production. Low cost technologies such as spray pyrolysis^{1.19, 1.20} have been reported. However, the efficiency of cells fabricated using this method is still low as compared to the vacuum deposited ones. Therefore, more efforts are needed to develop new methods for CuInSe₂ before they can replace the vacuum methods for the terrestrial large scale applications.

In our laboratory, a low cost electrodeposition method^{1.21} has been successfully developed for polycrystalline CuInSe₂ thin films. This method is not only simple but also has an optimum

material utilization rate. In addition, the energy consumption required in this method is very small as compared to the vacuum methods. Because all the materials are dissolved in a solution and the process is carried out at relatively low temperatures, potential safety hazard during the fabrication using this method is also minimum. Another advantage is that the facility and process can be relatively easily scaled up to deposit large area CuInSe_2 films. Using a prototype system designed in our laboratory, uniform films with an area up to $10 \times 10 \text{ cm}^2$ and a thickness of $1 \text{ }\mu\text{m}$ have been deposited. The deposited CuInSe_2 films were studied by several analytical methods to determine their quality. Both Schottky junctions and heterojunctions were then fabricated and investigated. Results of analysis and junction investigation are reported in this thesis.

In chapter 2 of the thesis, the theory of photovoltaic solar cells is briefly reviewed. Results of deposition and characterization of CuInSe_2 films are presented in chapter 3. The effect of post-deposition heat treatment on the quality of the CuInSe_2 films are described in chapter 4. In chapter 5, testing results on Al/CuInSe Schottky junctions are reported. Fabrication process for CdS/CuInSe_2 heterojunctions and the characterization results of vacuum deposited CdS films are described in chapter 6. Investigation of the fabricated CdS/CuInSe_2 heterojunctions is then presented in chapter 7, which is followed by chapter 8 on the admittance spectroscopy to study the deep levels in the electrodeposited CuInSe_2 . Finally, the discussion and conclusions of the thesis are given in chapter 9. Detailed film deposition

process will be released through a patent and will not be described in this thesis.

Table 1.1 Properties of the semiconductors CuInSe₂ and CdS^{1,5}.

Parameters	CuInSe ₂	CdS
Crystal Structure	Tetragonal	Wurtzite ^I
Microstructure	Columnar ^{II}	Columnar ^{III}
Energy Bandgap, E _g (eV)	1.04	2.40
Lattice constant, a (Å)	5.78 ^{1,4}	4.14
c (Å)	11.62	6.71
Relative Dielectric Constant,	10.00	9-10.3
Electron Affinity (eV)	4.30 ^{1,22}	4.50
m _e /m ₀	0.09 ^{1,23}	0.35
m _e /m _h	0.12 ^{1,23}	5.00
Mismatch between the two materials	1.12% ^{IV}	

I When deposited with the substrate temperature above 170 °C.

II With [221] direction perpendicular to the substrate surface.

III With the c-axis perpendicular to the substrate surface.

IV Between (112) plane of CuInSe₂ and (001) plane of CdS.

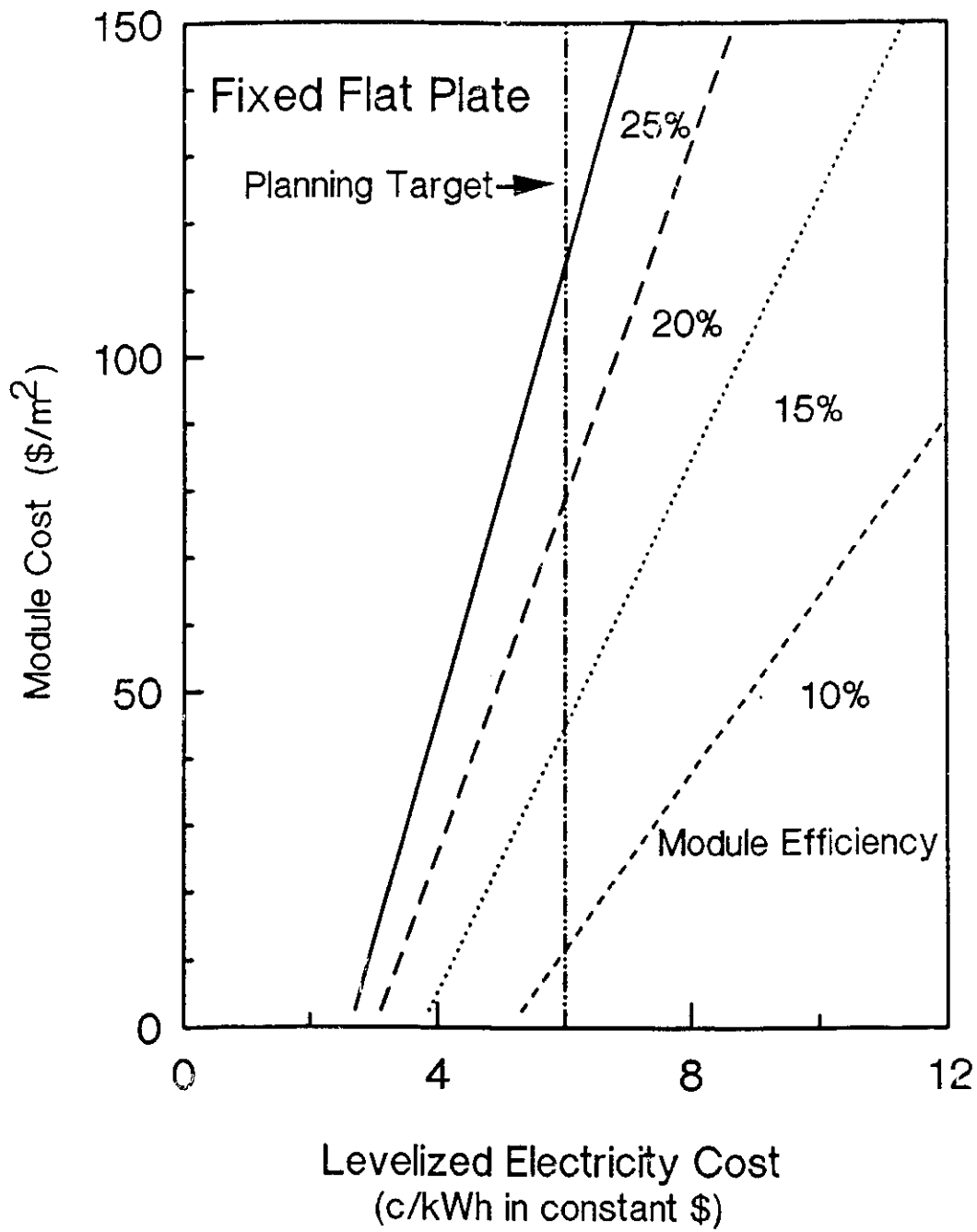


Fig. 1.1 The module cost as a function of cell efficiency for flat plate modules (after ref. 1.2).

Chapter 2 THEORY OF SOLAR CELLS

2.1 P-N Junction Solar Cells

The Solar cell is a photovoltaic device which is used as an energy converter. When the solar cell is illuminated by solar radiation, it converts the solar energy directly into electrical energy. In order to understand the conversion process, we can examine the energy band diagram of the solar cell under illumination. Fig. 2.1 illustrates the energy band diagram of an n^+p homojunction solar cell. In this figure, E_c is the conduction band edge, E_v is the valence band edge, and E_g is the bandgap of the semiconductor material.

Under the solar radiation, the semiconductor material absorbs most of the photons with an energy greater than the bandgap of the material, E_g . The absorbed photons excite electrons from the valence band to the conduction band. The excitation leaves free holes in the valence band, therefore, creating electron-hole pairs. These free electron-hole pairs will be separated and swept by the internal electric field of the depletion region. The free carriers are finally collected by the external circuit.

2.2 Absorption Coefficient and Spectral Response

The ability of a material to absorb photons at a given wavelength depends on its optical absorption coefficient, α . The inverse of α gives the absorption length which is also a function

of photon energy. Photons of low energy create free carriers even deep in the material and photons with high energy are mostly absorbed near the surface. Figure 2.2 shows the absorption coefficients of Si, CdTe, CuInSe₂, CdS and three other semiconductors in the energy range from 0.9 to 2.6 eV^{2.1}. The semiconductor Si is a material with an indirect gap and its absorption coefficient rises slowly with the photon energy. Because of the relatively small absorption coefficients, most of the absorption occurs in a relatively thick region about tens of microns from the Si surface. The semiconductor CuInSe₂ has a direct band gap, with its absorption coefficient rises steeply with the increase of photon energy near 1 eV and attains high value at about 1.1 eV. The absorption length in CuInSe₂ for the above-bandgap photons is about 1 μm. CdTe is also a direct gap material with the absorption coefficient, rises abruptly above the energy of 1.45 eV.

The spectral response of a solar cell is defined as the number of carriers collected per incident photon at a given wavelength. Ideally, the spectral response is a step function of energy when the surface recombination velocity is zero. The spectral response of a Si n-on-p cell with a non-zero surface recombination velocity is shown in figure 2.3(a)^{2.2}. The three calculated components due to the front, depletion region and base layers are seen to have peaks located at different energy values. In this figure, the total spectral response is seen to first increase with the increase of photon energy and reaches a maximum. It then decreases as the energy is increased further when most

of the electron-hole pairs are generated near the surface region and these recombine because of the non-zero surface recombination velocity. In Fig. 2.3(b), the total spectral response calculated for different surface recombination velocities are shown. We can see that the response in the high energy region decreases with the increase of the recombination velocity. The spectral response can be improved by increasing the diffusion length of the material. For a material having large absorption coefficient, the spectral response can also be improved by making shallow junctions.

2.3 Equivalent Circuit and I-V Characteristics

The equivalent circuit of a p-n junction under the solar radiation is shown in Fig. 2.4. Fig.2.4(a) gives the equivalent circuit for an ideal p-n junction and Fig. 2.4(b) shows the circuit for a junction with a series resistance R_s and a shunt resistance R_{sh} . In the figure, I_L is the light generated current and I_s is the saturation current. The I-V characteristics of the ideal diode under the illumination are given by

$$I = I_s [\exp(qV/kT) - 1] - I_L. \quad (2.1)$$

Here, I_s is the saturation current, or bucking current of the cell, V is the voltage across the cell. When the two terminals of the cell are shorted, $V = 0$,

$$I = I_{sc} = I_L \quad (2.2)$$

A plot of the equation (2.1) is shown in Fig. 2.5^{2.3}. Here V_{oc} is

the open circuit voltage and I_{SC} is the short circuit current, I_m and V_m are the current and voltage for the maximum output power, $P_m (= I_m V_m)$. The conversion efficiency of the device is defined as,

$$\eta = P_m/P_{in} = I_m V_m/P_{in} = FF * I_{SC} V_{OC}/P_{in}. \quad (2.3)$$

In equation (2.3), FF is the fill factor, which is given by,

$$FF = I_m V_m / I_{SC} V_{OC} \quad (2.4)$$

The open circuit voltage can be expressed as a function of the short circuit current,

$$V_{OC} = (kT/q) \ln(I_{SC}/I_S + 1) \approx (kT/q) \ln(I_{SC}/I_S). \quad (2.5)$$

For a given I_{SC} , the open circuit voltage increases logarithmically with the decrease of the saturation current I_S . It can also be shown that the open circuit voltage increases and the short circuit current decreases with the increase of the bandgap of the absorbing semiconductor. Therefore, the efficiency is a function of bandgap and has a maximum value at a bandgap of around 1.4 and 1.5 eV^{2.4}. For this reason, materials with bandgap lie between 1 and 1.7 eV can be considered to be potential candidates for photovoltaic applications.

For a practical solar cell (equivalent circuit shown in Fig. 2.4(b)), the I-V relation is^{2.5}:

$$\ln[(I+I_{SC})/I_S - (V-IR_S)/I_S R_{Sh} + 1] = (q/kT)(V - IR_S) \quad (2.6)$$

The effects of the series and shunt resistances can be seen in

Fig. 2.6^{2.5}. In most of the practical cases, the shunt resistance is large enough so that it can be ignored and only the series resistance is important. For p-n junction solar cells, the series resistance mainly depends on the resistivity of the p and n regions and the arrangement of the front contact.

2.4 Heterojunction Solar Cells

Heterojunctions are junctions formed between two different semiconductors often with different energy bandgaps. Fig. 2.7 shows the energy band diagram of an n⁺-p heterojunction. In this device, the n-type window layer has a larger bandgap, E_{g1} , which allows photons with energy smaller than E_{g1} to penetrate through it and reach the absorber layer with an energy gap of E_{g2} . Photons with energy less than E_{g1} and greater than E_{g2} will be absorbed by the bottom absorbing layer and create electron-hole pairs. The electron-hole pairs generated in the depletion region and within a diffusion length from the junction will be collected by the external circuit. Photons with an energy value larger than E_{g1} will be absorbed by the top layer. The electron-hole pairs generated within a diffusion length from the junction or in the depletion region will also be collected.

Heterojunction solar cells can achieve higher short wavelength spectral response over conventional homojunction cells. This is because the large E_{g1} which will allow the high-energy photons to be absorbed in the depletion region of the semiconductor with the energy gap E_{g2} . The top layer can be heavily doped so that the resistivity of the top layer is lower.

When fabricating a heterojunction solar cell, in addition to the bandgap requirement, the following factors should be taken into consideration: (1) The lattice mismatch between the two materials should be as small as possible. The lattice mismatch introduces interface states which affect not only the open circuit voltage but also the short circuit current. (2) The electron affinities of the two materials should be as close as possible to prevent any spike or step from forming in the conduction band. The spike or step reduces the I_{SC} and V_{OC} values.

2.5 Thin Film Cells

For thin film solar cells, the absorption layer is deposited on electrically conducting substrates. The films can be prepared by various deposition methods, such as evaporation, sputtering and electrodeposition. Thin film cells are usually fabricated from polycrystalline materials with large absorption coefficients. If the film thickness is larger than the inverse of the absorption coefficient of the semiconductor film, most of the photons incident on the absorber will be absorbed. Furthermore, if the film thickness is smaller than the diffusion length, most of the generated carriers can be collected by the external circuit. The main advantage of the thin film cells over the bulk cells is the low fabrication cost and the relatively small material consumption. However due to the relatively poor electronic quality of the polycrystalline films, the energy conversion efficiency of the thin film cells is lower than that of bulk monocrystalline cells fabricated using the same material.

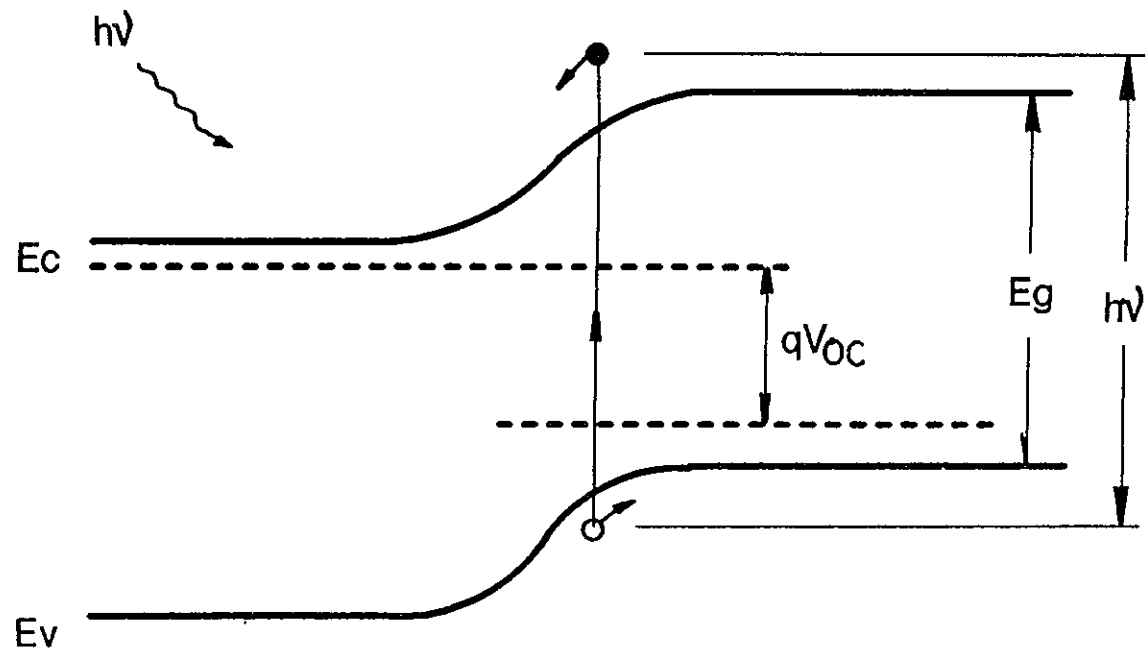


Fig. 2.1 Energy band diagram of an n^+p homojunction solar cell under illumination.

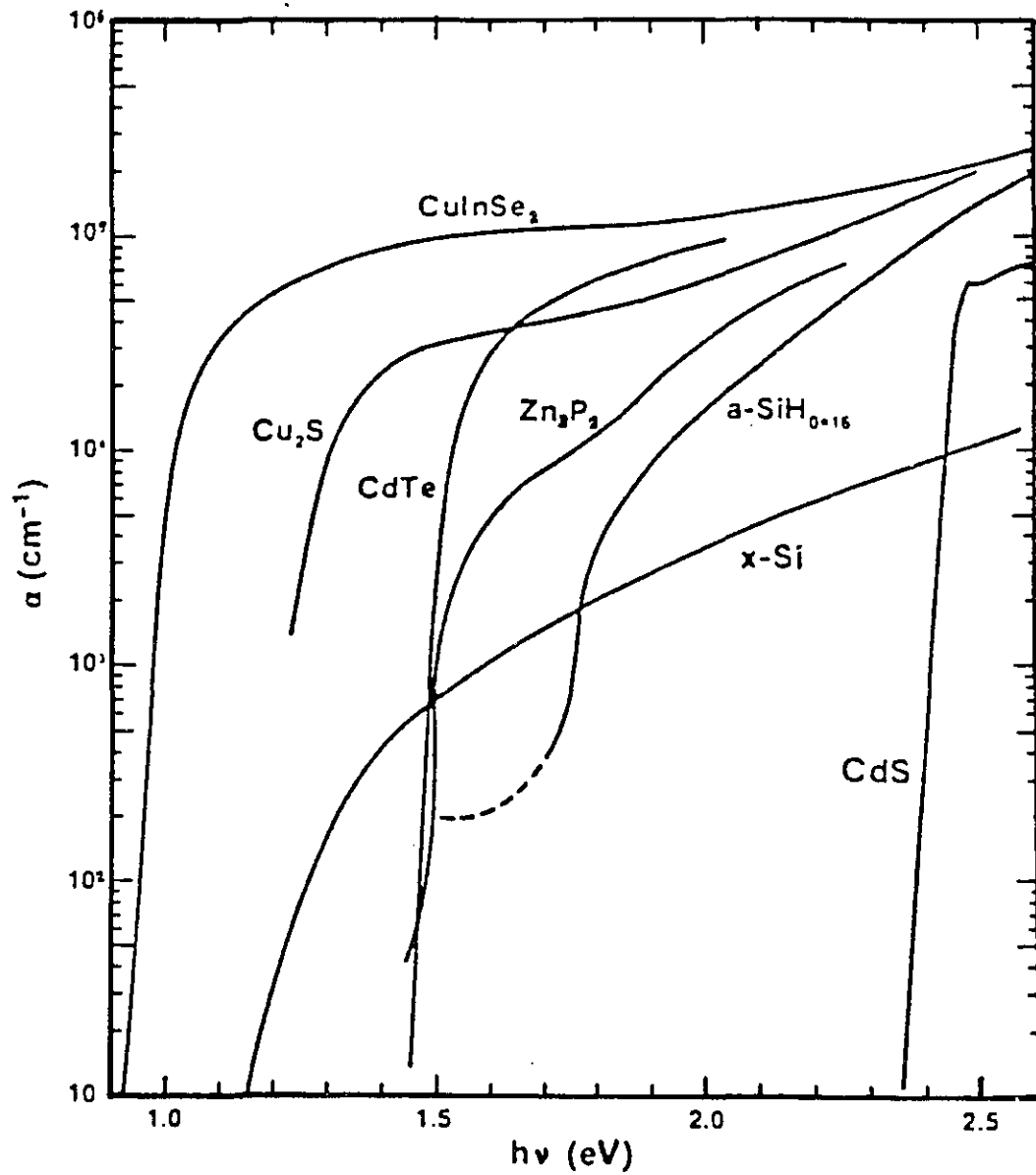
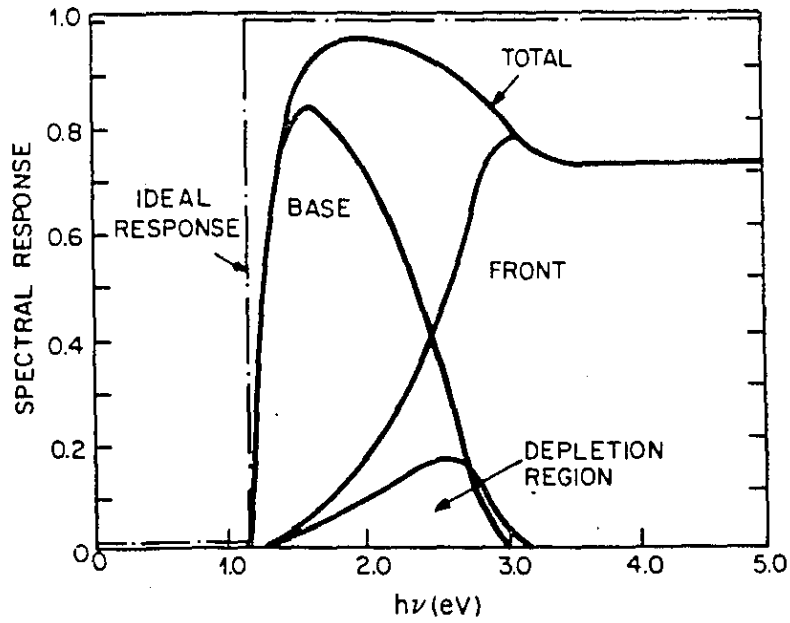
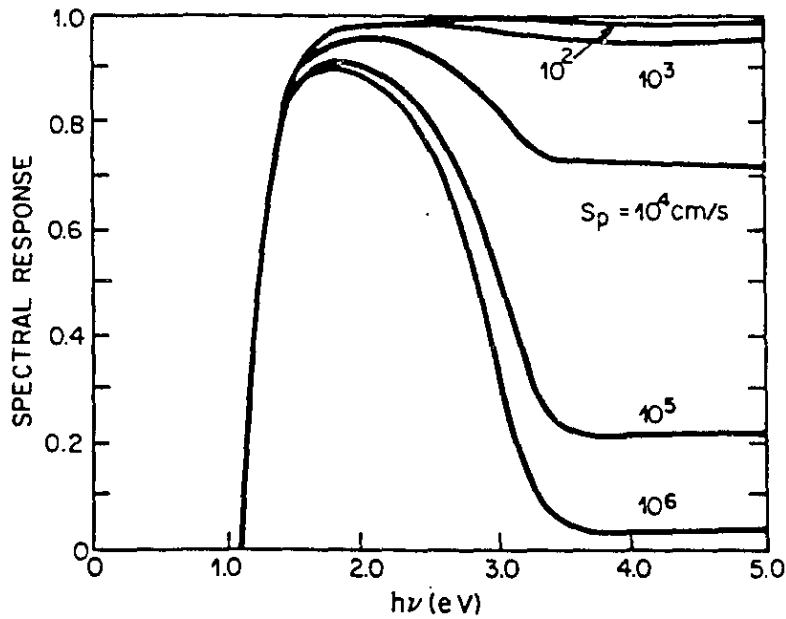


Fig. 2.2 Absorption coefficient for some semiconductor materials as a function of photon energy (after ref. 2.1).

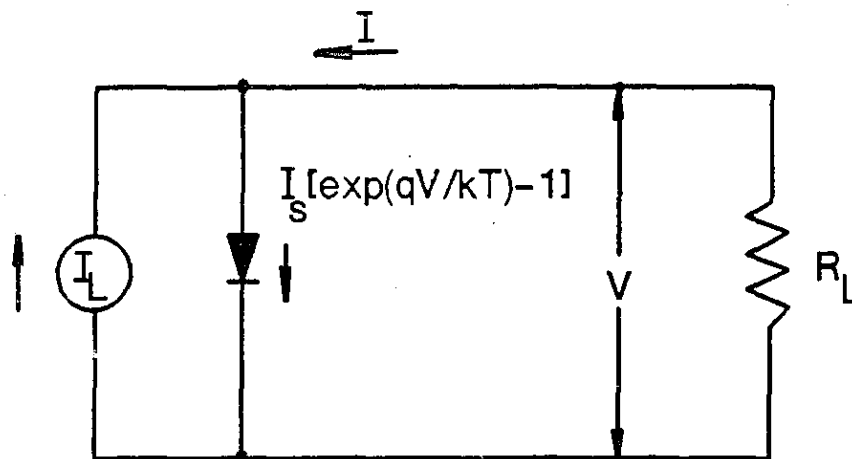


(a)

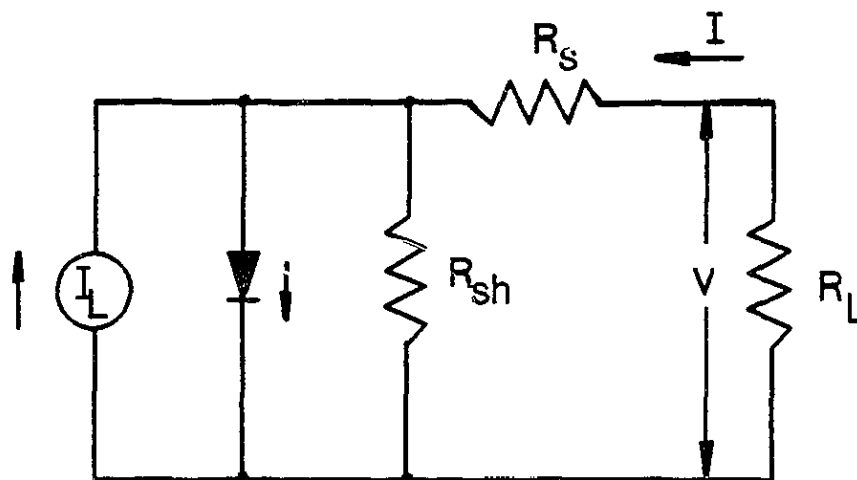


(b)

Fig. 2.3 Calculated spectral response of a Si n-on-p cell (a) showing the response components due to the three regions and (b) the response for the device with different surface recombination velocities (after ref. 2.2).



(a)



(b)

Fig. 2.4 Equivalent circuits of (a) an ideal p-n junction under the illumination and (b) a practical junction with a series resistance R_s and a shunt resistance R_{sh} .

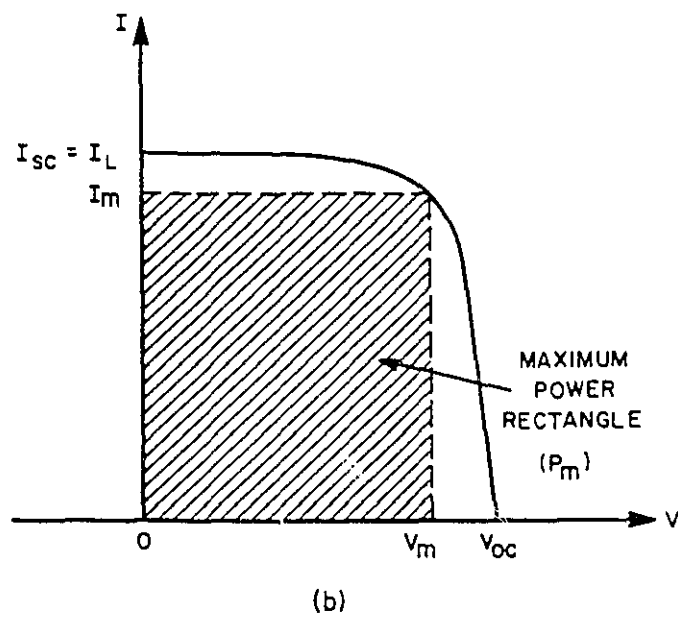
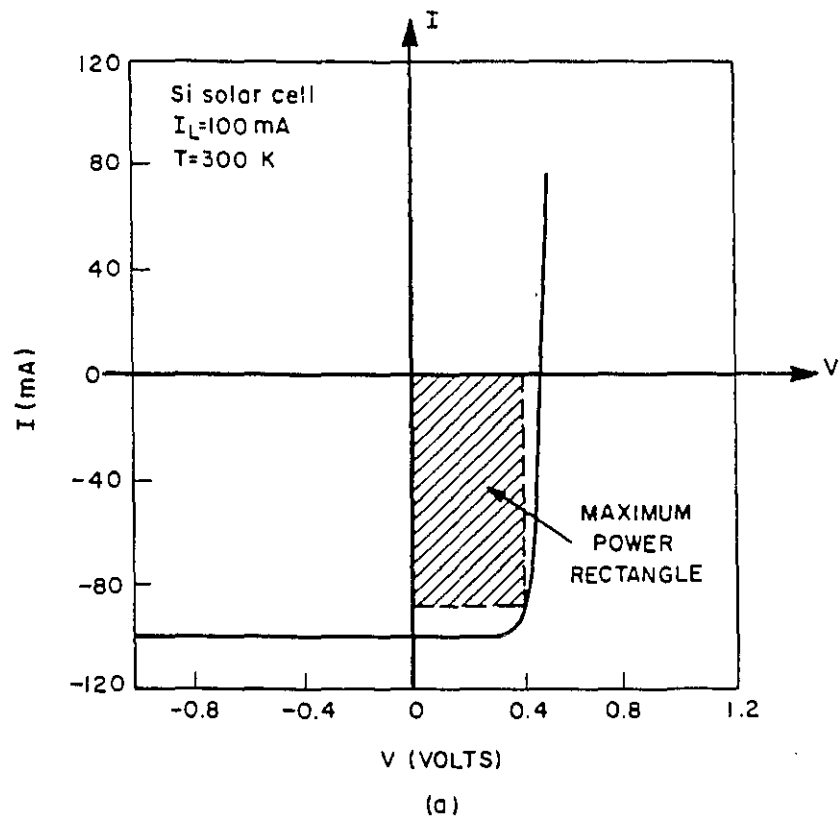


Fig. 2.5 (a) I-V characteristics of a Si solar cell under illumination. (b) Inverse of (a) (after ref. 2.3).

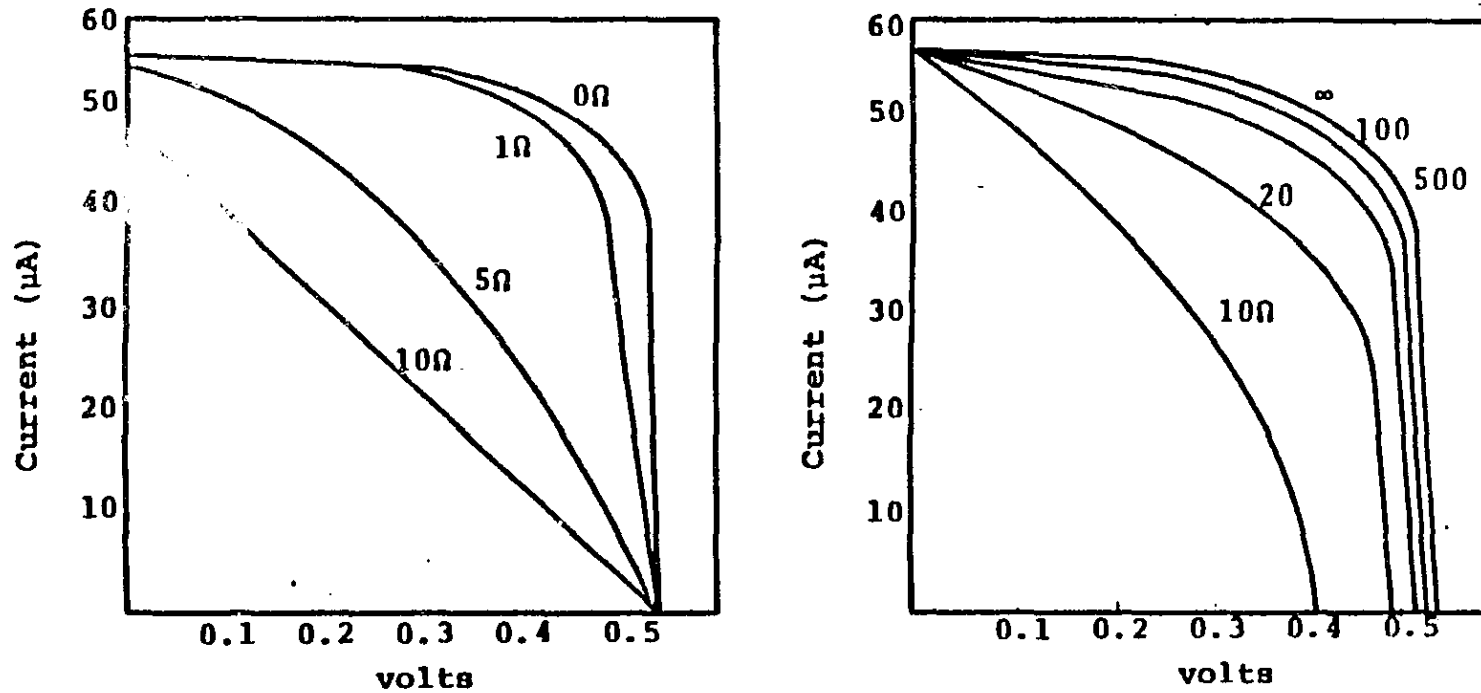


Fig. 2.6 I-V characteristics of a p-n junction showing (a) the effect of series resistance and (b) the effect of shunt resistance.

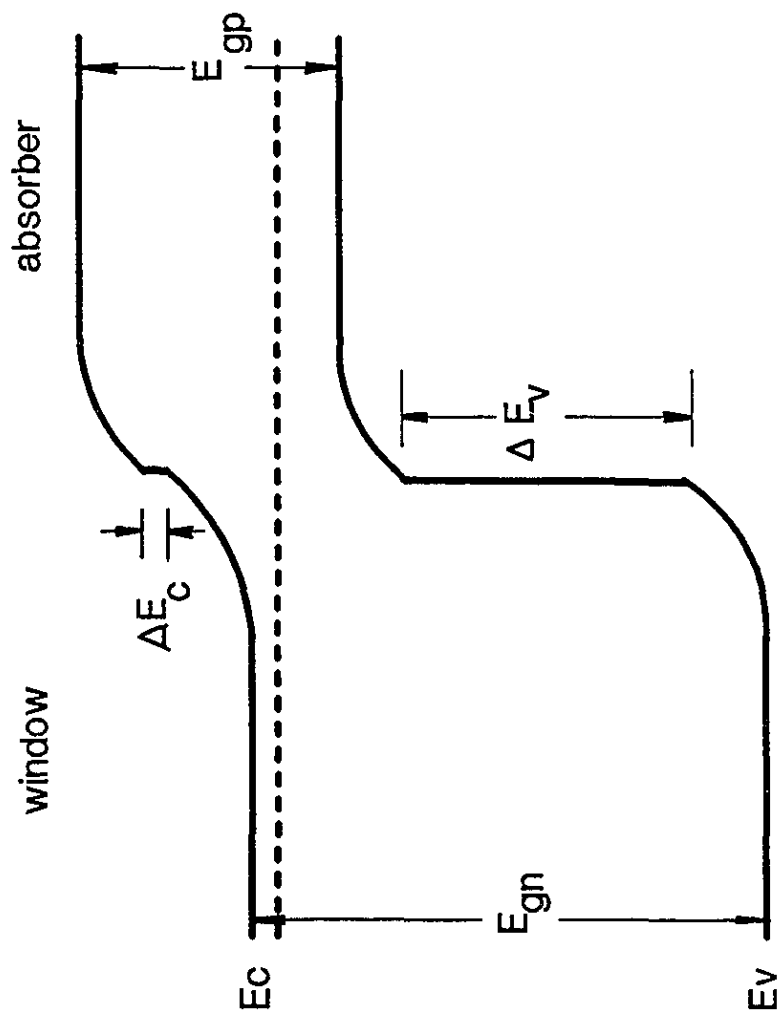


Fig. 2.7 Energy band diagram of an n^+p heterojunction.

Chapter 3 DEPOSITION AND CHARACTERIZATION OF CuInSe₂ THIN FILMS

3.1 Introduction

The electrochemical deposition method has long been used in industry for metal film plating. This technique has been adopted for mass production because the required equipment is inexpensive and the process can be easily controlled. Furthermore, the energy consumption is small and the material utilization rate is high. The electrodeposition method has also been used for the deposition of binary semiconductor compounds such as CdTe^{3.1,3.2}. In 1983, Bhattacharya reported that the ternary compound material CuInSe₂ can be deposited by using the electrodeposition method from a single non-aqueous solution^{3.3}. He made this claim based on X-ray diffraction results of his films. However, he did not realize the similarity between X-ray diffraction patterns of the CuInSe₂ phase and Cu_{2-x}Se phases in this compound system. The method reported by Bhattacharya was studied by Hodes and Cahen^{3.4} later and they found that the deposited films were Cu_{2-x}Se. Hodes and Cahen have also made an effort to develop an alternative process for the CuInSe₂ films. They first deposited a layer of In/Cu alloy then carried out chalcogenization in H₂Se to form the CuInSe₂ films. However, they had difficulties in controlling the morphology of the films. In 1986,

Bhattacharya et al^{3.5} reported their results on the deposition of CuInSe₂ films from a single bath. Again, control over the film composition appeared to be a problem.

The electrodeposition technique has been used in our laboratory for the deposition of semiconductor films^{3.6,3.7}. This technique has been successfully used for the deposition of CuInSe₂ thin films long before the first publication^{3.8}. Since then thousands of samples have been prepared. The quality of the deposited CuInSe₂ films was found to be satisfactory for photovoltaic applications. More recently, results of electrodeposition of CuInSe₂ have been reported^{3.9,3.10}. In this chapter, the deposition process and the film study results will be briefly described. Details of processes and results will be published separately.

3.2 Film Deposition

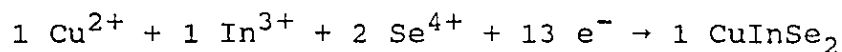
The system shown in Fig. 3.1 was used for the deposition of CuInSe₂ thin films. In the system, a glass crucible was used as the deposition chamber to contain the electrolyte. Two electrically conducting plates, placed face to face in the chamber, acted as anode and cathode respectively. During the deposition, a conducting substrate was used as the cathode and a platinum foil was used as the anode. A dc power supply connected between the anode and the cathode was employed to supply the electrical current and to drive the ions in the electrolyte in the desired direction.

It has been reported^{3,11} that molybdenum can make a good ohmic contact with the p-type CuInSe₂ films. Therefore, in the initial part of the experiments, CuInSe₂ films were deposited on molybdenum sheets with a thickness of 100 μm. In the subsequent deposition runs for solar cell fabrications, glass slides coated with a molybdenum layer were used to obtain good quality CuInSe₂ films. The thickness of the Mo coating layer was 0.8 μm. In addition to molybdenum, tungsten plates were also used in the initial experimental runs.

For all of the three substrates, a cleaning process before the deposition was always carried out. For the Mo sheets, a diluted aquaregia solution (1:1 with water) was first used to etch the surface (for about 30 seconds) and these were then rinsed with DI water. The etching time had to be controlled to avoid the formation of an uneven surface. A hot H₂O₂ solution (temperature above 40°C) was used to etch the W sheets (for about 1 minute). The substrates were then rinsed with water. For the Mo coated glass substrates, they were etched in a pure H₂SO₄ solution for about 30 seconds then followed by rinsing. For most of the experiments, the substrates were not dried before immersion in the electrolyte. However, it was found that drying the substrates by blowing with N₂ or Ar gas, before the deposition, gave better results.

The electrolyte used for the deposition was an aqueous solution containing ions of Cu²⁺, In³⁺ and Se⁴⁺ and complexes of these ions, which would move from anode to cathode under the influence of an electric field. After the electrolyte was pre-

pared, the cleaned substrate was immersed in it and a current was passed between the two electrodes. The reaction for the CuInSe₂ film deposition can be represented by the following simplified equation:



After the deposition of CuInSe₂ was completed, the substrate was removed from the chamber and washed with DI water and an another substrate was then loaded into the chamber to continue the deposition. The thickness of the CuInSe₂ films was controlled via the deposition time. A typical thickness of 2 μm was obtained after 20 minutes of deposition.

During the deposition, the temperature of the electrolyte was controlled to a value in the range of 25°C - 90°C and the pH value of the electrolyte was chosen in the range from 1 to 6. It was found that the deposition rate was affected by both the solution temperature and the pH values. The higher the temperature and the smaller the pH value, the larger the deposition rate was. In order to obtain a uniform film, a stirrer, controlled by a dc motor, was placed between the two electrodes to agitate the electrolyte. The stirring rate was also found to affect the deposition rate. It was observed in the present work that large deposition rates sometimes resulted in non-uniform deposition in the edge regions of the substrate.

The texture of the films under optical microscope was found to be similar to that of the substrates. The films on the Mo coated glass substrates were smooth and shiny while the ones on

the Mo plates showed a texture of the etched substrates. Furthermore, the morphology of the CuInSe_2 films was found to be affected by the metal ratio in the films. Films with a Cu/In ratio larger than unity usually showed a bluish color with very fine grains. A light gray color and larger grains were always observed for In-rich films.

In order to test the process for large area depositions, a deposition system with an inner diameter of 12.5 cm was used to deposit films with an area up to $10 \times 10 \text{ cm}^2$. For these deposition runs, an anode with an area close to that of the film was used for a better control of uniformity. The deposited CuInSe_2 films were found to be uniform with uniform edge regions.

3.3 Adhesion of the CuInSe_2 Films to the Substrates

After the deposition, a pulling test was carried out on these samples to determine the film adhesion: A piece of adhesive tape was applied to the film and the tape was pulled up. The deposited films were found to have very good adhesion to the two kinds of substrates. Examination under an optical microscope on the CuInSe_2 samples after the pulling test showed continuous films without visible defects.

3.4 Film Characterization

For the electrodeposited CuInSe_2 films, the following methods were used to investigate the compositional and structural quality: Scanning Electron Microscopy (SEM), X-ray diffraction (XRD), Electronprobe Microanalysis (EPMA) and Secondary Ion Mass

Spectroscopy (SIMS). The XRD technique was used to determine the crystalline structure and preferred orientation of the films. The micro structure of the films, the film thickness, smoothness and macro defects were examined using the SEM. EPMA was used to determine the overall composition while the SIMS was used to determine the vertical distribution of the elements in the films. In the following sections, results for all of the above mentioned analyses will be presented.

3.4.1 SEM Photographs

SEM photographs were taken for the CuInSe_2 films fabricated on both the Mo and the Mo/glass substrates. Fig. 3.2 shows top views of two samples, one on the etched Mo sheet (a) and the other on the Mo/glass substrate (b). It is seen that the film on the etched Mo plate substrate has a roughly vertical texture which is similar to that of the substrate (not shown). The film deposited on the Mo coated glass plate is very smooth with fine grains. The cross-sectional view of a CuInSe_2 film deposited on the Mo/glass substrate is shown in Fig. 3.3. Here it is evident that the film has a very uniform thickness and a smooth surface. In addition, a columnar structure is visible with the long axis perpendicular to the surface of the substrate. Each column in the film represents a single grain. This columnar structure has also been found in high quality CuInSe_2 films prepared by vacuum methods^{3,12}. Such a columnar structure is important for hetero-junction device fabrication involving CdS. From the X-ray diffraction, the direction of the columnar grains of the films was

found to coincide roughly with the direction of the (112) plane of the chalcopyrite structure. The lattice mismatch between this plane and (001) plane of CdS is only 1.2%.

It should be pointed out that the quality of the electrodeposited CuInSe_2 films is greatly affected by the quality of the substrates, because of the nature of the electrodeposition technique. An improper treatment of the substrates will result in defects (for example, voids) in the substrates which will affect the CuInSe_2 films. For example, Fig. 3.4 shows a CuInSe_2 film with a localized void (diameter about $3 \mu\text{m}$) on top of a smaller void in the Mo film. This void in CuInSe_2 will result in a short circuit if a conducting top layer is deposited directly on the CuInSe_2 film by the conventional vacuum method.

3.4.2 X-ray Diffraction (XRD)

The principle of the XRD technique can be understood by examining Fig. 3.5. In this diagram, the sample to be examined is placed in the chamber with an X-ray source and a detector. During the testing, an X-ray beam is incident on the sample surface while the sample and the detector rotate in the same direction with different angular velocities. The velocity of the detector is twice of that of the sample so that the angle between the incident beam and the sample (θ) is always equal to half of the angle between the incident beam and the diffracted beam. The intensity of the diffraction beam is recorded with respect to the angle, 2θ , and displayed on a recorder. When the sample is rotated to an angle θ and part or all of the material in the

sample satisfies the Bragg's Law:

$$n \lambda = 2d \sin \theta \quad (3.1)$$

(here, n is an integer, λ is the wavelength of the X-ray and d is the lattice spacing), then a diffracted beam can be detected. By rotating the sample over a range of angles and recording the diffracted peaks, information on the crystalline quality can be obtained.

In the experiments, a Phillips model PW1710 diffractometer with a Cu $K\alpha$ radiation (wavelength 1.54 Å) was used. The diffraction results obtained for the electrodeposited CuInSe_2 were compared with the powder CuInSe_2 data of American Society for the Testing and Materials (ASTM data). It was found that all of the films with In/Cu ratio greater than 1 had a single phase chalcopyrite structure. A second weak phase could also be detected for the films deficient in In. The X-ray pattern for one of the CuInSe_2 films (sample No. 1306, In/Cu > 1) deposited on the Mo plates is shown in Fig. 3.6. All the peaks shown in this pattern were identified to belong to the polycrystalline CuInSe_2 and the Mo substrate. From the X-ray pattern, one can also see that the ratio of the height of the (112) peak to that of the (204) peak is about 2.5, which is much greater than the value of 0.7 for a randomly powdered sample from ASTM data. This result indicates that the deposited CuInSe_2 films have the preferred (112) orientation, which is the desired orientation for CdS/ CuInSe_2 devices. Such an orientation will yield heterojunction devices with a minimum interface mismatch^{3,13}. Moreover, the lattice constant

deduced from the present X-ray results was found to be close to the data reported for CuInSe_2 .

Another interesting fact to be pointed out is that the CuInSe_2 films deposited on both the Mo sheets and the Mo/glass substrates have the same structure with the same preferred orientation even though the orientations of the Mo sheets and the Mo films coated on the glass slides are different (see Fig. 3.7). Therefore, the electrodeposition method developed in the present work can be used favorably for the preparation of CuInSe_2 films for the solar cell fabrications.

3.4.3 Electron Probe Micro Analysis (EPMA)

Wavelength dispersive electron probe micro analysis (CAMECA Analyzer) was carried out to determine the composition of the deposited CuInSe_2 films and to examine the uniformity of the elemental distribution. The sample to be examined was loaded into the chamber of the system and the chamber was evacuated to 10^{-6} Torr. An electron beam (current 10 nA) was ejected from an electron gun (accelerating voltage 15 kV) and directed onto the sample. The induced X-ray from the sample was detected by detectors and the data was analyzed to give the composition results (see figure 3.8).

From the EPMA experiments, it was found that the distribution of the three elements was uniform over the entire sample area for all of the samples. Furthermore, a slight excess of Se was found in most of the CuInSe_2 films. As an example, Fig. 3.9 shows the concentrational distribution of Cu, In and Se along one

of the samples, where one can see that the Se concentration is greater than 50%. The Cu/In ratio for the CuInSe₂ film was also found to be essentially constant over an area of up to 9 cm², which was very important for the control of electrical resistivity in the films.

The stability of the electrolyte, when depositing for more than 10 samples one after another, was also studied through the composition using the EPMA method. The results obtained are shown in Fig. 3.10 where the elemental concentrations are plotted versus the deposition runs. It can be seen that the composition of the 11 samples was essentially constant. Results from a separate set of experiments showed that the same electrolyte can be used to deposit more than 50 samples before replenishment is necessary.

3.4.4 Secondary Ion Mass Spectroscopy

Secondary Ion Mass Spectroscopy (SIMS) is a powerful method for surface analysis especially in depth profiling of compound semiconductor thin films. A schematic diagram of the SIMS system is given in Fig. 3.11. During the analysis, the sample under study is bombarded by an energetic primary ion beam. The primary ions incident on the sample surface will knock out atoms and molecules. Some of the atoms and molecules are charged (secondary ions). The composition of the secondary ions is related to that of the sample at the location of the bombardment. By collecting and analyzing these secondary ions, the composition of the sample can be obtained. For the depth profile analysis, the material is

removed continuously by the primary ions and the probing results are recorded as a function of depth.

In order to investigate the depth profile of the CuInSe_2 films, three samples deposited on Mo/glass substrates with a thickness of $4 \mu\text{m}$ were selected for SIMS analysis. A square with an area of $100 \times 100 \mu\text{m}^2$ was sputtered and analyzed. The results for one of the samples are shown in Fig. 3.12. Here the counts per second for all three elements are plotted against the distance from the surface. One can see that the distribution for Cu, In and Se is essentially uniform over the film thickness. This property of uniformity is very important for junction fabrications.

3.4.5 Hot probe

Hot probe measurements were carried out to determine the conducting type of the electrodeposited CuInSe_2 films. Samples with different composition (with the metal ratio varying in the range from $\text{Cu/In} < 1$ to $\text{Cu/In} > 1$) were selected for the measurements. It was found that all of the samples tested were p-type films. In table 3.1, the composition (from EPMA data) and the conducting type for 14 samples are given. It is noted that the films are p-type even for the one with deficient Se and Cu (CTN 3473). This may be due to the presence of oxygen atoms in the electrodeposited CuInSe_2 films. High resistivity n-type films (with composition $\text{Se/metal} > 1$ and $\text{Cu/In} < 1$) reported by Noufi^{3,14} using a vacuum method was not obtained in the present work using the electrodeposition method.

3.5 Conclusions

Using the electrodeposition technique, a stable process has been developed for the deposition of CuInSe_2 thin films with thicknesses in the range of 1-4 μm . The quality of the films was found to be suitable for the fabrication of optoelectronic devices. The crystalline quality of the films, examined by XRD, was observed to be close to that obtained for the vacuum deposited samples. A preferred (112) orientation was readily obtained on both molybdenum plates and Mo-coated glass substrates. The concentration distributions, which are very important for photovoltaic device applications, both over the sample area and across the film thickness were very uniform. A slight excess of Se was found in most of the deposited films. The columnar structure, which was always found in vacuum deposited CuInSe_2 samples was also observed in the electrodeposited CuInSe_2 films.

Since the electrodeposited CuInSe_2 films adhere well to the Mo substrates, separation of the films from the substrates without damage to the films was not possible. Thus, the electronic properties of the CuInSe_2 films, such as resistivity, carrier concentration and mobility of the majority carriers, are not obtainable at this stage. However from hot probe measurements, the CuInSe_2 films deposited by the electrodeposition method, with the Cu/In ratio varying from smaller than unity to greater than unity and with the Se/metal ratio greater than 1, were all found to be p-type. Preliminary four point probe results were also obtained on two small samples separated from the Mo/glass substrate

(thickness of about 1.3 μm). The sheet resistance was about 10.3 Ω/square , yielding a resistivity of about 0.0013 $\Omega\cdot\text{cm}$.

Table 3.1 Hot probe results for as-deposited CuInSe_2 samples with different composition.

Sample No.	Composition(%)			Metal Ratio Cu/In	Conducting Type
	Cu	In	Se		
CTN 3517	24.0	12.8	63.2	1.88	p
CTN 3484	27.0	17.1	55.9	1.58	p
CTN 3489	24.8	18.3	56.9	1.36	p
CTN 3518	22.3	19.0	58.8	1.16	p
CTN 3493	22.4	22.8	54.8	0.98	p
CTN 3471	23.9	24.6	51.5	0.97	p
CTN 3485	20.5	21.5	58.0	0.95	p
CTN 3472	24.0	25.6	50.5	0.94	p
CTN 3473	24.7	26.3	49.0	0.94	p
CTN 3486	21.6	23.9	54.6	0.90	p
CTN 3483	21.4	24.3	54.3	0.88	p
CTN 3482	20.9	24.7	54.5	0.85	p
CTN 3487	20.6	26.0	53.3	0.79	p
CTN 3488	19.3	26.0	54.8	0.74	p

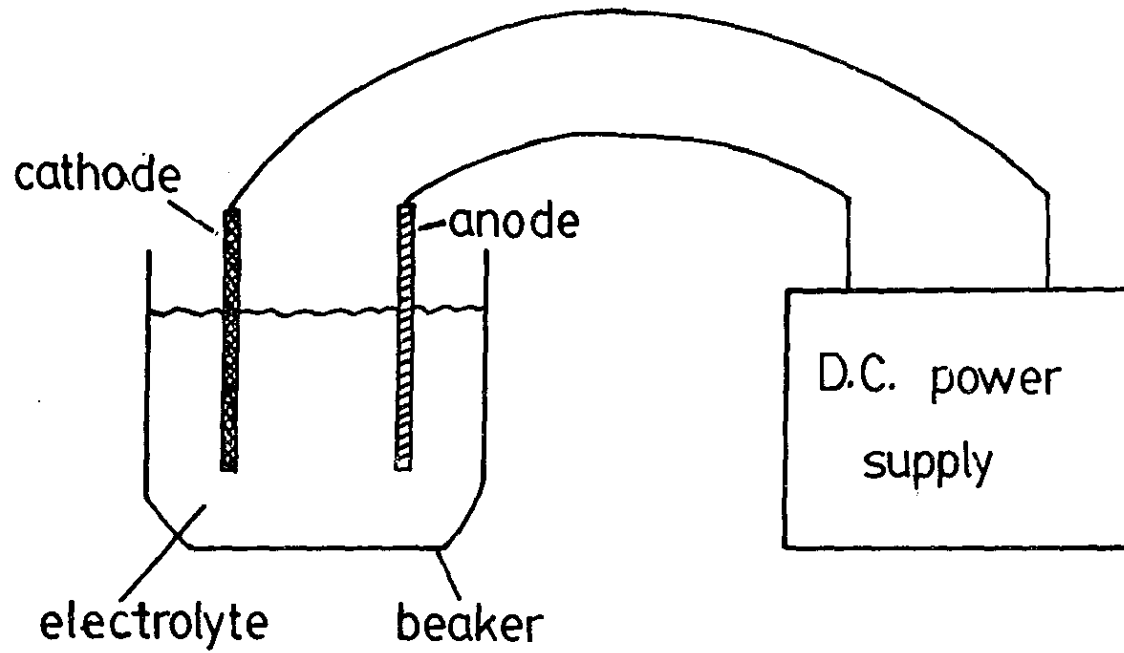
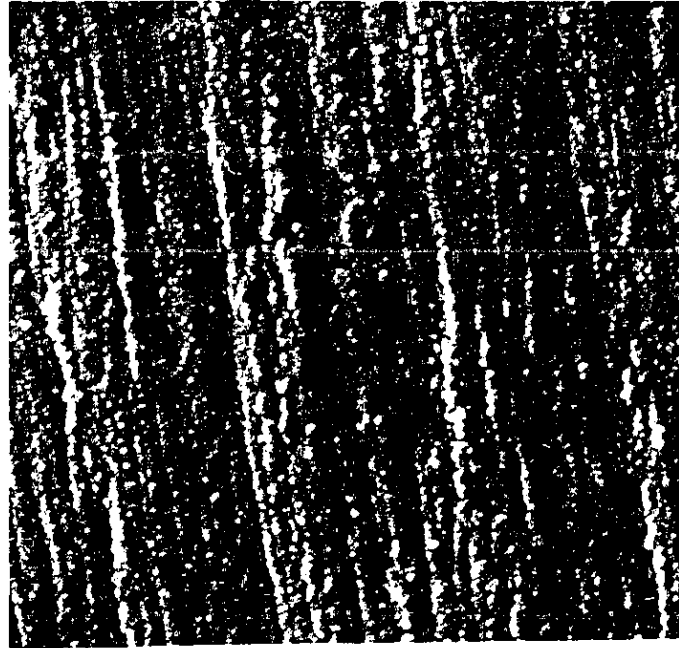
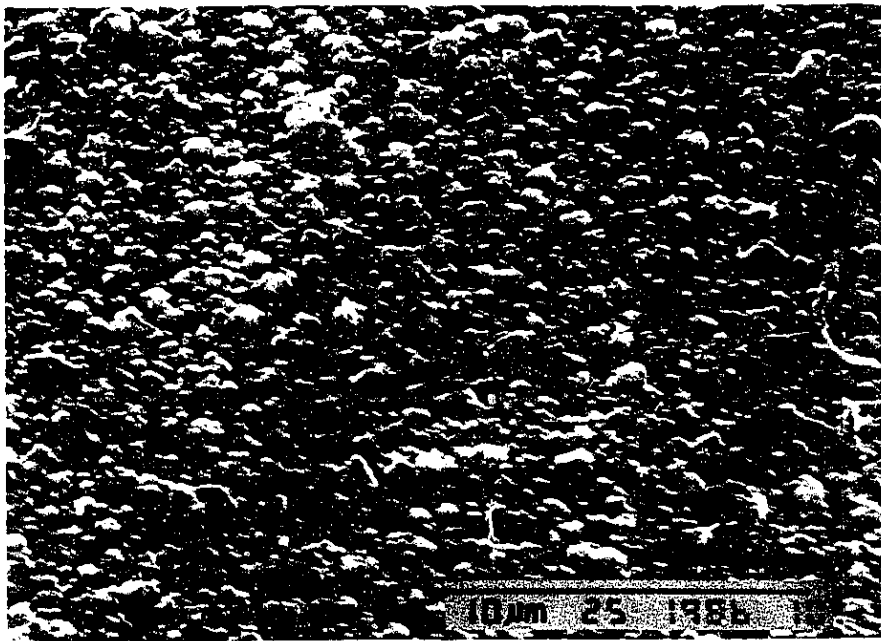


Fig. 3.1 A schematic diagram of the deposition system for the fabrication of CuInSe_2 thin films.



(a)



(b)

Fig. 3.2 SEM photographs showing (a) the morphology of a CuInSe_2 film deposited on a Mo plate and, (b) the surface of a film on a Mo/glass substrate.



Fig. 3.3 An SEM micrograph of a fractured CuInSe₂ film deposited on a Mo/glass substrate showing a uniform CuInSe₂ thickness.

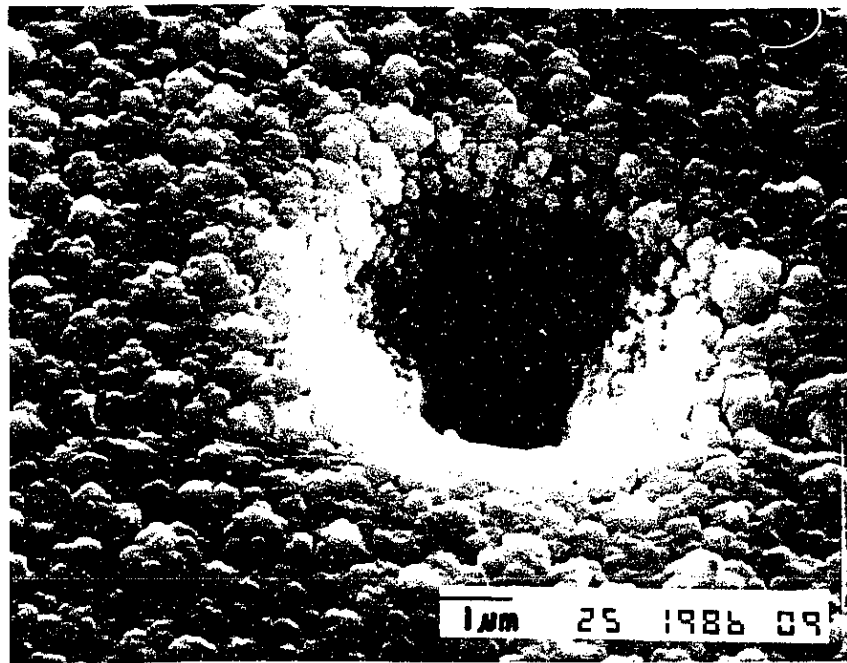
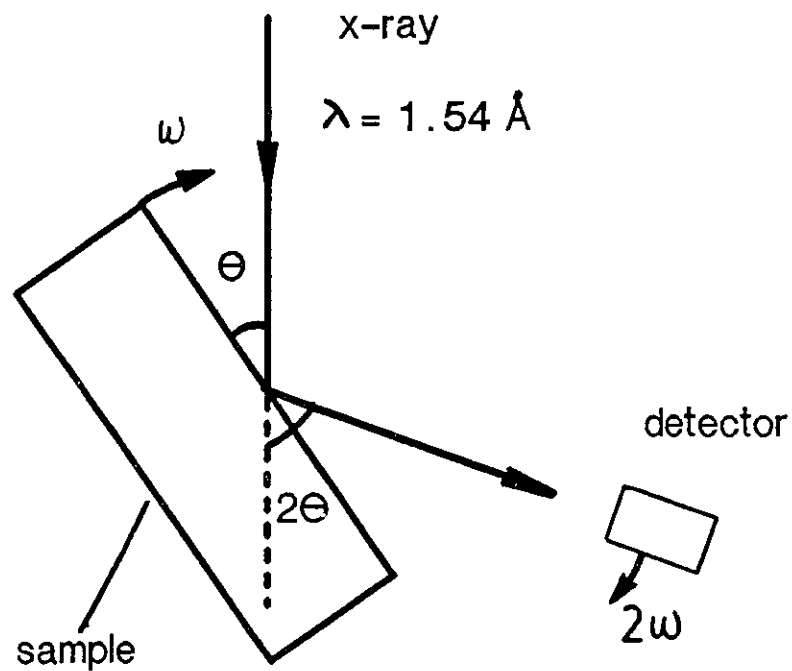


Fig. 3.4 An SEM photograph of a CuInSe₂ film with a localized hole, resulting from a pin hole in the Mo film.



$$2d \sin\theta = n\lambda$$

Fig. 3.5 A schematic diagram of the XRD measurement set up.

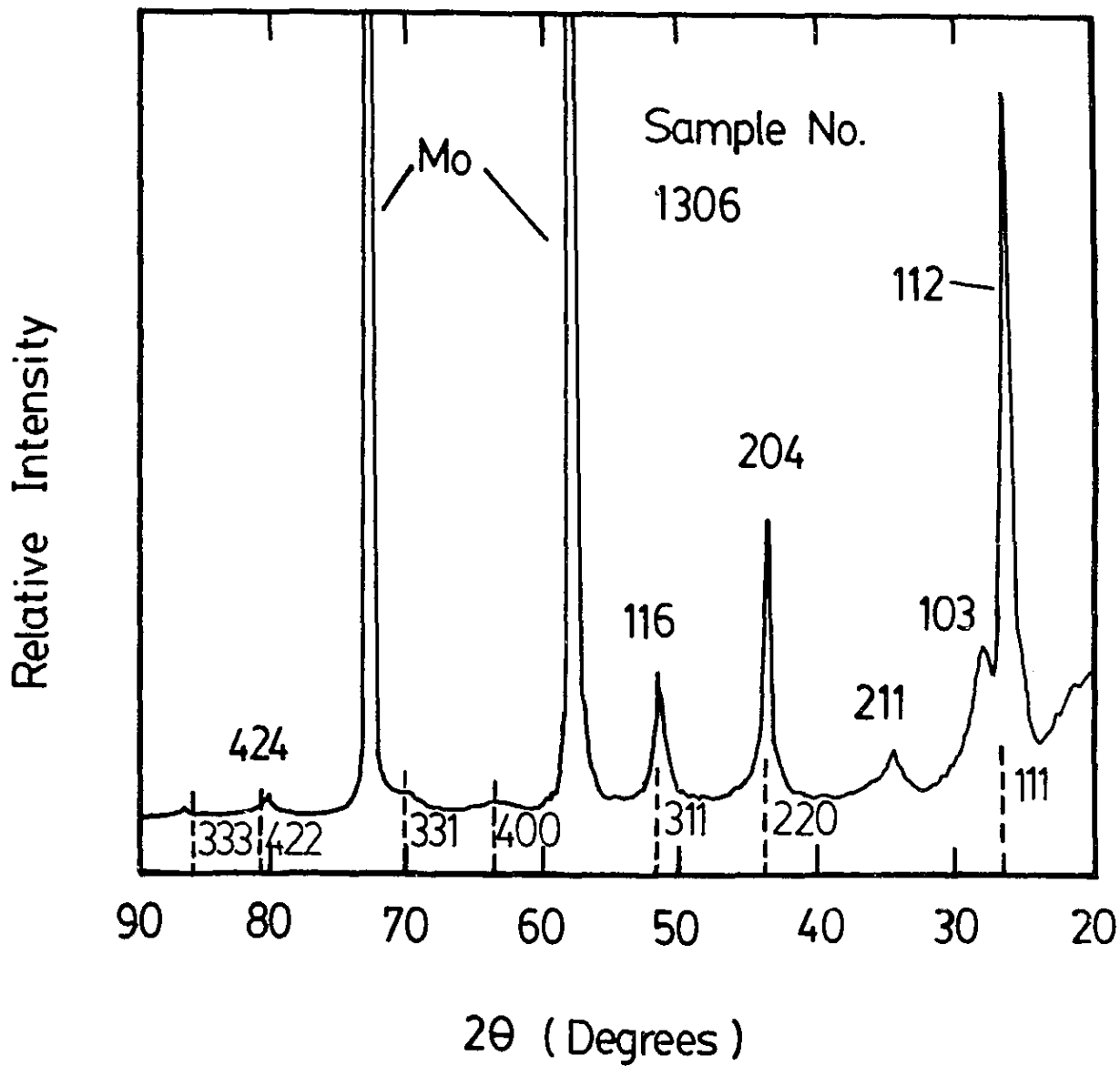


Fig. 3.6 Diffracted X-ray intensity vs. 2θ for one of the as-grown CuInSe_2 sample on a Mo plate. Dashed lines represent the diffracted peaks for $\alpha\text{-Cu}_2\text{Se}$ and are seen very close to the CuInSe_2 .

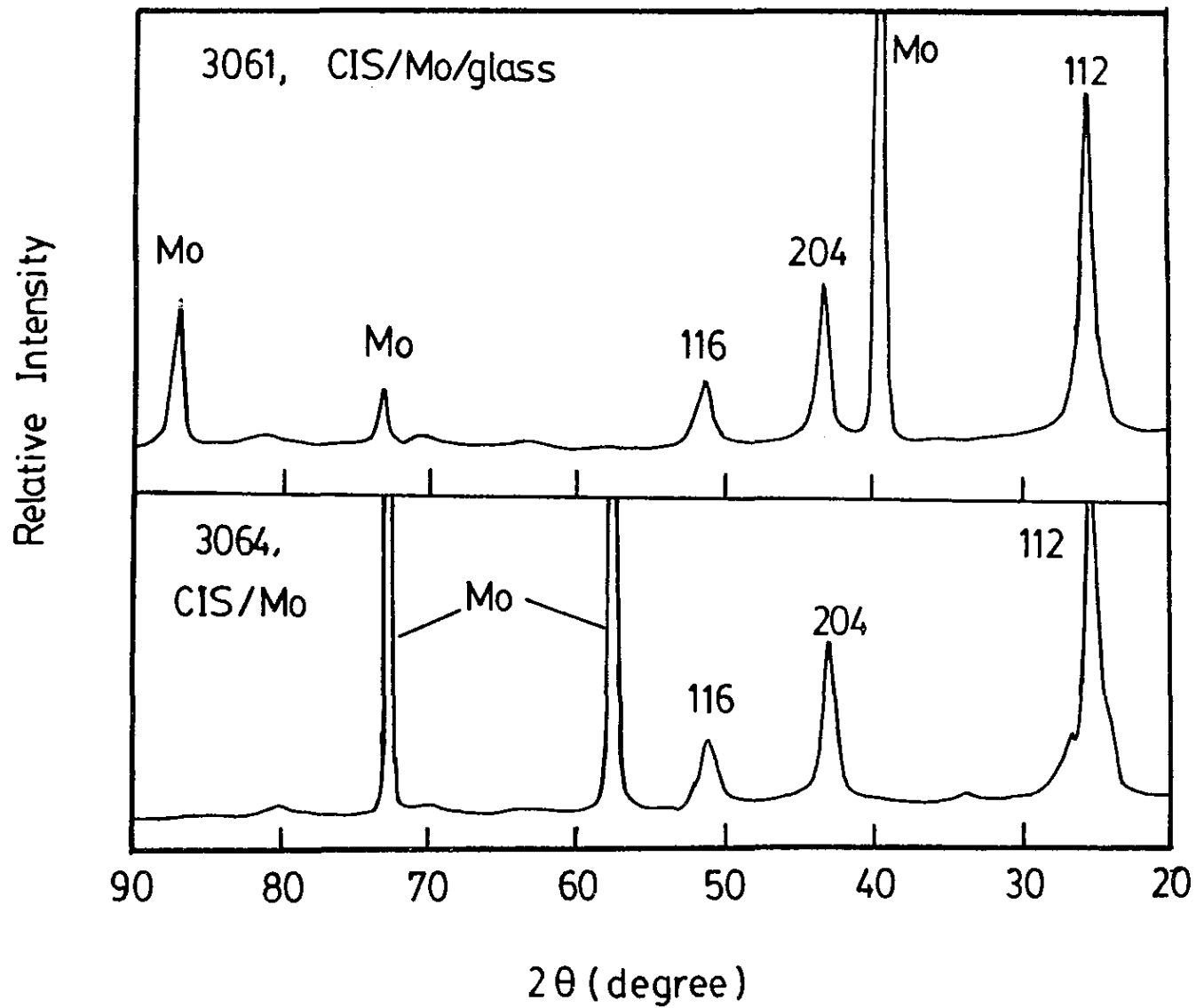


Fig. 3.7 X-ray diffraction pattern showing the same preferred orientation for the films deposited both on a Mo plate and on a Mo/glass substrate.

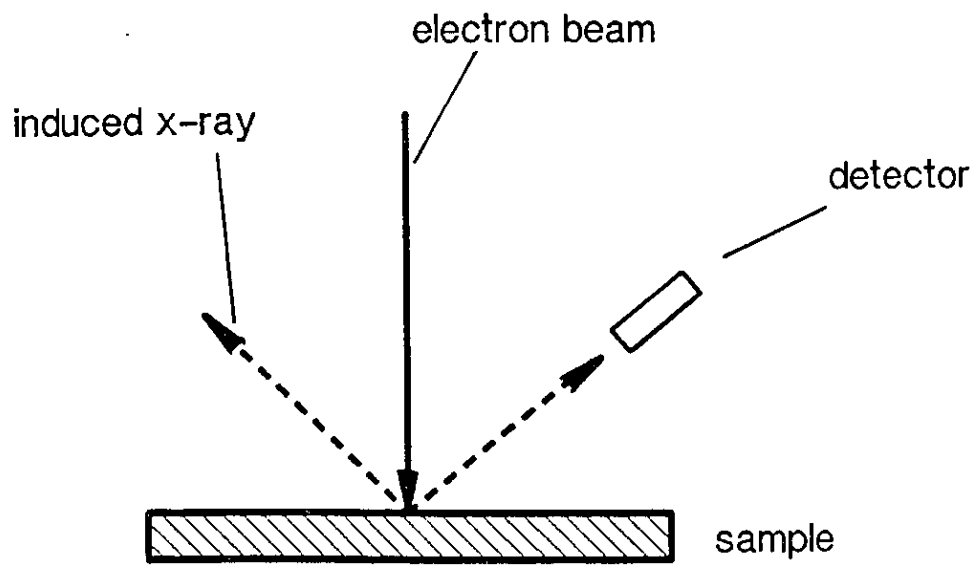


Fig. 3.8 A schematic diagram showing the principle of the EPMA measurement.

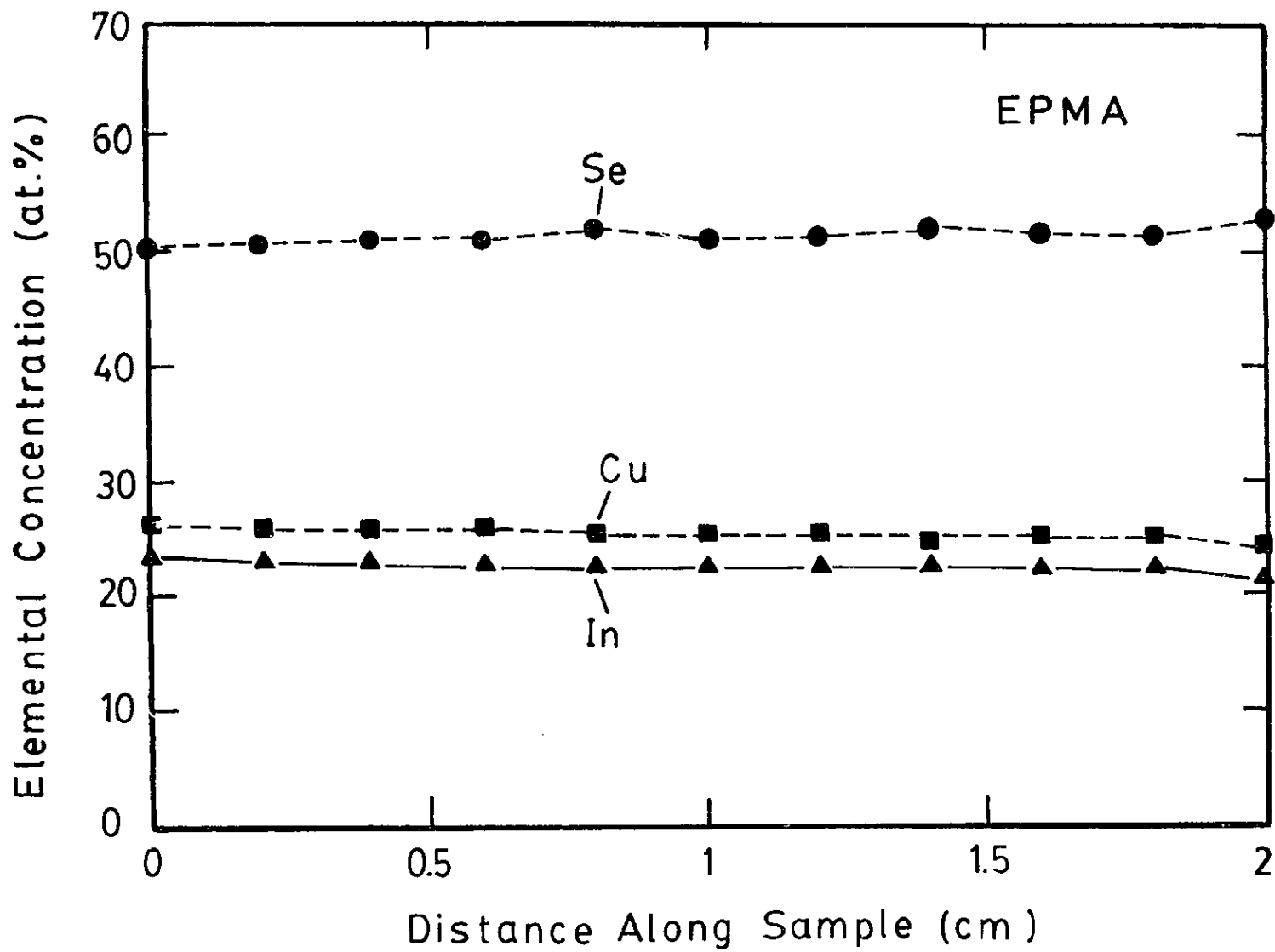


Fig. 3.9 EPMA results across a CuInSe_2 film showing an essentially constant elemental distribution.

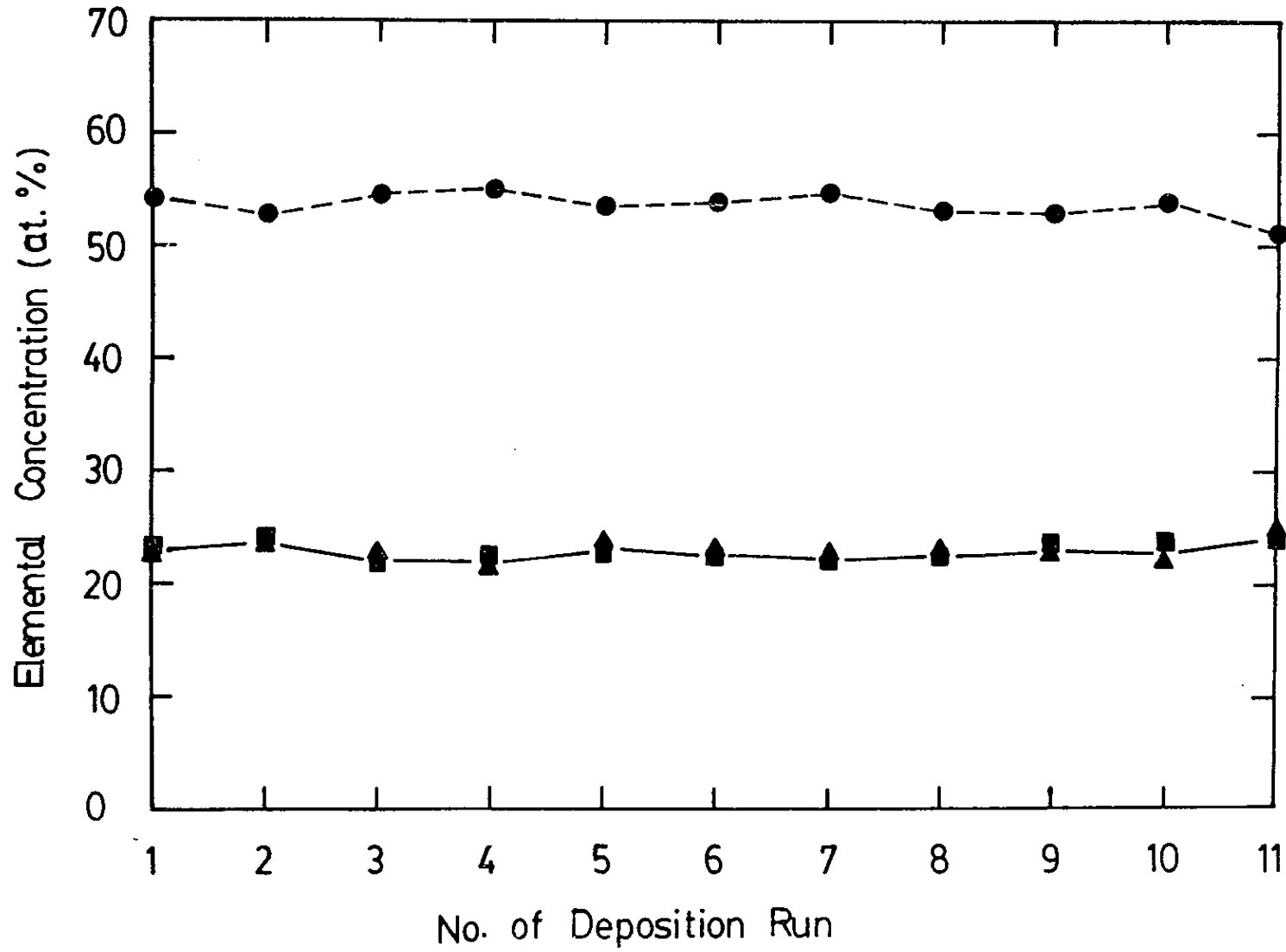


Fig. 3.10 EPMA results showing constant composition for different deposition runs.

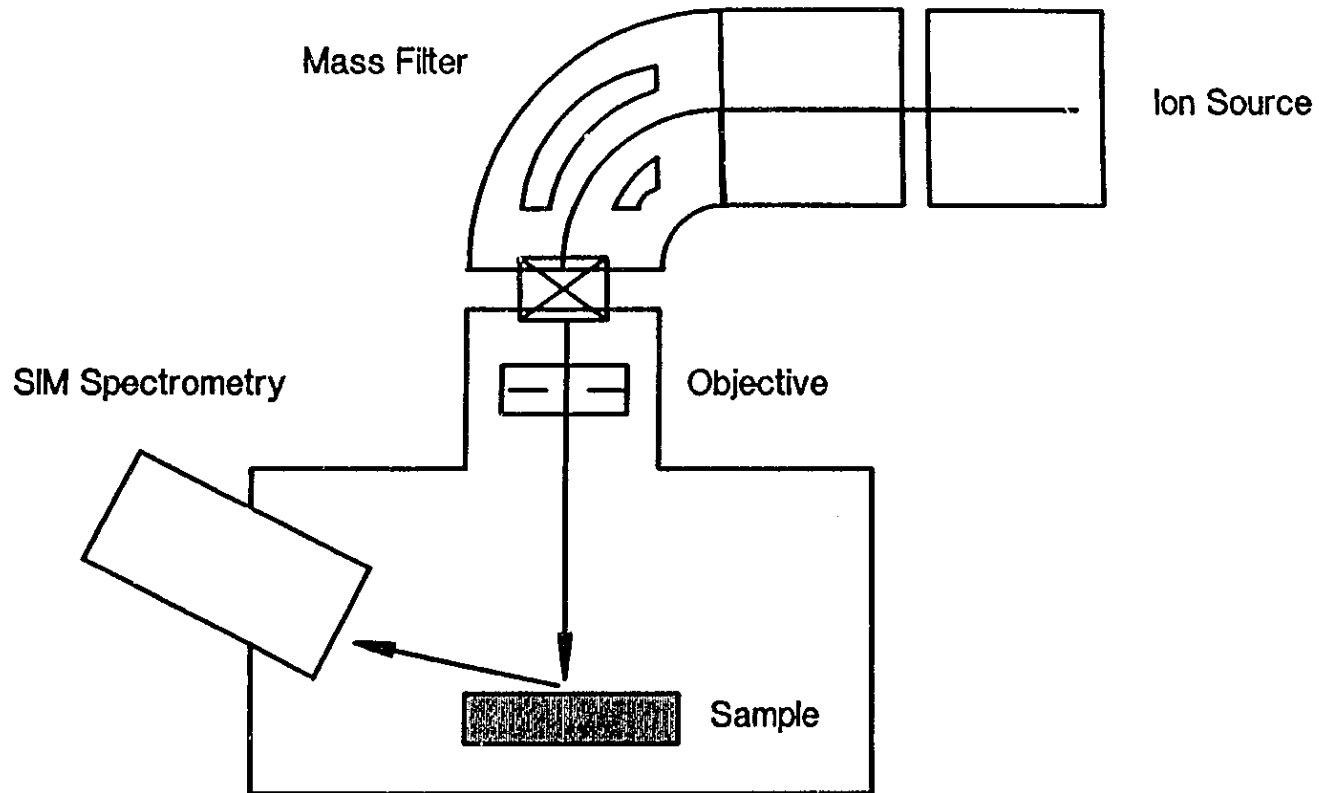


Fig. 3.11 A schematic diagram of the SIMS system.

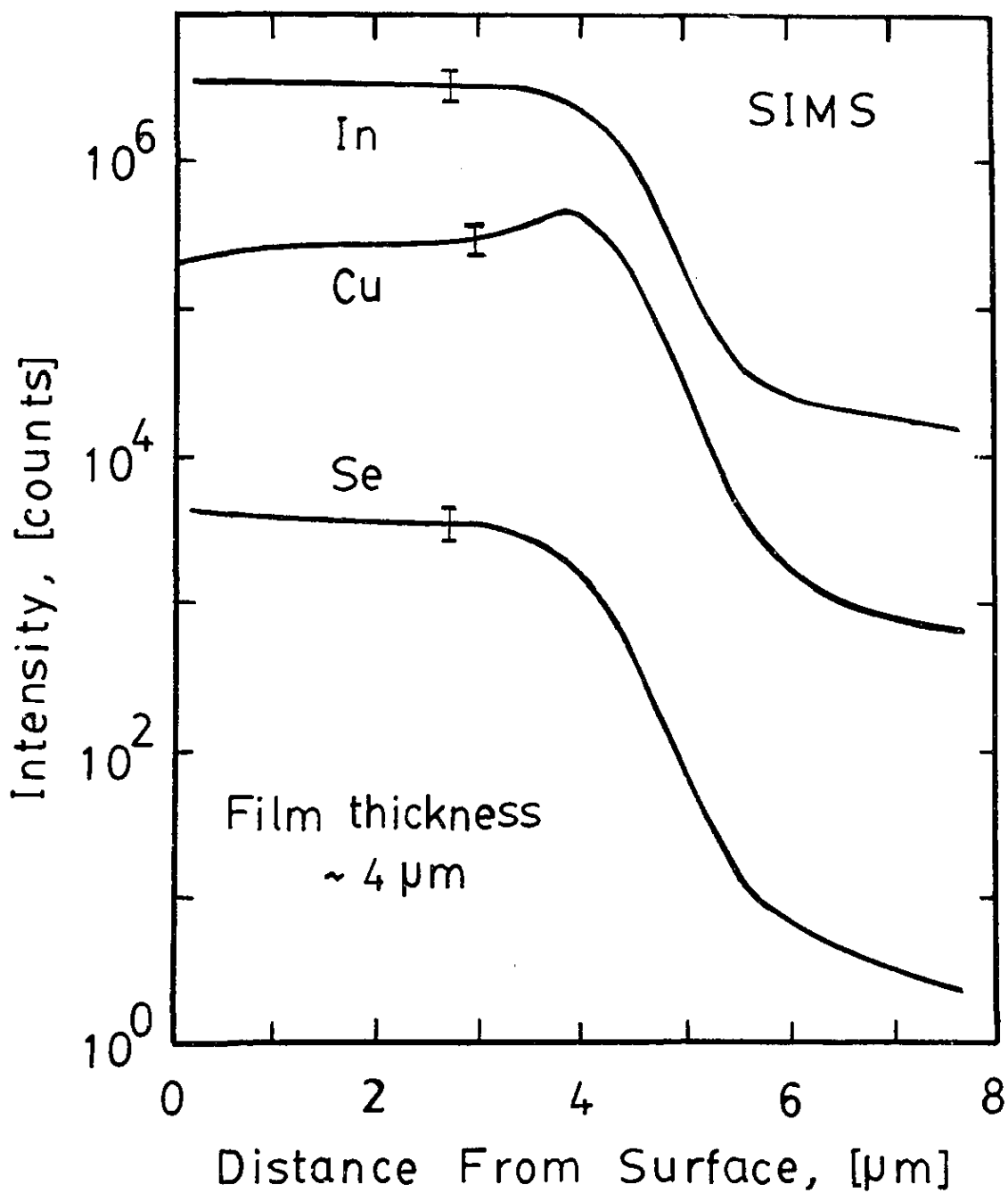


Fig. 3.12 SIMS results for one of the CuInSe_2 films with a thickness of 4 μm , showing essentially constant depth profile of the three elements.

Chapter 4 HEAT TREATMENT EFFECTS OF CuInSe₂ FILMS

4.1 Introduction

For photovoltaic cell applications, the crystalline quality of the CuInSe₂ films is as important as electronic properties. The CdS/CuInSe₂ cells reported by Devaney and coworkers^{4.1} with an efficiency of more than 12% were fabricated using vacuum deposited CuInSe₂ films. In their experiments, quality of the CuInSe₂ films was found to be optimum when the substrate temperature was in the range from 350 to 450°C^{4.2}. Therefore, in their experiments a post deposition annealing for the CuInSe₂ films before the deposition of CdS is not needed.

As described in chapter 3, the electrodeposition of CuInSe₂ films in the present work was carried out at low temperatures (T<100°C). Therefore, a post-deposition heat treatment is necessary to improve further the quality of the CuInSe₂ films. The heat treatment, to be carried out at an elevated temperature, will also vary the composition of the films because of the loss of elements during the treatment. In this chapter, the effects of heat treatment on both the crystallinity and composition of the films will be reported.

4.2 Heat Treatment Experiments

The treatment experiments were carried out in a horizontal furnace (Linberg Heavy Duty) with a temperature range from 200

to 600°C (experimental set-up shown in Fig. 4.1). The samples to be treated were first cut into rectangles of 1.5x3 cm². Quartz tubes with an inner diameter of 1.6 cm and a length of 60 cm with one end sealed, were prepared and cleaned before the treatment. The samples were placed side by side near the closed end in the tube with the surface facing upwards. Before the treatment, the tube was evacuated to a pressure of about 10⁻⁴ Torr by a rotary pump. With the pump still running, the tube with the CuInSe₂ samples in it was introduced into the central zone of the furnace. The heat treatment experiments were usually performed for a period of 5 to 40 minutes.

After the treatment was completed, the tube was withdrawn from the furnace and was cooled to room temperature in about 30 minutes. After the treatment, the surfaces of the samples were examined by an optical microscope and a scanning electron microscope (SEM). It was found from the SEM photographs that there was no visible change in morphology of the films after the treatment (cross-section shown in Fig. 4.2). However, there was a slight change in the color of the films. For the films with excess Se before the treatment, the color generally changed from dark gray to bluish gray. After the treatment, a layer of deposits with red-black color was also found in the inner wall of the part of the quartz tube located at low temperature zone during the experiment.

For some of the vacuum treatment experiments, Se pellets were also placed in the tube (beside the samples) in order to compensate the loss of Se during the treatment. It was observed

that the Se pellets vaporized completely during the treatment (even at a temperature of about 300°C).

Treatment experiments were also carried out in an inert gas in an open chamber and in glass ampoules. The system used for the treatment involving inert gas is shown in Fig. 4.3. Valve No. 1 was closed and valve No. 2 was open at the beginning of the experiments. After the tube was evacuated, valve No. 2 was closed and No. 1 was then opened to let the Ar gas fill the tube. After the above steps had been repeated several times, both valves No. 1 and 2 were closed and the tube was placed in the furnace to carry out the heat treatment. For heat treatment experiments using the ampoules, glass tubes (inner diameter also 1.6 cm) were used instead of quartz tubes. After the samples were put into the glass tube with one end sealed, the tube was evacuated to a pressure of about 10^{-4} Torr and then sealed to make ampoules of about 20 cm long. The ampoule with the samples was then put into the central zone of the furnace for the treatment.

4.3 Effect of Heat Treatment on Composition

After the treatment experiments, the composition of the CuInSe_2 films was determined by Electron Probe Micro Analysis (EPMA) and the results were compared with the data obtained from that before the treatment. Table 4.1 gives the results for six CuInSe_2 samples both before and after the vacuum treatment. Treatment temperatures from 350 to 450°C were used for these samples. Before the treatment, all six samples had excess Se and a Cu/In ratio which was smaller than 1. After the treatment, it

was found that the selenium concentration had decreased by an average amount of about 4 at% for all of the samples and the relative concentration of copper and indium had changed only slightly. There was an average increase in the ratio (smaller than 6.%) and the amount of increase in the ratio seemed to increase with the treatment temperature. These results thus suggest that the Cu/In ratio in the treated CuInSe₂ films can be controlled in the deposition experiment, as long as the post annealing temperature is not too high.

Table 4.2 shows the EPMA results for five vacuum-treated CuInSe₂ samples with different copper to indium ratios. The treatment temperature for the films was fixed at 350°C. The relative concentrations of copper and indium, both before and after the treatment, were also determined and are given in the table. It is clear from the table that the Cu/In ratios for all of the samples did not show a significant change while the average decrease of selenium concentrations amounted to about 6 at%. Furthermore, the selenium in the film after heat treatment was found to be affected by the Cu/In ratio: The larger the Cu/In ratio, the more the loss of Se.

After about 50 heat treatment runs, deposits on the wall of the quartz tube were separated from the tube (thickness of deposits about 10 μm). Samples were then selected and mounted on glass slides for compositional analysis. The results revealed that the deposits on the tube wall consisted mainly of Se with very small amounts of Cu and In (<0.5 at%). This fact confirmed the results obtained in the compositional study of the treated

films.

Compositional investigation was also made for the films annealed in argon gas and that annealed in closed ampoules. The results for four samples treated in argon gas at temperatures in the range from 400 to 600°C are listed in table 4.3. A set of vacuum treated samples with the same annealing temperatures is also listed in the table for comparison. It is seen that the variation of composition for the two sets of films is similar: Se concentration and Cu/In ratios changed in a similar manner. For most of the treated CuInSe_2 samples, the selenium concentration was found to be slightly less than 50%. Moreover, the variation of Cu/In ratio appeared to be affected by the initial film composition. EPMA results similar to those described above were also observed for films treated in the ampoules. However, the loss of Se was found to be smaller for the samples treated in ampoules than those treated in vacuum and in argon gas. This is because the amount of Se vapor transported from the high temperature zone to the low temperature zone during the heat treatment was less.

4.4 Effects of Heat Treatment on Crystalline Quality

The crystallinity of the treated films was examined by X-ray diffraction experiments. In these experiments, the scanning speed and the gain for the intensity of the XRD system was kept to be the same for the samples both before and after the treatment process. Fig. 4.4 shows X-ray intensity as a function of 2θ for two CuInSe_2 samples, one is an as-grown film and the other a film

treated at 350°C for 20 minutes in vacuum. It is obvious that the intensity of the diffraction peaks for the treated sample had increased significantly and the width of the peaks at half height had decreased. In other words, the crystalline quality of the CuInSe₂ films had been greatly improved by the heat treatment at 350°C. The diffraction peaks of the treated films were also compared with the ASTM data and all of the peaks were identified to belong to the single phase chalcopyrite CuInSe₂ with (112) preferred orientation.

The relationship between the diffraction intensity and the treatment temperature for the two strongest diffraction peaks, 112 and 204, was also examined on five samples. All of the five samples were treated in vacuum at temperatures between 200 and 400°C for 20 minutes. The results are shown in Fig. 4.5. It can be seen that the magnitude of the peaks increases as the treatment temperature is increased. A sharp increase in the magnitude is noted at a temperature of 300°C. The result suggests that the treatment temperature should be above 300°C in order to improve the quality of the CuInSe₂ films for device fabrications.

For treatment temperatures higher than 350°C, even stronger diffraction peaks were evident in the X-ray results, however, multiphases were also present. Fig. 4.6, 4.7 and 4.8 show X-ray results for three samples treated at 350, 400 and 550°C respectively. As presented before, the sample treated at 350°C (Fig. 4.6) showed single phase characteristics. Upon examining the X-ray data for the film treated at 400°C, one finds two unidenti-

fied peaks, one at about 31 degrees (2θ) and the other at about 51 degrees (as shown by the arrows in Fig. 4.7). The two peaks are believed to belong to a second phase that exists in CuInSe_2 films treated at the high temperature. The magnitude of the two unidentified peaks was greatest for the film treated at 550°C (see Fig. 4.8). A few more small peaks were also visible. Of these diffraction peaks, the one at 31 degrees (the second diffraction peak in Fig. 4.8) showed the strongest enhancement. The main peaks for the chalcopyrite structure, 112, 204 and 216, were reduced after the treatment at 550°C . This reduction could be a result of loss of the constituent elements due to the treatment.

4.5 Conclusions

In this chapter, the effects of heat treatment on electrodeposited CuInSe_2 films were described. It was found that treatments in vacuum at temperatures between 350 to 400°C significantly improved the crystalline quality of the films. Furthermore, the treatment did not alter the structure of the film when carried out below 400°C . Treatments at temperatures above 400°C resulted in films with multiphases. The second phase was greatly enhanced after the film was treated at 550°C and with a peak magnitude comparable with the chalcopyrite phase.

The composition of the CuInSe_2 films was changed by the treatment process. For all of the samples, the heat treatment resulted in a loss of selenium. However, the relative amount of copper and indium was essentially unchanged for the films treated at 350°C . When the treatment temperature was increased, the

change in the Cu/In ratio appeared to be larger. Similar results were also observed on samples treated in argon gas.

Table 4.1 Compositional results of p-type CuInSe_2 ¹ before and after vacuum treatments at different temperatures. No conducting type change was detected after the treatment.

Sample No.	Treatment Condition		Composition Before H.T.				Composition After H.T.			
	T (°C)	t (min)	Cu	In (at.%)	Se	Cu/In	Cu	In (at.%)	Se	Cu/In
2821	350	20	20.6	25.2	54.3	0.82	22.6	26.3	51.0	0.86
2822	350	20	20.1	24.7	55.2	0.81	22.6	27.2	50.2	0.83
2823	400	20	20.3	26.4	53.4	0.77	22.5	26.6	50.9	0.85
2824	400	20	20.4	25.2	54.4	0.81	23.3	26.1	50.6	0.89
2826	450	20	19.1	25.6	55.4	0.75	23.2	26.9	49.9	0.86
2828	450	20	20.1	25.6	54.3	0.78	22.0	26.7	51.3	0.82

1 All samples have roughly the same metal ratio and are p-type both before and after the treatment.

Table 4.2 EPMA results for vacuum treated CuInSe_2 films¹ with different as-deposited metal ratio.

Sample No.	Treatment Condition		Composition Before H.T.				Composition After H.T.			
	T (°C)	t (min)	Cu	In (at.%)	Se	Cu/In	Cu	In (at.%)	Se	Cu/In
2835	350	20	25.6	21.2	53.2	1.20	28.6	24.8	46.9	1.15
2834	350	20	22.1	20.5	57.4	1.08	26.7	24.9	48.4	1.07
2836	350	20	22.2	23.8	54.0	0.93	25.7	26.0	48.4	0.99
2837	350	20	22.2	24.0	53.8	0.93	24.7	26.6	48.7	0.93
2821	350	20	21.0	25.2	53.8	0.83	23.6	26.3	50.48	0.90

¹ p-type both before and after the treatment.

Table 4.3 Comparison of compositional results for samples¹ treated both in vacuum and in Ar gas at different temperatures.

Sample No.	Heat Treatment Condition			Composition Before H.T.				Composition After H.T.			
	T (°C)	t (min)	Vac./Ar	Cu	In (at.%)	Se	Cu/In	Cu	In (at.%)	Se	Cu/In
1146	400	20	Vacuum	19.6	24.9	55.6	0.79	24.1	26.3	49.6	0.92
1150	500	20	Vacuum	20.5	22.9	56.7	0.90	24.4	26.0	49.6	0.94
1154	600	20	Vacuum	20.8	25.2	54.0	0.83	24.0	27.5	48.6	0.87
1147	400	20	Ar	20.7	24.6	54.7	0.84	23.9	27.0	49.1	0.89
1151	500	20	Ar	21.2	24.5	54.2	0.87	22.9	25.9	51.2	0.88
1155	600	20	Ar	23.2	25.5	51.3	0.91	23.5	28.3	48.1	0.83

¹ p-type both before and after the treatment.

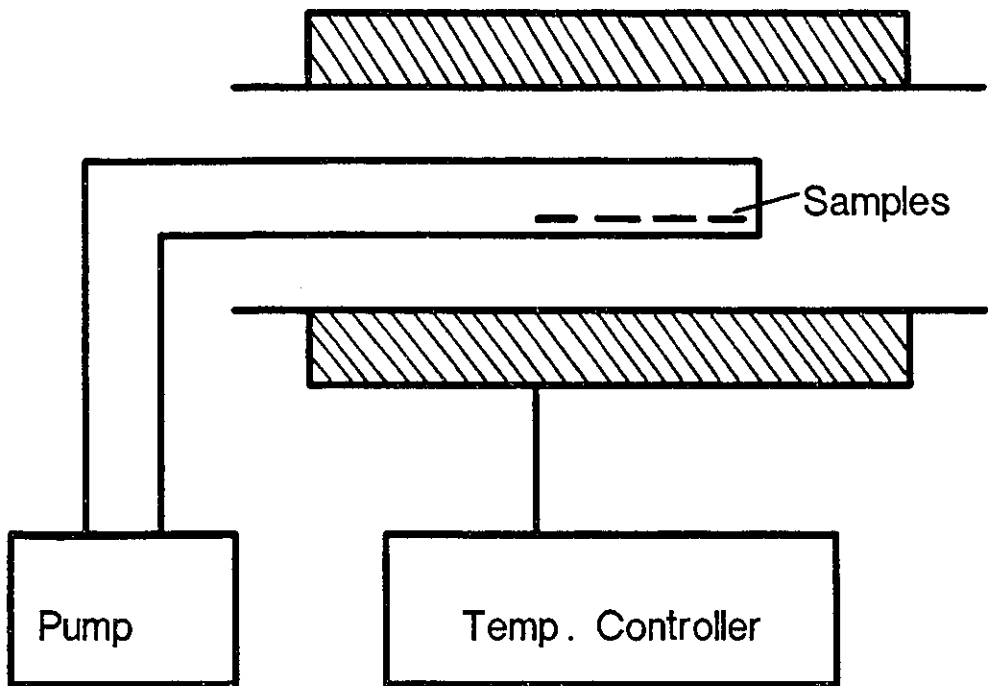


Fig. 4.1 A schematic diagram of the vacuum treatment system.

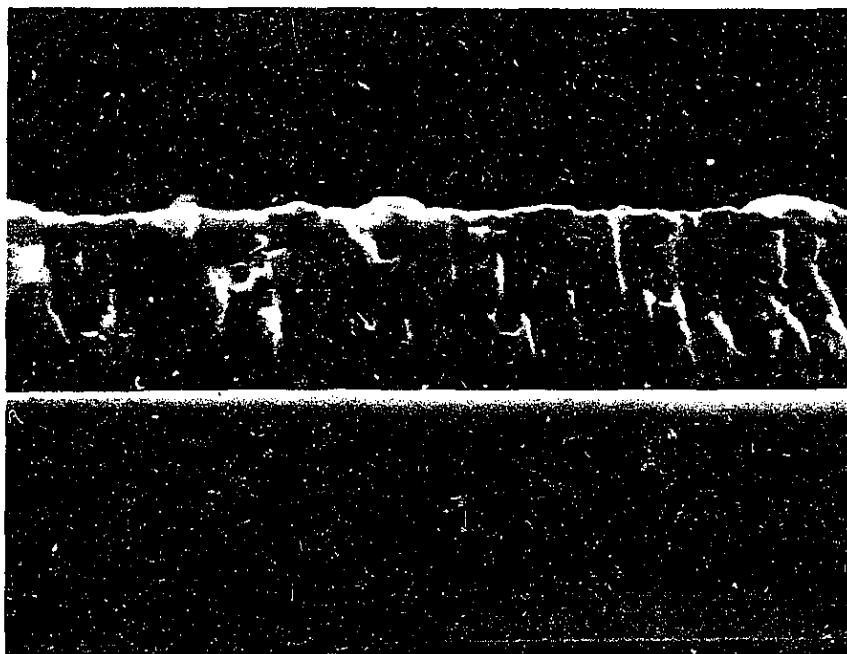


Fig. 4.2 A SEM photograph for a CuInSe₂ film after a treatment at 350 °C for 20 minutes in vacuum.

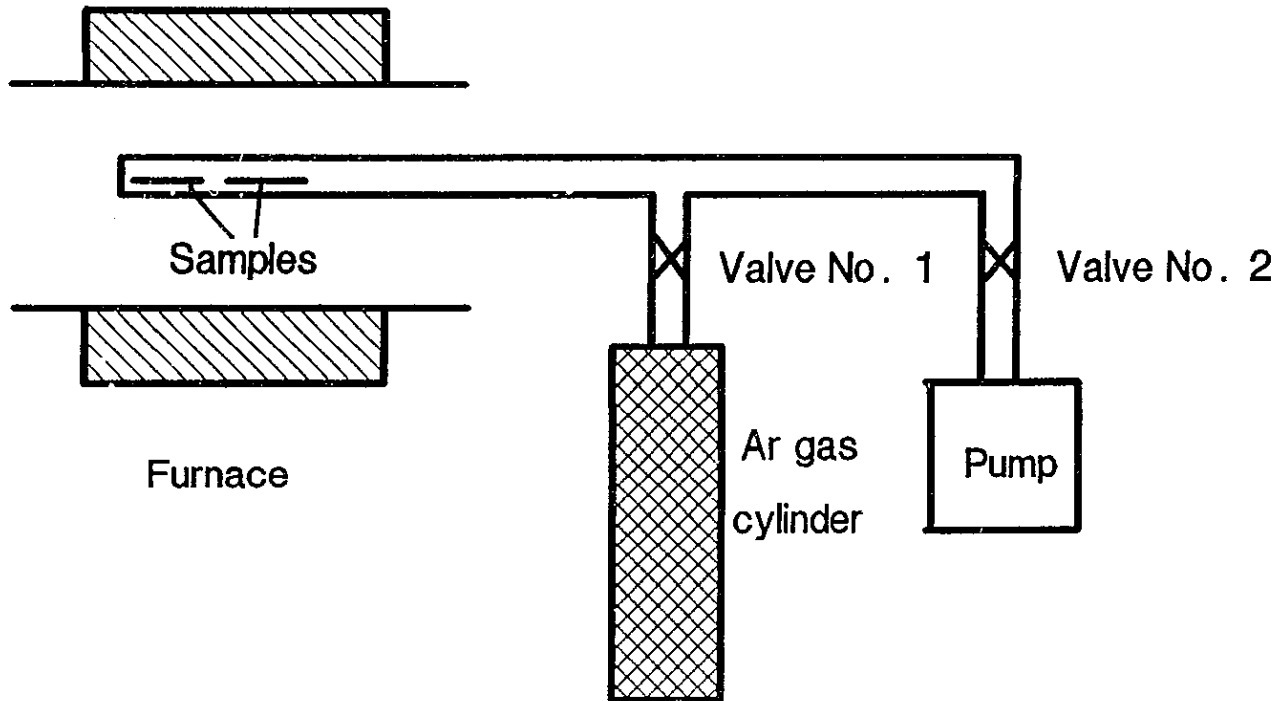


Fig. 4.3 A schematic diagram of the experimental set up for the heat treatment in argon.

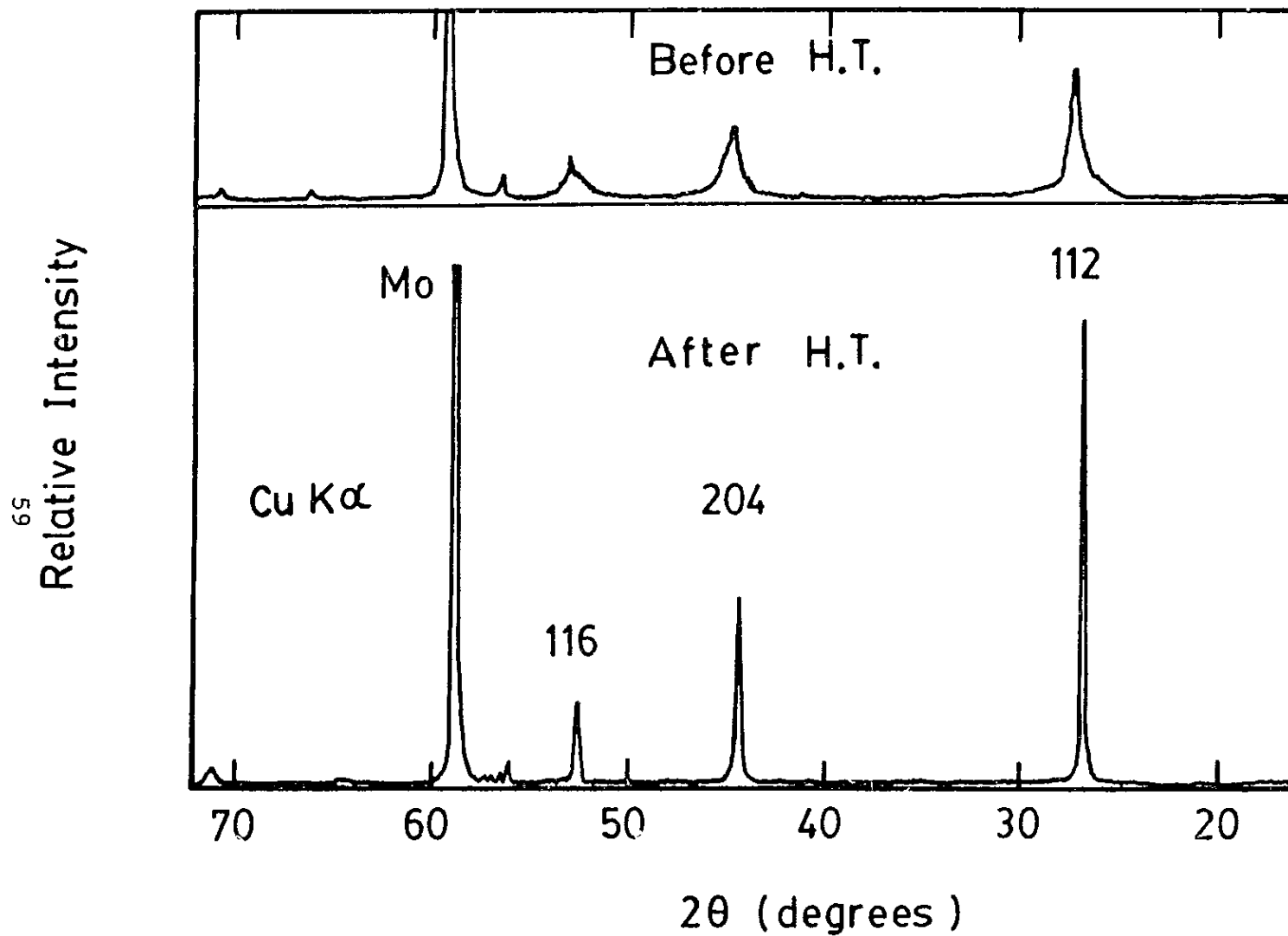


Fig. 4.4 Intensity of diffracted X-ray as a function of 2θ , showing a significant improvement of the film quality after a treatment at 350 °C for 20 minutes in a vacuum.

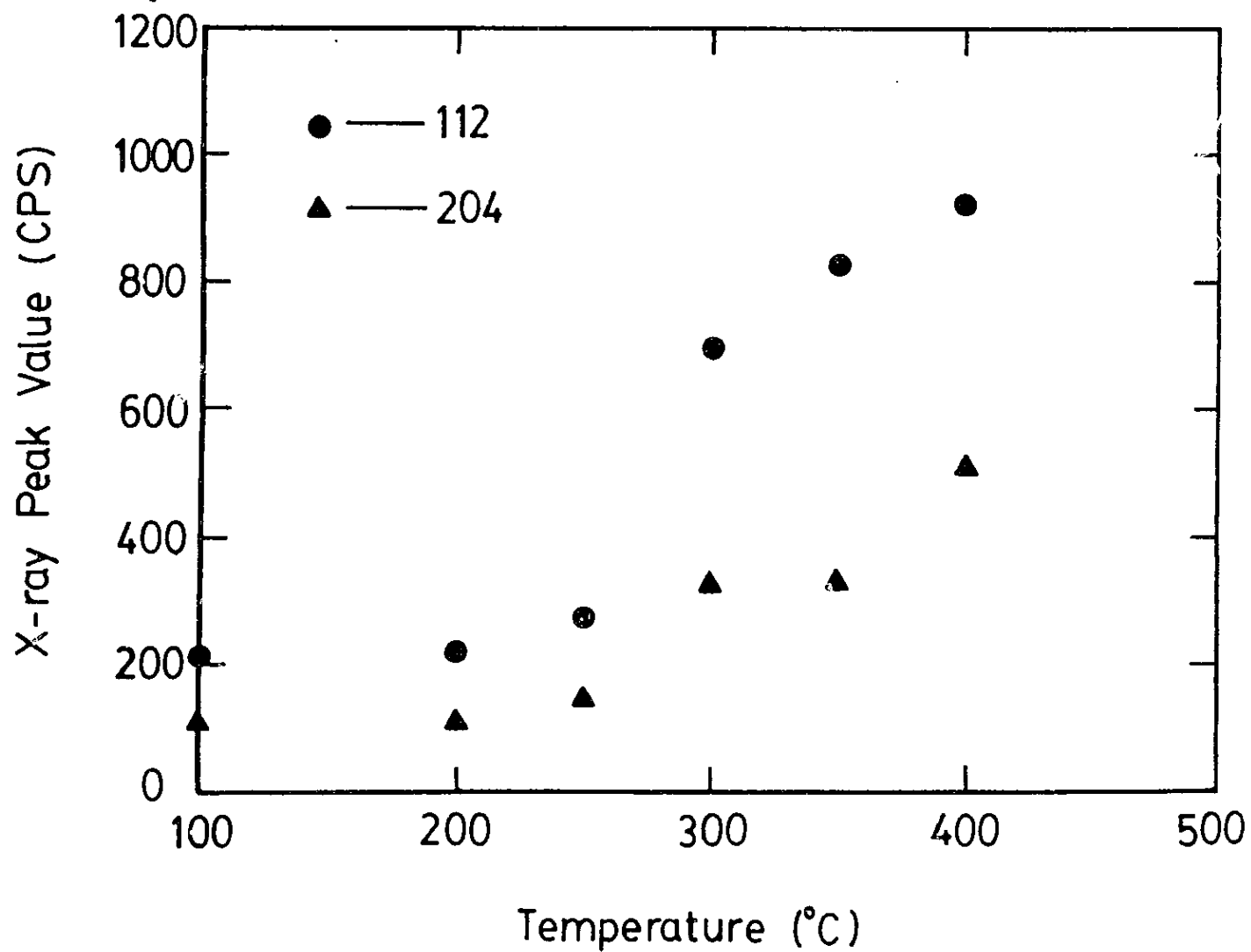


Fig. 4.5 Magnitude of the diffracted X-ray from the 112 and 204 planes plotted versus the treatment temperature, showing a large increase in the intensity at 300 °C.

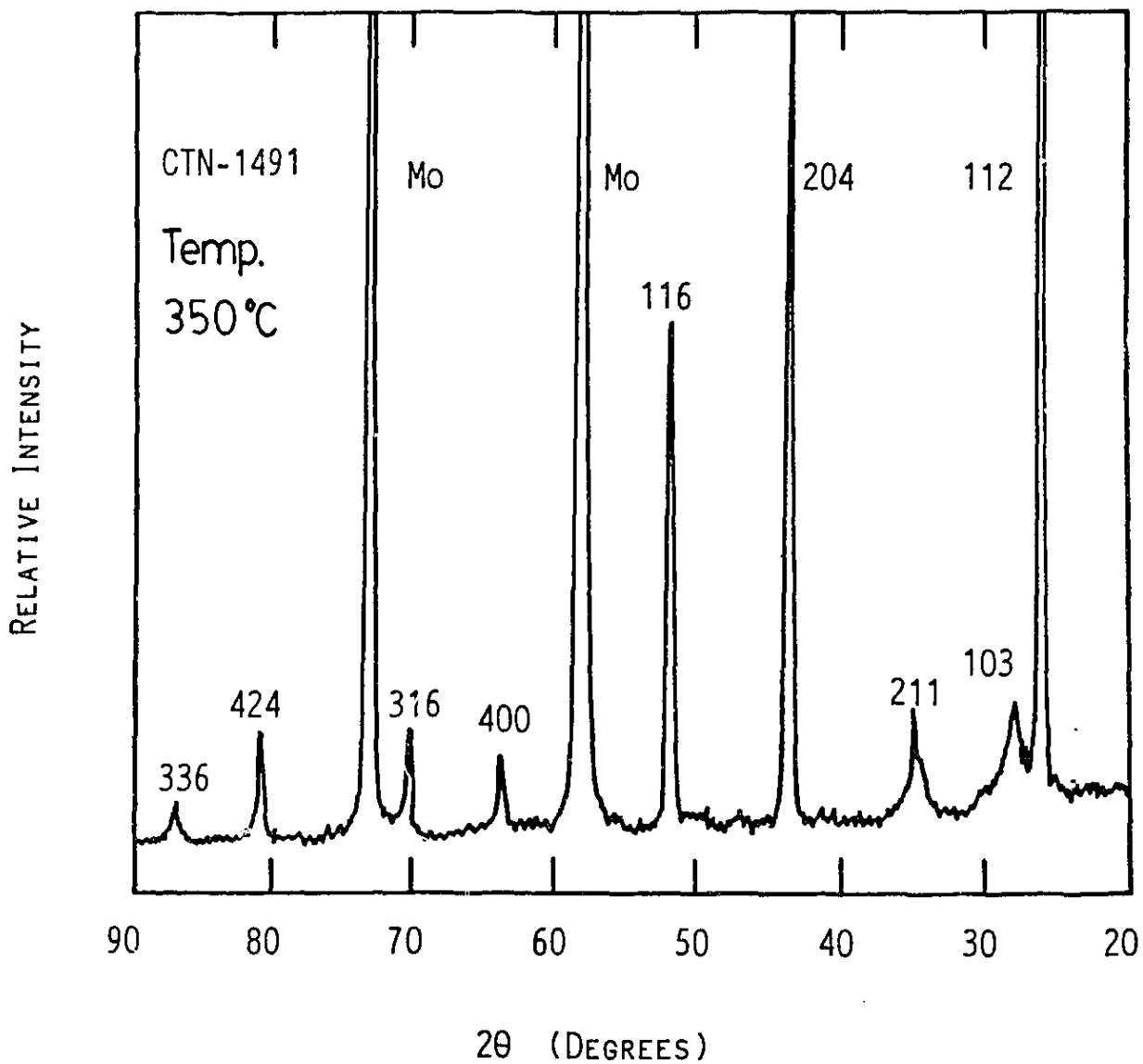


Fig. 4.6 Results of X-ray diffraction for a CuInSe_2 film treated at 350 °C for 20 minutes, showing the single phase nature of the film.

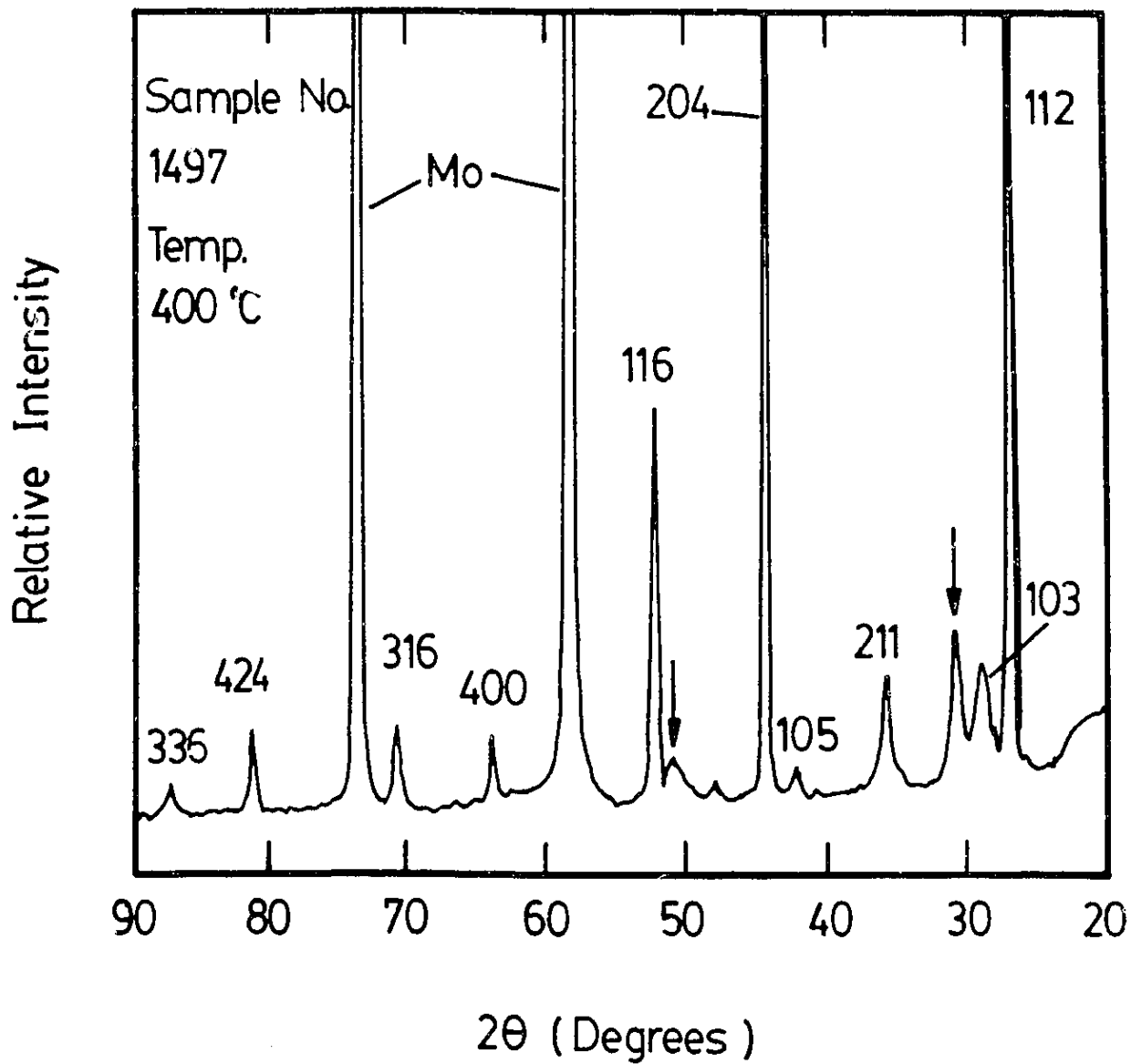


Fig. 4.7 Results of X-ray diffraction for a CuInSe_2 film treated at 400 °C, showing the presence of a second phase.

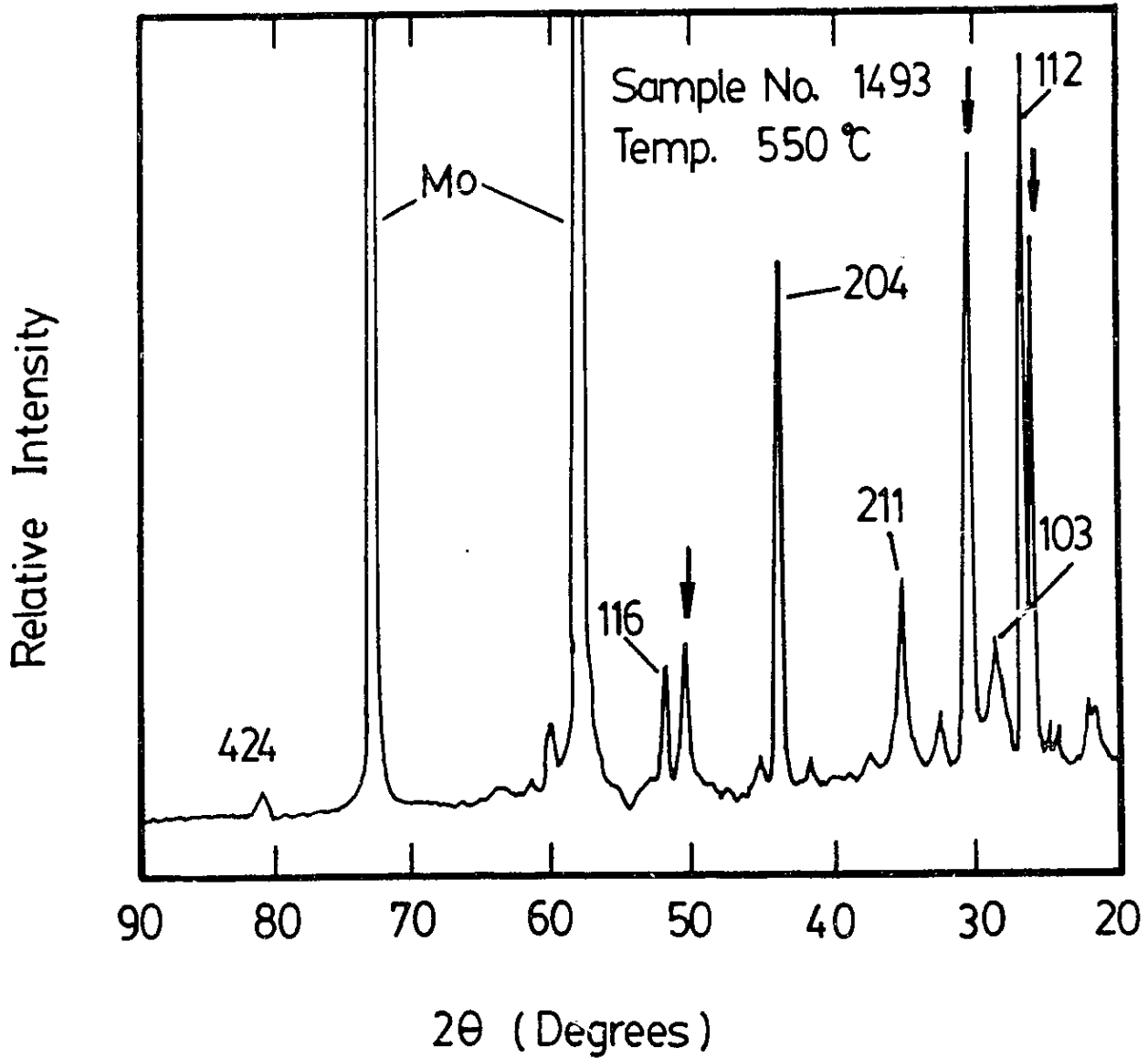


Fig. 4.8 Results of X-ray diffraction for a CuInSe_2 sample treated at 500 °C, showing strong peaks for the second phase.

Chapter 5 Al/CuInSe₂ SCHOTTKY JUNCTIONS FABRICATED USING P-TYPE CuInSe₂ FILMS

5.1 Introduction

The results of study on the electrodeposited CuInSe₂ films have been presented in the previous chapter. In that chapter, the properties of the CuInSe₂ films obtained from the X-ray diffraction and compositional analysis were found to be satisfactory for device fabrications. However, the electronic properties of the surface layer of the CuInSe₂, which are the most important for junction devices, were not known. In order to study the surface electronic properties of the CuInSe₂ films, both heterojunction and Schottky junctions can be used. During the fabrication of heterojunction solar cells involving CuInSe₂, elemental inter-diffusions will take place. This is specially so during the deposition of the window layer which is carried out at a relatively high substrate temperature (about 200°C). The elemental inter-diffusion can modify the surface properties of the CuInSe₂ films and affect the investigation. In order to minimize this problem, the deposition of top layer should be carried out at a low substrate temperature. One way to achieve this low substrate temperature is to fabricate Schottky junctions, which can be fabricated at or even below room temperature.

Several papers on the investigation of Schottky junctions of crystalline CuInSe₂ have been published by different workers.

Robinson and Wilson^{5.1} first reported the results on an Al/CuInSe₂(p) junction in 1975. From the $1/C^2$ versus V (C is the differential capacitance and V is the voltage), they obtained an intercept voltage of 1.38 V. This large value suggested that an interface layer was present in their Schottky junctions. Yalcin et al^{5.2}, using an n-type monocrystalline CuInSe₂ sample, fabricated Au/CuInSe₂(n) junctions. In their study they found a space-charge-limited current effect in the region immediately below the Au layer. A point contact method was used by Prasad et al^{5.3} to form Au/CuInSe₂(n) Schottky junctions. They also observed the space-charge-limited current effect in their devices. From I-V and C-V measurements, the electron affinity of CuInSe₂ was estimated by them to be 4.55 eV. Leccabue and coworkers^{5.4} fabricated Au/CuInSe₂(n) junctions and observed a quantum efficiency of about 60% in the wavelength range from 0.72 to 1.24 μm . Recently, results of Al/CuInSe₂(p) Schottky junctions made on monocrystalline CuInSe₂ have been reported by Chen and Shih^{5.5}. It is interesting to note that all of the reported Schottky junctions described above were fabricated on bulk crystalline samples.

In order to obtain more information on the electrodeposited CuInSe₂ films, Schottky junctions have been fabricated in the present work on p-type CuInSe₂ samples^{5.6}. Both I-V and C-V measurements have been performed and the results are presented in this chapter.

5.2 Theory of Schottky Junctions

A Schottky junction consists of a metal and a semiconductor. When the two materials are brought into contact, thermal equilibrium is established and the Fermi levels on both sides line up (as shown in Fig. 5.1). There are four basic current transport processes in the Schottky junction under forward bias: (1) thermionic emission current; (2) recombination in the space charge region; (3) tunneling and (4) recombination in the neutral region. Process (1) is dominant for devices with moderate doping concentration in the semiconductor and (3) is only important for heavily doped semiconductors (including ohmic contacts). For process (1), the device current density is given by

$$J = J_{ST} [\exp(qV/kT) - 1]. \quad (5.1)$$

Here $J_{ST} = A^* T^2 \exp(-q\phi_{Bn}/kT).$ (5.2)

Here, A^* is the effective Richardson constant and ϕ_{Bn} is the barrier height of the junction seen from the metal side.

Under the abrupt approximation, Schottky junctions can be treated the same way as one-sided p-n junctions. The depletion capacitance per unit area for a Schottky junction made of p-type semiconductor is given by

$$C = \epsilon_s/W = [q\epsilon_s N_A / (2(V_{bi} - V - kT/q))]^{1/2} \quad (5.3)$$

or $C^{-2} = 2(V_{bi} - V - kT/q) / q\epsilon_s N_A$ (5.4)

Here ϵ_s is the permittivity of the semiconductor, W is the depletion width, N_A is the acceptor concentration of the semiconductor and V_{bi} is the built-in potential at zero bias. If N_A is constant

throughout the depletion region, one can obtain a straight line by plotting C^{-2} versus V and from the slope of the line, the N_A value can be obtained.

5.3 Schottky Junction Fabrication

P-type CuInSe_2 thin film samples deposited on molybdenum-coated glass substrate were selected after the film deposition. The film thickness was about $2 \mu\text{m}$ and the typical size of the samples was $1.5 \times 3 \text{ cm}^2$. The samples were first treated at 350°C for 20 min in vacuum. After the treatment, the samples were mounted on an aluminum holder for Al contact deposition. An aluminum mask with 50 circular windows (area 0.06 cm^2) was mounted in front of the films to define the circular Al regions. High purity aluminum wire (99.9999%) was used as the source and evaporated using a tungsten filament (see Fig. 5.2) to a thickness of about $2 \mu\text{m}$. During the evaporation, the distance between the substrates and the filament was about 10 cm and the base pressure of the evaporator was 10^{-6} Torr. There was no intentional substrate heating during the Al evaporation.

The top view and the cross-sectional view of the final Schottky diodes are shown in Fig. 5.3(a) and 5.3(b). The ohmic contact to the p-type CuInSe_2 films was obtained directly from the part of Mo film not covered by CuInSe_2 .

5.4 Current-voltage Characteristics

Dark current-voltage characteristics measurements were carried out using a Hewlett Packard (HP) model 4145A semiconduc-

tor parameter analyzer. A block diagram of the measurement system is shown in Fig. 5.4. The parameter analyzer was connected to a personal computer for the data acquisition. A probe station was used for room temperature measurements and a liquid nitrogen cryostat was used for temperature dependent I-V measurements. Spring-loaded metal pins were attached to Al and Mo pads for electrical contact during the measurements.

The room temperature dark current-voltage characteristics for the Schottky junction No. 3824 are shown in Fig. 5.5. The I-V characteristics for a CdS/CuInSe₂ cell (area is different from that of the Schottky junction) fabricated on the same CuInSe₂ substrate are also shown in this figure. For this device, rectification ratio is about 200 at ±0.5 V. In Fig. 5.6, the temperature-dependent dark forward current of the same sample is plotted versus voltage in logarithm-linear scales. In the low voltage region, the current is seen to follow the relation $I=I_0\exp[qV/(nkT)]$, with an ideality factor (n) of about 2. This n value suggests that carrier recombination is a dominant process in this junction. As the temperature is decreased, the slope in the low voltage region decreases and the n value increases. The room temperature I-V curves for another sample (No. 3852) are shown in Fig. 5.7. For this sample, the ideality factor is about 1.7.

In order to obtain further information of the Schottky junctions, curve fitting was carried out following the method reported by McLean and his coworkers^{5,7} using the following equation:

$$I = I_S \{ \exp[(q/(kT))(V - IR_S)] - 1 \} + I_R \{ \exp[(q/(2kT))(V - IR_S)] - 1 \}. \quad (5.5)$$

Here I is the total junction current, I_S is the saturation current, I_R is the recombination current, and R_S is the series resistance. The fitted results of the saturation current I_S , the recombination current I_R , the n factor and the series resistance R_S for three devices are shown in table 5.1. It is seen that the I_R values are much larger than the I_S values for all of the devices. The fitted results thus suggest that carrier recombination is the dominant process in the Al/CuInSe₂ Schottky junctions. The fitted saturation current I_S was too small and was not used for the determination of the barrier height. It is also interesting to note that there is a relationship between I_R , I_S and the n factor: For a sample with a small n value (e.g. 3852, $n=1.7$), the difference between I_R and I_S is also small. Fitted values are also given in this table for the sample No. 3824 at different temperatures. As expected, when the device temperature is decreased, n factor values and the series resistances R_S increase.

5.5 Differential Capacitance Measurements

The differential capacitance-voltage (C-V) characteristics were obtained by using an HP model 4274A LCR meter. A block diagram of the measurement system is shown in Fig. 5.8. The measurements were carried out in order to determine the carrier

concentration of the CuInSe_2 film near the depletion edge of the Al/CuInSe_2 Schottky junctions. The measurements were carried out at frequencies in the range from 10 kHz to 100 kHz with the magnitude of incremental voltage set at 20 mV. A plot of $(A/C)^2$ versus voltage for an Al/CuInSe_2 Schottky junction at 100 kHz is shown in Fig. 5.9 (here A is the junction area). A similar curve for a $\text{CdS}(n^+)/\text{CuInSe}_2(p)$ heterojunction fabricated on the same substrate (detailed fabrication and characterization processes will be described in the chapters 6, 7 and 8) is also given in this figure. It is noted, from the slope of the curve, that values of carrier concentration of the CuInSe_2 film in the two devices are nearly the same. However, the intercept voltage (apparent diffusion potential) for the heterojunction is larger than that for the Al/CuInSe_2 Schottky junction. This voltage difference has been observed in all of the CuInSe_2 devices studied in the present work.

From the C-V measurements at 100 kHz, the effective carrier concentration, N_A , was determined using the equation:

$$N_A = [2/(A^2 q \epsilon_S)] [-d(C^{-2})/dV]^{-1} \quad (5.6)$$

The apparent diffusion potential, V_0 , of the devices was also obtained by extrapolating the linear part of the C-V curve to the x axis. The results for three Schottky junctions on CuInSe_2 films and one on CuInSe_2 bulk substrate reported in ref. 5.1, are given in table 5.2. It is noted that the effective carrier concentration in the thin film Schottky junctions is in the order of 10^{17} cm^{-3} and is less than 10^{16} for the bulk device. In addition, the

apparent diffusion potential for the bulk device is about 4 times of that for the thin films ones.

Another interesting phenomenon found in the present work is that the slope of the C^{-2} -V curves of the Schottky junctions shows a strong frequency-dependent variation when compared to that of the CdS/CuInSe₂ devices fabricated on the same substrate. This is illustrated in Fig. 5.10. In the figure, the C^{-2} -V curves at frequencies of 10, 20, 40 and 100 kHz are shown. It is clearly seen that for the Schottky junction, the slope increases as the measuring frequency is increased from 10 kHz to 100 kHz. For the CdS/CuInSe₂ heterojunction, the slope of the C^{-2} -V curves also varies with the frequency but with a very small change. Similar effects were also observed for other samples and the results for the sample No. 3824 are shown in Fig. 5.11.

It should be pointed out that several of the CuInSe₂ films used for the Schottky junctions were stored in the laboratory for more than 3 weeks after the CdS deposition for the heterojunctions and before the Al Schottky contact formation. In order to determine the effect of the exposure to air, several CuInSe₂ films were deposited, treated and used in the same day for the Schottky junction fabrication and the differential capacitance of the devices was measured. A capacitance dispersion effect similar to that shown in Fig 5.10 was also found on the untreated and treated junctions. This dispersion in capacitance could be due to the presence of slow traps with a large density or interface states having a large density in the Al/CuInSe₂ junctions.

In order to study the effects of post-fabrication heat

treatment on device performance, three devices were treated at 200°C in air for 20 min. After the treatment, dark I-V measurements were made. A decrease in the saturation current I_S was found for all samples. The differential capacitance of the devices was then measured. The results for one of the samples at 100 kHz are shown in Fig. 5.12. It is seen that the effective carrier concentration (obtained from the slope of the curve) in the surface region of the sample has increased from $1.3 \times 10^{17} \text{ cm}^{-3}$ to $3.1 \times 10^{17} \text{ cm}^{-3}$ after the heat treatment. Similar effects were also found with the other two samples. This increase in concentration is believed to be due to diffusion of oxygen atoms into the CuInSe_2 films during the treatment. The apparent diffusion potential of the devices was found to increase from 0.25 to 0.5 V after the treatment. This increase suggests that either the air treatment at 200°C had decreased the density of the interface states or the air treatment had caused a very thin interface layer in the present Schottky junctions.

5.6 Conclusions

Schottky junctions of the form $\text{Al/CuInSe}_2(\text{p})$ have been fabricated using electrochemically deposited polycrystalline CuInSe_2 thin films. The devices showed a rectification effect with a ratio of about 200 at $\pm 0.5 \text{ V}$. From the curve fitting results, the current-voltage characteristics of the devices were found to be controlled by a recombination process. The apparent diffusion potential obtained from the capacitance-voltage data was $0.3 \pm 0.06 \text{ V}$. This value is much smaller than that reported

for a bulk monocrystalline device, suggesting the presence of an interface layer in the bulk device. The $(A/C)^2-V$ curves of the Schottky junctions showed a large slope dispersion. This effect is believed to be due to the presence of slow traps or interface states in the Schottky junctions. (The possible causes for the dispersion effect will be discussed further in chapter 7 and 9.) The concentration results obtained for the Schottky junctions were similar to those obtained for the CdS/CuInSe₂ heterojunctions. Therefore, a Schottky junction fabricated by the simple method could be used to monitor CuInSe₂ film concentration during CdS/CuInSe₂ photovoltaic device fabrication.

The apparent diffusion potential and the effective carrier concentration of the Al/CuInSe₂ junction increased after air treatment at 200°C. The increase in the concentration is believed to be caused by oxygen atoms diffusing into the CuInSe₂ films. In addition, an interfacial layer may have formed during the air treatment. This would be the reason for the increase in the apparent diffusion potential.

Table 5.1 Fitting results for Al/CuInSe₂ Schottky junctions.

Sample No.	Area (cm ²)	Temp. (K)	n	I _R (A)	I _S (A)	R _S (Ω)	J _R [*] (A/cm ²)
3852	0.04	298	1.7	6.56x10 ⁻⁶	1.89x10 ⁻⁸	9.8	1.6x10 ⁻⁴
3841	0.06	298	1.9	2.19x10 ⁻⁵	7.48x10 ⁻⁸	16.7	3.7x10 ⁻⁴
3824A	0.06	298	2.0	5.58x10 ⁻⁷	1.08x10 ⁻¹³	266.5	9.3x10 ⁻⁶
3824B	0.06	283	2.05	2.08x10 ⁻⁷	1.03x10 ⁻¹⁴	422.3	3.5x10 ⁻⁶
3824C	0.06	273	2.1	1.08x10 ⁻⁷	4.17x10 ⁻¹⁵	573.8	1.8x10 ⁻⁶
3824D	0.06	263	2.2	4.84x10 ⁻⁸	8.13x10 ⁻¹⁶	774.7	8.1x10 ⁻⁷
3824E	0.06	253	2.28	2.37x10 ⁻⁸	4.94x10 ⁻¹⁶	1306.6	4.0x10 ⁻⁷

* J_R = I_R/A

Table 5.2 Room temperature electrical results obtained from the C-V measurements at 100 kHz.

Sample No.	N_A (cm^{-3})	V_O (V)
3824	1.3×10^{17}	0.24
3841	1.6×10^{17}	0.36
3852	2.4×10^{17}	0.33
bulk*	6.77×10^{15}	1.38

* Al/CuInSe₂ device fabricated on single crystal sample reported in ref. 5.1.

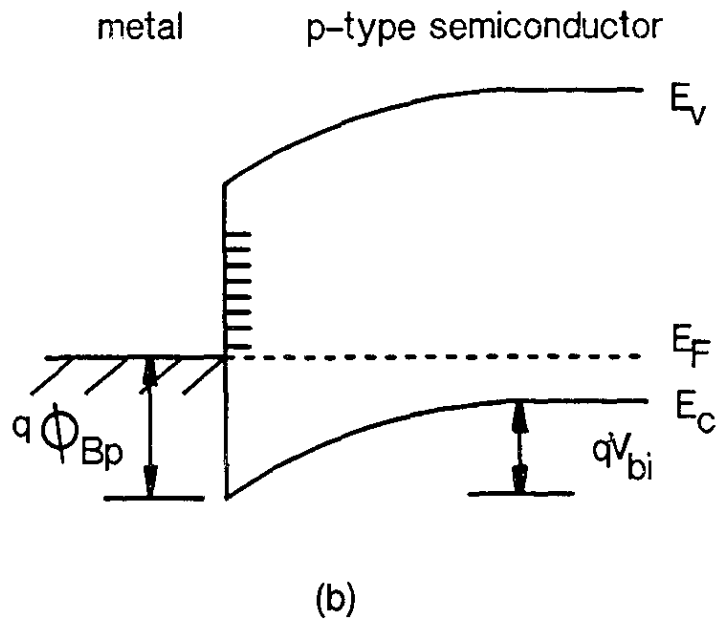
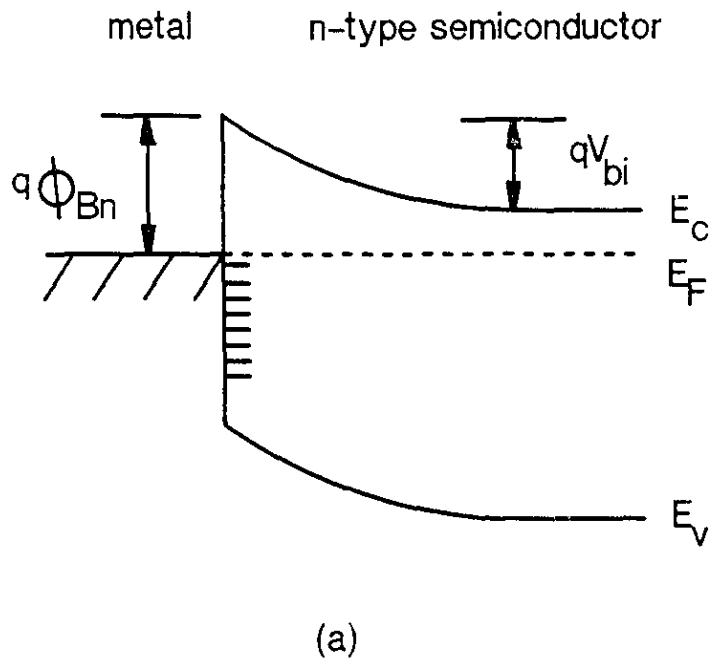


Fig. 5.1 Energy band diagram of Schottky junctions (a) in an n-type semiconductor and (b) in a p-type semiconductor.

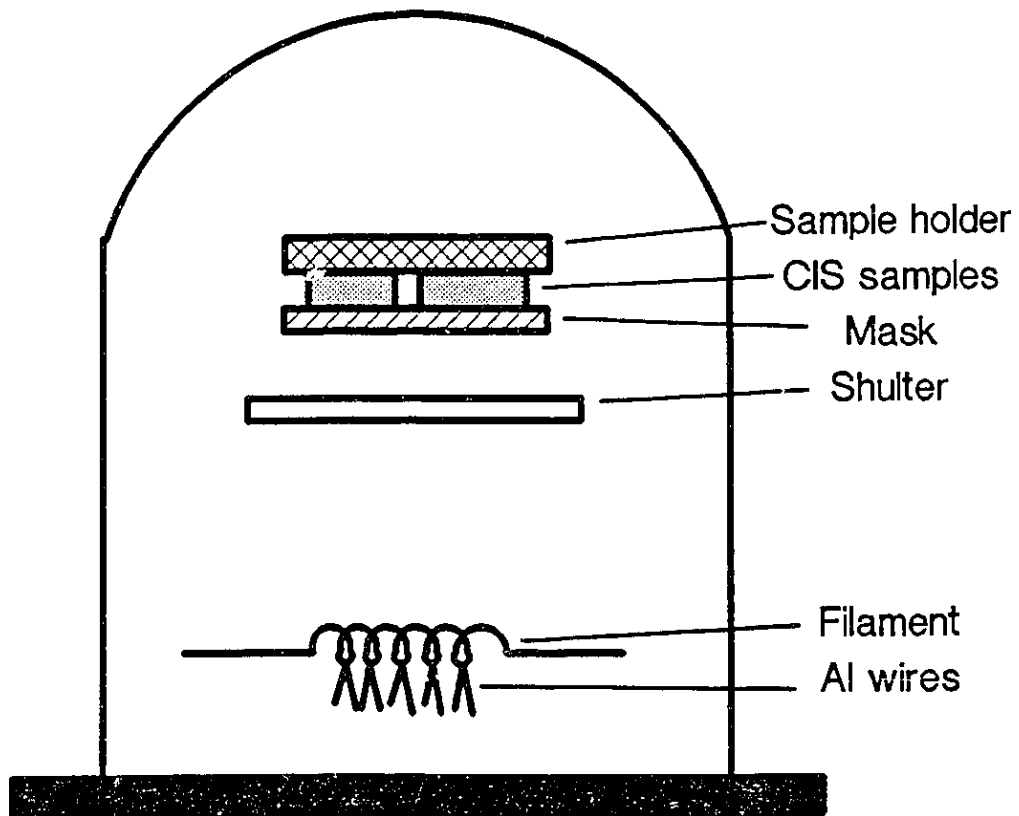
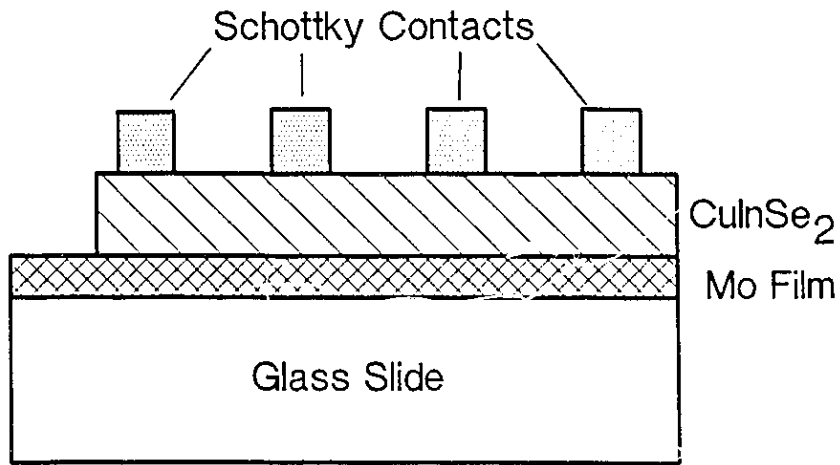
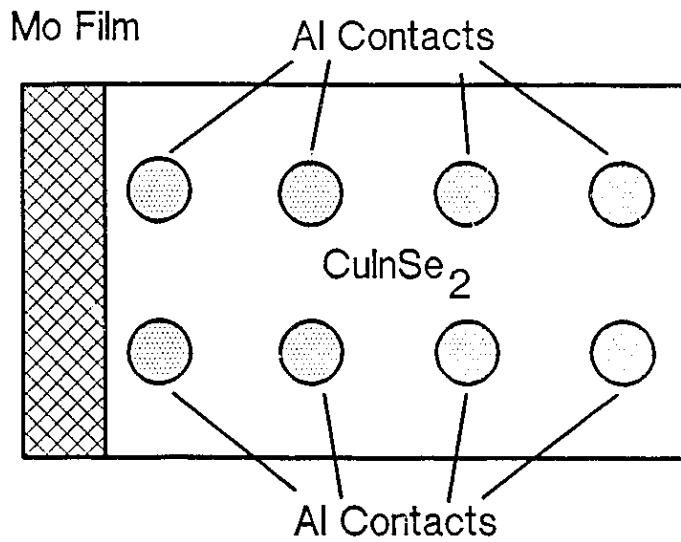


Fig. 5.2 A schematic diagram of the evaporation system for the fabrication of Schottky contacts.



(a)



(b)

Fig. 5.3 (a) A cross-sectional view of the Al/CuInSe₂ Schottky junctions. (b) Top view of a sample showing the position of the Schottky contacts.

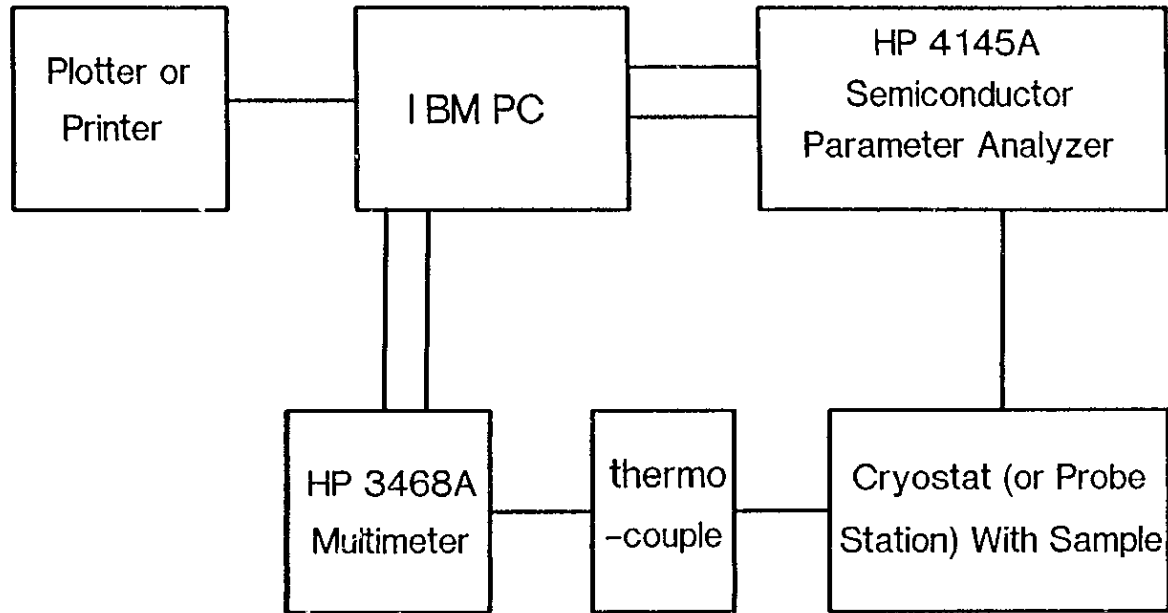


Fig. 5.4 A schematic block diagram of the system used for the current-voltage measurements.

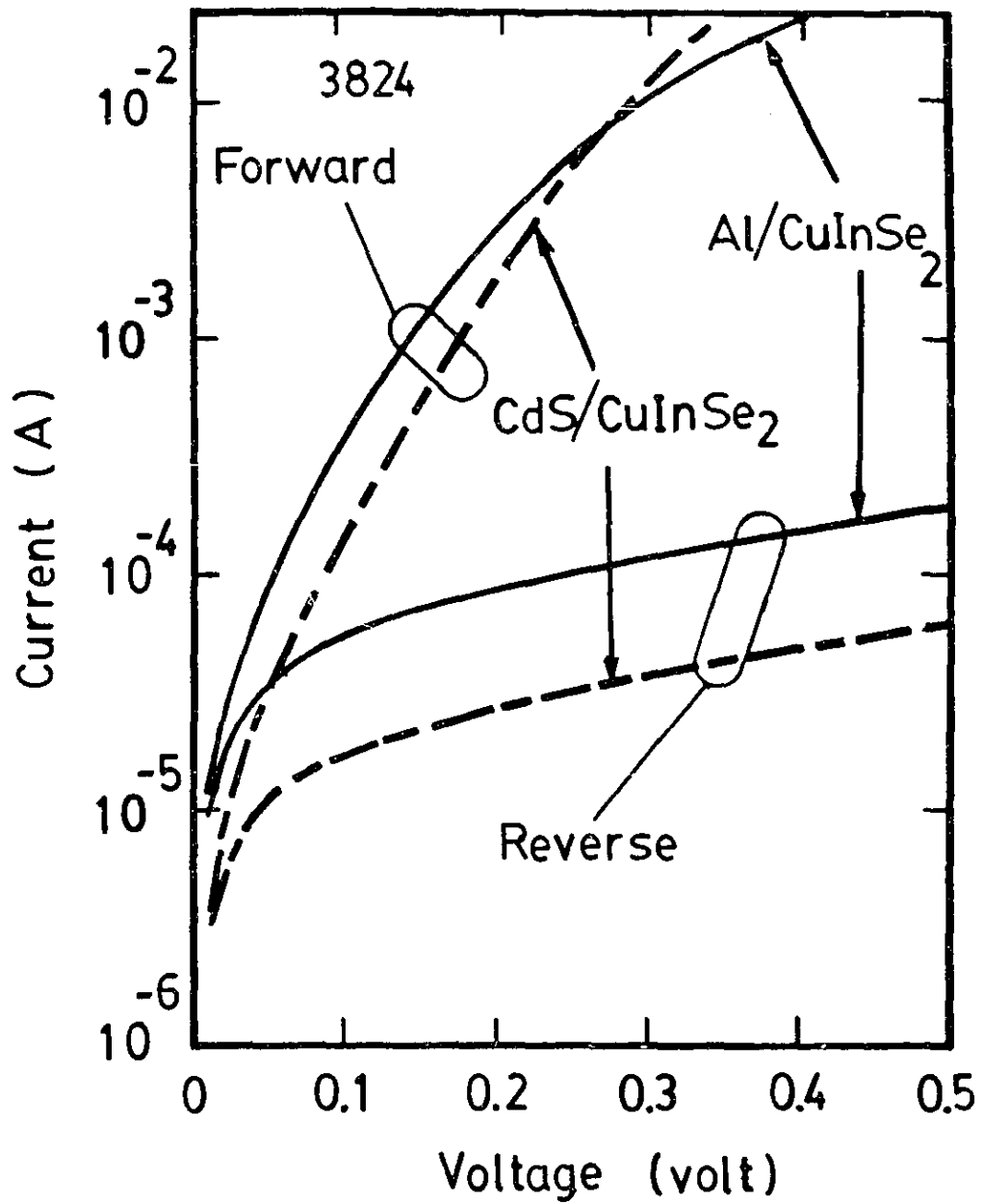


Fig. 5.5 Dark I-V characteristics of an Al/CuInSe₂ Schottky junction and a CdS/CuInSe₂ heterojunction fabricated on the same CuInSe₂ sample.

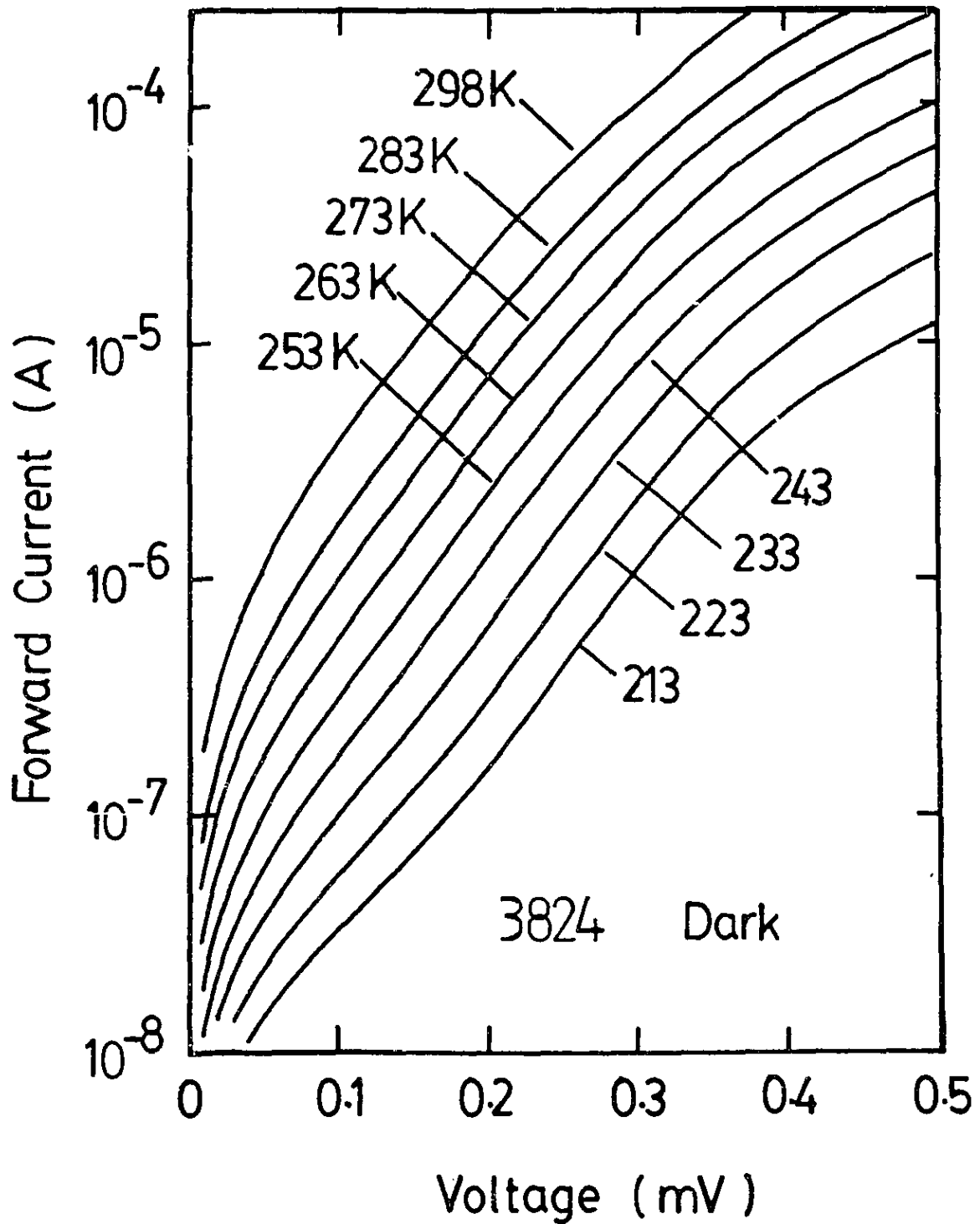


Fig. 5.6 Temperature-dependent forward I-V curves for the Schottky junction No.3824, the room temperature ideality factor of which is about 2.

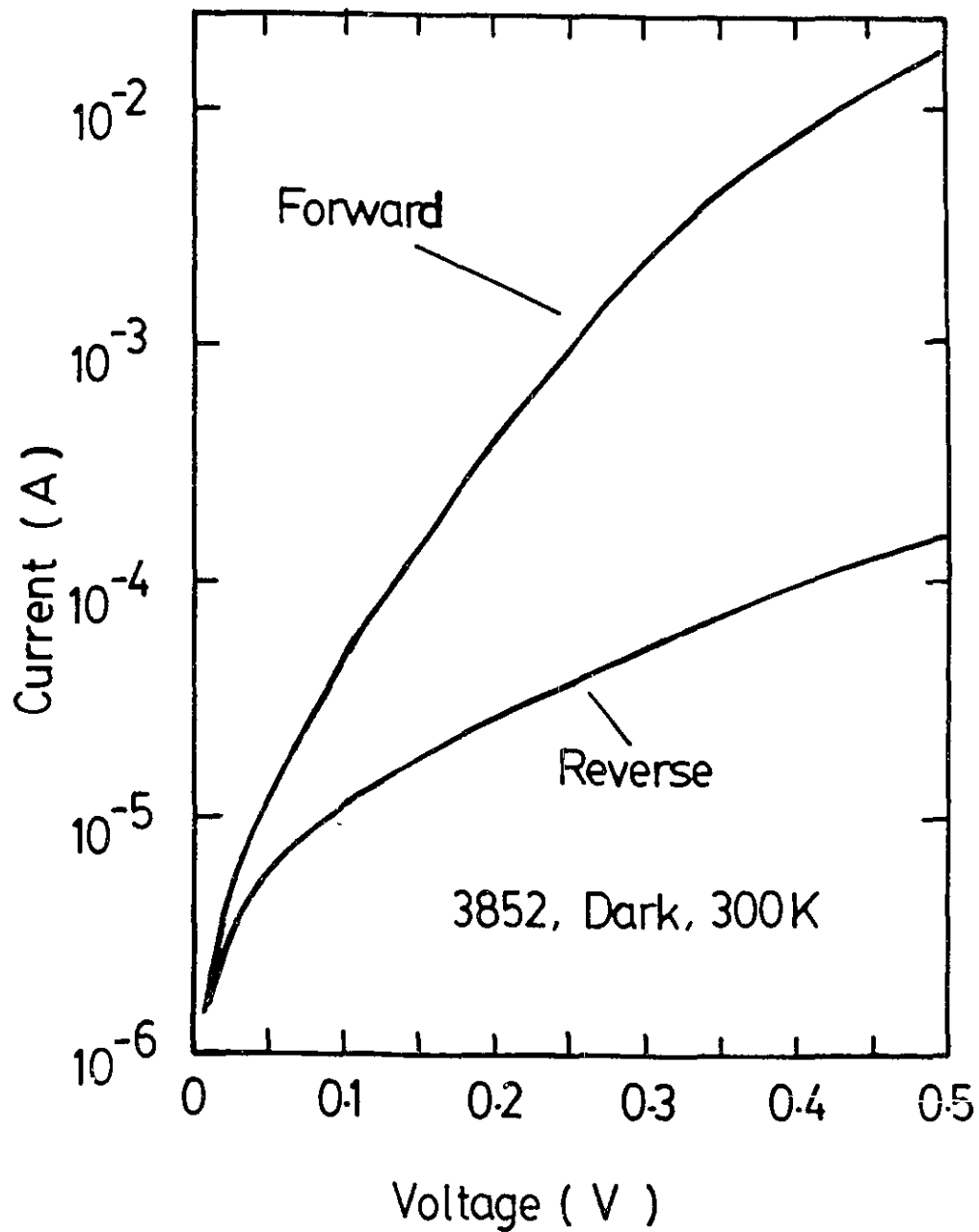


Fig. 5.7 Dark I-V results for the sample No. 3852 showing an ideality factor of about 1.7.

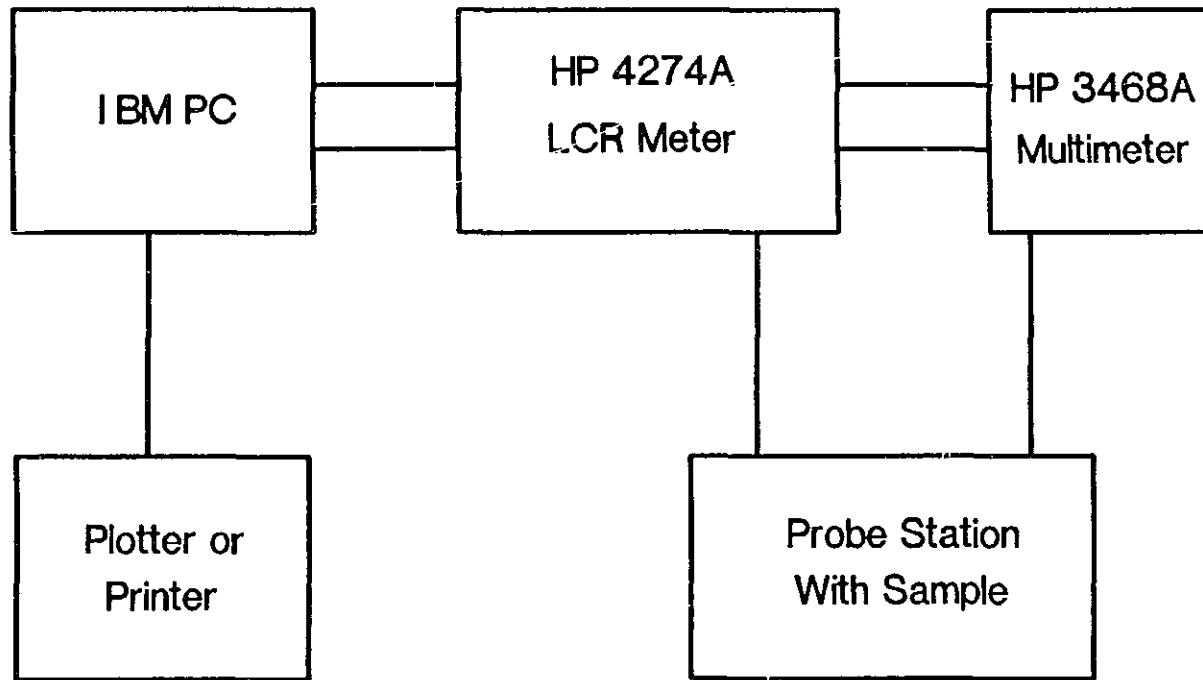


Fig. 5.8 A block diagram of the C-V measurement set-up.

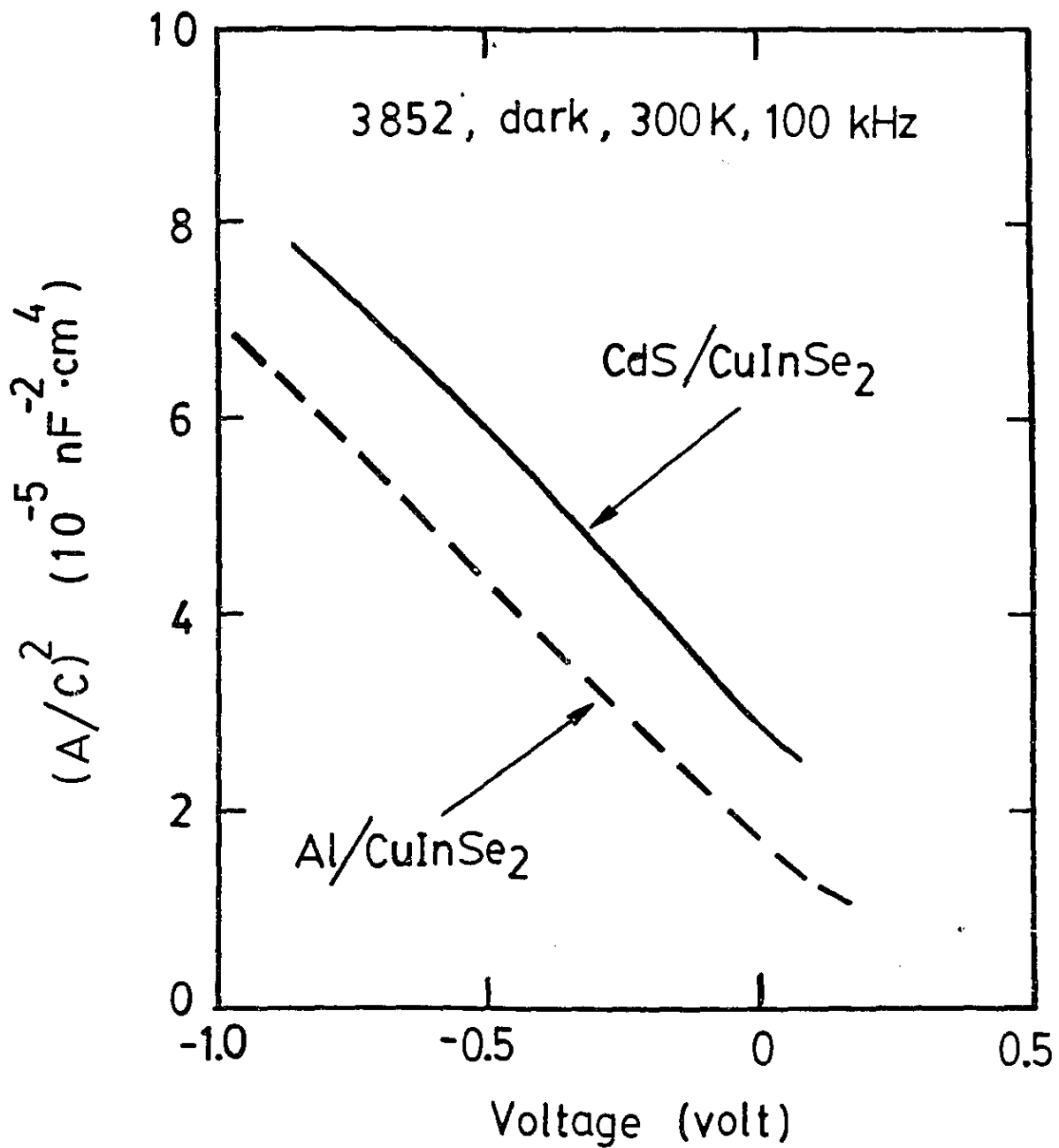


Fig. 5.9 Plot of $(A/C)^2$ vs. V for a Schottky junction and a heterojunction, fabricated on the same CuInSe_2 film, showing nearly equal carrier concentration.

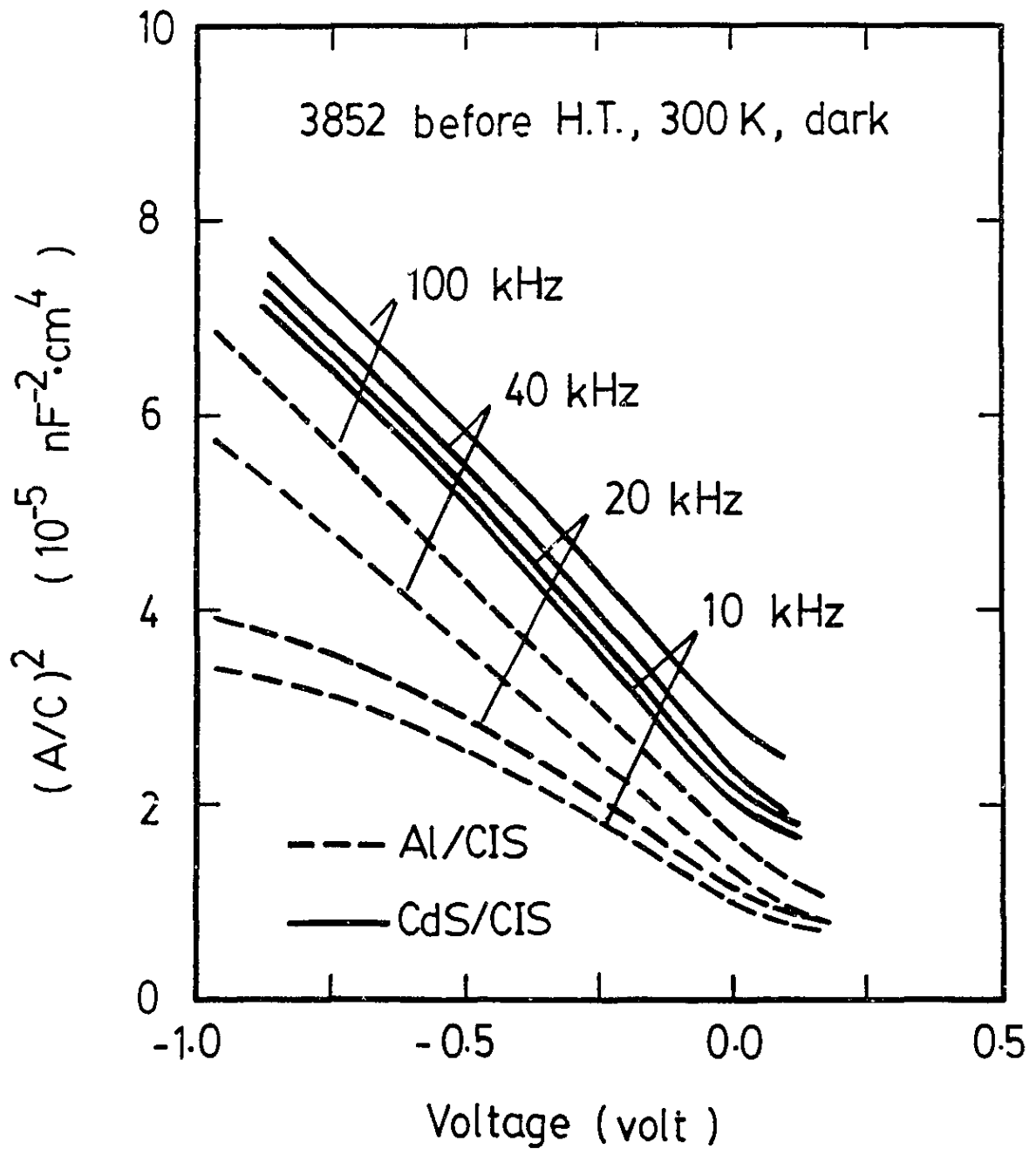


Fig. 5.10 $(A/C)^2$ measured at 4 different frequencies for a Schottky junction and a heterojunction. A dispersion effect is seen for the Schottky junction.

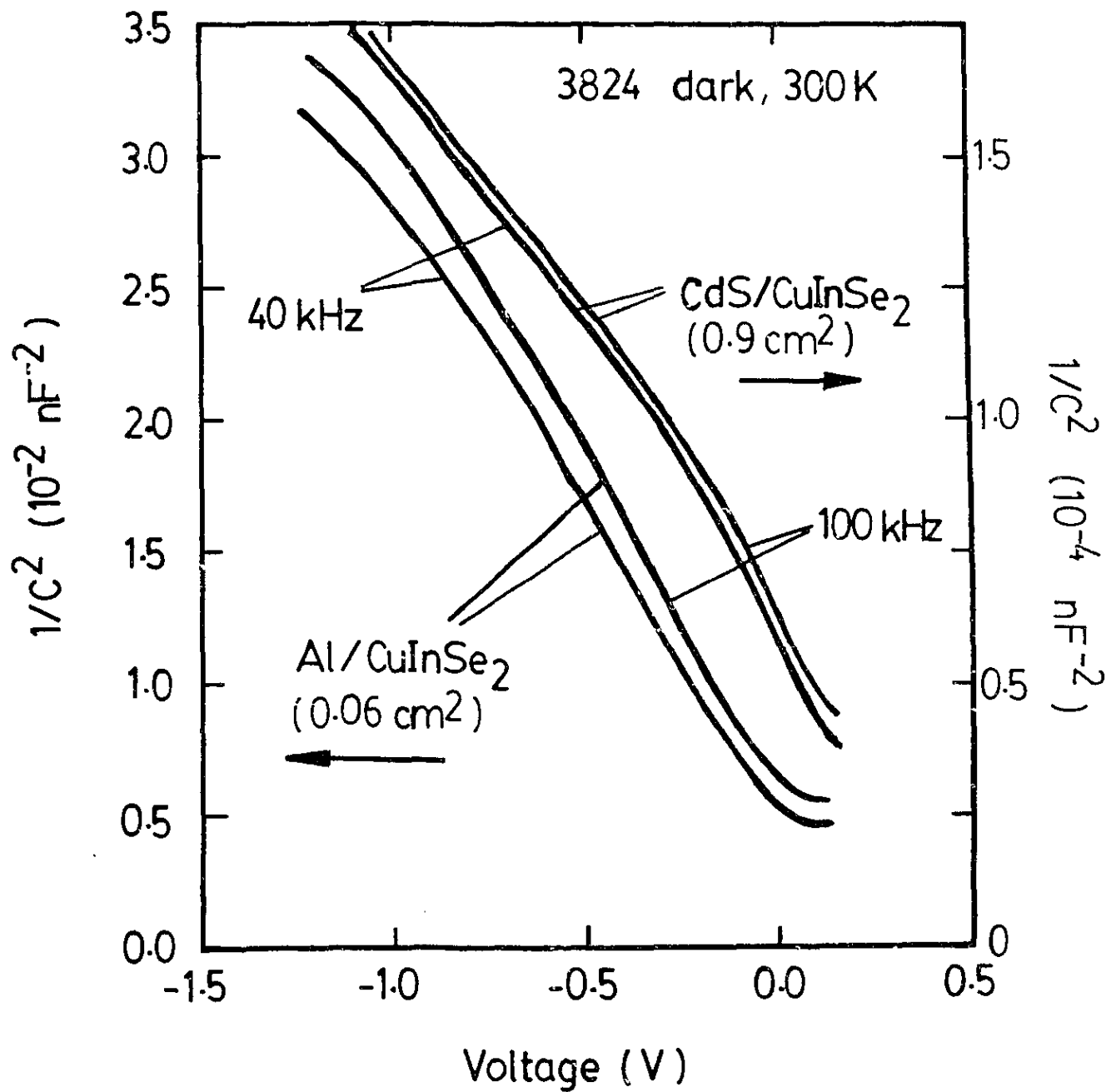


Fig. 5.11 Results of C-V measurements for the sample No. 3824 showing the dispersion effect for this Schottky junction.

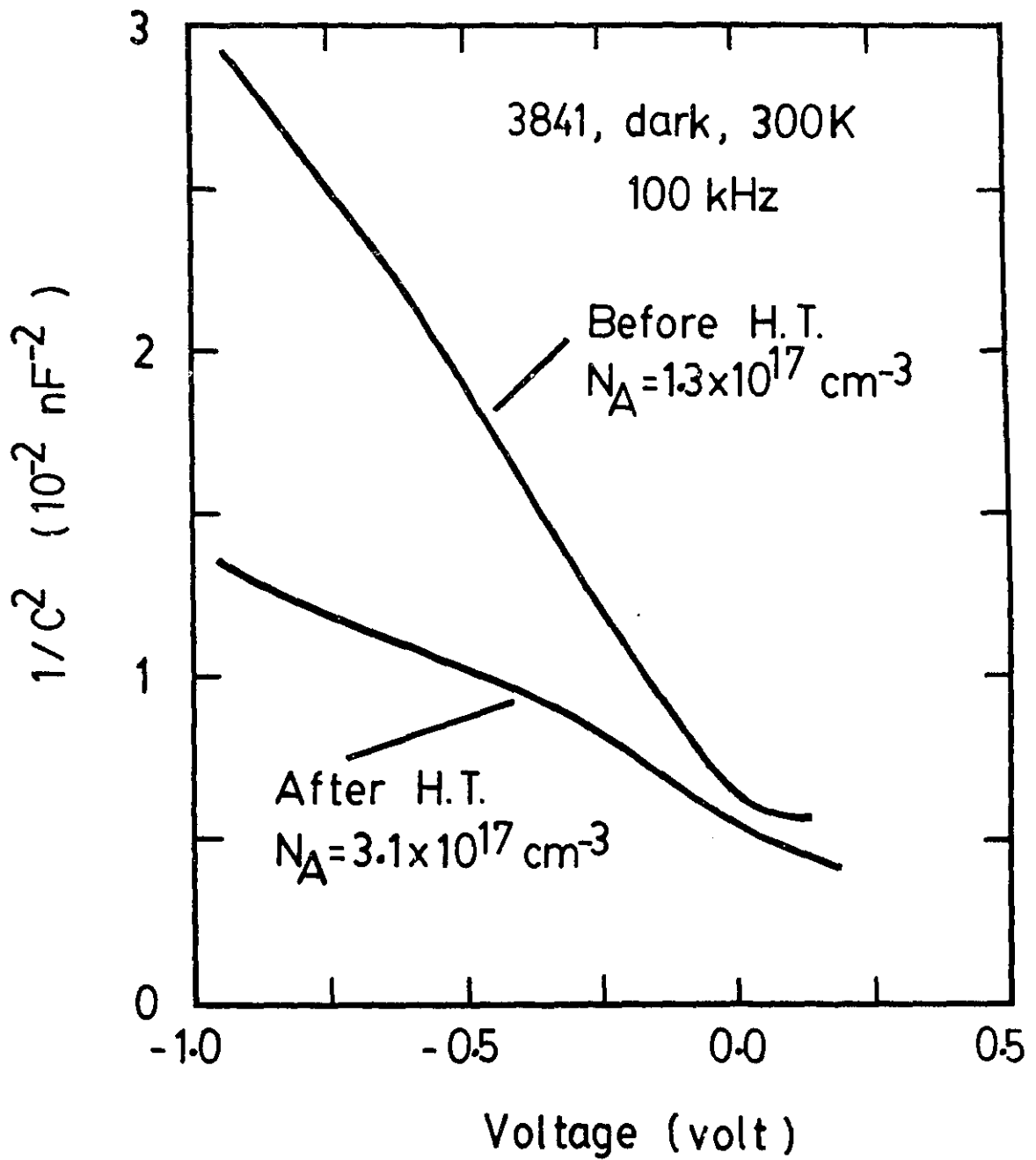


Fig. 5.12 $1/C^2$ plotted vs. V for the Schottky junction No. 3841. An increase in the carrier concentration is seen after the treatment in air.

Chapter 6 FABRICATION OF CdS/CuInSe₂ PHOTOVOLTAIC CELLS

6.1 Introduction

Because of the large bandgap (2.4 eV) and good thermal stability, the semiconductor cadmium sulfide (CdS) has been used as a window layer in heterojunction photovoltaic devices. For heterojunction cells, it is important to reduce the lattice mismatch between the absorber and window material. The lattice mismatch between (112) oriented CuInSe₂ and (001) oriented CdS is very small (about 1%). Therefore, thin films of CdS have been used for the fabrication of high efficiency CdS/CuInSe₂ solar cells^{6.1}. Different deposition methods have been used for the preparation of CdS thin films. These methods include: single source evaporation, two source evaporation, dc and rf sputtering, screen printing, spray pyrolysis and chemical vapor deposition^{6.2}.

For solar cell applications, the CdS layer must have a low electrical resistivity. The low resistivity is needed in order to minimize the unwanted voltage drop across the series resistance associated with the window material. To reduce the resistivity of the CdS films, one can either control the stoichiometry of the films or introduce foreign atoms (dopants) into the films. It has been reported^{6.3} that thermal stability of the doped CdS films is good. Therefore, in the present work the resistivity of

the CdS films was controlled by adding impurities.

In a conventional evaporation technique for CdS, a separate boat is usually used for the dopant^{6.4}. In this technique, a precise control over the temperature of the two (sometimes even three) sources is needed. In our laboratory, we have developed a single boat method for the deposition of low resistivity CdS films^{6.5}. In this method, a tantalum boat was used to contain both the dopant (indium, in a form of In_2S_3) and the CdS material. This method was found to be effective in producing good quality CdS films with a low resistivity. The deposition process and the results of investigation for the CdS films will be described in this chapter. Results on the anti-reflection coating and deposition of electrical contacts also will be reported.

6.2 Deposition Process of Low Resistivity CdS Films

The deposition experiments for the CdS films were carried out in a conventional vacuum system with a diffusion pump capable of a chamber base pressure of about 10^{-6} Torr. The schematic diagram of the chamber is shown in Fig. 6.1. Weighed amounts of high purity (99.9999%) CdS powder and high purity (99.9999%) In_2S_3 powder (2 wt%) were well mixed and used as the source material. Indium was added in order to reduce the electrical resistivity of the CdS films. The mixed powder was loaded into a tantalum (Ta) boat with a tungsten wool placed at the outlet of the boat to prevent spattering of the source material during the evaporation. Four CuInSe_2 samples, prepared by electrodeposition, were mounted on an aluminum block which was resistively heated

during the deposition. A glass slide was also placed beside the CuInSe₂ samples to obtain CdS films for monitoring purpose. An aluminum mask with square windows of an area 0.9 cm² each was placed in front of the samples. The mask was designed so that on each CuInSe₂ film, there were two CdS regions, therefore two heterojunction devices. The distance between the substrates and the boat was about 12 cm during the evaporation process. The temperature of the sample holder was monitored by an iron-constantan thermocouple and controlled by a temperature controller. An aluminum shutter was provided to control the evaporation time-sequence and the thickness of the films.

After the vacuum chamber was evacuated to a pressure of about 10⁻⁶ Torr, the sample holder and the samples were heated up slowly (average heating rate of about 6°C/min). The deposition process was started when a substrate temperature of about 180°C was reached. This temperature was maintained during the deposition process. The deposition rate was controlled by adjusting the current flowing through the boat. Typical deposition runs usually took about 6 minutes which resulted in films with a thickness of about 3-4 μm, giving an average deposition rate of about 0.6 μm/min. When the deposition process was completed, the sample holder was cooled to room temperature by a water cooling system. The samples were then removed from the vacuum chamber. The electrical properties and the crystallinity of the CdS films were obtained from the films deposited on the glass slides.

6.3 Examination of CdS Films

X-ray diffraction measurements were made on the films deposited on the glass slides, using a Philips model PW1710 diffractometer. It was found from the X-ray results that all of the films doped with 2 wt% indium had a wurtzite structure with the preferred (001) orientation. These results are important because the CdS films with this orientation have a minimum mismatch with the (112) oriented CuInSe_2 . Fig. 6.2 shows intensity of diffracted X-ray versus 2θ for one of the CdS samples deposited on the glass slides. We can see two peaks in the 2θ range from 10 to 70 degrees, one at 27.5 degrees and the other at about 55 degrees. From ASTM data, these peaks were identified as diffraction peaks from CdS films having a wurtzite structure with the (001) plane aligned to the film surface.

The microstructure of the CdS films was examined by SEM and a columnar structure was found for all of the samples. The long axis of the columns was observed to be perpendicular to the substrate surface (see Fig.6.3). For a powdered CdS sample, the ratio of height for the (100) peak ($2\theta=24.8^\circ$) to that for the (002) peak is 1.25. In Fig. 6.2, the (100) peak is not visible and the above ratio is equal to 0. It is thus evident that the direction of the long axis is perpendicular to the (001) plane. From the film thickness of about $4\ \mu\text{m}$ in Fig. 6.3, the average deposition rate is estimated to be $0.6\ \mu\text{m}/\text{min}$. SEM pictures were also taken on several CdS/ CuInSe_2 structures and one of these is shown in Fig 6.4. In this picture, one can see that the long

axis of the CdS grains is aligned almost along the long axis of the CuInSe₂ grains. However, a small inclination is also visible in the CdS film. This inclination effect was found for all of the samples located at positions away from the outlet of the CdS boat during the deposition process. Therefore, the long axis of the CdS grains can be controlled by controlling the relative position of the substrate and the boat^{6.5}.

In order to determine the electrical properties of the CdS films, room temperature Hall effect measurements were carried out using the Van der Pauw method. From the measured values, both carrier concentration and mobility were deduced. The results for four of the as-deposited CdS samples are given in Table 6.1. Results for the sample 2351 after an air treatment at 200 °C are also shown. The carrier concentration of the as-deposited CdS films is in the range from 10^{20} to 10^{21} cm⁻³. The value is seen to decrease after the air treatment at 200°C due to the oxygen diffusion. The mobility value of the sample also decreased after the treatment. From the Hall effect measurements, the resistivity of the CdS films was found to be about 10^{-3} Ω-cm, which is consistent with that obtained using a four point probe method.

The optical properties of the CdS films were investigated by transmission measurements in the wavelength range from 0.4 to 2 μm. A Beckman model 2400 monochromator with the input light chopped at 86 Hz was used as the light source. The light intensity, both transmitted through a glass slide and through a CdS coated glass slide, was measured. Two detectors were used for the intensity measurements. One was a calibrated silicon detector for

the range from 0.4 to 1.1 μm and the other an InSb detector operated at 77K in the range from 1 to 2 μm . A 10 Ω resistor was connected across the detector and the voltage developed across it under illumination was measured by a lock-in amplifier. The light intensity was determined from the ratio of measured voltage to resistance. Finally the transmission values were obtained by taking the ratio of the light intensities transmitted through the CdS coated glass slide to the intensity transmitted through the uncoated glass slide.

It was found that the transmission values, especially those in the long wavelength region, were affected by the resistivity of the CdS films. As an example, Fig. 6.5 shows the transmission results for two samples with different resistivities. In the short wavelength range, the transmission for both samples increases as the wavelength is increased from 0.5 μm until a maximum transmission value (at about 0.7 μm) is reached. For the sample with a resistivity of 9×10^{-3} $\Omega\text{-cm}$, the transmission remains essentially constant as the wavelength is further increased. However, the transmission shows a continual decrease for the sample with resistivity of 2×10^{-3} $\Omega\text{-cm}$.

In order to study the effects of heat treatment on the transmission of the CdS films, the sample 3659 was treated in air at 200°C for 1 hour. This treatment did not result in a large change in the resistivity. After the treatment, the optical transmission of the sample was measured again and the results are shown in Fig. 6.6. The transmission value in the long wavelength range was increased by the treatment.

For photovoltaic window applications, it is important to have a high optical transmission value in the short wavelength region (0.5-1.0 μm). In this region, the density of the solar photons is highest. In addition to controlling the window material, this high optical transmission value can be further improved by depositing a thin layer of anti-reflection material, SiO_x on top of the CdS films. In the present experiment, several CdS films were selected and a SiO_x layer was evaporated. The thickness of the SiO_x film was controlled by controlling the amount of the source material introduced into the Mo boat. It was found that a SiO_x layer with a thickness of 900 Å was effective in reducing the reflection losses and therefore in increasing the transmission value in the short wavelength region (see Fig. 6.7). For this sample, a 10% increase in the transmission is seen in the short wavelength range from 0.5 to 1.0 μm .

6.4 Al Contacts Deposition

After the CdS film deposition, the top electrical contacts were deposited by evaporating aluminum grids through an aluminum mask in a separate vacuum system. The thickness of the grids was about 2 μm and the active area of the cells was about 0.71 cm^2 . Fig. 6.8 shows the top view of a CdS/CuInSe₂ cell after the contact deposition. The width of the fingers is about 250 μm and the separation between the fingers is about 800 μm . A schematic cross-sectional view of the device is also given in Fig. 6.9.

The contact resistance between the Al grids and the CdS film was determined to ensure an ohmic contact. The investigation was

done by carrying out dark I-V measurements between disconnected fingers. The results for one of the devices are shown in Fig. 6.10, where the I-V characteristics between the fingers (0-1, 0-2, 0-3, 0-4 and 0-5) are plotted. It is seen that the current varies linearly with voltage for all four sets of measurements. Therefore, the resistance between the fingers can be calculated from the slope of the lines. This resistance is the sum of the lateral resistance associated with the CdS film between the two fingers and the resistances of the two contacts (see Fig. 6.11). In Fig. 6.12, the resistance between the fingers versus the finger spacing is plotted for two devices. Here, finger spacing is the number of the unit space, which is defined as the space between the two nearest fingers. The contact resistance can thus be obtained by extrapolating the resistance line to the vertical axis. For the sample No. 1, the contact resistance value is about $2.5/2 \Omega$ for one finger contact and that of the sample No. 2 is even smaller. The results for sample No. 2 after an air treatment at 200°C for 20 minutes (to simulate the post treatment for the CdS/CuInSe₂ cells) are also shown in this figure. It was found that the contact resistance was not affected by the treatment.

6.5 AR Coating Deposition

For the photovoltaic device fabrication, the anti-reflection (AR) layer was deposited after the deposition of the electrical contacts. The thickness of the AR coating was usually small (about 900 \AA) and the coating could easily be penetrated by the probe during the test. AR coating with the right thickness was

always a dark blue color, however, green colored AR coating also showed some improvement in the short circuit current.

6.6 Conclusions

A single-boat evaporation method has been used for the deposition of the low resistivity CdS thin films. An addition of 2 wt% In_2S_3 was found to be effective in producing CdS films with resistivity as low as $2 \times 10^{-3} \Omega\text{-cm}$. A columnar structure with the long axis of grains perpendicular to the surface of the substrate was observed for all of the samples deposited in the region immediately above the CdS boat. From the X-ray measurements, the direction of the long axis of the columns was confirmed to be perpendicular to the (001) plane. This orientation is important in reducing the lattice mismatch between the CdS film and the (112) oriented CuInSe_2 film. An inclination of the long axis of the columns was observed for the films deposited at a position away from the projection of the CdS source, which can be used to fine tune the lattice constant of the CdS films.

For CdS with low resistivity, the optical transmission was found to decrease continuously with the increase of wavelength in the long wavelength range. The transmission increased after an air treatment at 200°C (which decreased carrier concentration). This fact thus suggested that the variation of the transmission coefficient could be due to a free carrier absorption effect. Optical transmission of the CdS films was found to be further improved by depositing an anti-reflection SiO_x layer with a thickness of about 900 Å. Top electrical contacts to the CdS films were achieved by evaporating aluminum grids. It was con-

firmed that the contact between the Al and the CdS film was ohmic.

Table 6.1 Hall effect results of In-doped CdS films.

Sample No.	n (cm^{-3})	μ ($\text{cm}^2\text{V}^{-1}\text{sec}^{-1}$)	Conditions
2789	1.4×10^{20}	47	2% In, untreated
2842	3.1×10^{20}	22	2% In, untreated
2846	1.7×10^{21}	4	2% In, untreated
2351	3.0×10^{20}	13	2% In, untreated
2351	6.0×10^{19}	6	Air heat treated at 200°C , 20 hrs

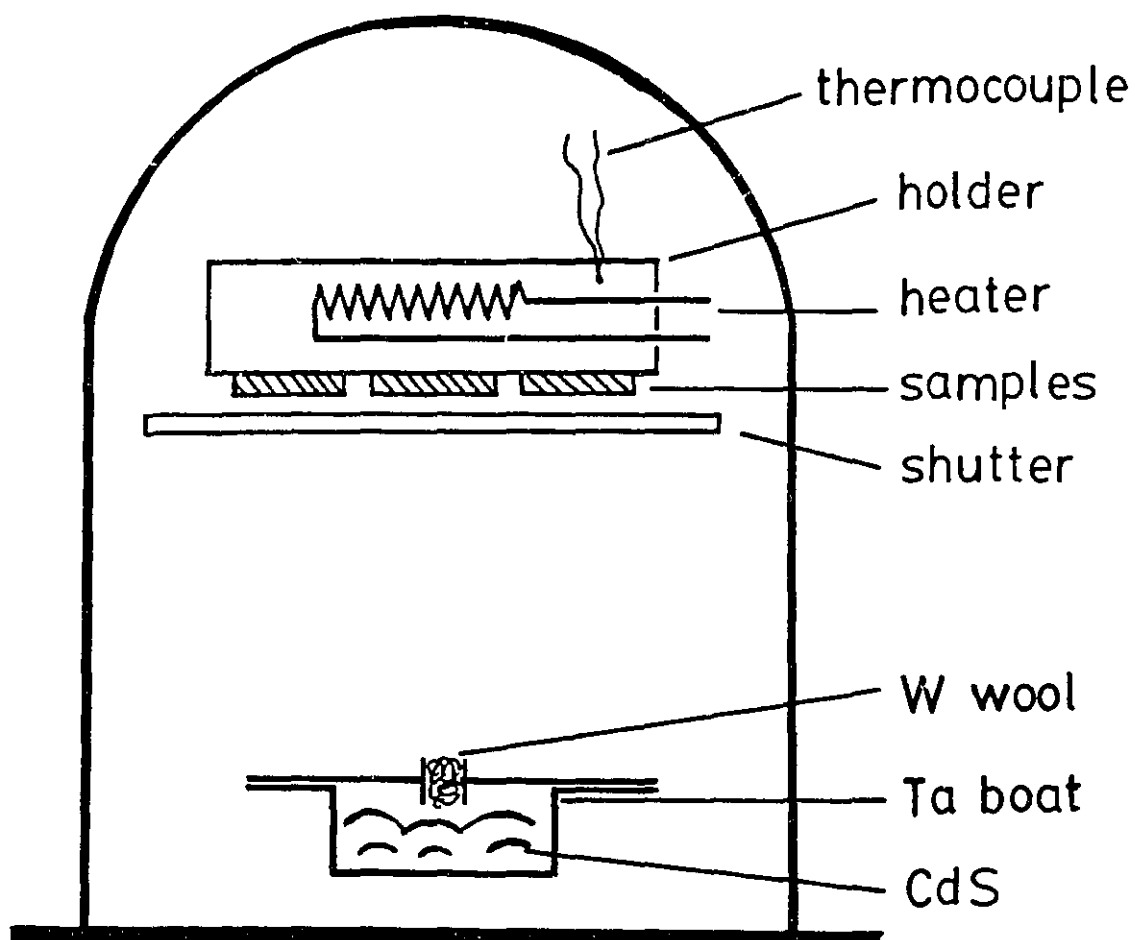


Fig. 6.1 A schematic diagram of the evaporation system for the deposition of CdS films.

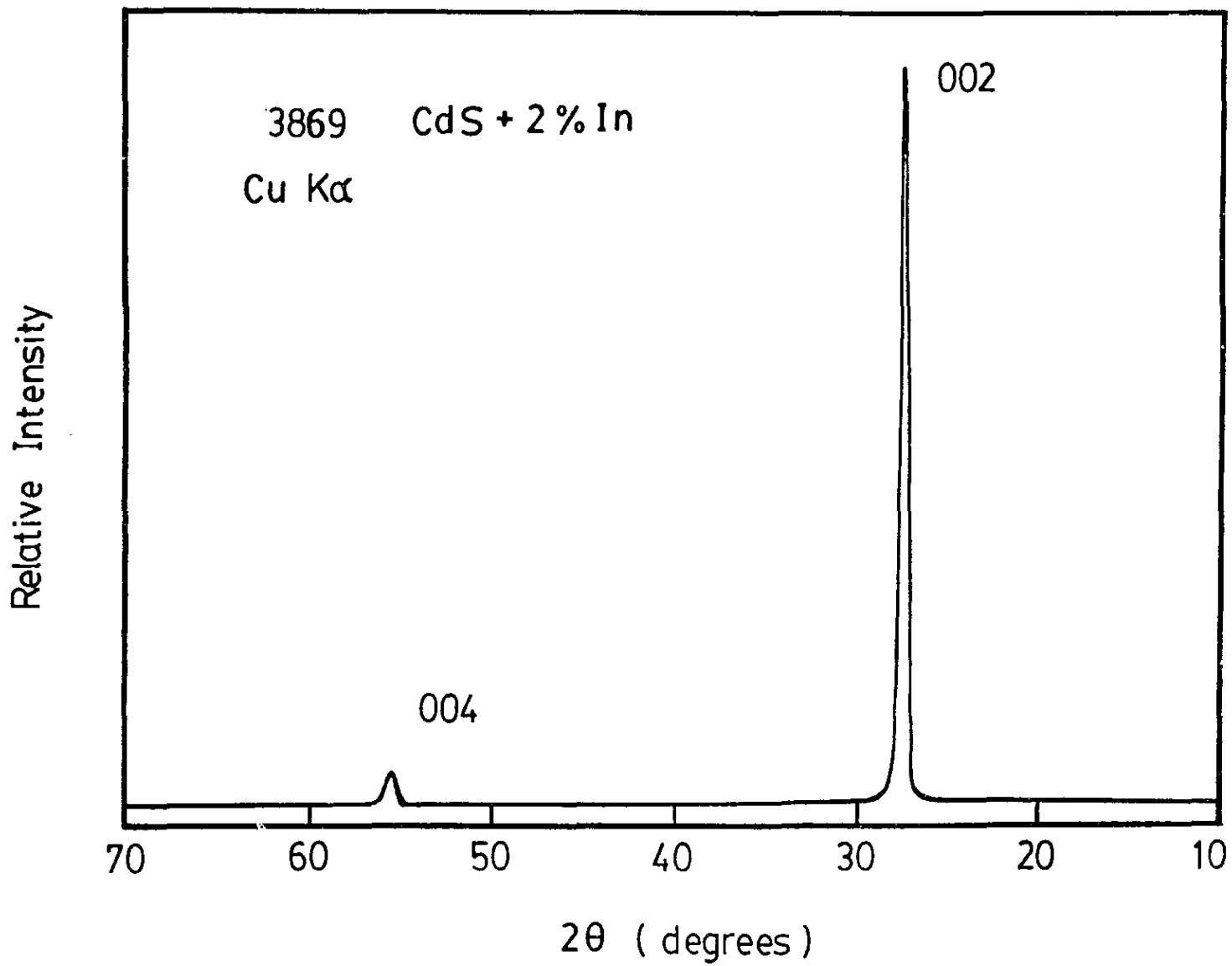


Fig. 6.2 XRD pattern for a CdS film doped with 2 wt% In.

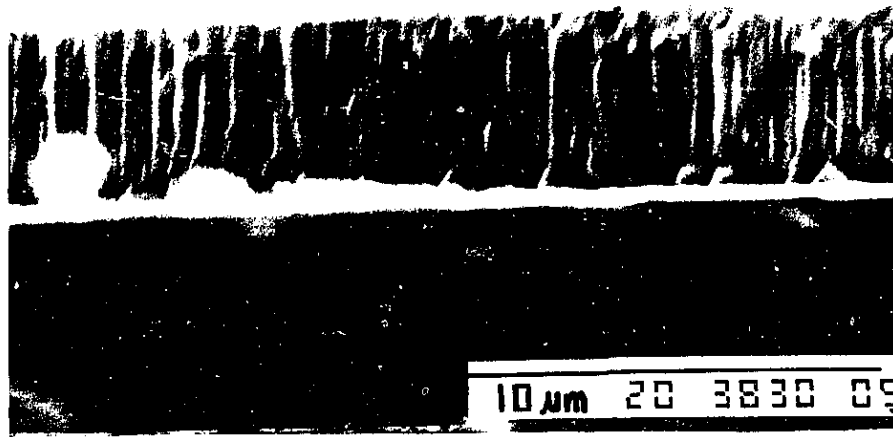


Fig. 6.3 An SEM photograph showing the cross section of a CdS film on a glass substrate.

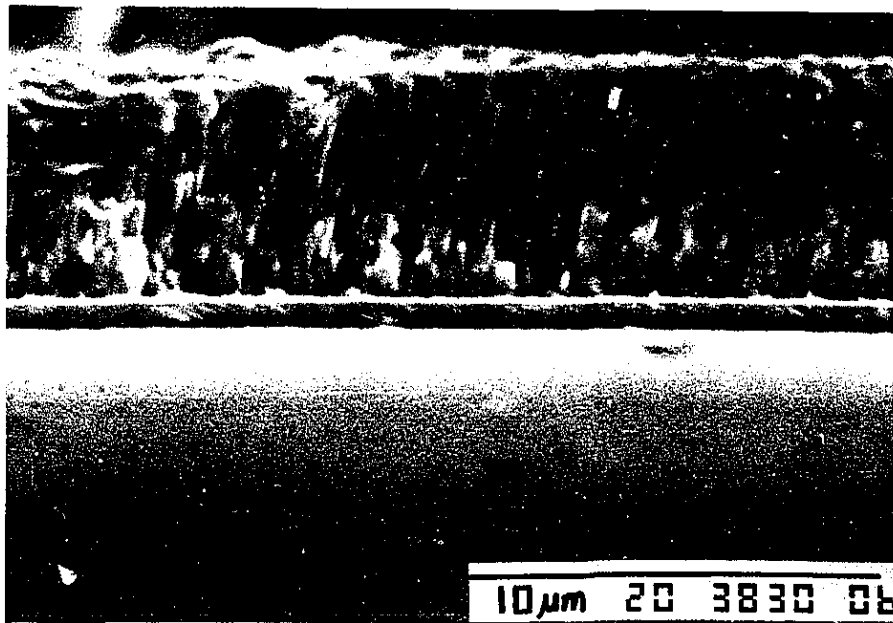


Fig. 6.4 A cross-sectional view of a CdS/CuInSe₂ structure on a Mo/glass substrate. The columnar micro-structure is clearly seen for both CdS and CuInSe₂ layers.

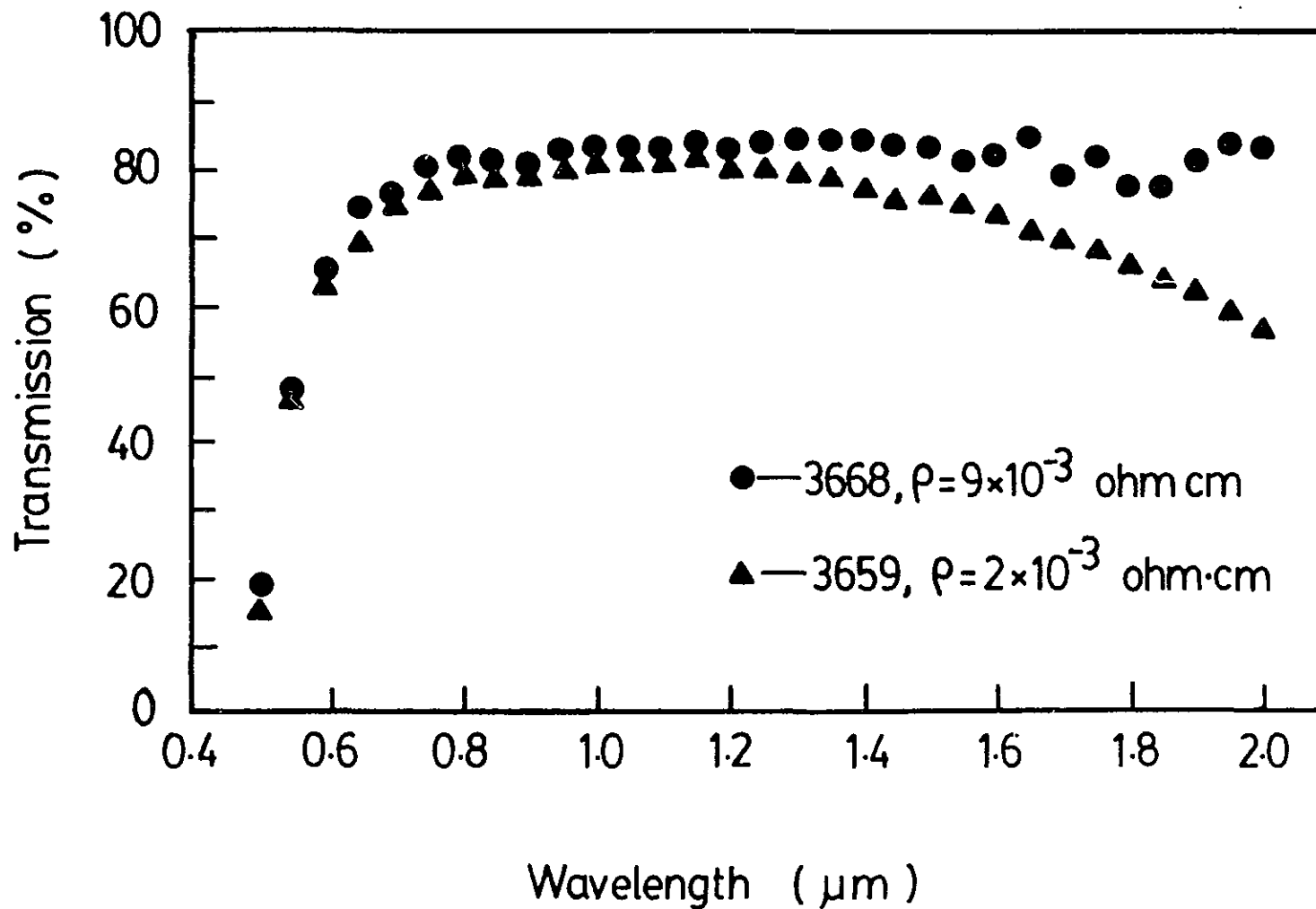


Fig. 6.5 Results of optical transmission measurements for two CdS films, showing the effect of film resistivity on the long wavelength transmission.

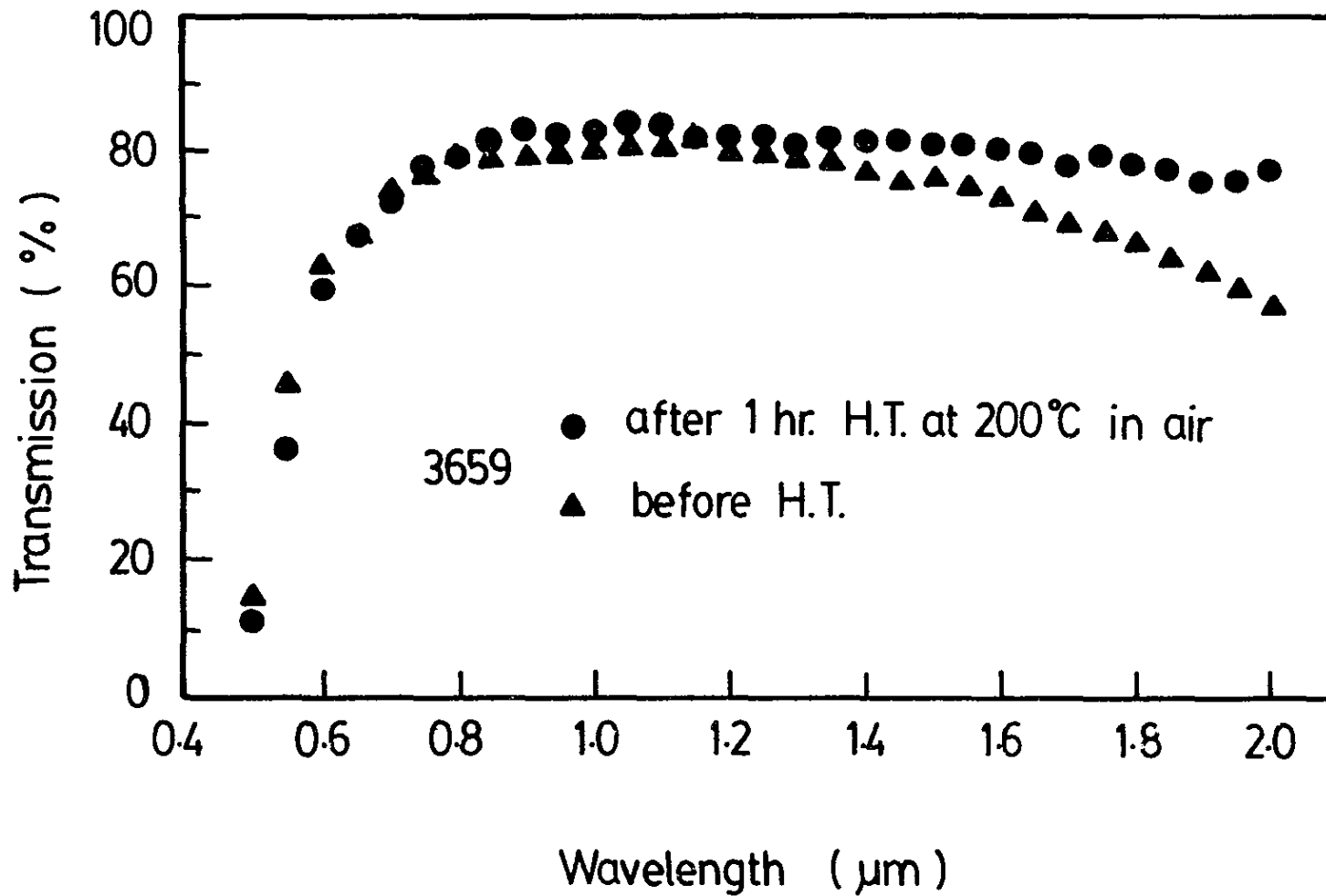


Fig. 6.6 Results of optical transmission measurements for a CdS film before and after an 1 hr heat treatment in air.

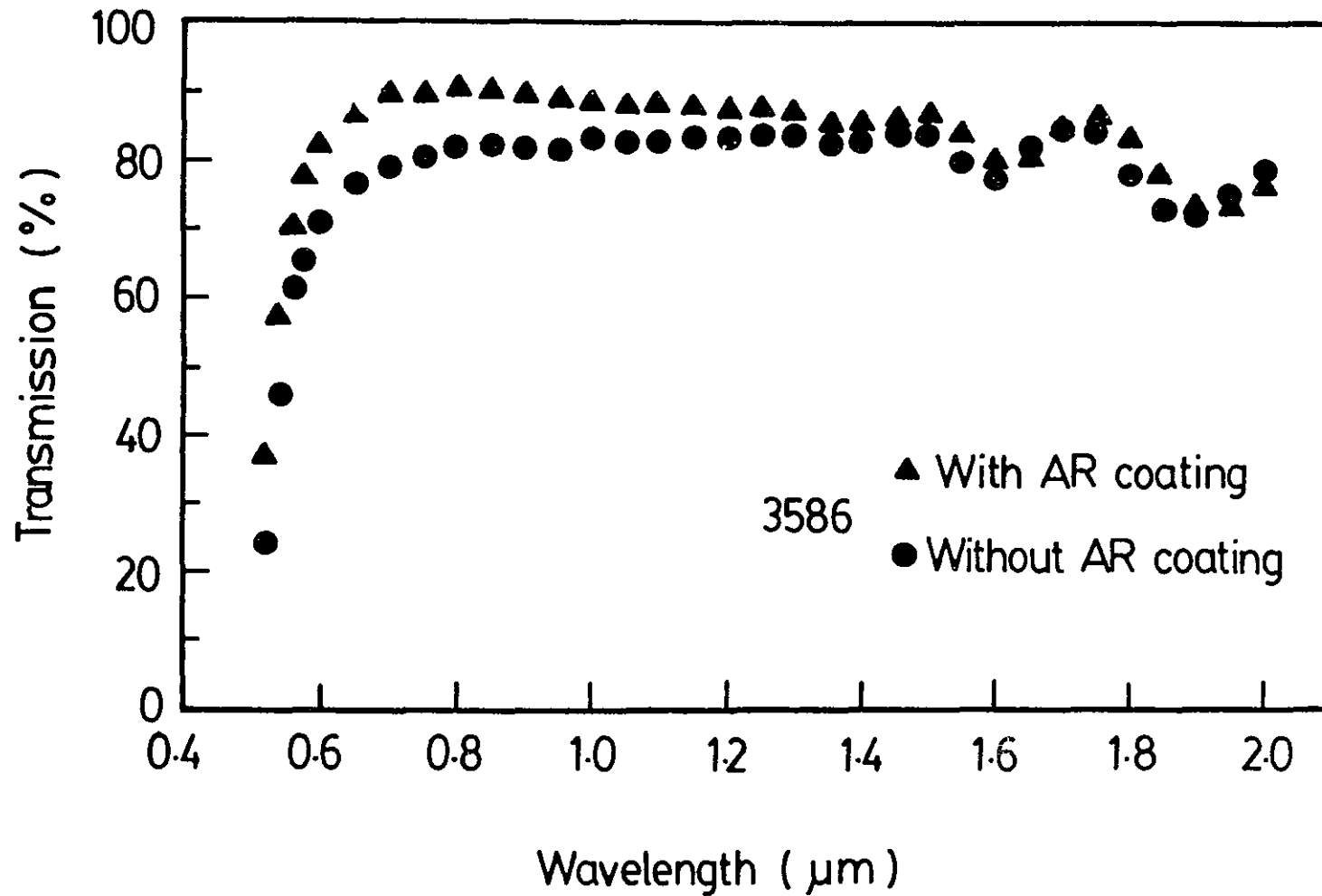


Fig. 6.7 Results of optical transmission measurements for a CdS sample before and after the AR coating deposition.

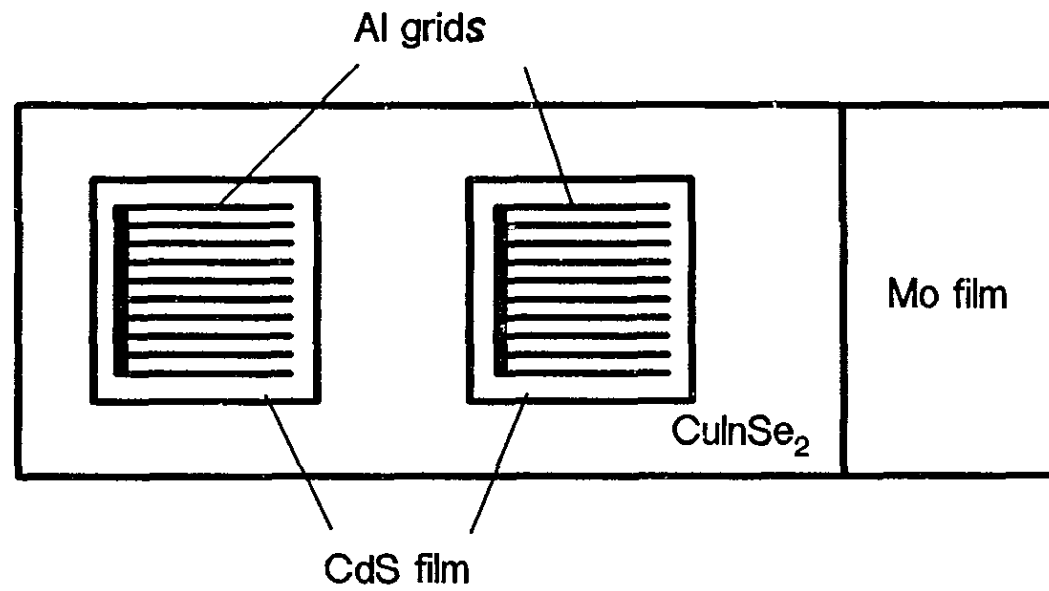


Fig. 6.8 A top view of two CdS/CuInSe₂ cells fabricated on a CuInSe₂ film.

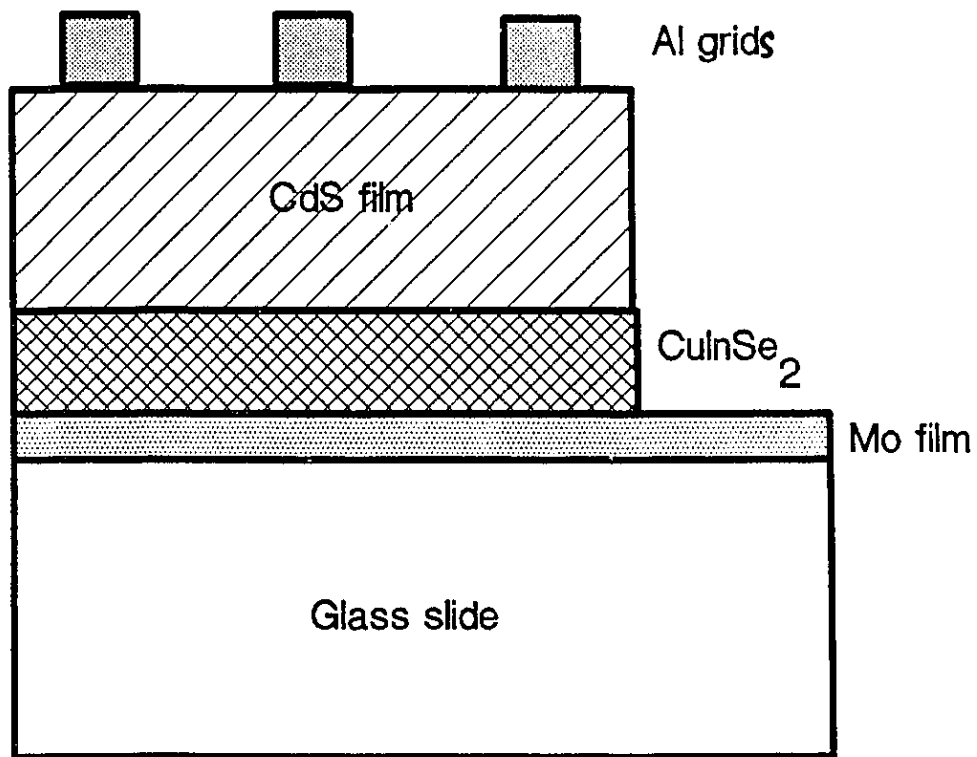


Fig. 6.9 A cross-sectional view of the CdS/CuInSe₂ solar cell.

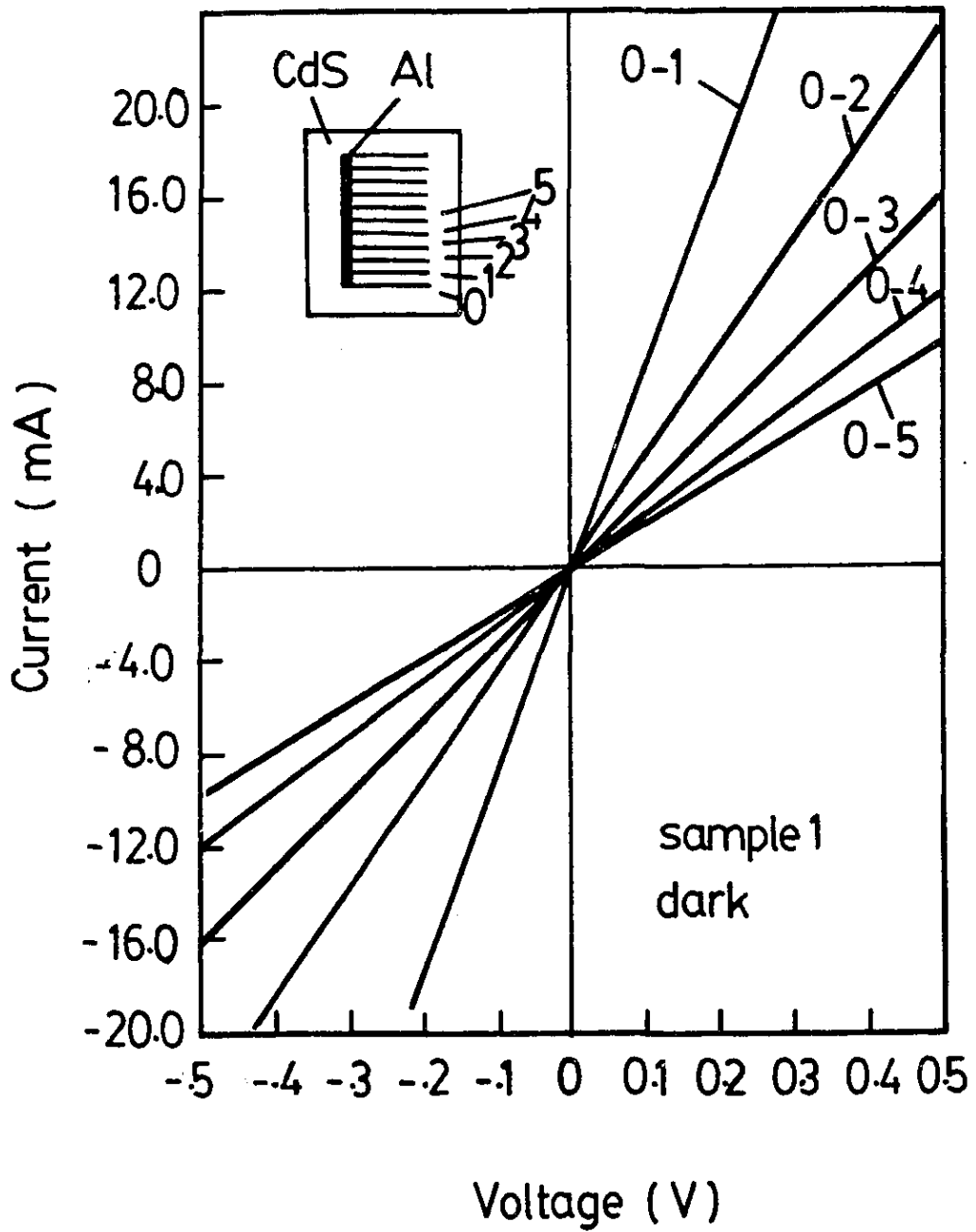


Fig. 6.10 I-V curves measured between disconnected Al fingers on CdS.

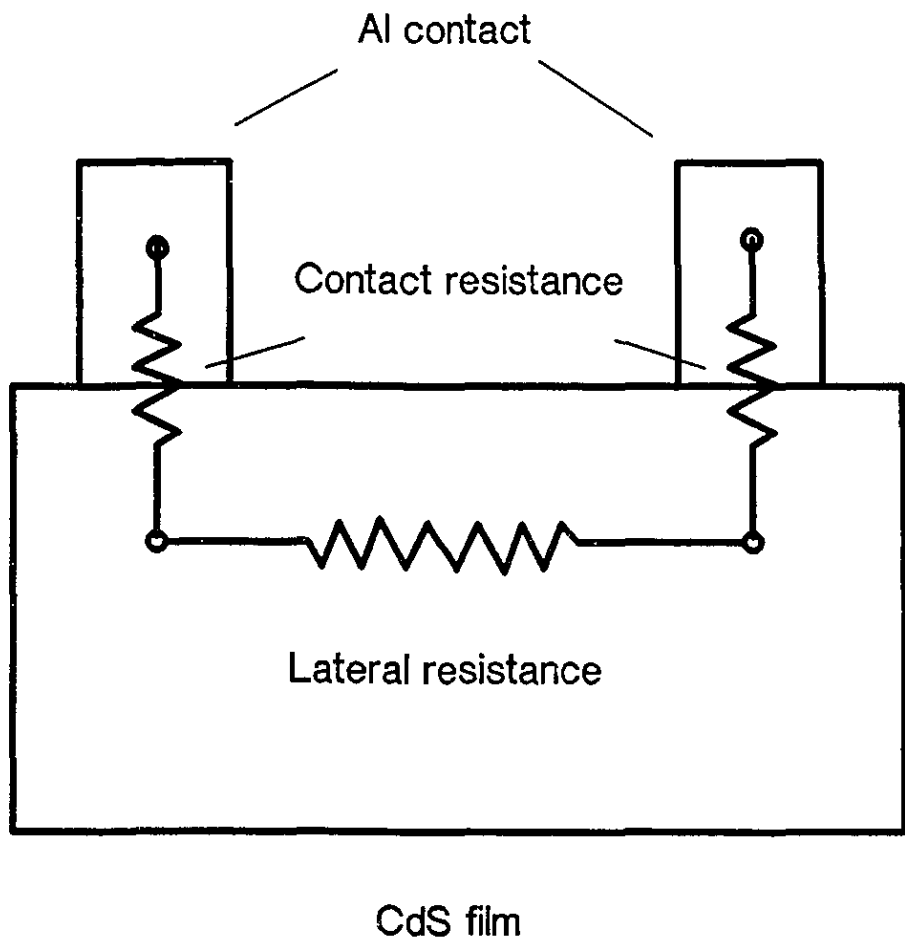


Fig. 6.11 A schematic diagram showing the lateral and contact resistance in a CdS film.

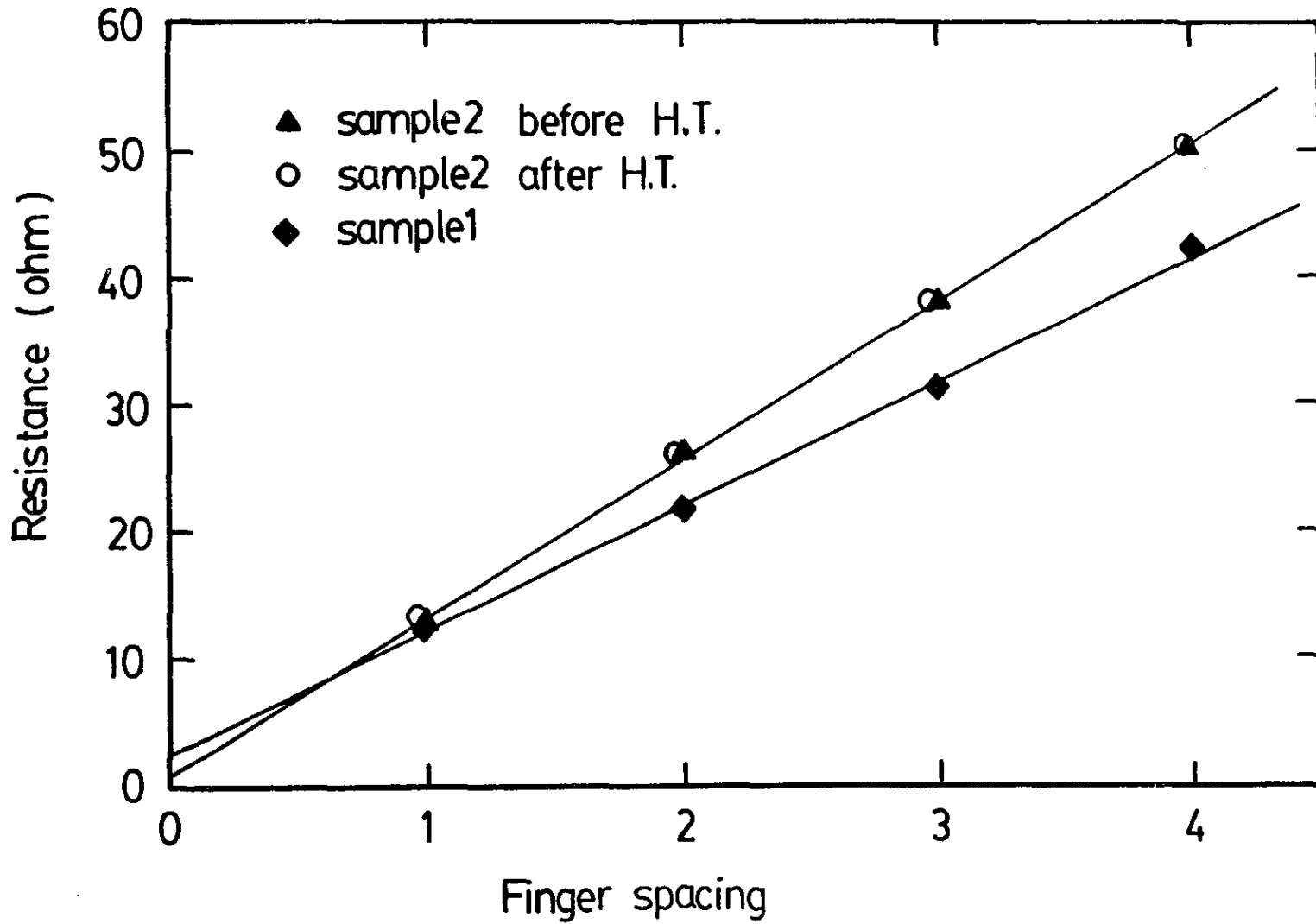


Fig. 6.12 Resistance between the Al fingers on CdS plotted against the finger spacing, extrapolation gives the contact resistance.

Chapter 7 CHARACTERIZATION OF THE CdS/CuInSe₂ SOLAR CELLS

7.1 Introduction

After the first report of a high efficiency monocrystalline CuInSe₂ cell^{7.1}, further efforts have been made by several research groups to fabricate thin film CdS/CuInSe₂ cells and to improve the efficiency. As mentioned in chapter 1, the semiconductor CuInSe₂ is one of the best candidates for low cost photovoltaic cells if a low cost deposition technique can be developed. For the CuInSe₂ films, the electrodeposition method developed in our laboratory appears to be the most economic one because of the high material utilization and low energy consumption. Like all the other deposition methods, this technique can be proved to be useful only by fabricating photovoltaic cells and testing their optoelectronic properties. Therefore, in the present work cells of CdS/CuInSe₂ were fabricated on the electrodeposited CuInSe₂ films and the optoelectronic properties were investigated.

In the present work, the following specific research experiments have been carried out on CdS/CuInSe₂ cells: (1) Investigation on the effects of post-fabrication air heat treatment, (2) Examination of the effects of film composition on the cell performance, and (3) Investigation of the current transport mechanism of the CdS/CuInSe₂ devices and study of interface state

effects on cell efficiencies. Results of the above studies on the CdS/CuInSe₂ solar cells, are described in this chapter.

7.2 Current-voltage Characteristics

After the fabrication of the CdS/CuInSe₂ photovoltaic cells using the procedure described in chapters 3, 4 and 6, both dark and illuminated I-V characteristics of the cells were measured using an HP mode 4145A Semiconductor Parameter Analyzer. For the preliminary testing of the illuminated I-V characteristics, a tungsten light source, with light intensity adjusted to the AM1 condition (using a Si cell), was used. In order to obtain the solar to electrical conversion efficiency, devices were illuminated by noon sun light. In order to prevent heating of the cells by the illuminated light during the testing, the illuminated I-V characteristics were measured immediately after the application of the light.

7.2.1 Effects of post-fabrication air heat treatments

7.2.1.1 Cells fabricated on the Mo plate substrates

Using molybdenum plates as the substrates, the as-fabricated cells were either shorted or very leaky with very little photovoltaic effect. A short post-fabrication air heat treatment, at temperatures in the range from 180 to 200 °C, was found to be efficient to improve the I-V characteristics of the cells. In most of the cases, the treatment was carried out for a period of 10 minutes to form the junction. An additional heat treatment was found to improve further the I-V characteristics by reducing

the reverse current. The dark current-voltage characteristics for a sample (CTN-2436) after different heat treatment experiments are plotted in Fig. 7.1. After the first heat treatment for 20 minutes, the I-V curves show a rectification ratio of about 100 at ± 0.4 volt and a near ideal ideality factor of about 1.15. The reverse current of the cell is seen to be reduced by additional treatments for 10 and 20 minutes. It is noted that after the additional treatments, the forward current is essentially not affected and the n factor is not changed.

Illuminated I-V characteristics obtained under the AM1 condition for the cell No. 2436 are shown in Fig. 7.2. A photovoltaic effect is seen after the fabrication, with a small open circuit voltage (V_{OC}) of 0.083V and a fill factor (FF) of 0.25. After the first heat treatment for 10 minutes, the short circuit current (I_{SC}), open circuit voltage and the fill factor are seen to improve. A further treatment in air is seen only to increase the V_{OC} value. This increase in the open circuit voltage is consistent to the decrease in the saturation current (Fig. 7.1). It should be pointed out that the open circuit voltage for all of the cells fabricated on the Mo substrates was generally small even after a prolonged treatment. This is due to the relatively rough surface of the $CuInSe_2$ films deposited using the Mo plates.

7.2.1.2 Cells on the Mo/glass substrates

For the as-fabricated cells on the Mo/glass substrates, the open circuit voltage was generally larger than that on the Mo

substrates. As an example, Fig. 7.3 shows the dark and illuminated I-V curves for the cell No. 3827. A rectification ratio of more than 100 at ± 0.4 volt was obtained for the untreated device. Under the AM1 illumination condition, the cell showed an open circuit voltage of about 0.26 V and a short circuit current of more than 21 mA, corresponding to an active current density of about 30 mA/cm^2 (active area 0.71 cm^2). After 10 minute air treatment at 200°C , the cell showed an increased J_{SC} of about 33.2 mA/cm^2 and a V_{OC} of more than 0.3 V, yielding an active area efficiency of 5.2%. Therefore, it is evident that the performance of the cell was improved greatly by the 10 minute treatment. For the cell No. 3827, additional heat treatments were found not to improve much of the efficiency.

7.2.2 Compositional effects on the I-V characteristics

For the CdS/CuInSe_2 cells made of electrodeposited CuInSe_2 films, an interesting effect has been observed: The short circuit current was found to depend on the composition, or the metal ratio of the CuInSe_2 films. Figure 7.4 shows the illuminated I-V characteristics for four devices (all on Mo substrates) with different In/Cu ratios in the CuInSe_2 film: sample No. 3387: In/Cu=0.98, sample No. 3388: sample In/Cu=1.01, sample No. 3389: In/Cu=1.05 and sample No. 3390: In/Cu=1.08. The four samples were all deposited on Mo plates and the CdS films were deposited in the same deposition run. One can see from the figure, that the I_{SC} value increases progressively with the increase in the In/Cu ratio.

Dark current-voltage characteristics for the four devices were also measured and are given in Fig. 7.5. It can be seen that the rectification ratio of the devices, except No. 3388, increases as the In/Cu ratio is increased. Furthermore, the reverse current for device No. 3388 is the smallest among the cells which explains the relatively large V_{OC} of the cell. The compositional effect was also observed on other devices. Fig. 7.6 shows another set of samples with different In/Cu ratios in the $CuInSe_2$ film: sample No. 3636: In/Cu=1.05; sample No. 3638: In/Cu=1.06; sample No. 3639: In/Cu=1.08 and sample No. 3640: In/Cu=1.10. It is thus evident that, from the present results, the larger the In/Cu ratio is, the larger the I_{SC} is obtained. It is not correct to say, however, that the In/Cu ratio should be as large as possible, because larger In/Cu ratios usually resulted in smaller open circuit voltage of the cells, as shown in the figures. A compromise must be made in order to obtain higher efficiency.

7.2.3 Anti-reflection (AR) coatings

A layer of AR coating (900 Å thick SiO_2) was deposited on the $CdS/CuInSe_2$ cells to increase the I_{SC} value. For most of the cells, an increase of about 10-15% in I_{SC} was obtained. As an example, Fig. 7.7 gives the illuminated I-V characteristics for sample No. 3742 (active AM1 efficiency of 4.4% with the AR coating). One can see that the short circuit current is increased by about 15% after the deposition of the AR coating. The open circuit voltage, however, remains unchanged. For sample 3821, the increase in the short circuit current is also about 15% (see Fig.

7.8). In our experiments, only cells with an active efficiency more than 4% were coated with the AR coating.

7.2.4 Series resistance effect

It was observed that a prolonged air heat treatment would produce poor I-V characteristics on some of the cells, probably due to elemental interdiffusion in the junction. The same effect was also perceived on some devices with a short air treatment. For those devices, a very small fill factor was observed and a large photocurrent was obtained only in the reverse bias region. Figure 7.9 shows the I-V curves for samples No. 2889 and 2881. For the two cells, most part of the I-V curves in the forward voltage range are linear. The resistance for the linear region of the I-V curve was calculated for the two devices. The value for sample No. 2889 is 9.45Ω and is 4.9Ω for sample No. 2881. These results indicated the presence of a large series resistance in the cell, which was believed to arise mainly from the bulk region of the CdS and the CuInSe₂ films. Another possible source for the series resistance is the resistance of the front or/and the back contact. When a layer of high resistivity formed between the contact and the semiconductor during the treatment, a large R_s would be produced. The latter appeared to be the reason for the cells treated only for a short period of time.

In order to confirm the series resistance effect, one set of experiments was carried out. In the experiments, resistors with resistance in the range from 1 to 10Ω were connected in series with a CdS/CuInSe₂ cell (see inset of Fig. 7.10). The resistance

values used were 1, 2.2, 4.7 and 10 Ω . External I-V characteristics of the cell with the resistor were measured and the results are given in Fig. 7.10. The knee of the I-V curves is seen to smooth out gradually when the R_s value is increased from 0 to 10 Ω . As a result, the fill factor as well as the short circuit current decreases greatly with the increase of the R_s value. It is seen that the decrease is more rapid for this device as the resistance value is greater than 2.2 Ω . The open circuit voltage value, however, is not affected by the series resistance. For a non-zero R_s value, the I-V curve shows characteristics similar to those presented in Fig. 7.9. It is therefore believed that a large R_s is responsible for the small fill factor for some of the present cells.

7.2.5 Temperature-dependent I-V characteristics

In order to understand current transport mechanism for the CdS/CuInSe₂ heterojunction devices, temperature-dependent dark forward I-V measurements were carried out in the temperature range from 173 K to 300 K. The same measurement set-up described in chapter 5 was used in the experiments. Fig 7.11 shows the results measured at 7 different temperatures for one of the devices (No. 3870) fabricated on a Mo substrate. The n factor for the curve taken at room temperature is about 1.1. When the temperature decreases from 298K to 193 K, the slope of the curves in the middle voltage region remains essentially unchanged. The ideality factor of the curve at 181 K (curve not shown) was about 1.4. As the temperature is decreased from room temperature to a value

below 233 K, a second current component with a larger n factor (could be due to a tunneling current) appears in the low voltage region. Similar results were also observed on other samples. Fig. 7.12 shows the results for sample No. 3784 (fabricated on a Mo substrate) at five different temperatures. For this device, the ideality factor at 273 K is close to unity.

Since the room temperature n factor was close to unity for most of the cells fabricated on Mo substrates, the current transport mechanism was assumed to be governed by a diffusion current component. Based on this assumption, the saturation current I_0 was obtained simply by extrapolating linear part of the forward I-V curve to the vertical axis. The I_0 value for the cell No. 3870 was found to vary over a range of more than three orders of magnitude in the temperature range of 173 to 298 K. For the sample No. 3784, the saturation current increased by three orders of magnitude as the temperature was increased from 193 to 273 K. For an n^+p one-sided heterojunction, the barrier height may be obtained from the Schottky junction model. Therefore the barrier height, ϕ_B , of the one-sided junction can be estimated from the slope of the $(J_0/T^2)-(1/T)$ plot according to the following equation:

$$J_0 = (1/A) A^* T^2 \exp(q\phi_B/kT). \quad (7.1)$$

Here, A is the area of the device, A^* is the effective Richardson constant and k is the Boltzmann constant. In Fig. 7.13, J_0/T^2 values for the sample No. 3784 are plotted versus $1000/T$ in a semi-logarithmic scale. From the figure, the barrier height of

the cell was estimated to be about 0.4 V. This value is smaller than the value of 0.9 V obtained on cells fabricated using a different method^{7.2}. In Fig. 7.14, a comparison is made between four devices: two Boeing cells^{7.3} and two cells from our laboratory (No. 3784 and 3870). The same method was used to calculate the barrier height for the Boeing cells. The barrier height for samples 3870 and 3784 is about 0.4 V and is 0.66 V for the two Boeing cells.

7.2.6 Fitting results of the cells

In order to obtain further information for the junctions, the saturation current (I_S) and recombination current (I_R) were determined by the fitting program used in chapter 5 (see equation 5.5). The fitted I_S and I_R as well as the series resistance R_S for two CdS/CuInSe₂ cells are listed in table 7.1. At room temperature, I_R is in the order of 10^{-5} A and I_S is about one order of magnitude less for the sample No. 3772. The fitted room temperature series resistance for this device is about 5.2 Ω . For the sample No. 3784, fitting results for seven different temperatures are listed. It is noted that as the temperature is decreased, both I_R and I_S values decrease. When the temperature is decreased from 273 K to 188 K, I_S decreases almost three orders of magnitude. In the same temperature range, I_S varies from 6.5×10^{-7} A to 5.4×10^{-13} A, a change of about 6 orders of magnitude. The series resistance varies in the opposite manner. It increases from 7.6 to 17.1 Ω as the temperature is decreased from 273 to 188 K.

Using the fitted I_S values, I_S/T^2 was recalculated and plotted versus $1000/T$ in Fig. 7.15. The data points in the figure are well fitted by a straight line. The slope of the line, corresponds to a barrier height of about 0.64 V. This value is larger than the one obtained from the measured data in Fig. 7.13 and is believed to be more close to the real barrier height value.

7.3 Differential Capacitance-voltage Measurements

To determine the differential capacitance-voltage (C-V) characteristics of the cells, the LCR meter (HP model 4274A) employed in chapter 5 was used. The differential capacitance was measured at four different frequencies: 10, 20, 40 and 100 kHz.

7.3.1 Dark C-V results

Fig. 7.16 shows the dark C-V results for a cell with low efficiency (No. 3079), fabricated on Mo/glass substrate. In the figure, C^{-2} values are plotted versus voltage for four different frequencies. The depletion width, W , at zero bias is obtained directly from the zero bias capacitance $C(0)$ using the equation:

$$W(0) = \epsilon_0 \epsilon_r A / C(0). \quad (7.2)$$

Here A is the area of the cell and ϵ_r is the dielectric constant of CuInSe_2 . At 100 kHz, the depletion width is about $0.08 \mu\text{m}$ for the cell. One should note that this value is much smaller than $0.28 \mu\text{m}$ for the high efficiency cells reported by Boeing^{7.2}. It is also smaller than that for the cells with an active efficiency in the range of 3 to 5%. Of those cells, the zero bias depletion

width is around $0.15 \mu\text{m}$. It is highly unlikely that a cell with such a small depletion width would give a large short circuit current density and a high conversion efficiency. It was found that after a short air treatment at temperatures from 180 to 200°C , a larger depletion width was usually obtained. For example, $W(0)$ increased from 0.066 to $0.12 \mu\text{m}$ for sample No. 3827 after a treatment for 10 minutes. Further heat treatment led to a further increase in the width of the depletion region but with a slower rate. These results suggested a reduction in the space charge concentration near the junction after the treatment.

It is seen from Fig. 7.16 that the measured capacitance is frequency-dependent. However, the slope of the curves is essentially independent of the measurement frequency. This fact suggests that the density of deep levels near the junction is not very large. In addition, it is also seen that the slope of C^{-2} curves is not a strong function of the bias voltage, indicating that carrier concentration in the CuInSe_2 film is relatively uniform.

For the present cells, the carrier concentration in the CdS is much greater than that in the CuInSe_2 . Therefore, the carrier concentration of the CuInSe_2 film can be determined from the slope of the C^{-2} curves. For the concentration determination, it is necessary to have low density of deep levels and interface states. From the slope of the curve taken at 100 kHz, the apparent acceptor concentration (N_A) was estimated from the following equation:

$$N_A = [2/q\epsilon_0\epsilon_r A^2] [-dV/d(1/C^2)]. \quad (7.3)$$

For the device in Fig. 7.16, the N_A value is about $1.3 \times 10^{17} \text{ cm}^{-3}$ near the depletion edge at zero bias. The carrier concentration deeper in the CuInSe_2 film is slightly higher ($1.8 \times 10^{17} \text{ cm}^{-3}$). The apparent diffusion potential V_D for this cell is about 0.68 V at 100 kHz.

It is important to point out that a variation in the voltage intercept for the $1/C^2$ curves at different frequencies was common to most of the present cells. This characteristic suggested the presence of interface states (or deep levels near the interface) with different relaxation time constant.

7.3.2 Effect of heat treatment

In Fig. 7.17, dark C-V results for a cell with an efficiency of 5.2% (No. 3827) measured at 100 kHz are given to show the effect of the air heat treatment on the effective carrier concentration. The upper curve was measured after a treatment for 20 minutes and the other after an additional treatment for 10 minutes. Note that the C^{-2} values after the treatment for 30 minutes treatment have been divided by 10 before plotting on the graph. After the 20 minute treatment, the carrier concentration is about $1.0 \times 10^{17} \text{ cm}^{-3}$ in the voltage region from -0.2 to -1.0 V. The concentration value near the physical junction is slightly smaller ($8 \times 10^{16} \text{ cm}^{-3}$). After the additional treatment for 10 minutes, the N_A value decreases to about $1.6 \times 10^{16} \text{ cm}^{-3}$ in the voltage region of -0.5 to -1 V. The charge carrier concentration near the physical junction is also decreased after the air heat

treatment. The results indicate that the air heat treatment, which is required to form the junction, causes a decrease in the charge carrier concentration of the CuInSe_2 film. This is different from what has been seen for the Al/CuInSe_2 Schottky junctions described in chapter 5. Furthermore, the concentration in the voltage range of -0.5 to about 0.2 V is now larger than the bulk value and the value increases as one goes toward the interface. The slower rate of decrease for the concentration near the physical junction can be explained by the compensation effect of oxygen atoms diffused into the junction. The diffused oxygen atoms act as acceptors in the p-type CuInSe_2 films.

7.3.3 Illuminated C-V results

In order to investigate the interface states of the cells, illuminated capacitance was measured. Under external illumination, charge carriers in the junction are excited. If the light intensity is sufficiently high, the excited carriers can fill the deep traps or the interface states^{7.4}. The occupation probability for the bulk deep traps or the traps at the interface is close to 1 under high light intensities. The filled deep traps decrease or increase the measured capacitance, depending on the type of the traps (majority or minority). More importantly, the charged deep levels will modify the slope of the C^{-2} curve (or modify the apparent acceptor concentration of the CuInSe_2 side). If the density of the charged interface states is large, the C-V curve will be shifted toward a more negative voltage region.

The measurements were carried out under a constant illumina-

tion condition in a frequency range of 1 kHz to 100 kHz. The light intensity, measured using a calibrated silicon detector, was maintained to be about 30 mW/cm² for some of the experiments. While for some other experiments, devices were illuminated under an AM1 condition. In Fig. 7.18, both the dark and illuminated C-V results for sample No.2514 are plotted. This cell was fabricated on a Mo substrate. It is seen that the slope of the curve is not altered by the illumination, indicating that the change in the effective carrier concentration with illumination is negligible. This fact suggests that under the present light intensity (30 mW/cm²), the density of the charged deep levels in this device is small as compared to the total density of the shallow levels. At a given dc bias voltage, the total space charge density or the apparent carrier concentration under the illumination is given by a modified equation from equation (7.3):

$$N_A + n_t = [2/q\epsilon_s a^2][-dV/d(1/C_L^2)]. \quad (7.4)$$

In this equation, C_L is the illuminated capacitance and n_t is the density of filled (or charged) deep traps by the illumination. If the deep levels are electron traps, then n_t is positive. From equation (7.4), value of n_t can be estimated. However, the equation cannot be used for accurate calculation of trap concentration unless the effects of the charged interface states are small. Because the shift of the C^{-2} curve under the influence of the charged interface states, one obtains an apparent N_A value at a smaller voltage than the applied bias voltage.

Under the illumination, the C^{-2} curve for sample No. 2514 is

seen to shift by about 0.2 V to more negative voltage region, yielding same amount of a reduction in the apparent diffusion potential V_D . The shift of the C^{-2} curve under illumination is a common effect for our CdS/CuInSe₂ cells and is also observed by other researchers on some of their thin film CdZnS/CuInSe₂ devices^{7.5}. It is believed that the presence of light induced interface states accounts for the shift in the C^{-2} curve. If the interface states for a CdS/CuInSe₂ device are charged, no matter whether they are filled by light or electrical current, the effective diffusion potential V_D is lowered by an amount of $Q_{is}^2/2q\epsilon_s N_D$. In another words, the apparent diffusion potential V_{Di} is given by

$$V_{Di} = V_D - Q_{is}^2/2q\epsilon_s N_D \quad (7.5)$$

$Q_{is}(\text{cm}^{-2})$ is the charge per unit area of interface states and can be expressed as $Q_{is}=qn_{is}$, with n_{is} to be the density of the charged interface states per unit area. It can be shown^{7.5} that the open circuit voltage is related to the diffusion potential in the following way:

$$V_{oc} = V_D + (kT/q) \ln(J_L/qSN_A). \quad (7.6)$$

Here, S is the interface recombination velocity. Therefore, the open circuit voltage is also reduced by the amount of $qn_{is}^2/2\epsilon_s N_D$ with the presence of the charged interface states. This effect has been confirmed by experiments. Ahrenkiel^{7.5} has demonstrated that very small shift in the C_L^{-2} curve was found for a 10.2% cell and a relatively large shift was observed for a 9% cell. The

large shift in the C^{-2} plot for our cells is also consistent with the small open circuit voltage of the cells.

To ensure the interface state effect on the intercept of the C^{-2} -V curve, dark and light capacitance measurements were also carried out on a commercial Si solar cell with a conversion efficiency of 12%. The density of interface states in the Si homojunction cell was assumed to be very small as compared to that in the CdS/CuInSe₂ cells. The light intensity used for the Si cell was about AM2. The AM2 condition (instead of AM1) was used to prevent the high level injection condition to occur. The C-V results for the Si cell are given in Fig. 7.19. From the figure, one can see that the two curves have essentially the same intercept. Therefore, the diffusion potential of the device was unaffected by the illumination.

Figure 7.20 is the plot of C^{-2} versus V for the 5.2% cell (3827) both under dark and AM1 conditions. Under the AM1 illumination, an increase of about 30% in the effective carrier concentration is observed in the voltage region of 0.4 to -1V ($N_A = 10^{17}$, $n_t = 3 \times 10^{16}$ and $N_A' = 1.3 \times 10^{17} \text{ cm}^{-3}$). This increase is due to the negatively charged electron trap centers. In the figure, a large shift of about 0.2 V from the dark C-V curve, is also seen for the light C-V curve. Using equation (7.5), the density of the charged interface states for sample No. 3827 was estimated. A space charge density of 10^{19} cm^{-3} for the CdS side was assumed. The n_{is} value obtained for this cell is $5 \times 10^{12} \text{ cm}^{-2}$, which is about one order of magnitude larger than that reported

on ARCO cell by Tavakolian and Sites^{7.7}. This large density of interface states would result in an interface recombination dominated current transport (see chapter 9). Comparing the effects of the deep levels and the interface states, one conclusion can be made on the present CdS/CuInSe₂ cells. The density of interface states must be reduced in order to increase the open circuit voltage and the conversion efficiency of the cells.

7.3.4 Effect of series resistance on the C⁻² curve

It has been reported^{7.8} that a minimum in the C⁻² curve would occur if there was a non-zero series resistance in the junction device and the value of the series resistance can be estimated from the equation

$$1/C'_{\min}{}^2 = 4 \omega^2 R^2. \quad (7.7)$$

C'_{\min}{}^{-2} is the minimum value in the C⁻² curve, ω is the measurement frequency and R is the series resistance. For some of our CdS/CuInSe₂ cells, minimum C⁻² value has been observed for the C⁻²-V curves (see Fig.7.21, sample No. 3784). In Fig. 7.21, a constant R value could not be obtained for all four curves, by using the equation (7.7). The estimated resistance value is frequency-dependent and it increases with the decrease of the frequency: R(100kHz) = 113 Ω , R(40kHz) = 239 Ω , R(20kHz) = 447 Ω , and R(10kHz) = 841 Ω . One possible explanation for the frequency-dependent series resistance is that the back contact (between CuInSe₂ and the Mo substrates) is non-ohmic. The contact impedance is a complex number and can be expressed as

$$Y' = G' + j\omega C', \text{ or}$$

$$Z = G' / [G'^2 + (\omega C')^2] - j\omega C' / [G'^2 + (\omega C')^2]$$

(7.8)

as shown in the inset of Fig. 7.21. The real part of the impedance decreases with the increase of the frequency.

7.4 Spectral Response

Spectral response of the CdS/CuInSe₂ cells was determined in the wavelength (λ) range from 0.5 to 1.2 μm . For the measurements, a monochromatic light source (Beckman model 2400) with a slit width of 1 mm was used. The light intensity was determined by a calibrated Si detector (model PIN 6DP). Short circuit current of the devices was measured at a λ interval of 0.02 μm by a pico-ammeter.

Fig. 7.22 gives the spectral response for a low efficiency device No. 2954 (efficiency smaller than 2%). In the short wavelength region, the quantum efficiency increases rapidly with the increase of λ and reaches a maximum at about 0.6 μm . As λ is further increased from 0.6 μm to about 1 μm , quantum efficiency remains essentially constant. The quantum efficiency value starts to decrease linearly with λ when λ is increased to beyond 1 μm . This decrease is different from that of the vacuum deposited high efficiency CdS/CuInSe₂ cells, where essentially constant quantum efficiency region extends to about 1.2 μm ^{7.2}. The spectral re-

sponse in the long wavelength region could be affected by the narrow depletion region for most of our cells or could be due to a loss through interface states. The former appears to be the most possible reason for the long wavelength loss. To increase the field region width, one has to reduce the concentration in the CuInSe₂ surface. Alternatively, a high resistivity CdZnS layer could be deposited on the CuInSe₂ before the low resistivity CdS to reduce the lattice mismatch with the CuInSe₂ film and thus the density of interface states.

7.5 I_{sc}-V_{oc} Relationship

The relationship between the short circuit current and the open circuit voltage for the CdS/CuInSe₂ cells was studied. A set of I_{sc} and V_{oc} values was first obtained by applying light with different light intensities. The results for sample No. 2781 are given in Fig. 7.23. In the figure, a linear relationship between I_{sc} and V_{oc} is seen. This is expected for an ideal cell, for which the relationship between I_{sc} and V_{oc} is given by

$$V_{oc} = (kT/q) \ln(I_{sc}/I_s). \quad (7.9)$$

For a real device with series resistance R_s, the relationship is more complex and a simple equation between V_{oc} and I_{sc} cannot be obtained. However, if the series resistance is small enough, the above equation can still be used as a close estimation.

7.6 Conversion Efficiency

Active area conversion efficiency, short circuit current

density J_{SC} , open circuit voltage V_{OC} and fill factor FF, of some CdS/CuInSe₂ cells are listed in Table 7.2. It is seen that for the devices fabricated on the Mo plates, the short circuit current values are around 20 mA and the open circuit voltage values are small (average about 0.2 V). The average AM1 active area efficiency is around 2.3% for the cells fabricated using Mo plates. For the cells on the Mo/glass substrates, the average efficiency is more than 4%. Although the devices made on the Mo/glass substrates have larger open circuit voltage values, they are still low (average 0.3 V). As described in section 7.3.3, the low V_{OC} value of the cells is due to the large density of interface states. Fig. 7.24 shows the illuminated I-V characteristics for the 5.2% cell, No 3827. This cell is the best among the single layer CdS/CuInSe₂ cells with an area of 1 cm².

In order to test the stability of the cells fabricated using the electrodeposited CuInSe₂ films, the cell was tested after being stored in the laboratory for several months. The measured I_{SC} was found to decrease slightly but the open circuit voltage was found to increase, yielding essentially the same conversion efficiency.

7.7 Small Area Cells

As presented in chapter 3, small pin holes exist in the CuInSe₂ films due to the defects in the Mo films (see Fig. 3.4). Those defects in the CuInSe₂ films act as leakage paths for current if the cells are formed by directly evaporating low resistivity CdS films on the CuInSe₂ films. This leakage would

increase the saturation current and therefore decrease the open circuit voltage (see equation (7.9)). In addition to the pin holes in the CuInSe_2 films, defects were also observed in the CdS films. Fig. 7.25 shows a hole found in the CdS film for a 4% cell. In the circular area, only bare CuInSe_2 film is seen. These defects in the CdS films could also act as leakage paths when the metal contact is evaporated.

To minimize the effect of defects, small area devices with an area of 0.09 cm^2 were fabricated. The same fabrication processes as that for the large area devices were used. After the deposition of CdS films, aluminum contact bars of about 1.2 mm^2 were evaporated on the CdS surface through a metal mask. A conventional photolithograph technique was then applied to pattern the CdS films into regions with the areas of 0.09 cm^2 . Concentrated HCl was used to etch the unwanted CdS films. After the etching of CdS film and removing of the photoresist, the samples were washed with de-ionized water and air dried. Eight CdS areas, each with an Al bar in the center, were fabricated on each substrate (four on each original 0.9 cm^2 CdS pat). These CdS areas were divided into two groups with a center-to-center distance of 1.4 cm (see Fig. 7.26).

The as-fabricated cells usually showed a poor rectification. After an air treatment at 190°C for 20 minutes, a layer of SiO_x with a thickness of about $0.1 \mu\text{m}$ was evaporated to reduce the optical reflection. The fabricated cells were tested at about 25°C under solar illumination (incident power density 100 mW/cm^2). The I-V results showed a 10% variation in J_{SC} and V_{OC}

for different cells on the same single substrate. This variation is believed to be due to the non-uniform properties of the CdS films. The I-V characteristics for one of the best cells are shown in Fig. 7.27. The short circuit current density is 40 mA/cm² and the open circuit voltage is 0.28 V, yielding an active area conversion efficiency of 5.6% for this cell. It is noted that this value is slightly higher than that for the large area devices (5.2%).

7.8 Energy Band Diagram

The energy band diagram for the present studied CdS/cells was constructed based on the results obtained from the measurements and is given in Fig. 7.28.

7.9 Conclusions

I-V and C-V characteristics of the CdS/CuInSe₂ cells fabricated using the electrodeposited CuInSe₂ films have been studied. For the as-fabricated cells on the Mo plate, a short circuit current output was always obtained even though the rectification was generally poor. With a short heat treatment in the air at a temperature in the range of 180 to 200 °C, the rectification of the cells was found to improve significantly with an n-factor of about 1.15. For the as-fabricated cells on the Mo/glass substrates, the properties were often better. The ideality factor was found in the range from 1 to 1.5 for most of the cells. The I-V results also demonstrated the effect of composition or metal ratio (In/Cu) in the CuInSe₂ films on the electrical properties.

An In/Cu ratio of 1.1 was found to give better devices. Temperature-dependent I-V measurements showed a continuous decrease of current and an increase of the ideality factor with the decrease of the temperature. The barrier height value, obtained directly from the plot of J_0/T^2 vs T^{-1} was about 0.4 V, which was smaller than that for high efficiency devices fabricated by vacuum methods. The fitted I-V results gave a barrier height of about 0.64 V (see figure 7.28). The fitted results also showed that the room temperature saturation current was about one order of magnitude less than the recombination current.

The effective carrier concentration for the CdS/CuInSe₂ cells was obtained from the C-V measurements. A value ranging from 10^{16} to 10^{17} cm⁻³ is typical for the present cells. The carrier concentration was found to decrease after the air heat treatment. A slower decrease rate was observed for the region near the physical junction. The differential capacitance was found to vary with the measurement frequencies. The slope of the C^{-2} plot was, however, essentially independent of the frequency, indicating a relatively small density of the deep levels. The density of the charged deep levels under the AM1 illumination condition for one of the cells was estimated to be about one order of magnitude less than the effective carrier concentration. In addition to the above, the shift in the C^{-2} -V plot with illumination and the frequency-dependent apparent diffusion potential allow one to conclude that interface states with a large concentration were present in the CdS/CuInSe₂ junction. This conclusion was further supported by the small open circuit voltage of the

cells. From the illuminated capacitance measurements, the density of the charged interface states under AM1 illumination was estimated to be $5 \times 10^{12} \text{ cm}^{-2}$. This value is large enough to affect the junction current transport mechanism. These interface states could also reduce the open circuit voltage.

The spectral response of the cells was found to be affected by the presence of the interface states. The loss in the long wavelength of the quantum efficiency could be the result of a small depletion width due to the presence of charged interface states. Another reason for the narrow field region is the single-layer device structure used in the present study. For the present cells, low resistivity CdS film (with high electron density) was deposited directly on the CuInSe_2 films (also with a relatively high carrier concentration). The short wavelength cut off was controlled by the bandgap of CdS and can be improved by replacing the CdS material with a larger bandgap window material, like ZnO.

The conversion efficiency of the present cells are still low due to the small open circuit voltage. In order to increase the open circuit voltage, a layer of high resistivity CdZnS should be deposited. This layer can reduce the lattice mismatch with the CuInSe_2 . The pin hole defects in the electrodeposited CuInSe_2 films and the CdS films are also sources for the leakage current, which also must be minimized. The pin holes in the CuInSe_2 films can be reduced by adopting an improved cleaning process for the Mo films or by using thicker Mo films. The relatively large variation in the device performance with the position in the

present cells is due to the non-uniform properties with the position for the CdS films which were deposited in a vacuum system with a relatively small chamber.

Table 7.1 The fitted I-V results for CdS/CuInSe₂ cells using the McLean's equation.

Sample No.	Temp. (K)	I _R (amp)	I _S (amp)	R _S (Ω)
3772	298	3.2x10 ⁻⁵	4.4x10 ⁻⁶	5.2
3784	273	5.0x10 ⁻⁶	6.5x10 ⁻⁷	7.6
3784	263	3.5x10 ⁻⁶	2.9x10 ⁻⁷	7.8
3784	248	1.1x10 ⁻⁶	5.4x10 ⁻⁸	8.6
3784	233	3.2x10 ⁻⁷	6.5x10 ⁻⁹	9.9
3784	218	9.6x10 ⁻⁸	7.0x10 ⁻¹⁰	12.2
3784	203	2.9x10 ⁻⁸	3.3x10 ⁻¹¹	14.3
3784	188	7.8x10 ⁻⁹	5.4x10 ⁻¹³	17.1

Table 7.2 Illuminated I-V results for some of the CdS/CuInSe₂ cells^a.

Sample No.	Subs.	I _{SC} (mA)	V _{OC} (mV)	FF	η (%)
2954	Mo	20.0	195	0.43	2.36
2620	Mo	15.8	235	0.43	2.25
3742	Mo/G	25.4	250	0.47	4.22
3797	Mo/G	18.7	294	0.44	3.41
3821	Mo/G	23.6	290	0.46	4.40
3824	Mo/G	24.3	275	0.45	4.24
3827	Mo/G	23.6	310	0.51	5.25
3829	Mo/G	23.7	266	0.45	4.00
3851	Mo/G	21.1	303	0.45	4.05

^a Active cell area = 0.71 cm² and all cells have AR coating.

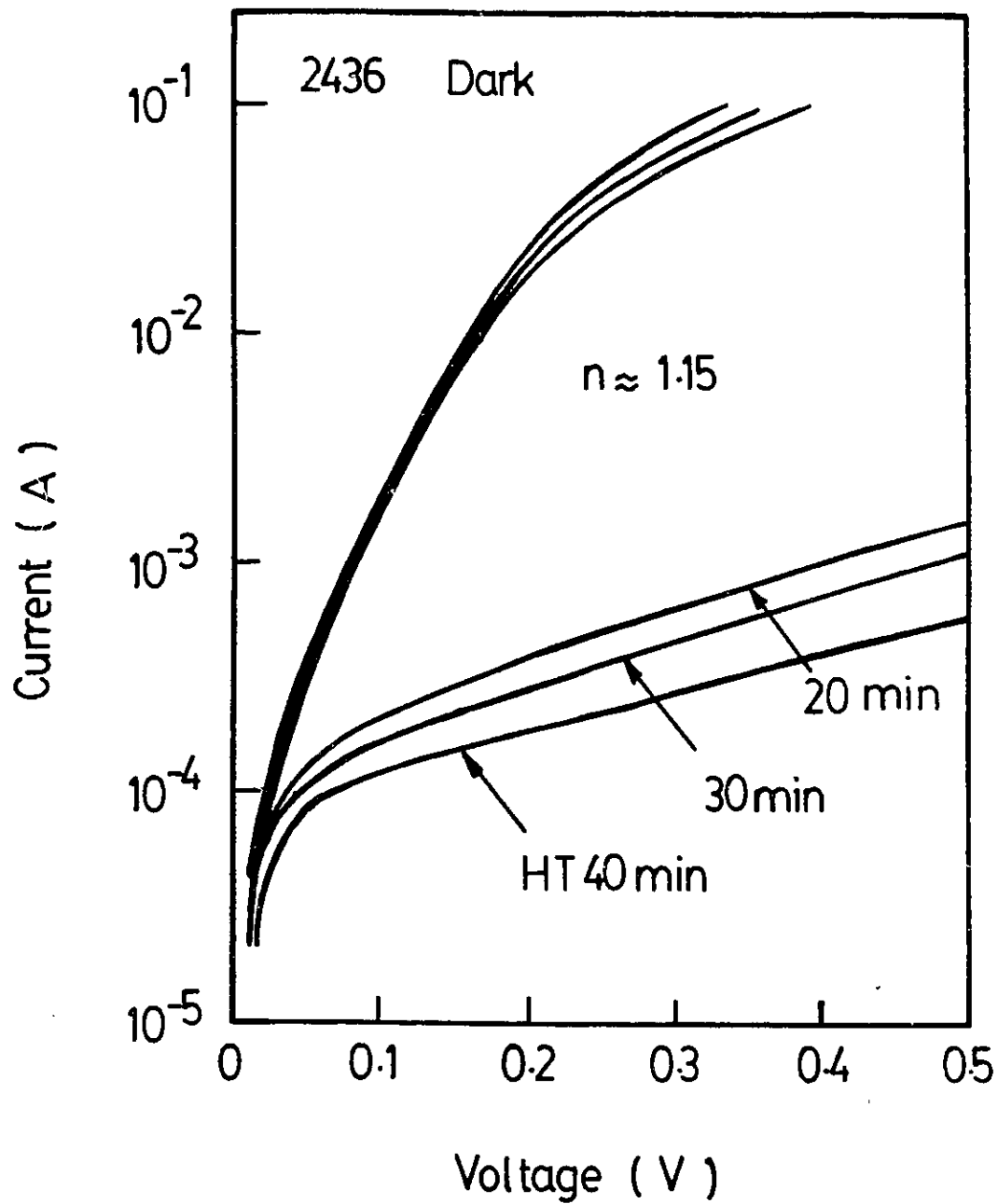


Fig. 7.1 Dark I-V characteristics for a CdS/CuInSe₂ cell on a Mo substrate, measured after each successive 10 minute heat treatment.

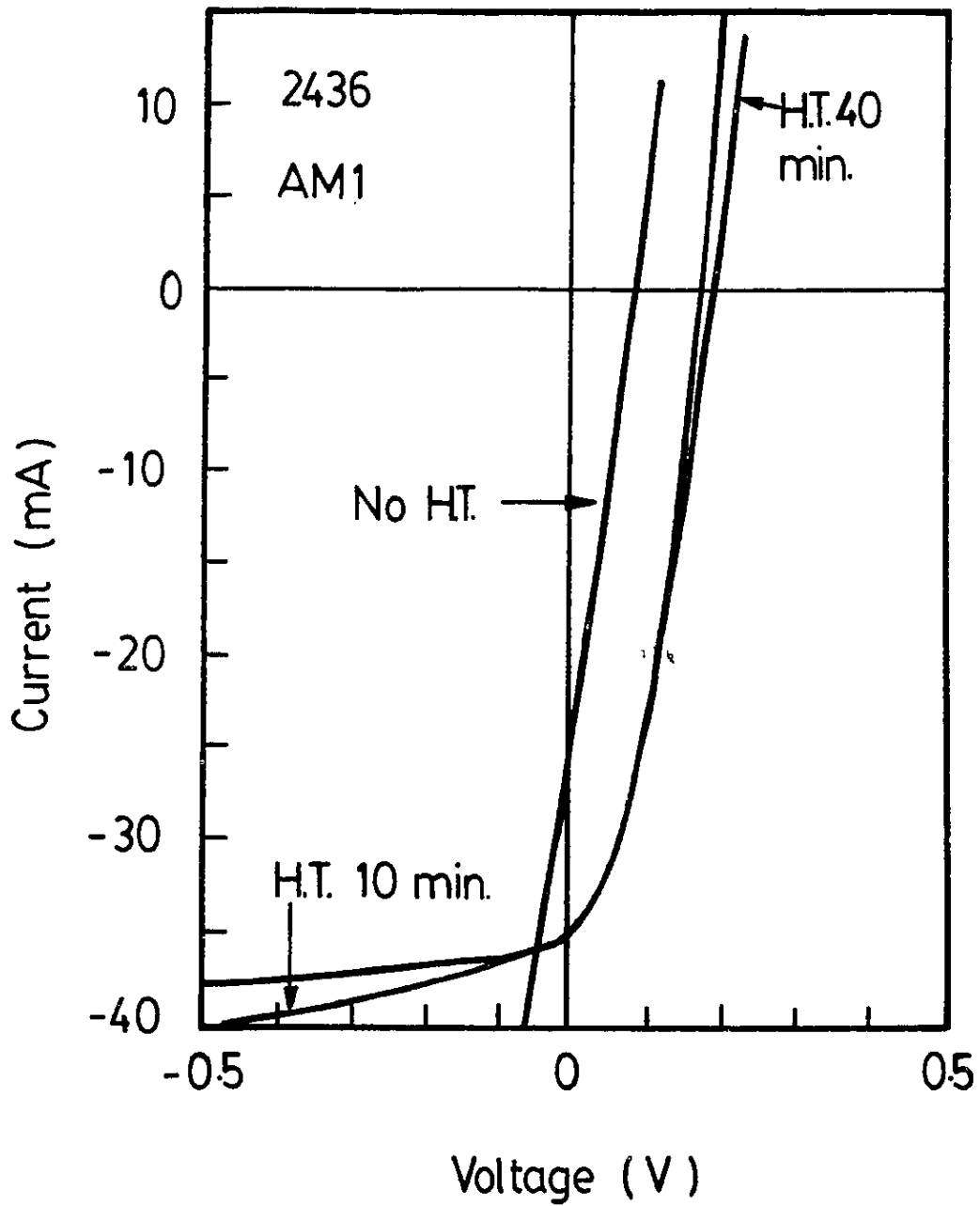


Fig. 7.2 Illuminated I-V characteristics for a cell fabricated on a Mo substrate, showing the effect of the air heat treatment.

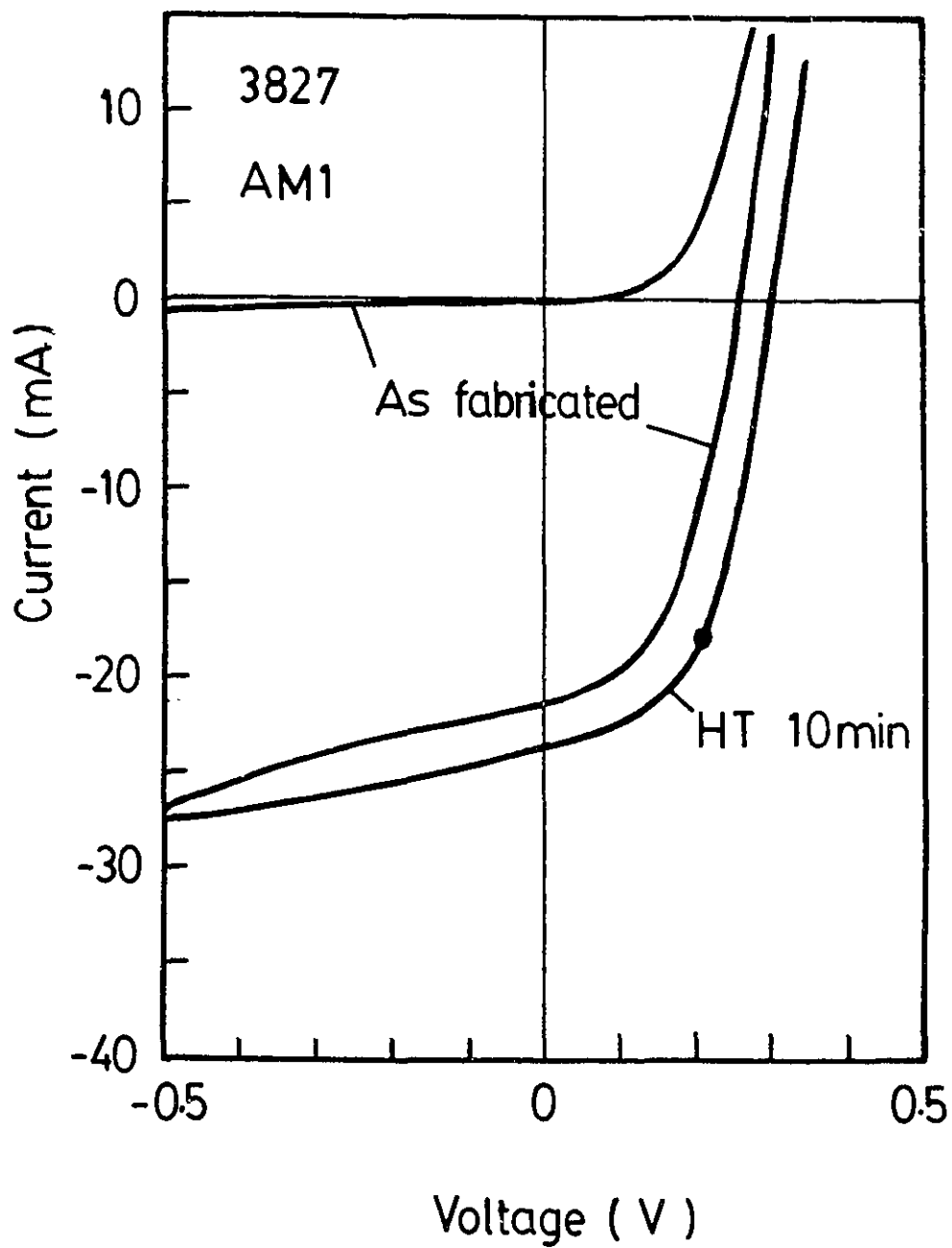


Fig. 7.3 Dark and illuminated I-V characteristics for a cell on a Mo/glass substrate. An air heat treatment for 10 minutes improved the cell efficiency.

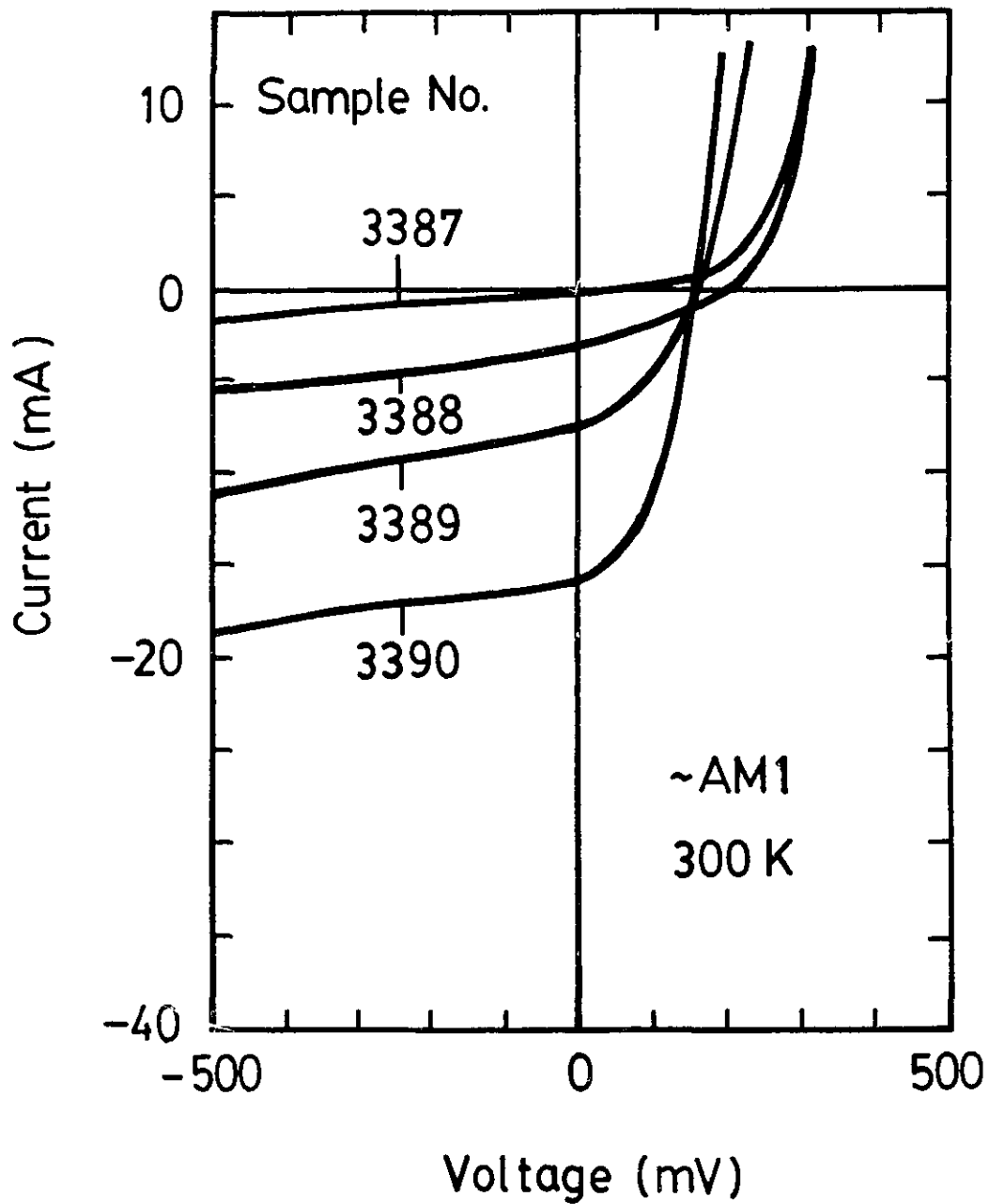


Fig. 7.4 Illuminated I-V characteristics for four cells with different In/Cu ratio in the CuInSe_2 films: Sample 3387: In/Cu=0.98; Sample 3388: In/Cu=1.01; Sample 3389: In/Cu=1.05 and Sample 3390: In/Cu=1.08.

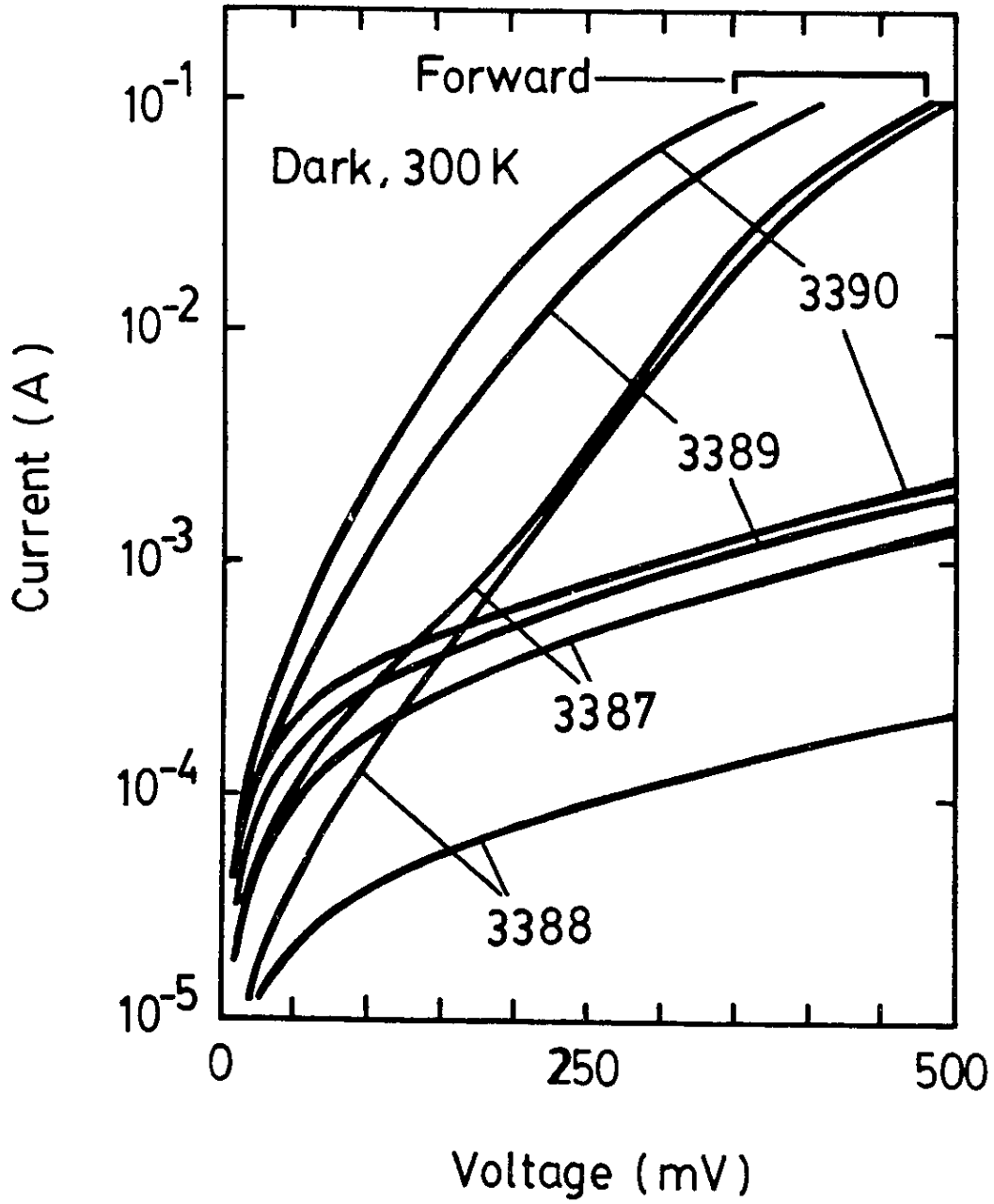


Fig. 7.5 Dark I-V results showing the effect of composition in the CuInSe_2 films.

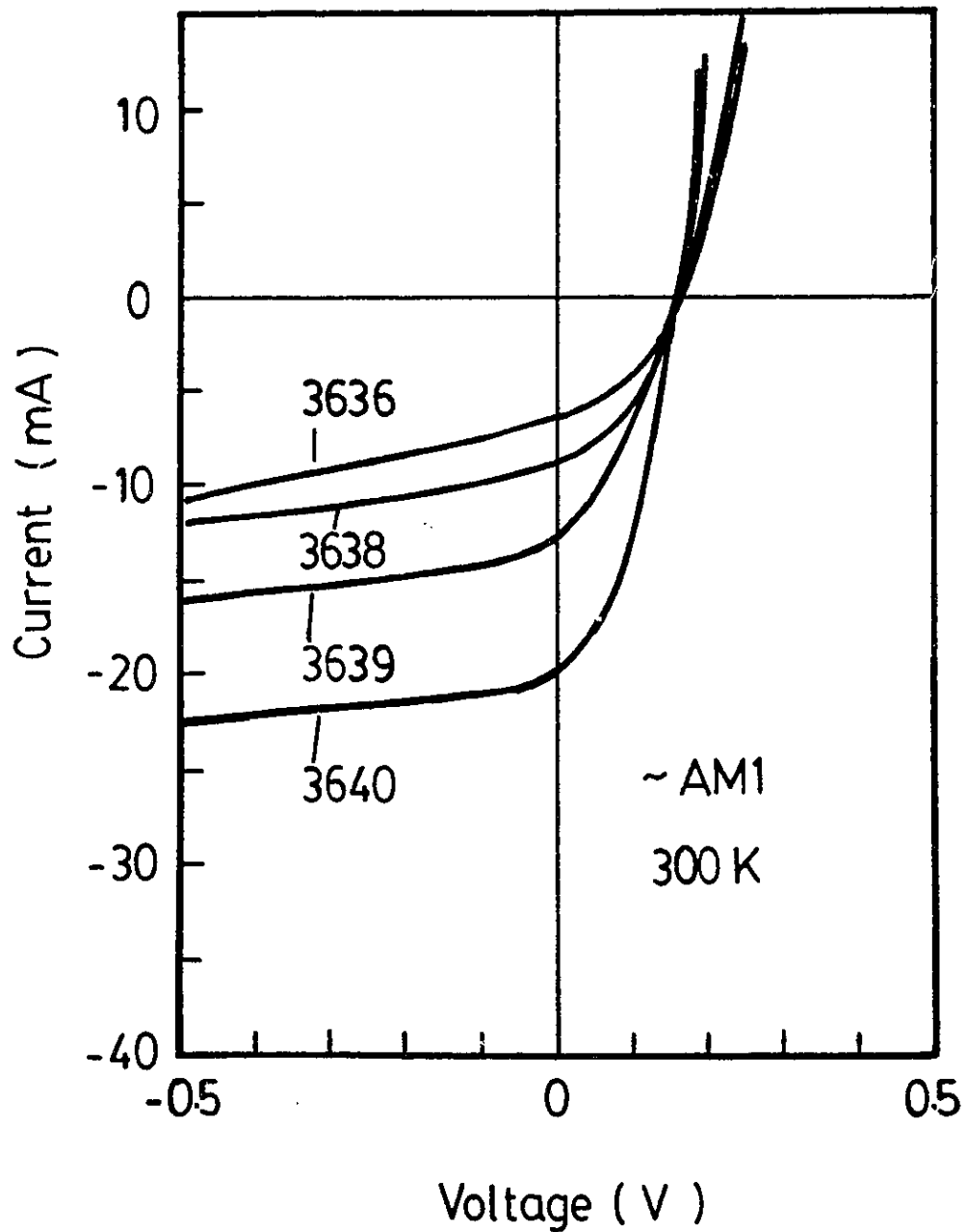


Fig. 7.6 Illuminated I-V curves showing the compositional effect similar to that given in Fig. 7.4. Sample 3636: In/Cu=1.05; Sample 3638: In/Cu=1.06; Sample 3639: In/Cu=1.08 and Sample 3640: In/Cu=1.10.

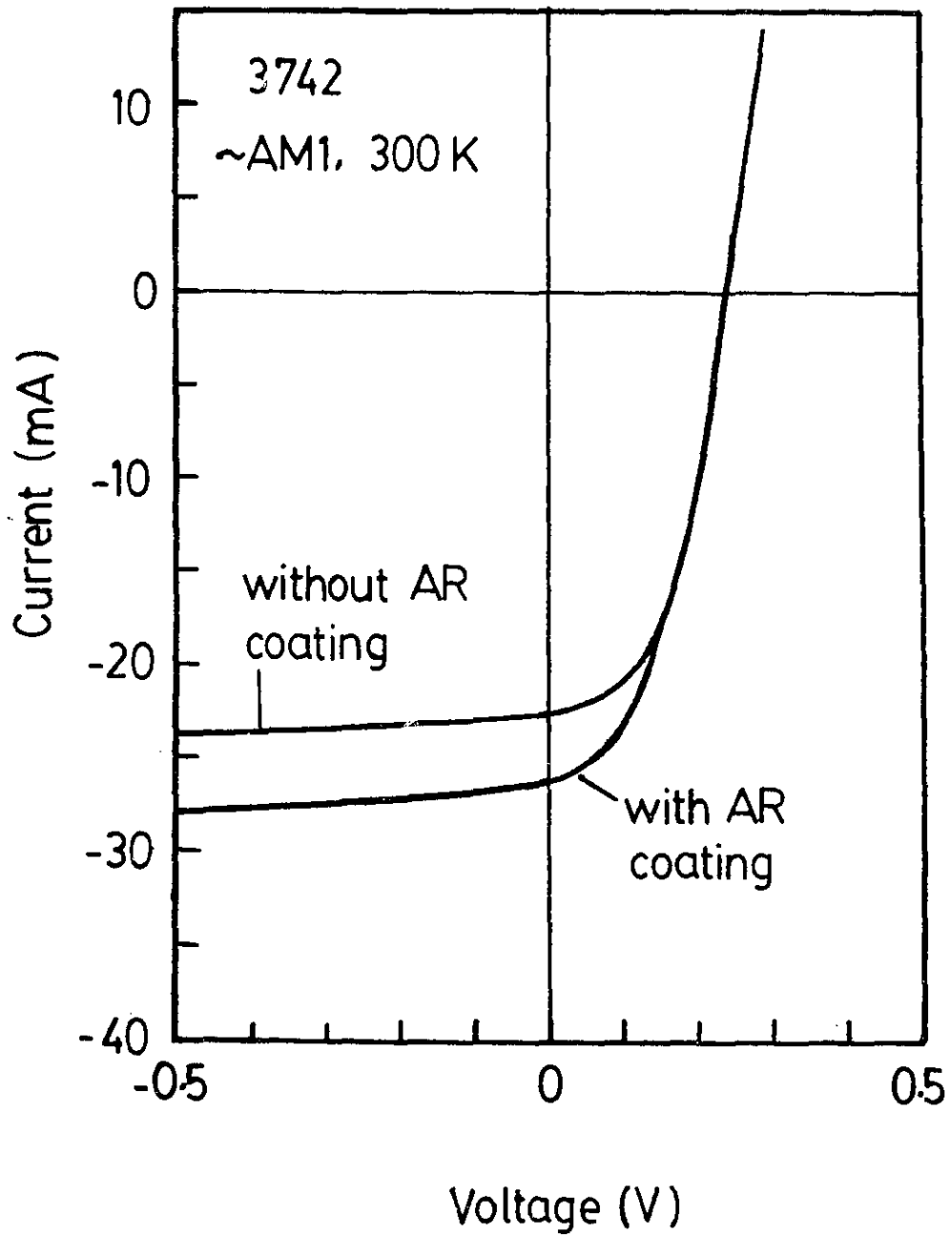


Fig. 7.7 Illuminated I-V curves for a cell, showing a 15% increase in I_{sc} after the deposition of AR coating.

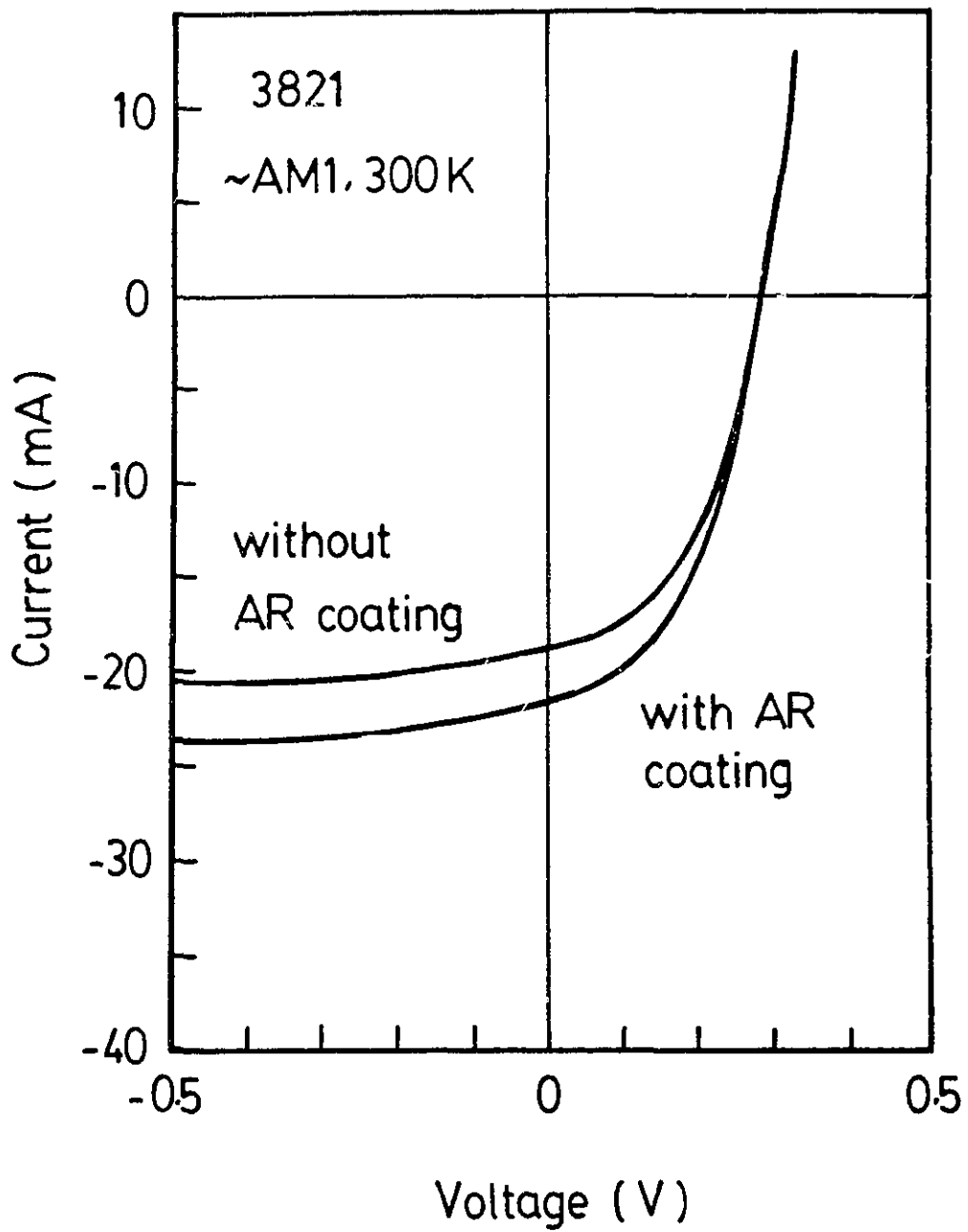


Fig. 7.8 Illuminated I-V characteristics for the cell No. 3821, showing the effect of AR coating.

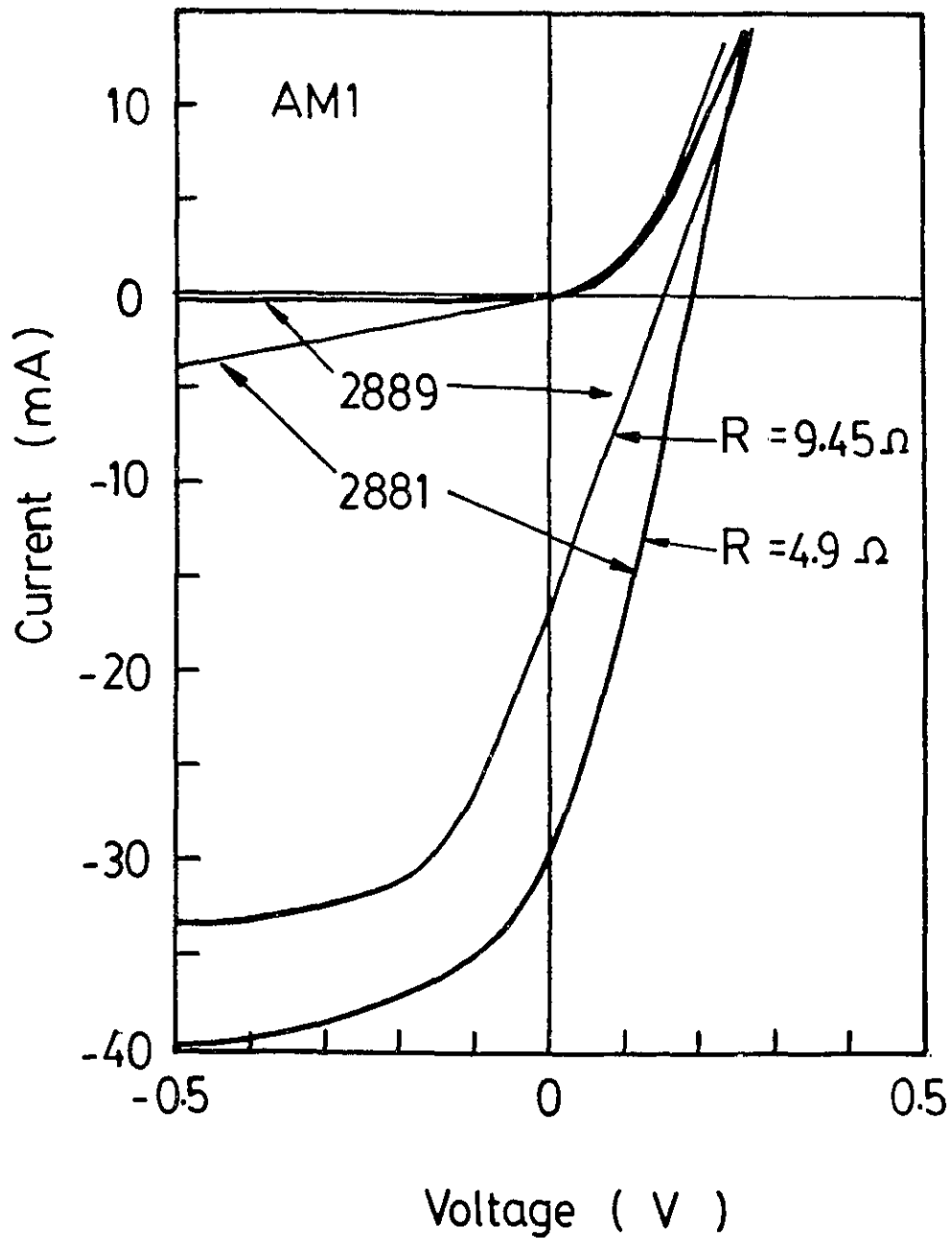


Fig. 7.9 Dark and Illuminated I-V characteristics for two cells (No. 2881 and No. 2889) showing very poor fill factors.

***** GRAPHICS PLOT *****
2954

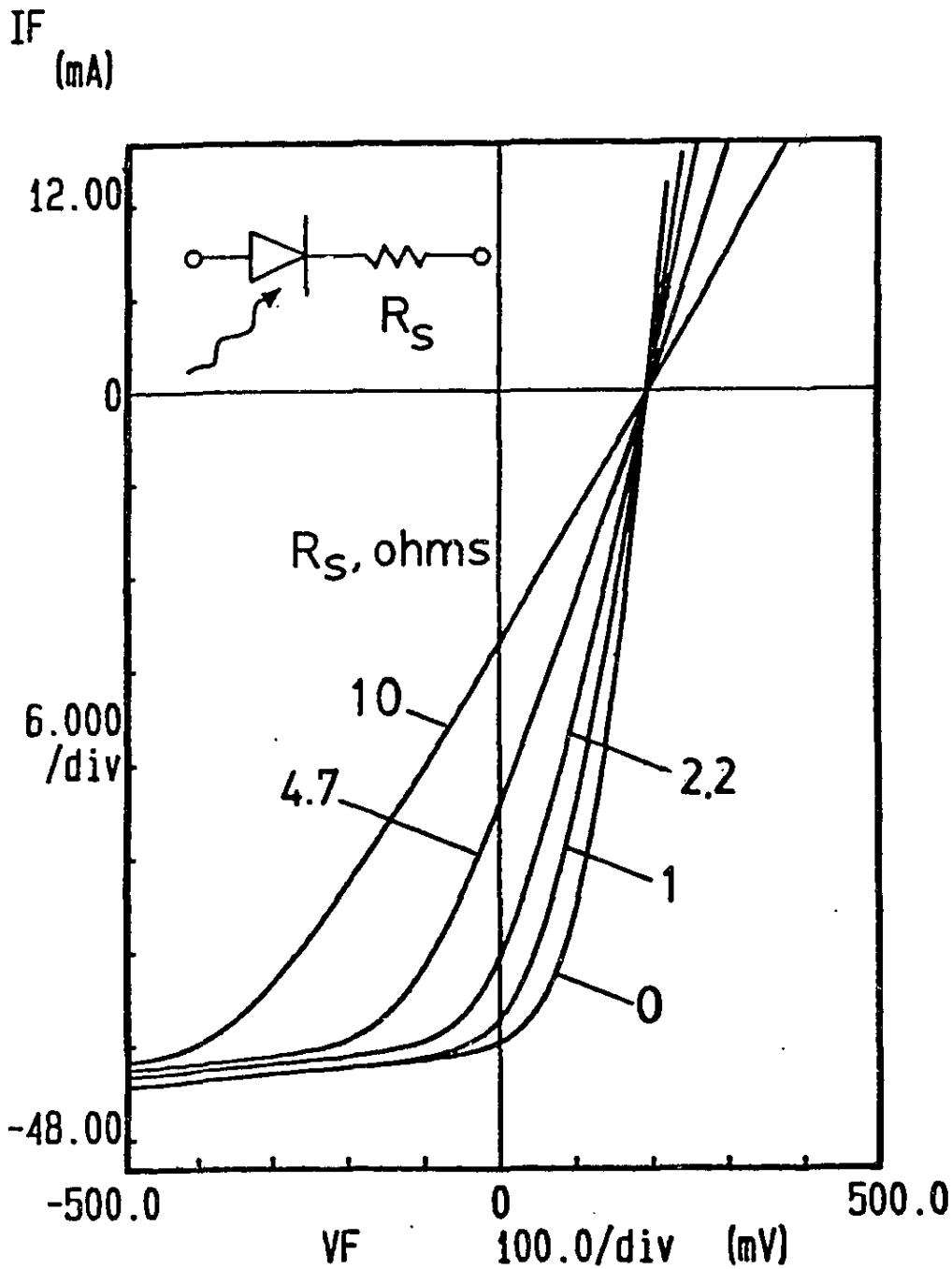


Fig 7.10 I-V curves showing the effect of series resistance. Inset gives a schematic diagram of the measurement set-up.

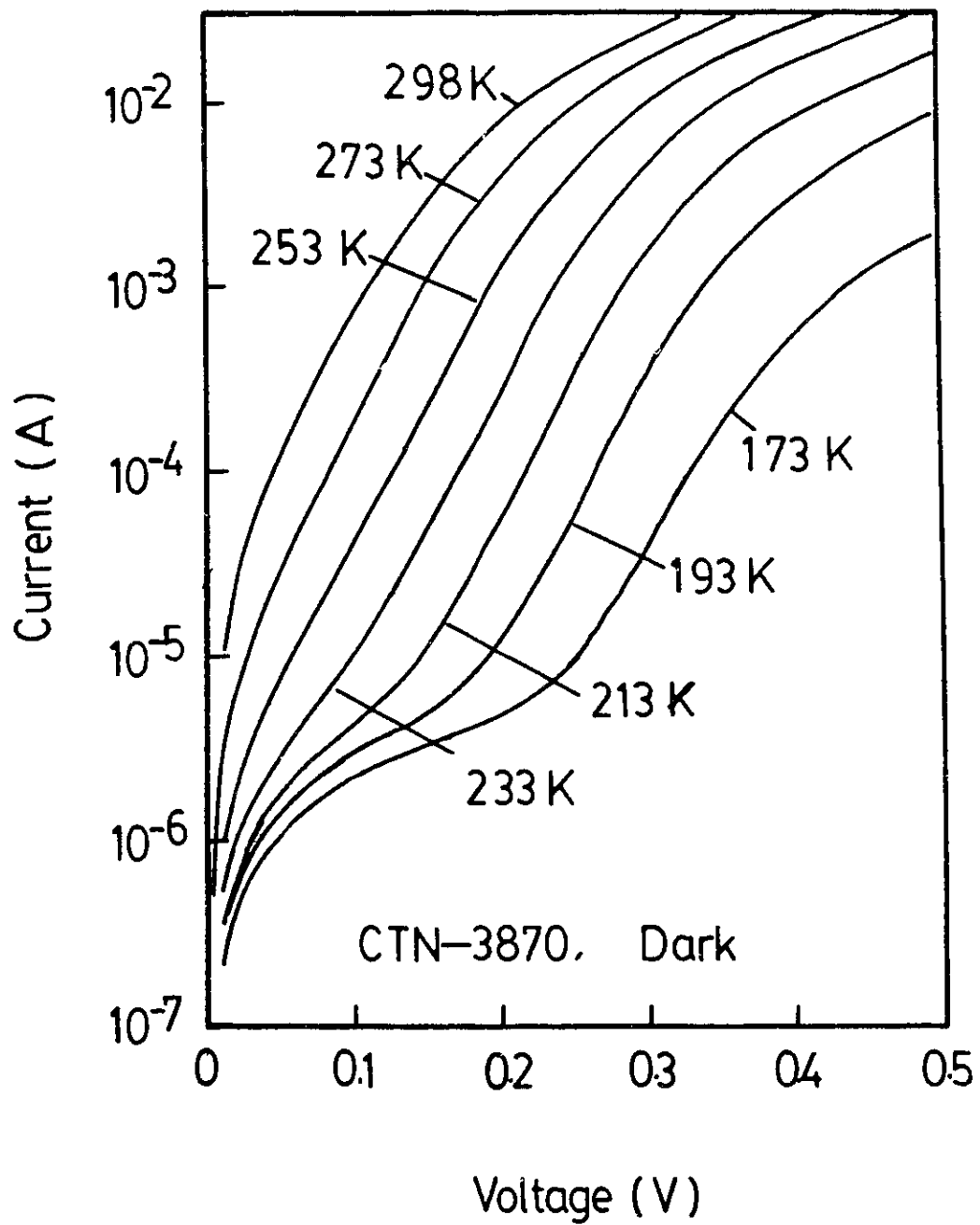


Fig. 7.11 Temperature-dependent I-V curves for the sample No. 3870.

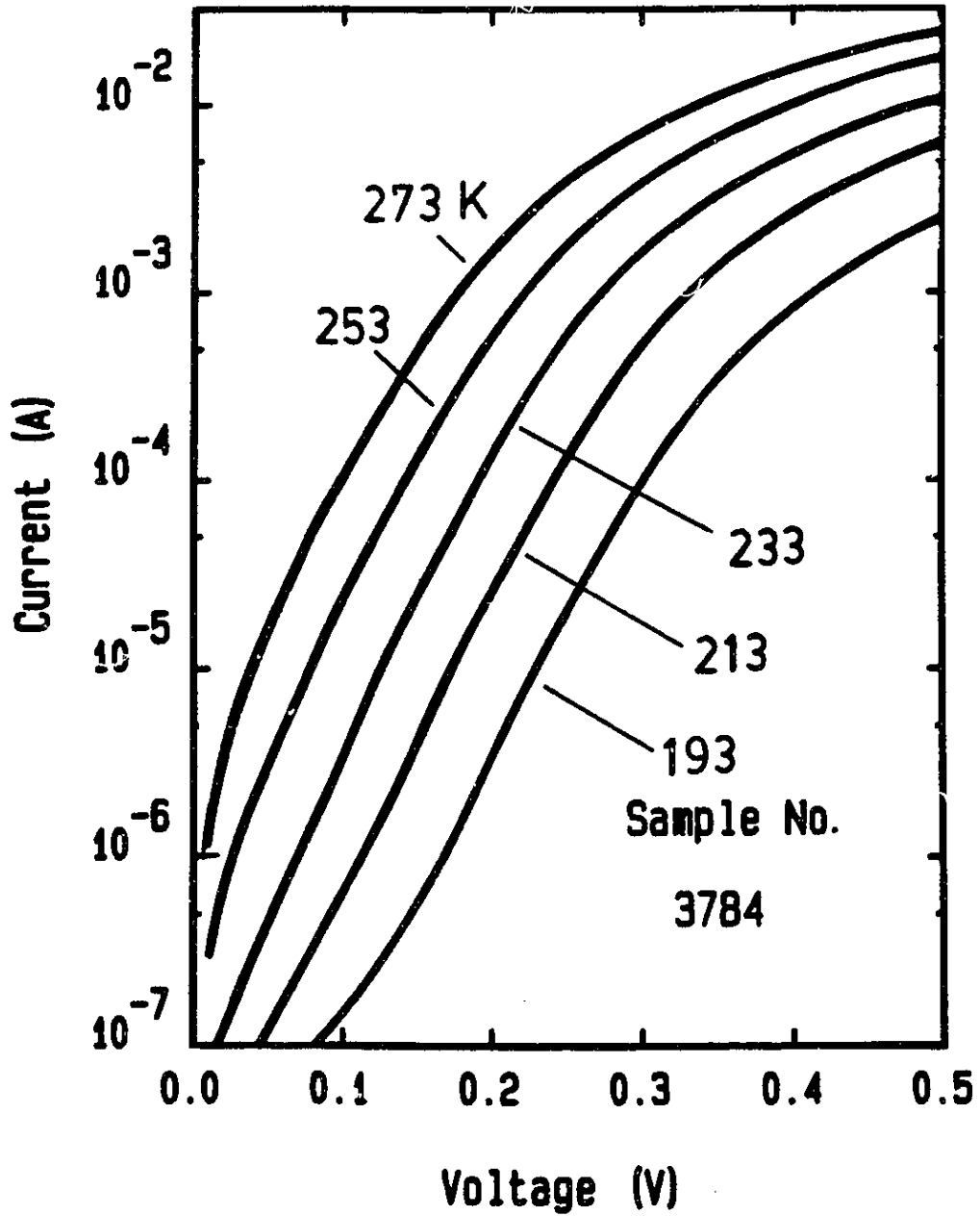


Fig. 7.12 Results of I-V measurements on a device at 5 different temperatures.

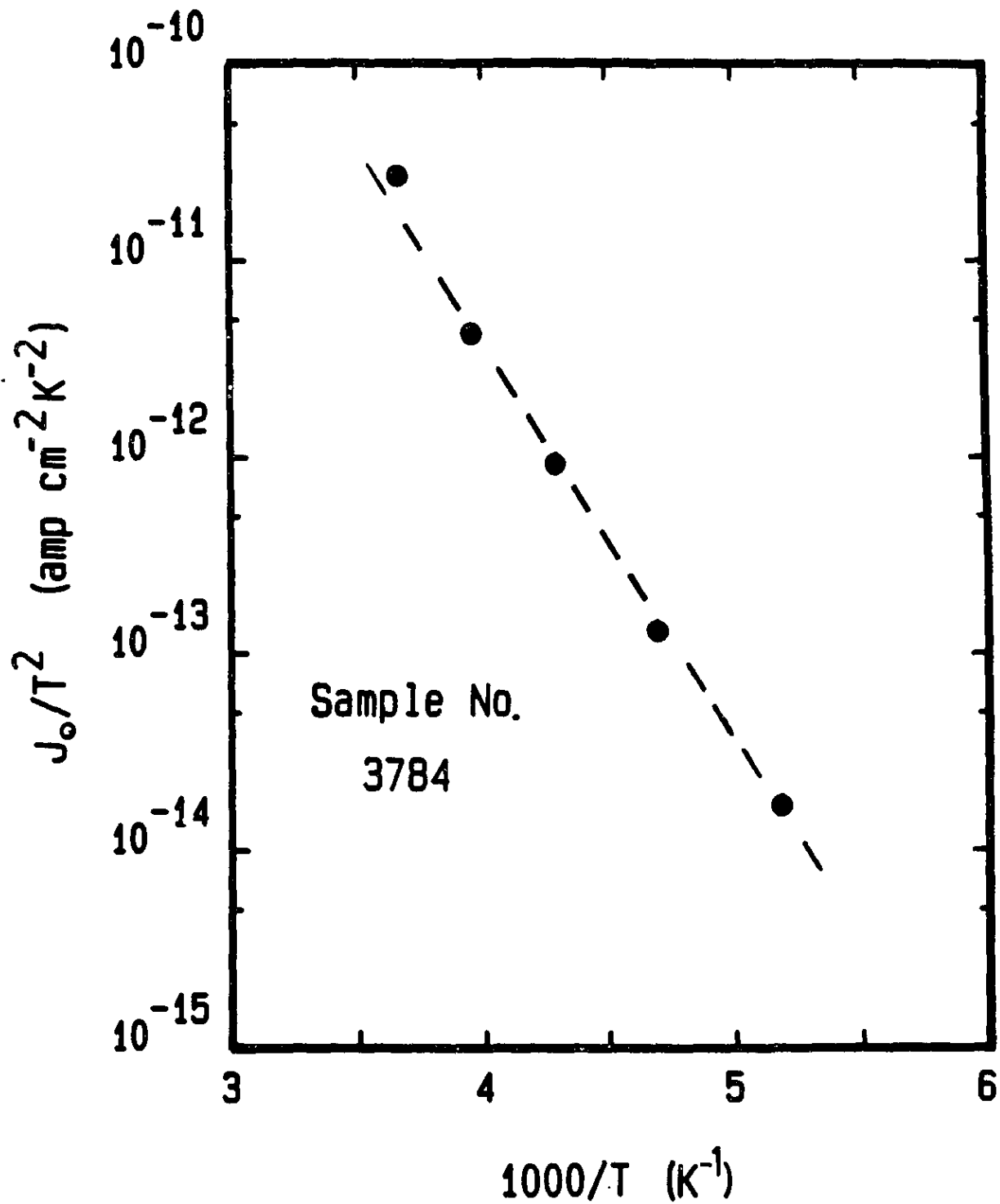


Fig. 7.13 A plot of J_0/T^2 vs. $1000/T$ for the sample No. 3784, slope of the curve gives the barrier height (0.4 V).

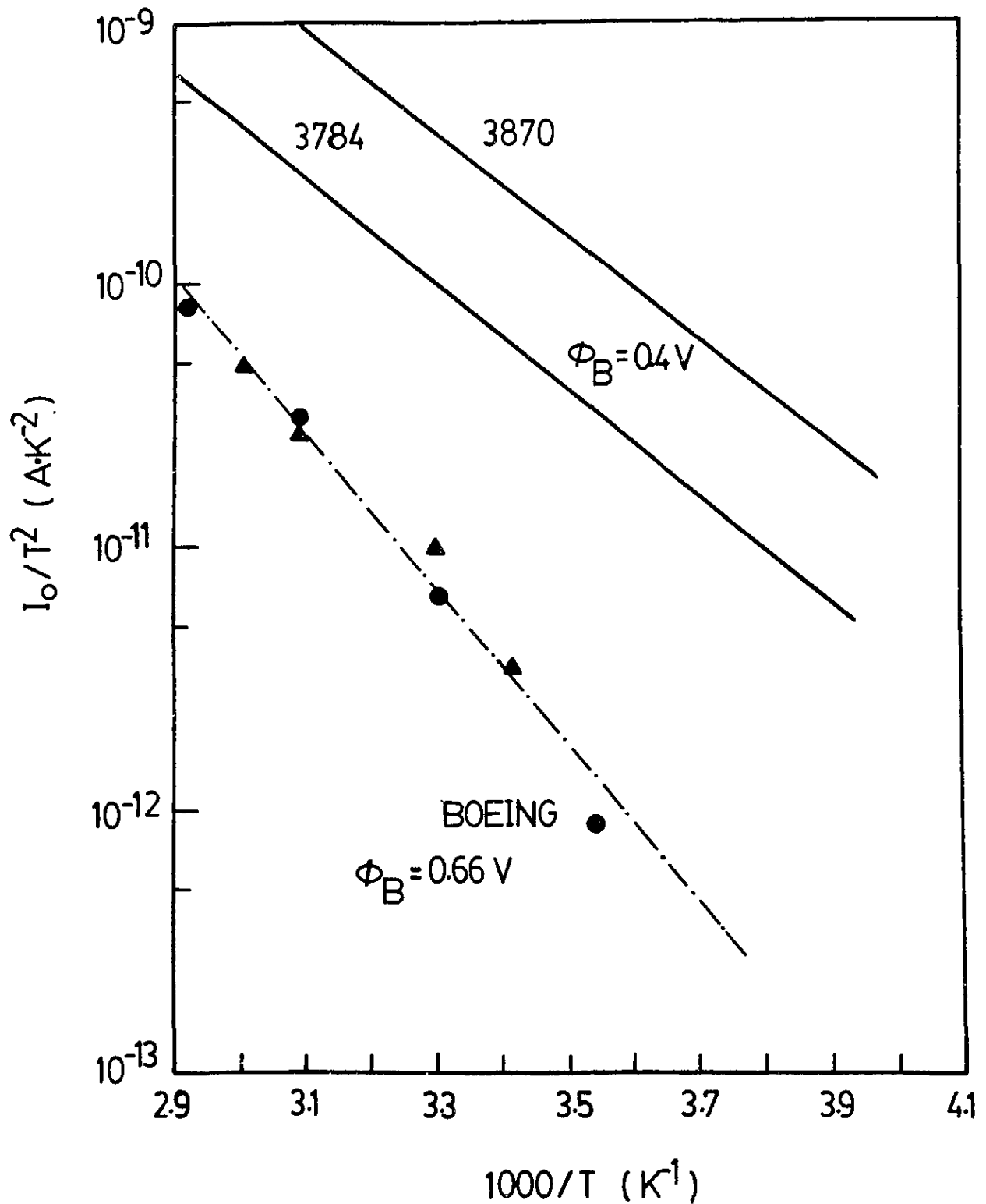


Fig. 7.14 A plot of I_0/T^2 vs. $1000/T$ for two cells (No. 3784 and No. 3870). Results for two Boeing cells fabricated by vacuum deposition are also given for comparison.

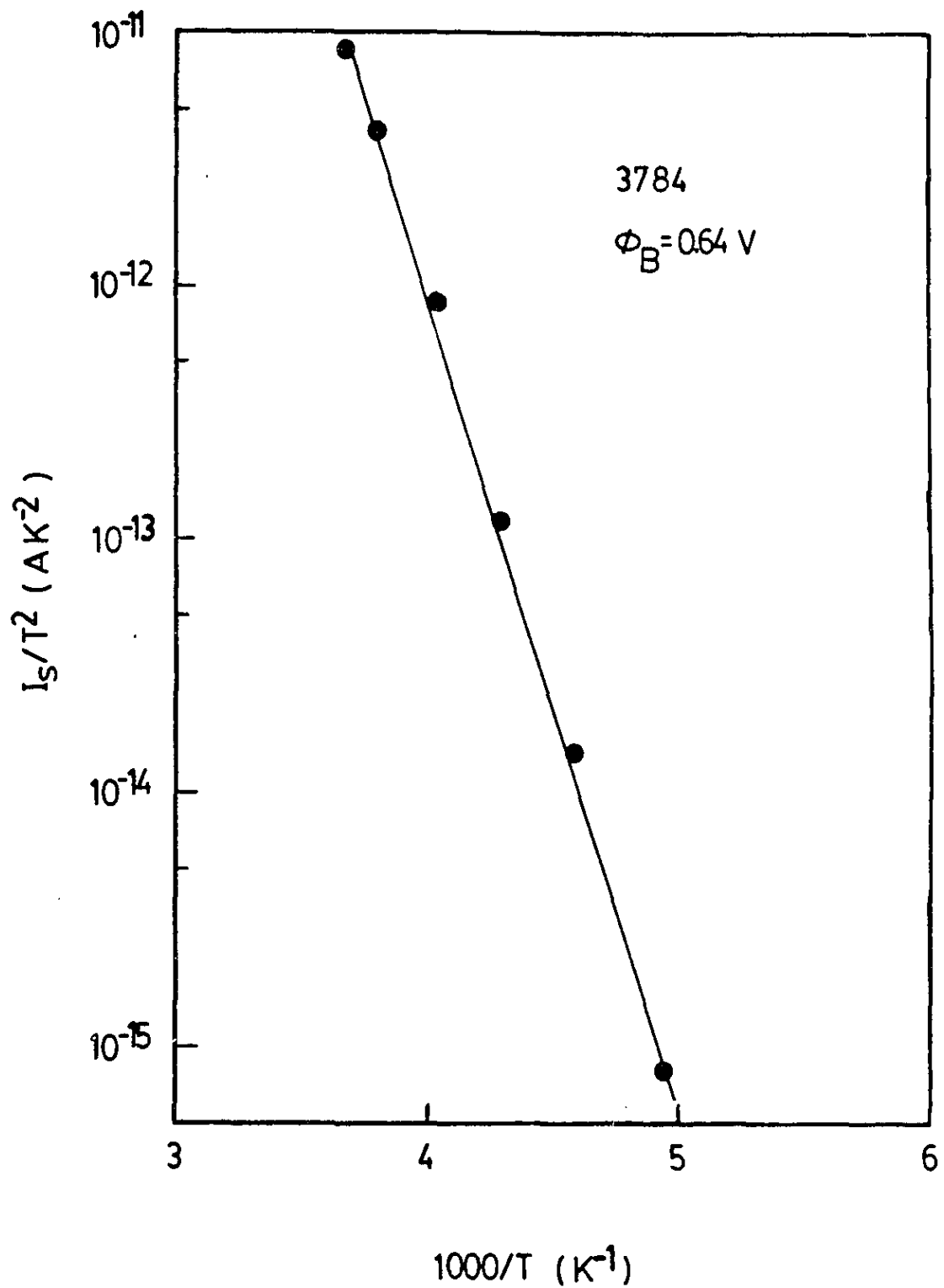


Fig. 7.15 A plot of I_s/T^2 vs. $1000/T$ for the sample No. 3784, using the fitted saturation current I_s . The corrected barrier height for this device is about 0.64 V.

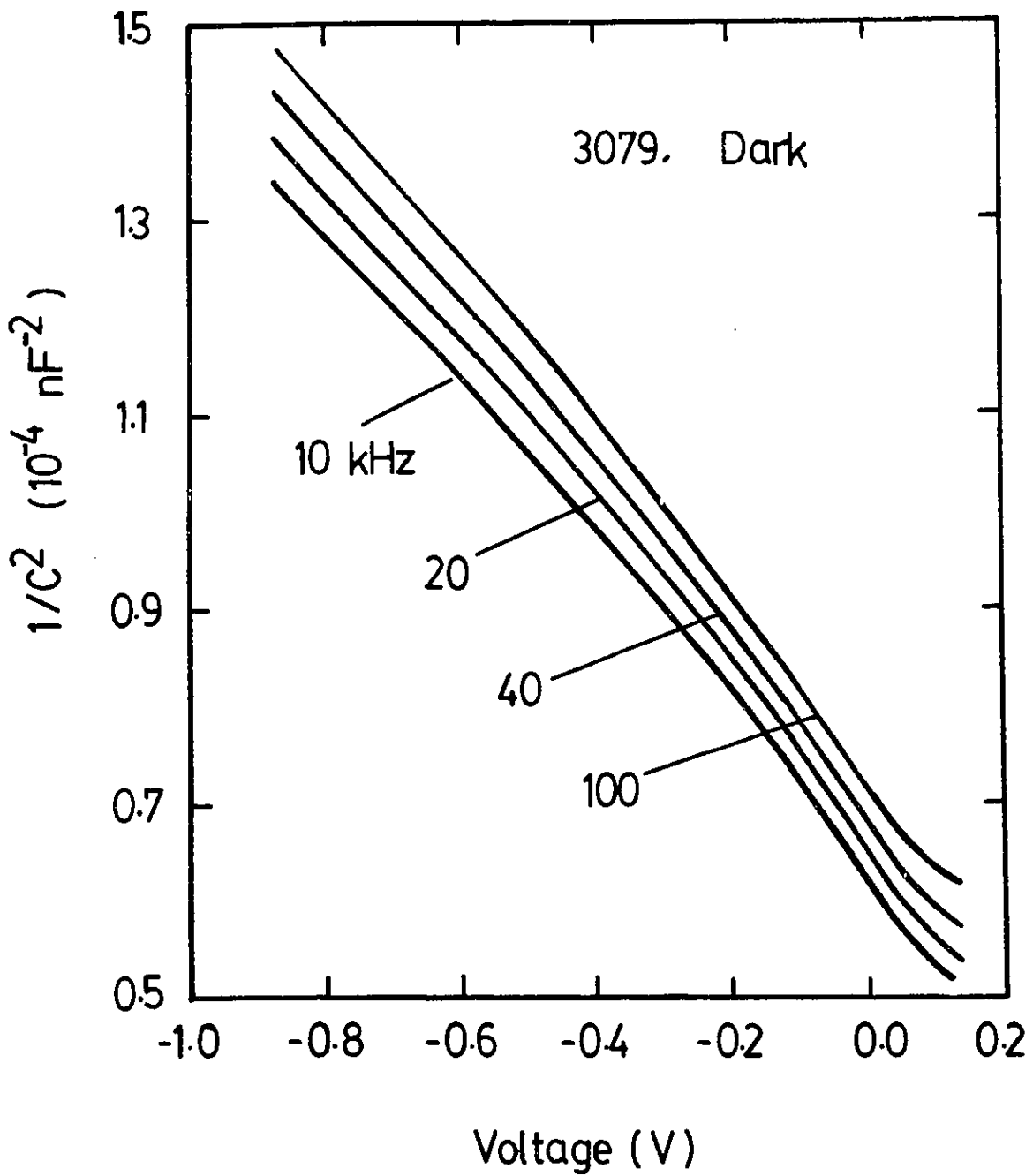


Fig. 7.16 Results of dark differential capacitance measured at 4 different frequencies for the sample No. 3079.

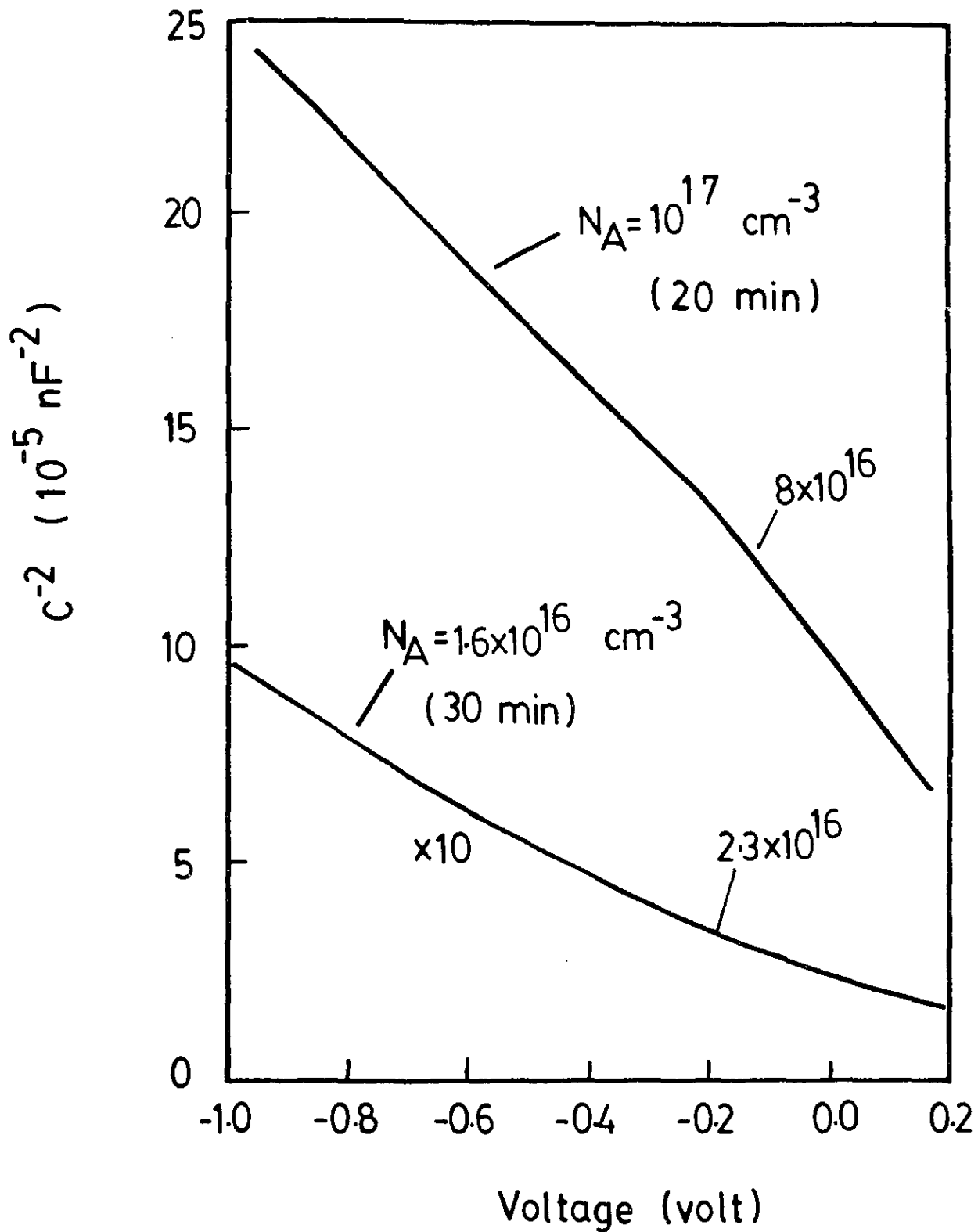


Fig. 7.17 Dark C-V results showing the effect of air heat treatment on the carrier concentration of the CIS film.

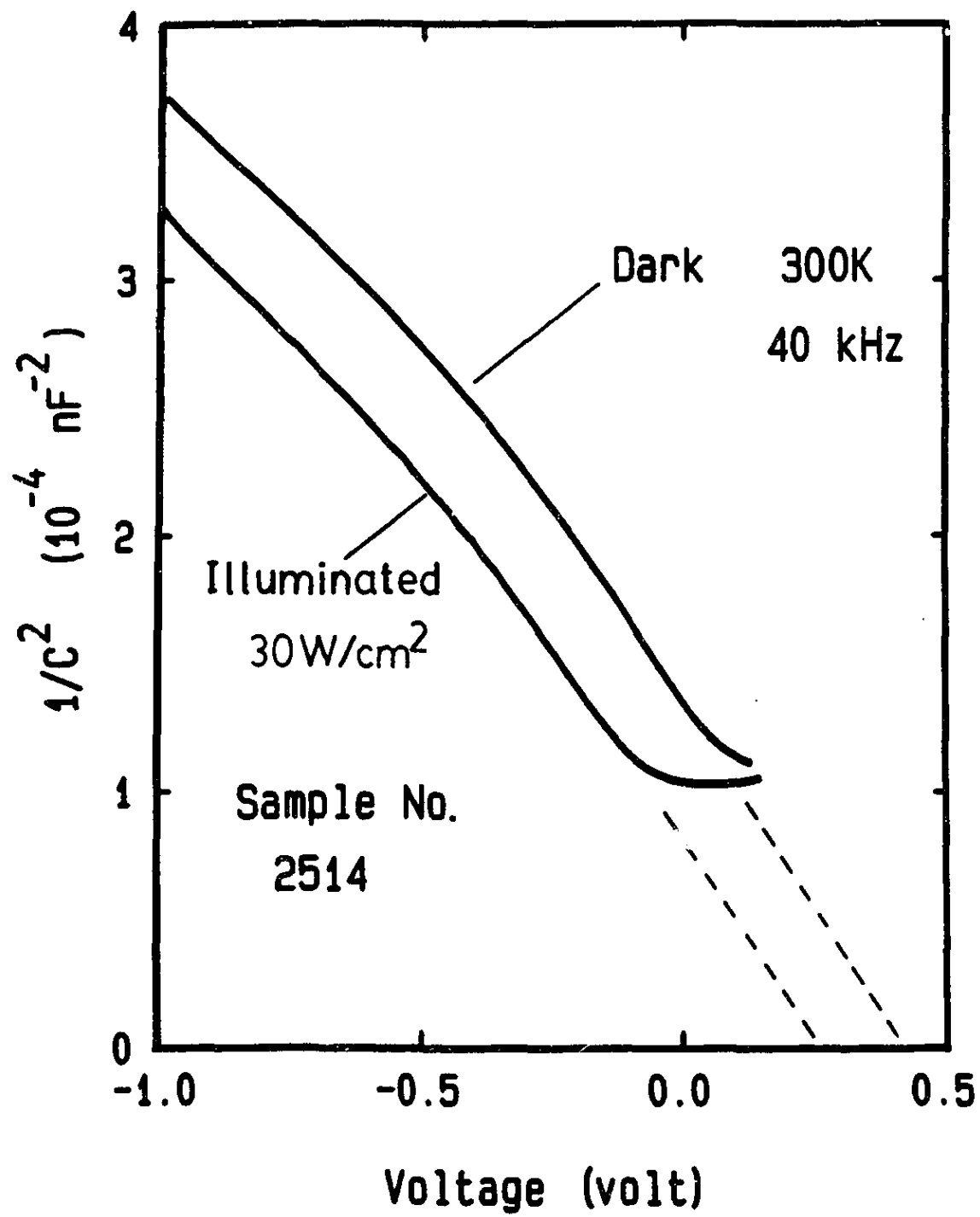


Fig. 7.18 Dark and illuminated C^{-2} - V curves measured at 40 kHz, showing a shift towards negative voltages under the illumination.

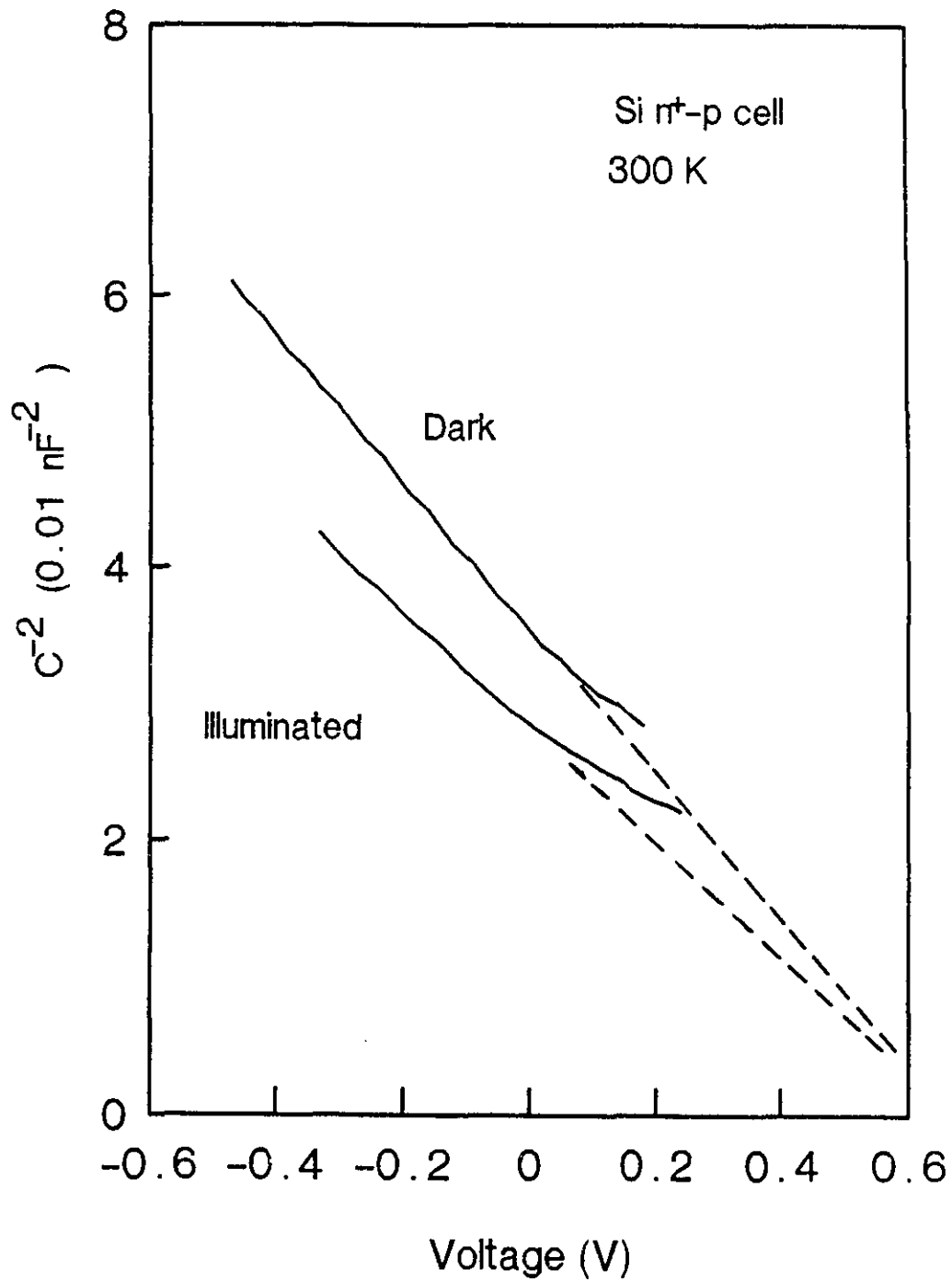


Fig. 7.19 Dark and illuminated C-V results for a commercial Si cell (100 kHz, conversion efficiency 12%). No difference in intercept is seen for this device.

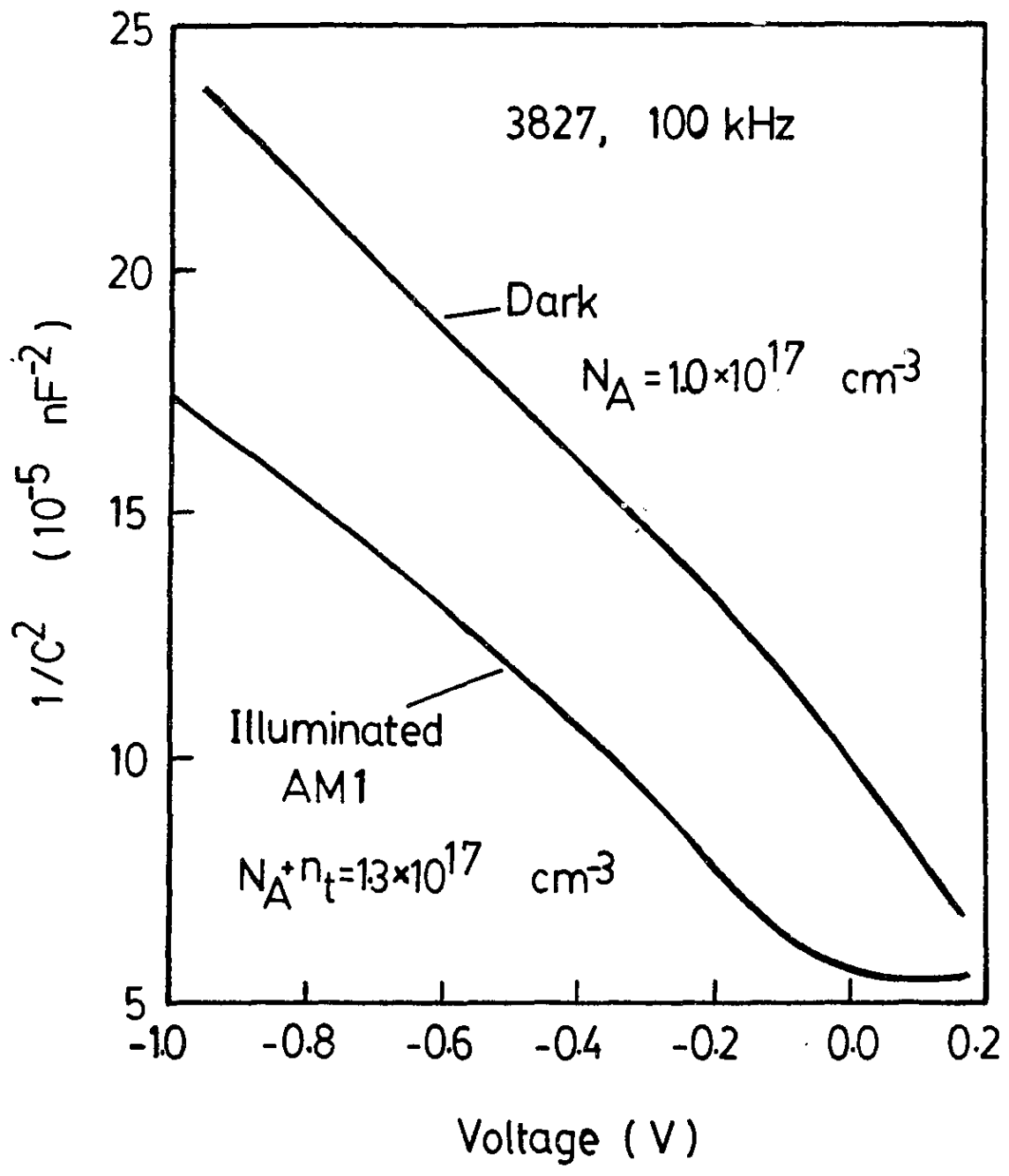


Fig. 7.20 Dark and illuminated C-V results for the cell No. 3827 (100 kHz), showing a light-induced increase in the apparent carrier concentration and a light-induced decrease in V_D .

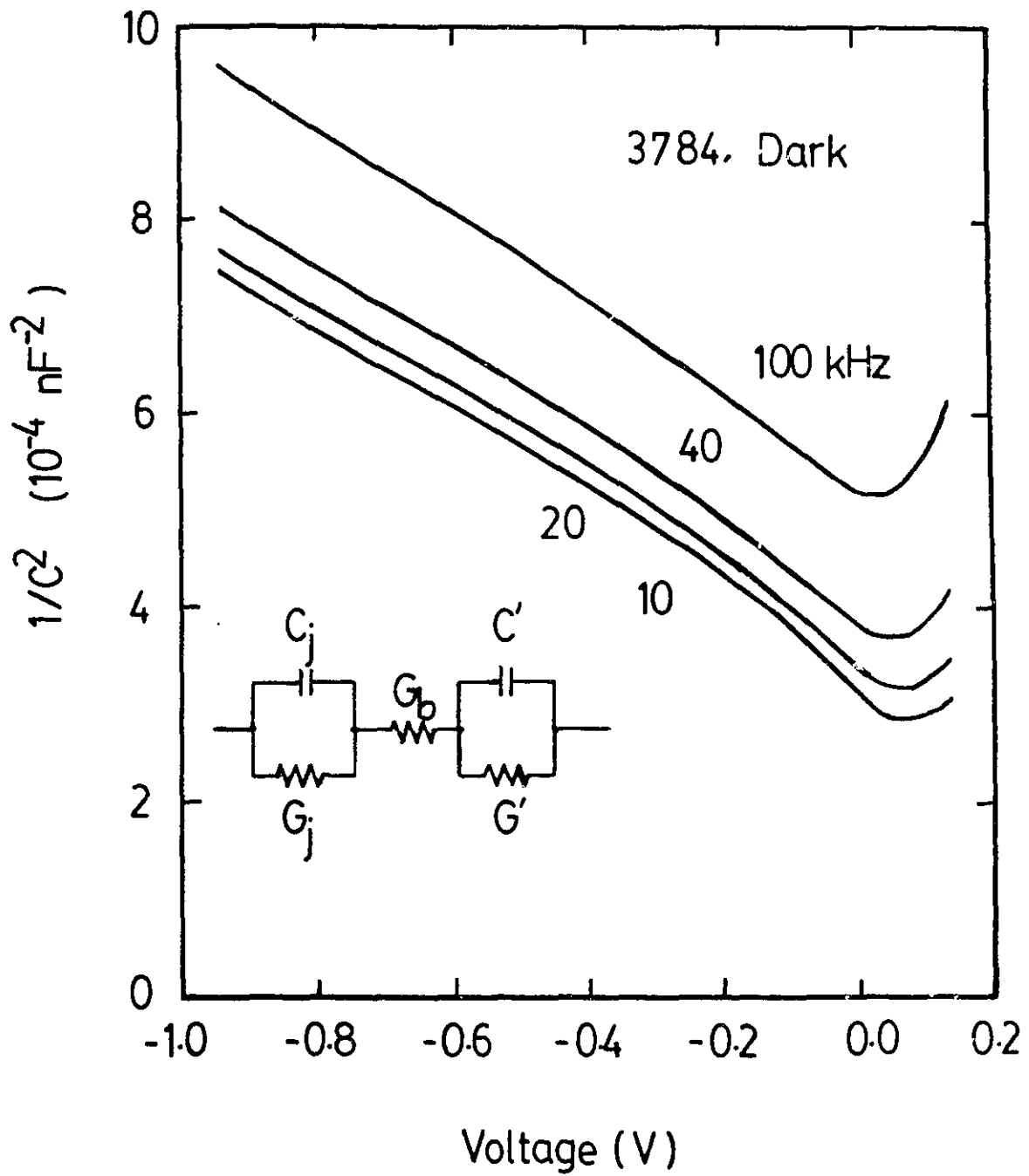


Fig. 7.21 Dark C-V results for the sample No.3784 showing a minimum C^{-2} value in each curve. Inset is the proposed model for the device.

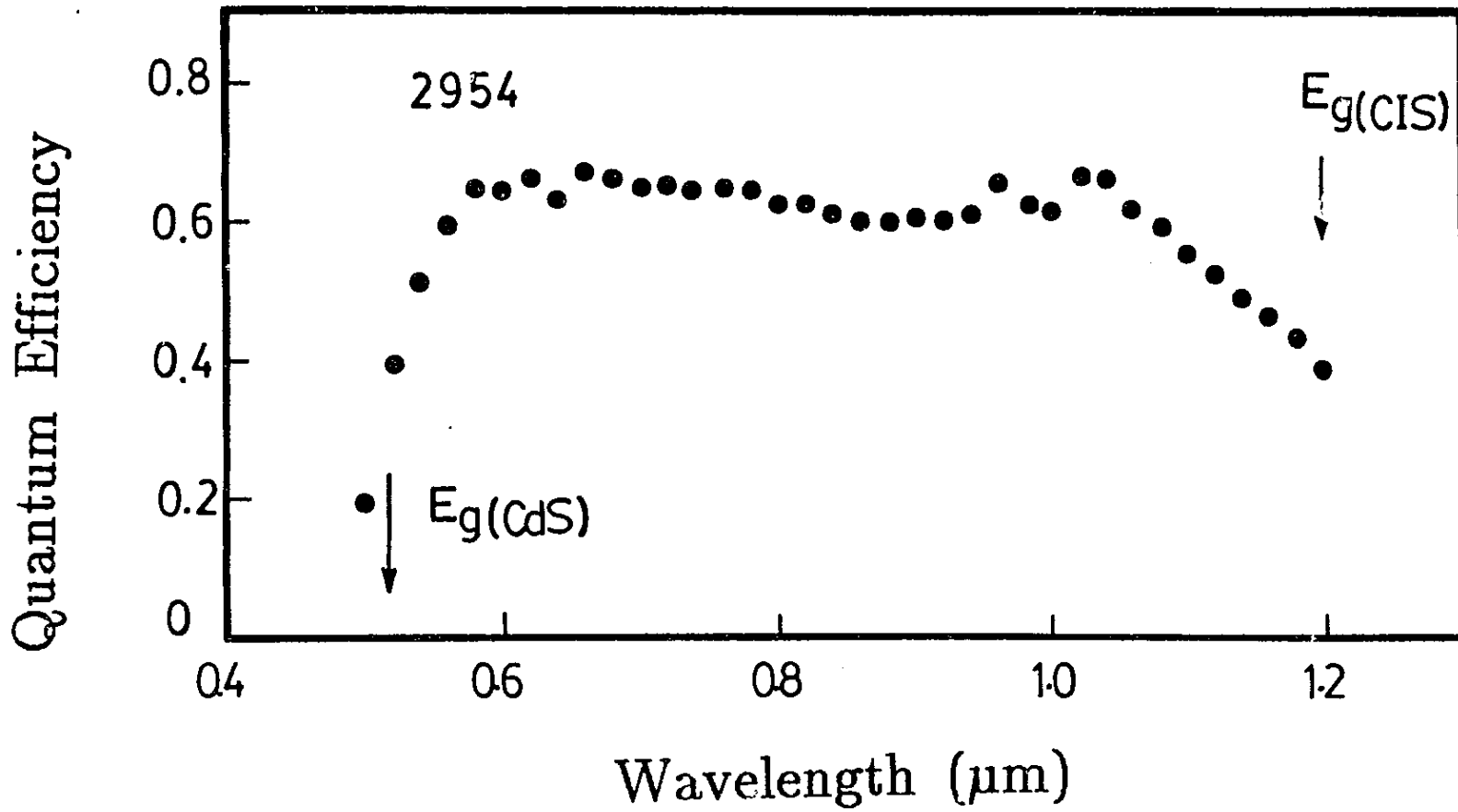


Fig. 7.22 Measured quantum efficiency vs. wavelength for a cell with a low conversion efficiency.

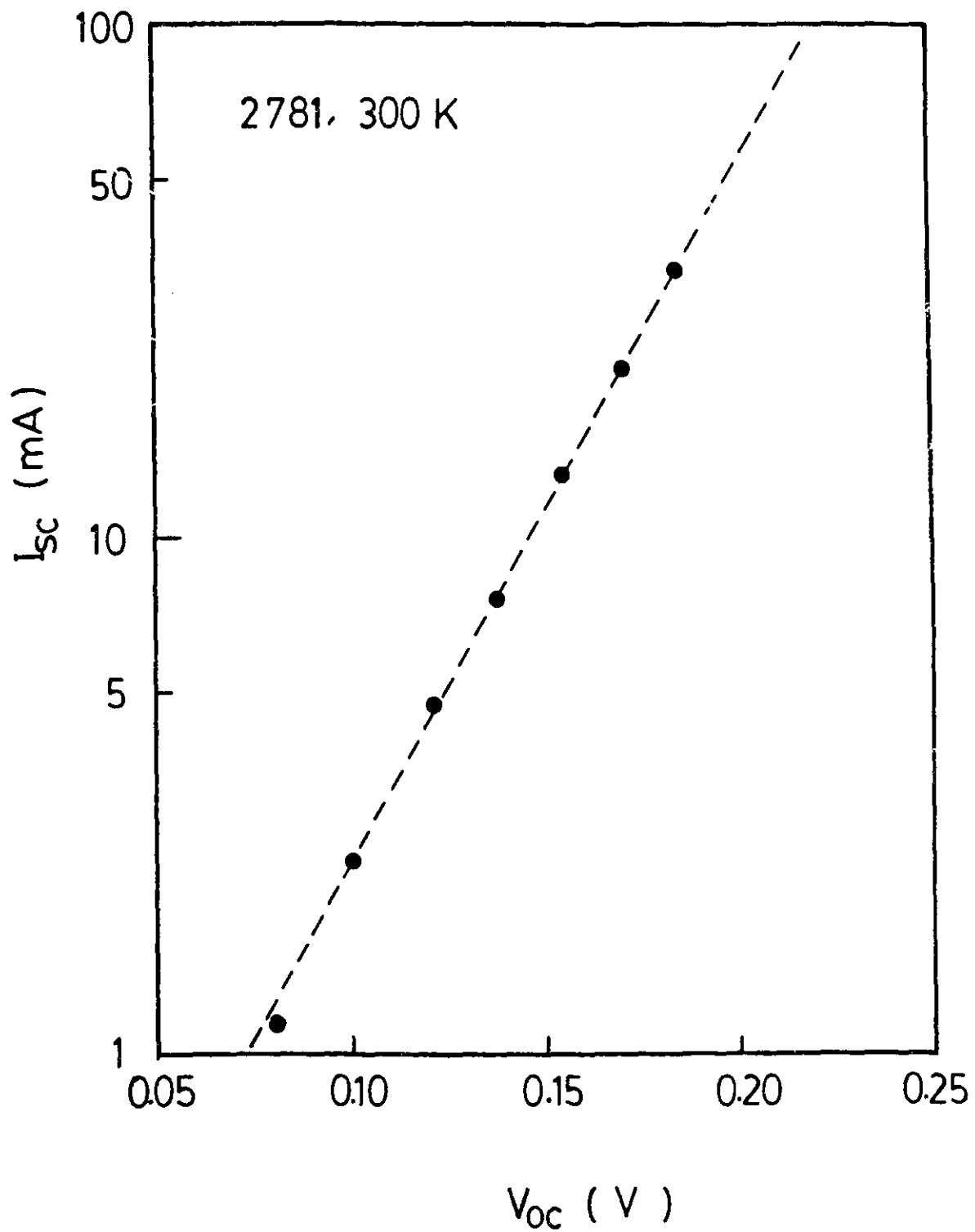


Fig. 7.23 A plot of I_{sc} versus V_{oc} for the sample No. 2784, showing a linear relationship.

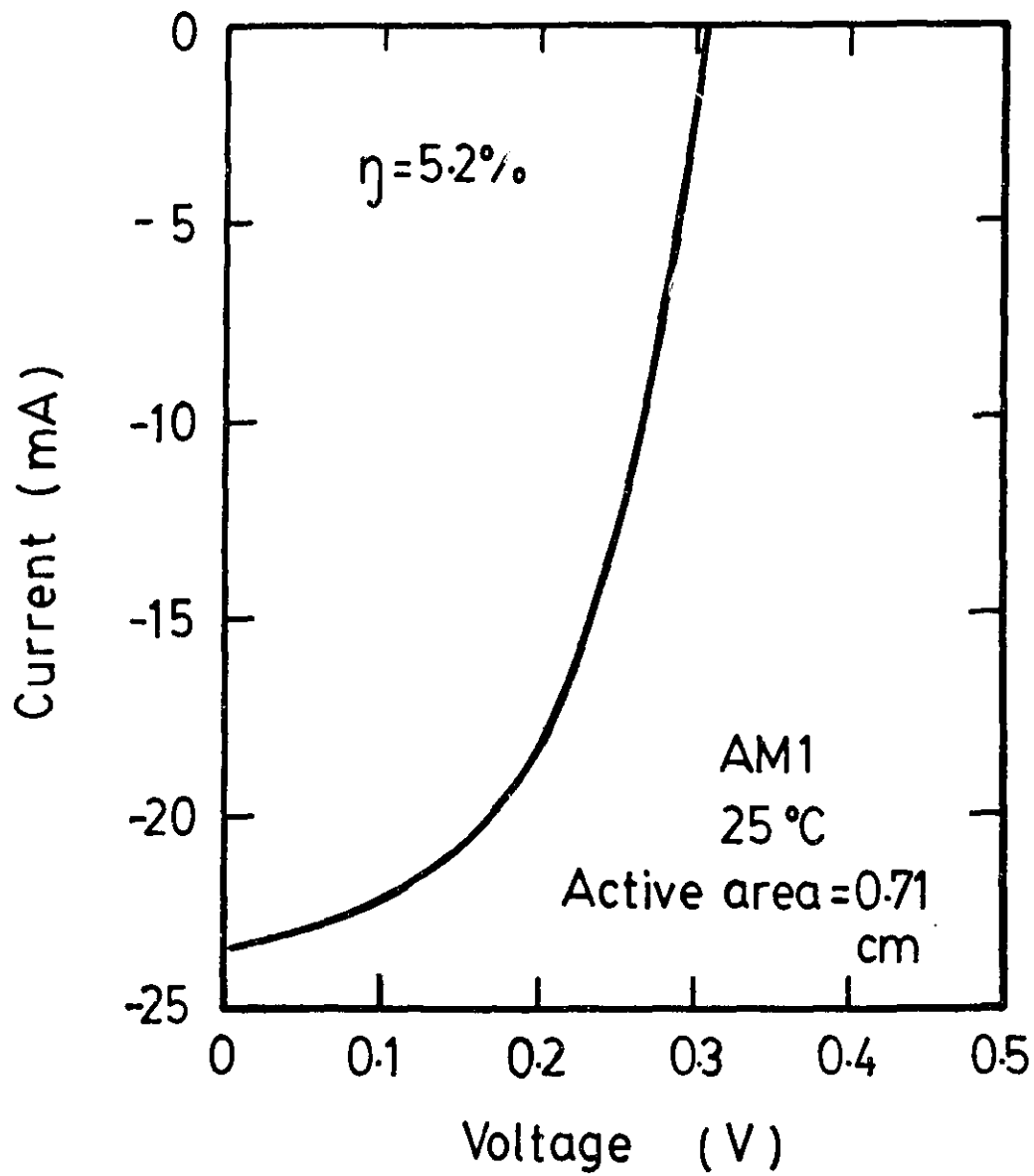
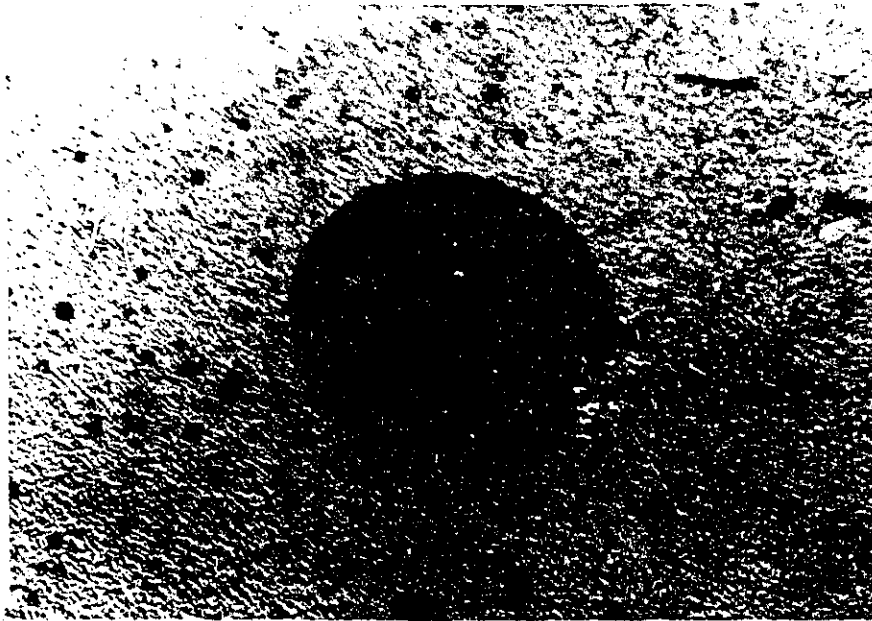


Fig. 7.24 Illuminated I-V characteristics of the cell with an active area efficiency of 5.2%.



50 μm

Fig. 7.25 An SEM photograph showing a pin hole in the CdS film for a 4% cell.

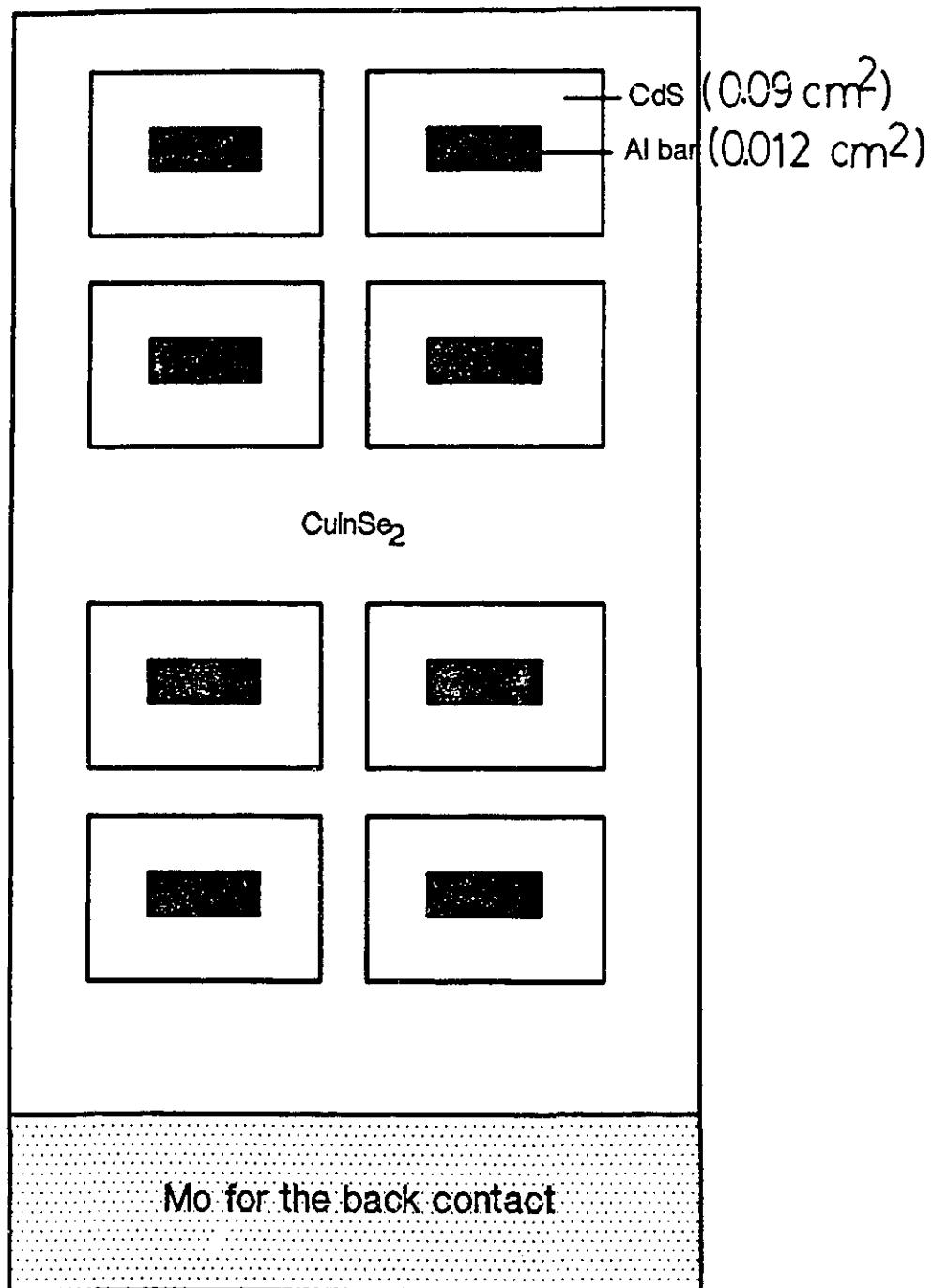


Fig. 7.26 A schematic diagram showing the top view of the small area cells.

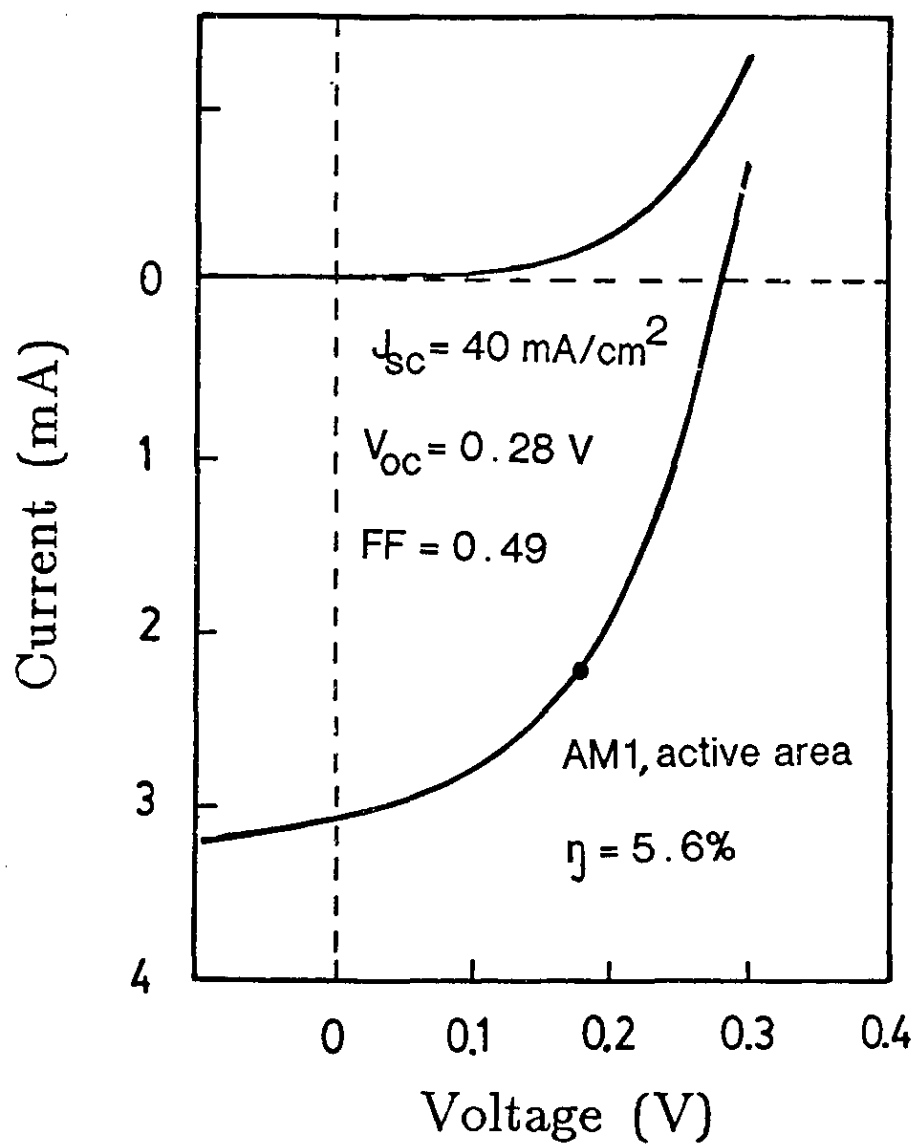
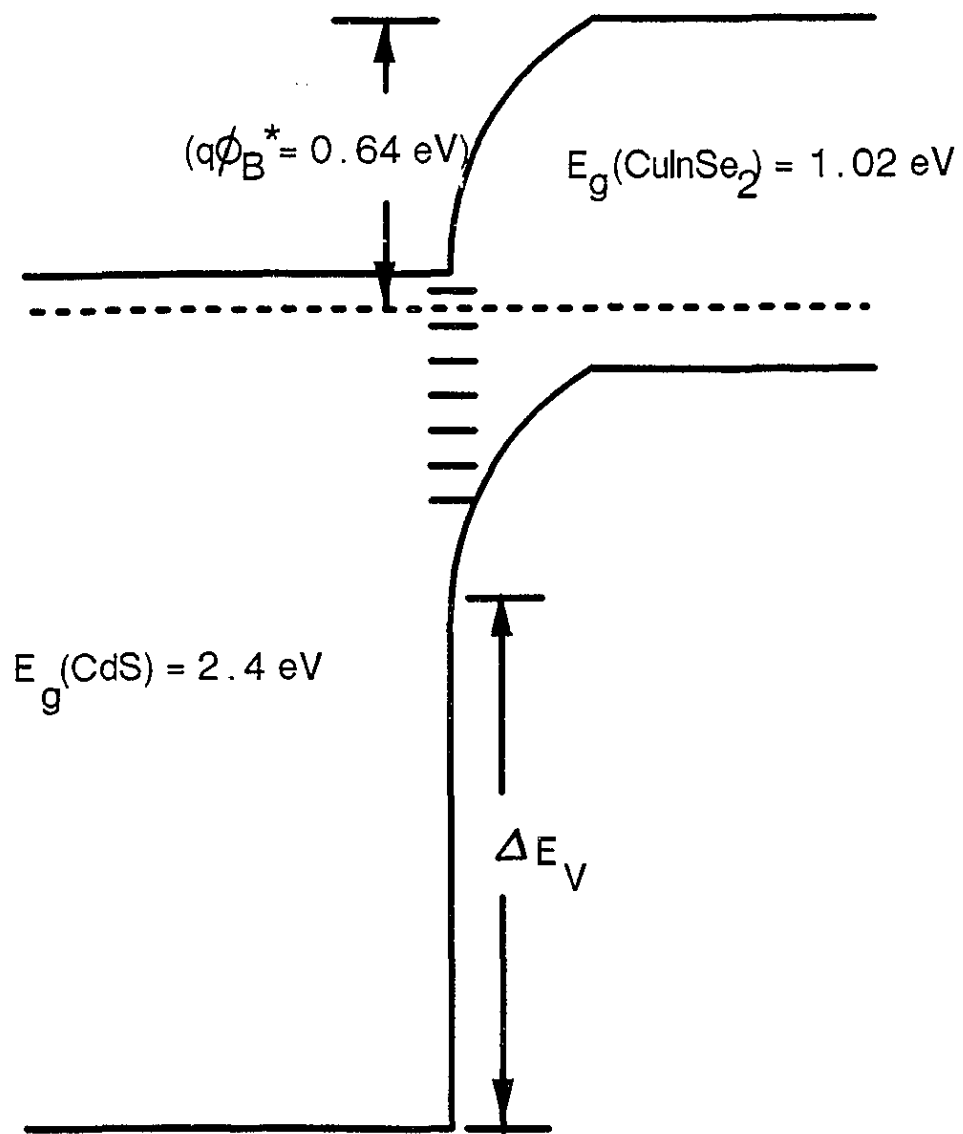


Fig. 7.27 Illuminated I-V characteristics for the small area device with the active area efficiency of 5.6%.



* Obtained from I-V measurements

Fig. 7.28 Energy band diagram constructed for the CdS/CuInSe₂ devices studied in this work.

Chapter 8 ADMITTANCE SPECTROSCOPY FOR THE STUDY OF DEEP LEVELS IN THE ELECTRODEPOSITED CuInSe₂ FILMS

8.1 Introduction

The conversion efficiency of solar cells is often found to be affected by electrically active deep energy levels present in the semiconductor. These deep levels can capture charge carriers and reduce their life time. Many methods have been used for the investigation of energy levels in the semiconductors, including DLTS^{8.1}, photoluminescence^{8.2}, thermally stimulated capacitance^{8.3} and admittance spectroscopy. The admittance spectroscopy technique was first introduced by D. L. Losee^{8.4, 8.5} and was further developed by Paustrat et al^{8.6}. It has been applied to several semiconductors like: Si^{8.7, 8.8}, CdS^{8.9}, CdTe^{8.10}, and GaAs^{8.11}. Results obtained for Schottky junctions using the admittance spectroscopy method also have been compared with those obtained using the deep level transient spectroscopy (DLTS) method. The admittance spectroscopy is a relatively simple and useful method for the investigation of comparatively fast trap levels of majority carriers.

Fabick and Eskenas^{8.12} have studied ZnO/CdS/CuInSe₂ thin film heterojunction devices using the admittance spectroscopy method. With this method, they found a single conductance peak between 160 K and 230 K in the frequency range from 10 kHz to 500 kHz. The data obtained suggested that a single deep level at

about 0.237 eV from the valence band edge was present in the p-type CuInSe₂ films. Vaidhyanathan et al^{8.13} have also applied the admittance spectroscopy technique to CdS/CuInSe₂ devices fabricated using vacuum deposited CuInSe₂ films. They observed two conductance peaks in the temperature range of 40 to 280 K at a frequency of 5.3 kHz. The two peaks located at about 50 and 160 K and the corresponding activation energies were 50 and 150 meV, respectively. Using devices fabricated on vacuum deposited CuInSe₂ thin films, Demetriou and Rothwarf^{8.14} reported the presence of a deep level at 130 meV with a capture cross section of $3.3 \times 10^{-17} \text{cm}^2$ from the admittance spectroscopy results.

In order to obtain further information and to increase the conversion efficiency on cells fabricated using the electrodeposited CuInSe₂ films, admittance spectroscopy measurements have been carried out on several devices. The main purposes of this work are (1) to obtain activation energy of electrically active level(s), and (2) to investigate the relationship between the activation energy of the deep level(s) and the composition of the films.

8.2 Theory of Admittance Spectroscopy

In a Schottky junction or a one-sided heterojunction, the admittance is affected by the presence of traps of majority carriers. If the dc bias voltage and the frequency of ac signal are kept constant during the measurements, the conductance values obtained from the admittance measurements can be used to deduce the activation energy of the traps. The small signal

equivalent circuit of a junction is shown in Fig. 8.1(a). In this figure, R_s is the series resistance and G_D is the shunt conductance of the device. C^* is the capacitance resulting from the charging and discharging of both the shallow and deep levels. The capacitance, C^* , which is complex when deep levels are involved, is given by: $C^* = C - jG/\omega$. Here, C is the junction capacitance; G is the junction conductance and ω is the angular frequency of the ac signal. The measured admittance is represented by the parallel circuit given in Fig. 8.1(b): G_e is the measured conductance and C_e is the measured capacitance. Fig. 8.2(a) shows the energy band diagram of a Schottky junction (using a p-type semiconductor) with a shallow level located at E_s and a deep level at E_t . Here W is the depletion width and x_t is the position at which the deep level crosses the Fermi level. The corresponding space charge density variation is illustrated in Fig. 8.2(b).

When there is a small increase in the bias voltage, δV , the total change in the electric charge δQ is given by the sum of the charge increase at x_t and at W (δQ_t and δQ_s). The capacitance C^* then is given by the following equation:

$$C^* = C - jG/\omega = \delta Q/\delta V = (\delta Q_s + \delta Q_t)/\delta V. \quad (8.1)$$

It can be shown^{8.8} that

$$C = C_s + (C_{s+t} - C_s)/[1 + (\omega\tau)^2] \quad (8.2)$$

$$G = (C_{s+t} - C_s) \omega^2\tau/[1 + (\omega\tau)^2]. \quad (8.3)$$

In the above equations,

$$\tau^{-1} = 2e_n (1 + N_t x_t / N_s W), \quad (8.4)$$

$$e_n = AT^2 \exp[-E_t/kT]^{8.15} \quad (8.5)$$

In the equations, ω is the angular frequency of the ac voltage and T is the emission time constant of the majority carriers from the deep levels located at E_t . When $\omega\tau \gg 1$, holes trapped in deep level at position x_t can not follow the change in the voltage. Therefore equation (8.1) becomes

$$C^* = C = C_s = \epsilon/W. \quad (8.6)$$

When $\omega\tau \ll 1$, holes in the deep level at x_t respond to the voltage change without delay. Under this condition, the capacitance C^* is real:

$$C^* = C = C_{s+t} = \epsilon(N_s + N_t)/(N_s W + N_t x_t). \quad (8.7)$$

To obtain the activation energy, the measurements are carried out over the temperature range in which the emission rate, e_n , of majority carriers from the deep level traps varies. For such measurements, it is possible to reach a temperature value so that $\omega\tau = 1$. When the condition $\omega\tau = 1$ is satisfied, the junction conductance (G) given above will reach a maximum value. For devices with a relatively small series resistance R_s (usually true at high temperatures), $G_e \approx G + G_D$. Because G_D increases monotonically with temperature, the temperature value for the peak of conductance G can be obtained directly from the measured conductance G_e versus temperature curve. This is especially true if the peak in the junction conductance G appears in the low

temperature region where the shunt conductance G_D is relatively small. Furthermore, the magnitude of junction conductance peaks is directly proportional to (see equation (8.3)).

By applying equations (8.4), (8.5) and the condition $\omega\tau = 1$, the activation energy of the deep level, E_t , can be obtained from a plot of $\ln(\omega/T_m^2)$ versus $1/T_m$. Here T_m is the temperature value for the conductance peak at a fixed frequency.

To estimate the density of a deep level, C-V measurements at temperatures both below and above the conductance peak, associated with this level, have to be carried out. The slope of the C^{-2} -V curve measured below the conductance peak gives the density of the shallow level, N_s . And that of the C^{-2} curve obtained above the peak yields the total density, $N_s + N_t$. By comparing the two concentration values, the density of the deep level can be obtained.

8.3 Measurement Results

For the admittance spectroscopy measurements, CdS/CuInSe₂ devices with different as-deposited Cu/In ratios in the CuInSe₂ films were selected. The In/Cu ratio was in the range from 1.1 to 1.25. The selected devices were tested for I-V characteristics. The dark I-V results showed that the diode factor of the selected devices was slightly greater than 1. Fig. 8.3 shows the dark I-V results for one of the CdS/CuInSe₂ devices, No. 3772. The energy conversion efficiency of the selected devices was about 3-4% under AM1 illumination condition.

After the initial testing, the device was mounted on the

cooling finger of a liquid nitrogen cryostats for temperature-dependent admittance measurements. The temperature of the device was first reduced from room value to liquid nitrogen temperature (77 K) over a period of about 30 minutes. After a short stabilization, the device was warmed up gradually at a rate of about 0.5-2.5 K/min. and the admittance of the device was measured at seven different frequencies: 1, 2, 4, 10, 20, 40 and 100 kHz. The measurements were made over a temperature range from 80 K to 300 K with a fixed temperature step of 5 K. A block diagram of the measurement set up is given in Fig. 8.4. The admittance measurements were made using an HP 4274A LCR meter controlled by a microcomputer. The temperature of the device was monitored by a thermocouple connected to a computer-controlled voltmeter. The measurements were performed under a dark condition with a zero dc bias voltage. However, for some of the measurements, a dc reverse voltage was applied to the device to enhance the conductance peaks^{8.8}.

More than 10 devices were measured using the admittance spectroscopy method described above. For all of the samples, a peak was found for each G_e vs. T curve. In addition, a step was found for each C_e vs. T curve. The mid-point of the step was located at the same temperature as the conductance peak.

From the temperature-dependent conductance characteristics, the devices may be divided into two groups. Devices in the first group had conductance peaks in the temperature range from -170°C to -130°C as frequency was increased from 4 kHz to 40 kHz. In the second group, conductance peaks were in the temperature range

from -90°C to -50°C for the same frequency range. This effect is illustrated in Fig. 8.5. In this figure, the conductance peak of the sample No. 3093 occurs at -130°C (T_m). The temperature T_m for the samples No. 3853 and 3870 is about -70°C . It is also noted that the conductance values of samples 3853 and 3870 are smaller than those of sample 3093 over the entire temperature range studied. In Fig. 8.6, the measured capacitance C_e for samples 3093 and 3853 are plotted vs. device temperatures. The difference in the temperatures for the mid-point of the capacitance step is obvious.

In order to obtain the relationship between the temperature T_m and the measurement frequency, conductance results measured at four different frequencies are plotted in Fig. 8.7 for the sample No. 3853. The C_e - T results for the same device are also plotted in Fig. 8.8. In Fig. 8.7, the position of the conductance peak is seen to shift progressively towards lower temperatures as the frequency is decreased. This effect is also observed for the mid-point of the capacitance step (Fig. 8.8).

From the $G_e(T, \omega)$ - T plots, ω/T_m^2 values were obtained. These values were plotted versus $1/T_m$ in Fig. 8.9 for the devices No. 3621, 3093 and 3772 (all with In/Cu ratio of about 1.1). It is clear from the theory of admittance spectroscopy that the slope of the $\ln(\omega/T_m^2)$ vs $1/T_m$ plot yields the activation energy of the active states in the semiconductor. The activation energy value obtained for the samples No. 3621, 3093 and 3772 is about 50 meV. The conductance results for three other devices (with a In/Cu ratio of 1.25) are also shown in Fig. 8.9, giving activation

energy values of about 160 meV.

It was reported that a reverse voltage applied to the devices would enhance the conductance peak without changing the position of the peaks^{8.8}. In the admittance measurements, two devices (3853 and 3770B) were biased to -1 volt. The results were plotted in Fig. 8.10. The results for the two devices under zero bias condition were also shown. Activation energy values between 140 and 160 meV were obtained without the reverse bias. A small deviation for the energy values was observed when the devices were biased to -1 volt. This deviation could be due to the variation of the shunt conductance, G_D , with the voltage. It could also indicate a non-uniform distribution for the deep levels near the CuInSe_2 film surface, resulted from element interdiffusion.

Since the activation energy value for the three samples with the In/Cu ratio of 1.1 is relatively small (50 meV), it is also possible to obtain the energy value of a shallow level by plotting $\ln(G_S)$ vs $1/T$. Here G_S is the conductance value of the series resistor of the device. The slope of the plot gives the activation energy of the shallow levels^{8.7}. The required values of G_S were deduced from the measured C_e and G_e using the following equation:

$$G_S = G_e [1 + (\omega C_e/G_e)^2], \quad (8.8)$$

The results for the sample No. 3093 measured at 40 kHz are shown in Fig. 8.11. The data may be fitted by a straight line with an apparent activation energy of 36 meV. This value is roughly equal

to that obtained from Fig. 8.9.

For the devices with the large activation energy of 160 meV, the plot of $\ln(G_{\text{peak}})$ versus $\ln(f)$ showed a linear variation. The slope of the line was about 1 (see Fig. 8.12). The results thus suggest that the conductance peaks observed in the CdS/CuInSe₂ devices were due to a single trapping level in the electrodeposited CuInSe₂ films^{8.12}.

In the present experiment, density of the deep levels was not obtained. This is because that by using the present measurement instrument, the temperature of the device could not be maintained at a given temperature value for the C-V measurement.

In table 8.1, the energy levels found in the CuInSe₂ thin films using the admittance spectroscopy measurements are summarized. The results obtained in the present work and those obtained by other workers are given in the table.

8.4 Conclusions

Thin film cells of the form CdS/CuInSe₂ fabricated using electrodeposited p-type CuInSe₂ have been studied by the admittance spectroscopy method (in a temperature range from 80 to 300 K). From the temperature values of the conductance peaks measured at different frequencies, the activation energies of the deep levels in the electrodeposited CuInSe₂ films were determined. The results obtained show that the activation energy values of the deep levels in the CuInSe₂ films were dependent on the stoichiometry. For those devices fabricated using films with an In/Cu ratio of about 1.1, the activation energy of the level was about

50 meV. For those devices fabricated using CuInSe_2 films with an In/Cu ratio of about 1.25, the average activation energy value was about 160 meV. Limited by the measurement instrument, density of the deep levels in the electrodeposited CuInSe_2 films was not obtained.

Table 8.1 Summary of different energy levels obtained in p-type CuInSe_2 from admittance spectroscopy measurements by different groups.

Worker	Preparation method	level 1	level 2
Fabick ^{8.12}	Vacuum Evap.	237 meV	
Vaidhyanathan ^{8.13}	Vacuum Evap.	150 meV*	50 meV
Demetriou ^{8.14}	Vacuum Evap.	130 meV	
McGill**	Electrodeposition	160 meV	50 meV

* levels one and two were found in the same sample.

** Level 1 was found in sample with Cu/In ratio of 1.25. Level 2 was found in samples with Cu/In ratio of 1.1.

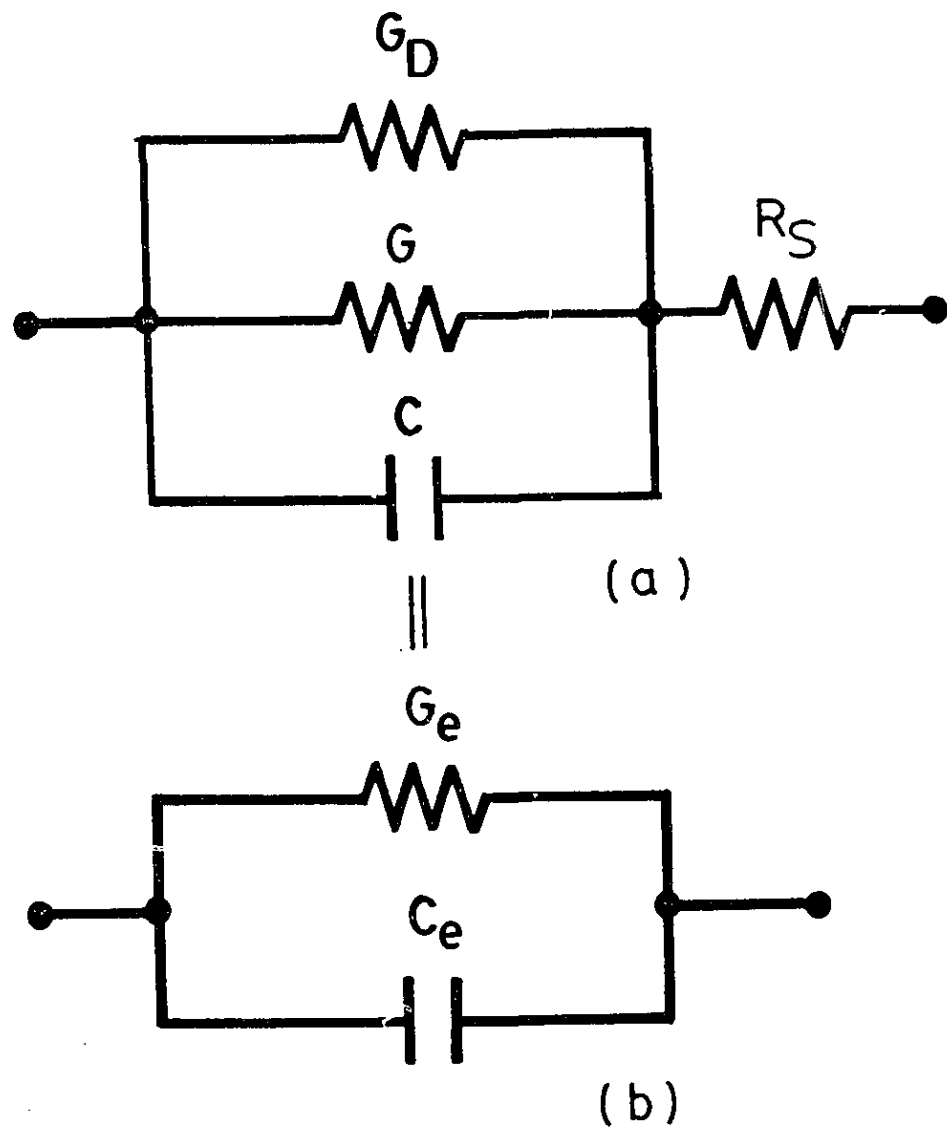


Fig. 8.1 (a) Small signal equivalent circuit of a junction and (b) the measured admittance in a parallel mode.

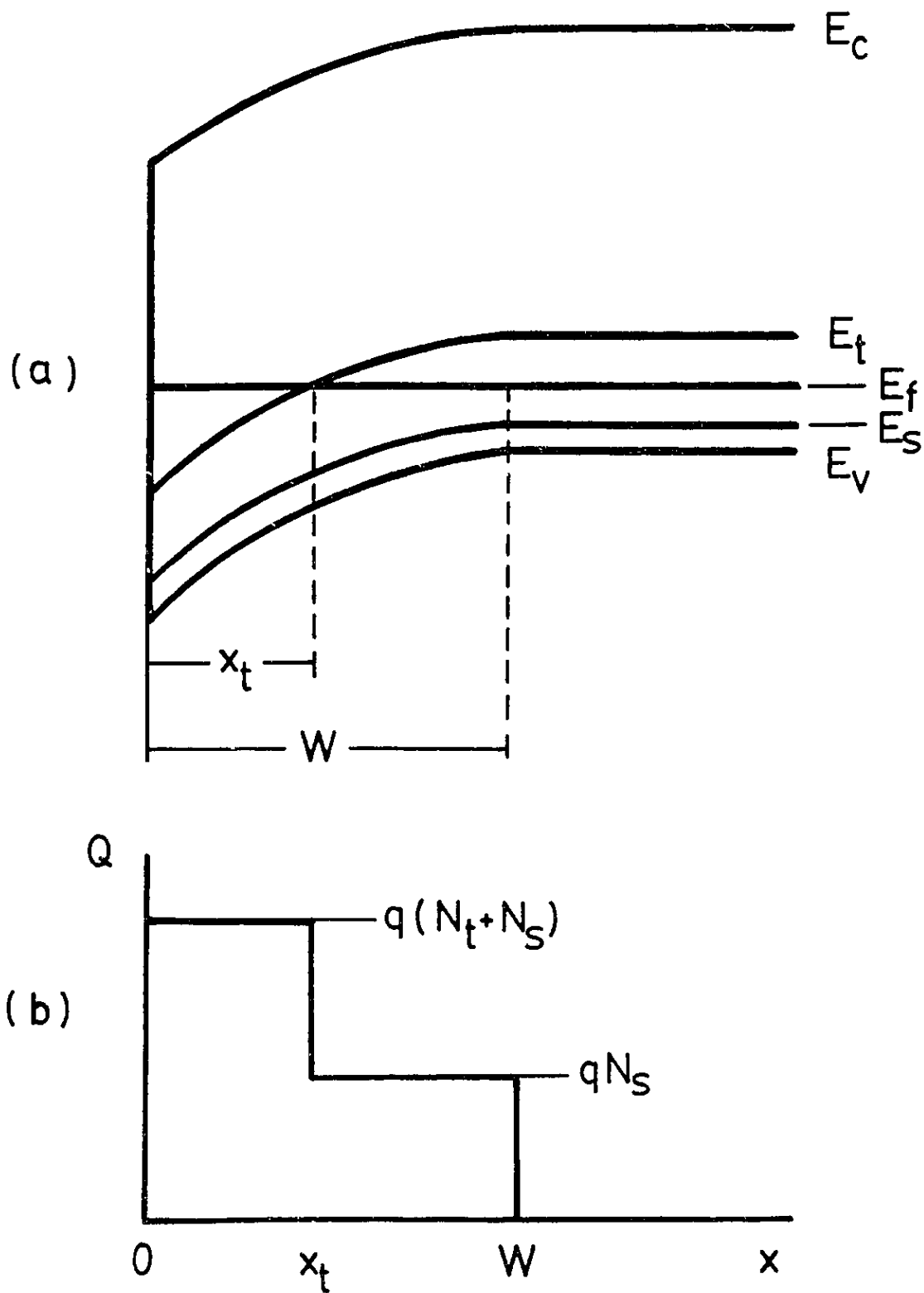


Fig. 8.2 (a) Energy band diagram of a Schottky junction on a p-type substrate with the presence of a deep level and (b) the corresponding space charge density variation.

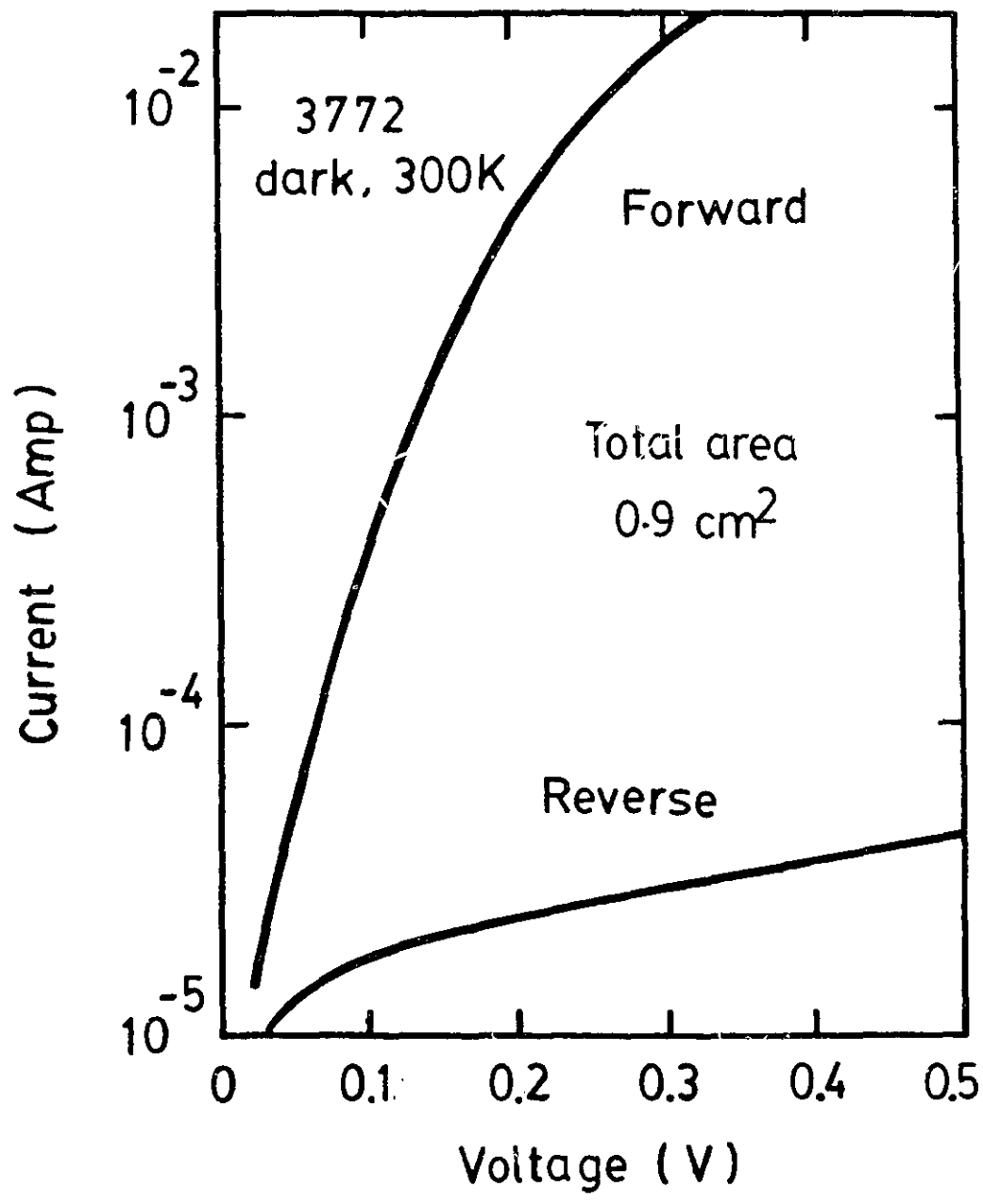


Fig. 8.3 Dark I-V curves of a CdS/CuInSe₂ solar cell.

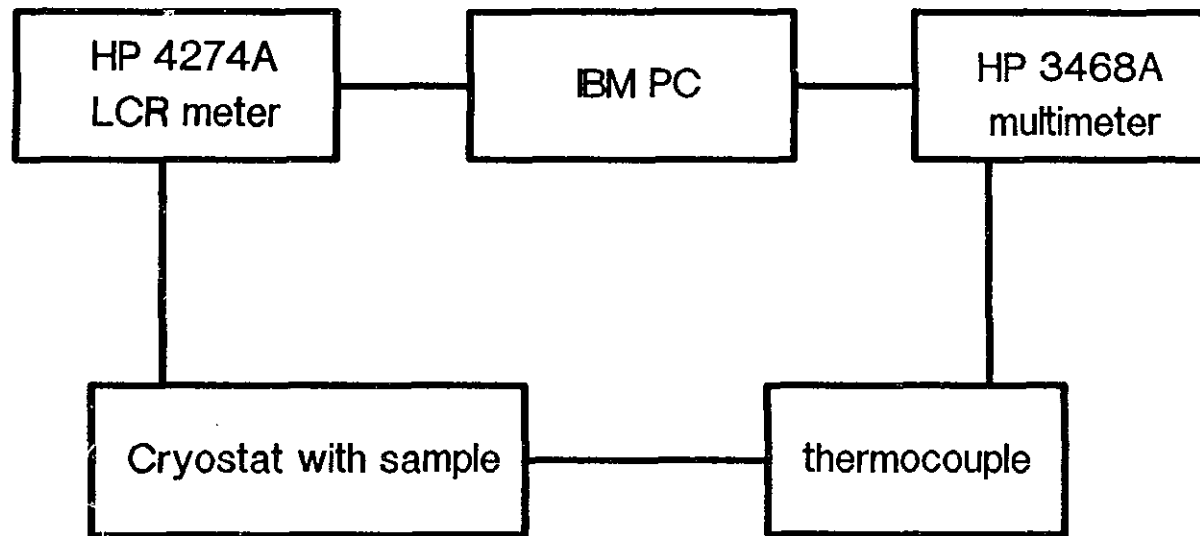


Fig. 8.4 A block diagram of measurement set up for the admittance spectroscopy.

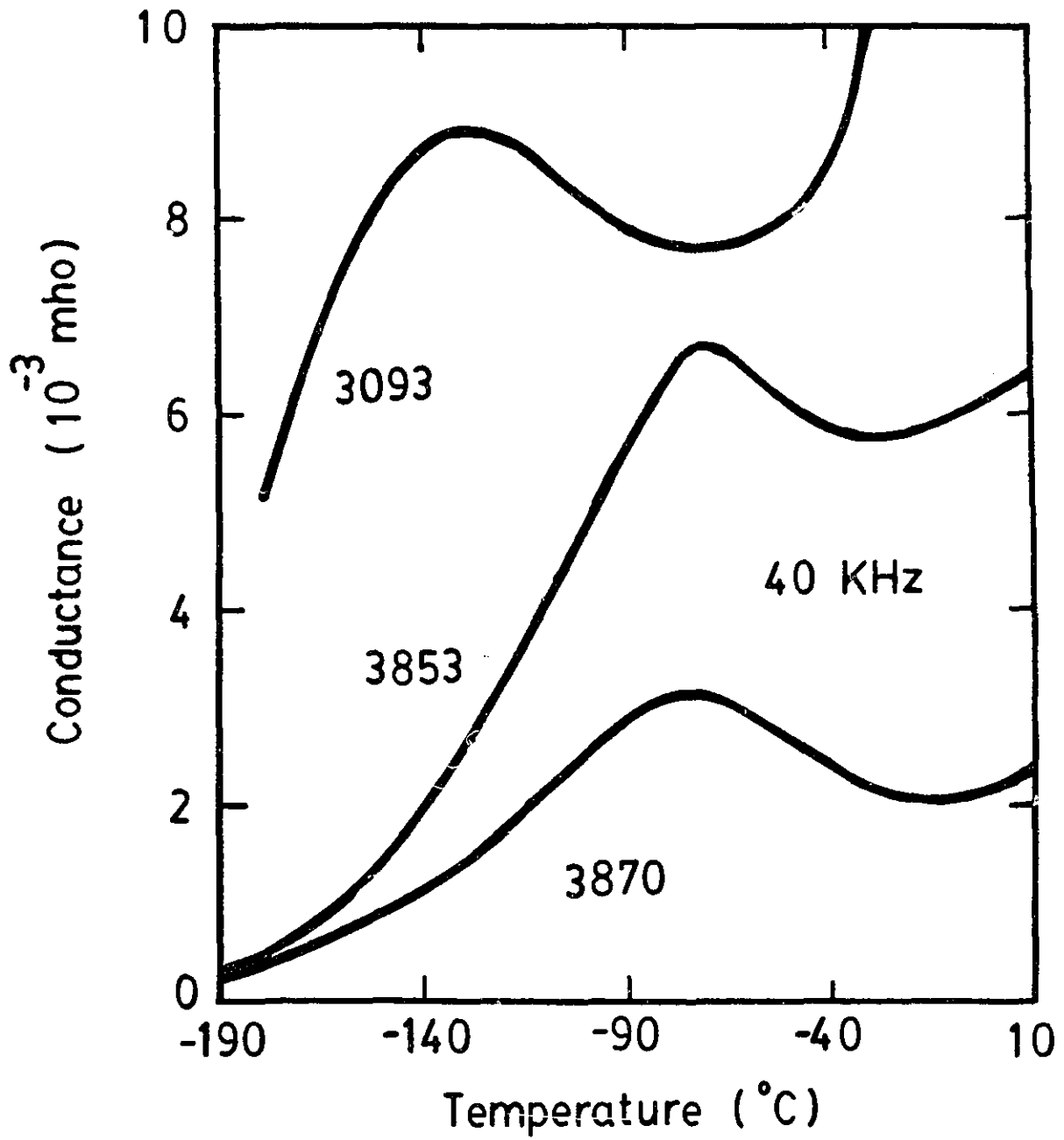


Fig. 8.5 Results of conductance for three samples.

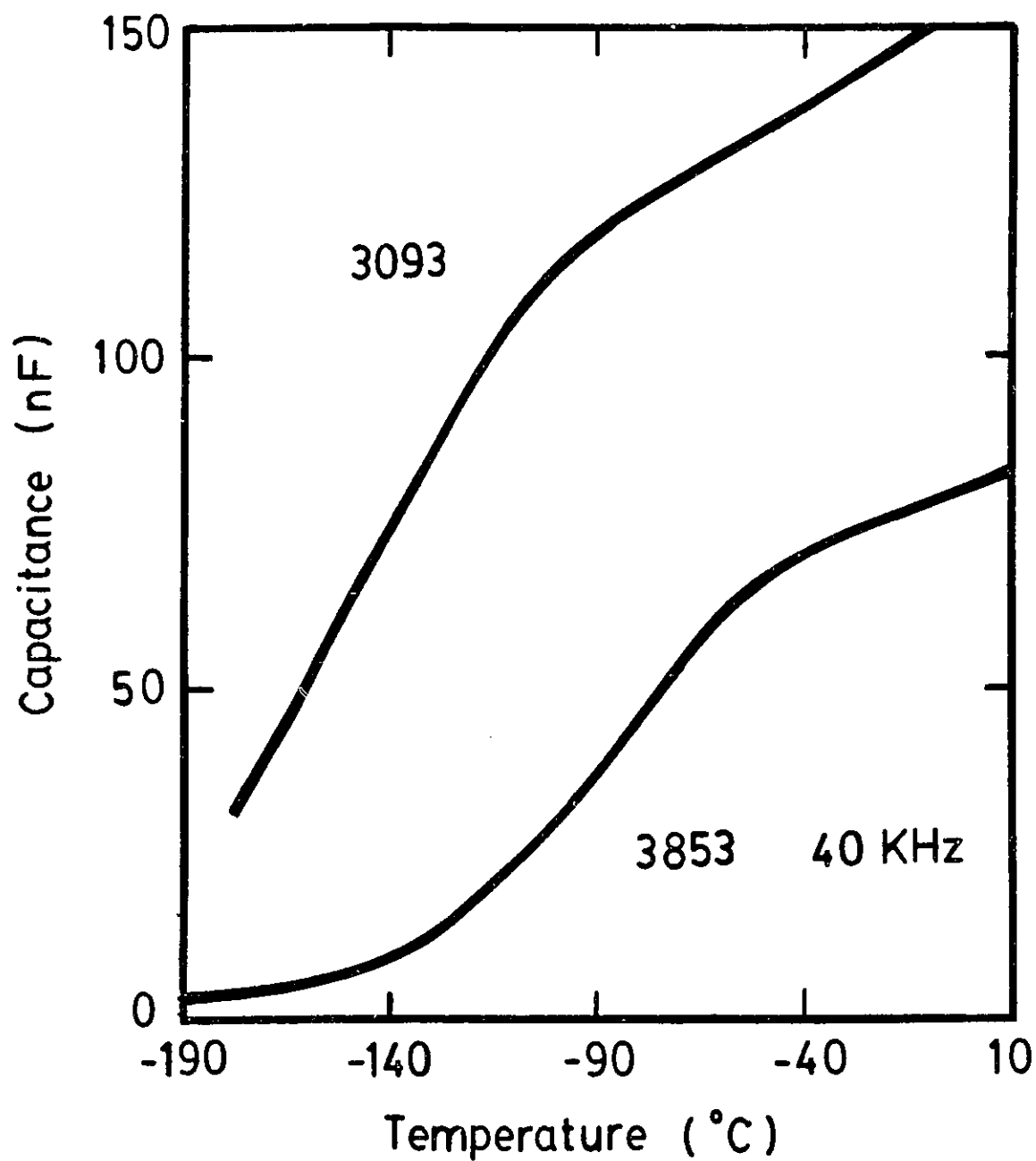


Fig. 8.6 Results of capacitance for the samples No. 3093 and No. 3853, showing different temperatures for the midpoint of the capacitance steps.

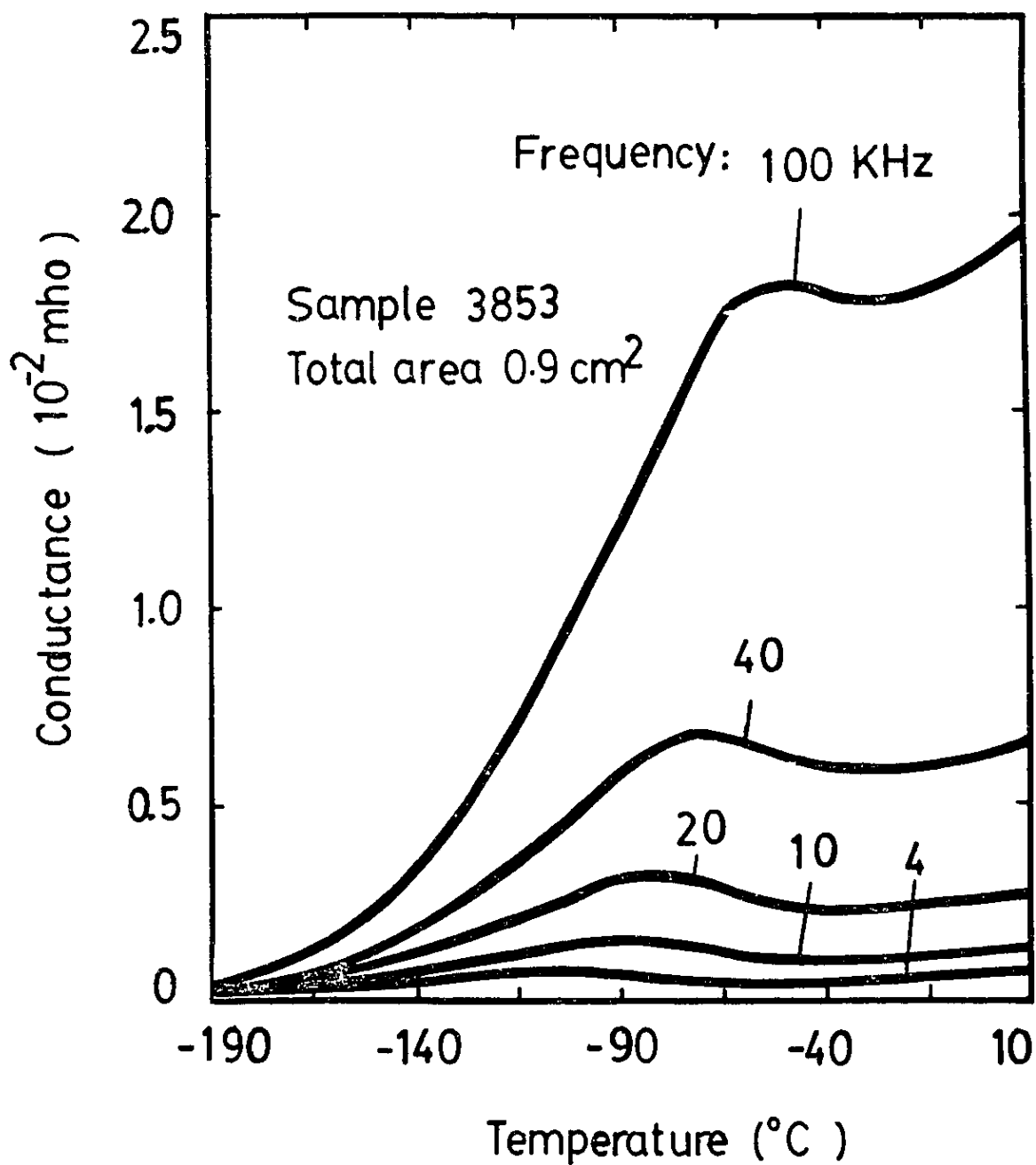


Fig. 8.7 Results of G_e -T measurements on a CdS/CuInSe₂ cell (No. 3853). The conductance peak occurs at higher temperature as the frequency is increased.

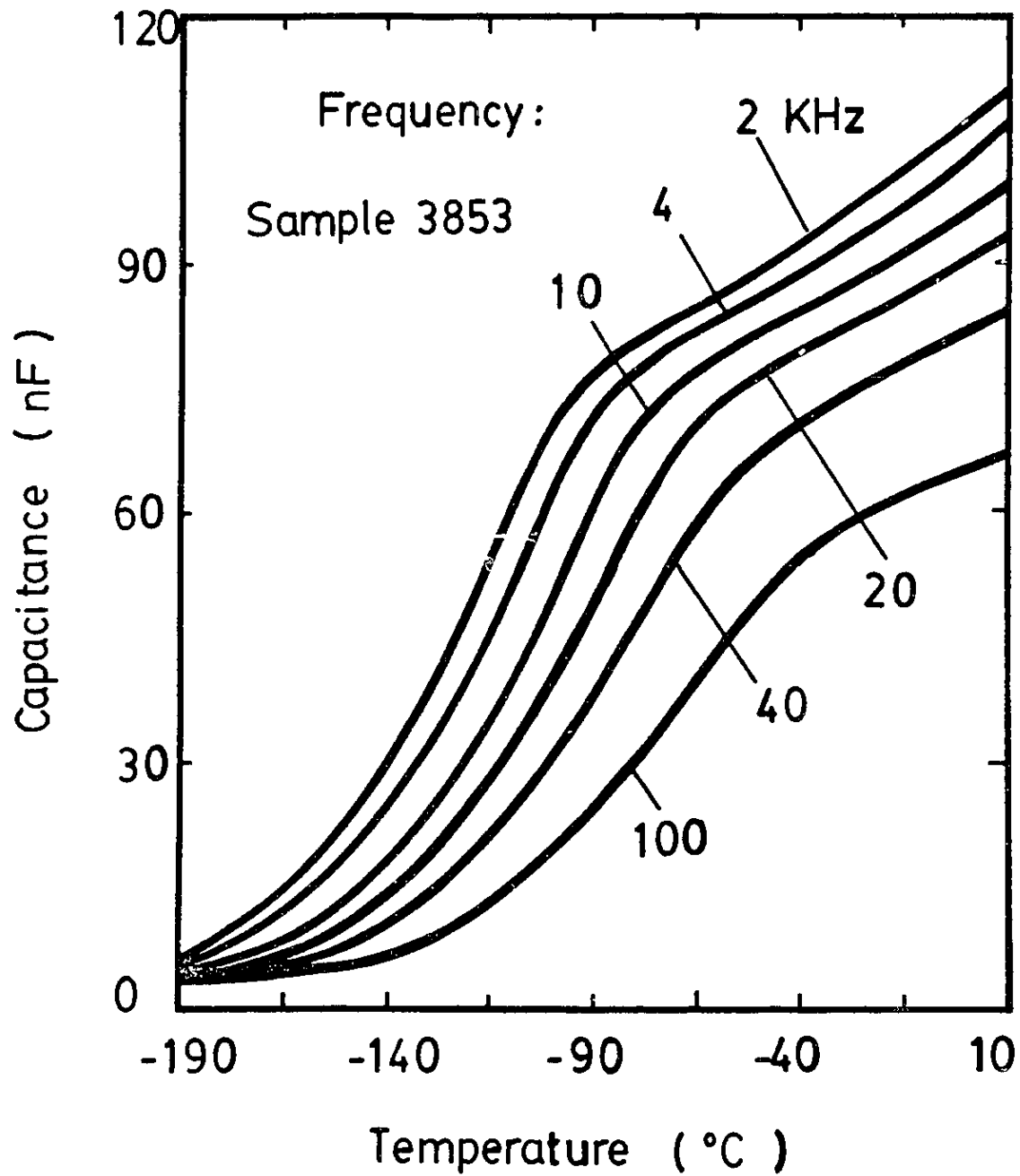


Fig. 8.8 Results of C_e -T measurements (sample No.3853), showing effect of frequency on the position of the capacitance step.

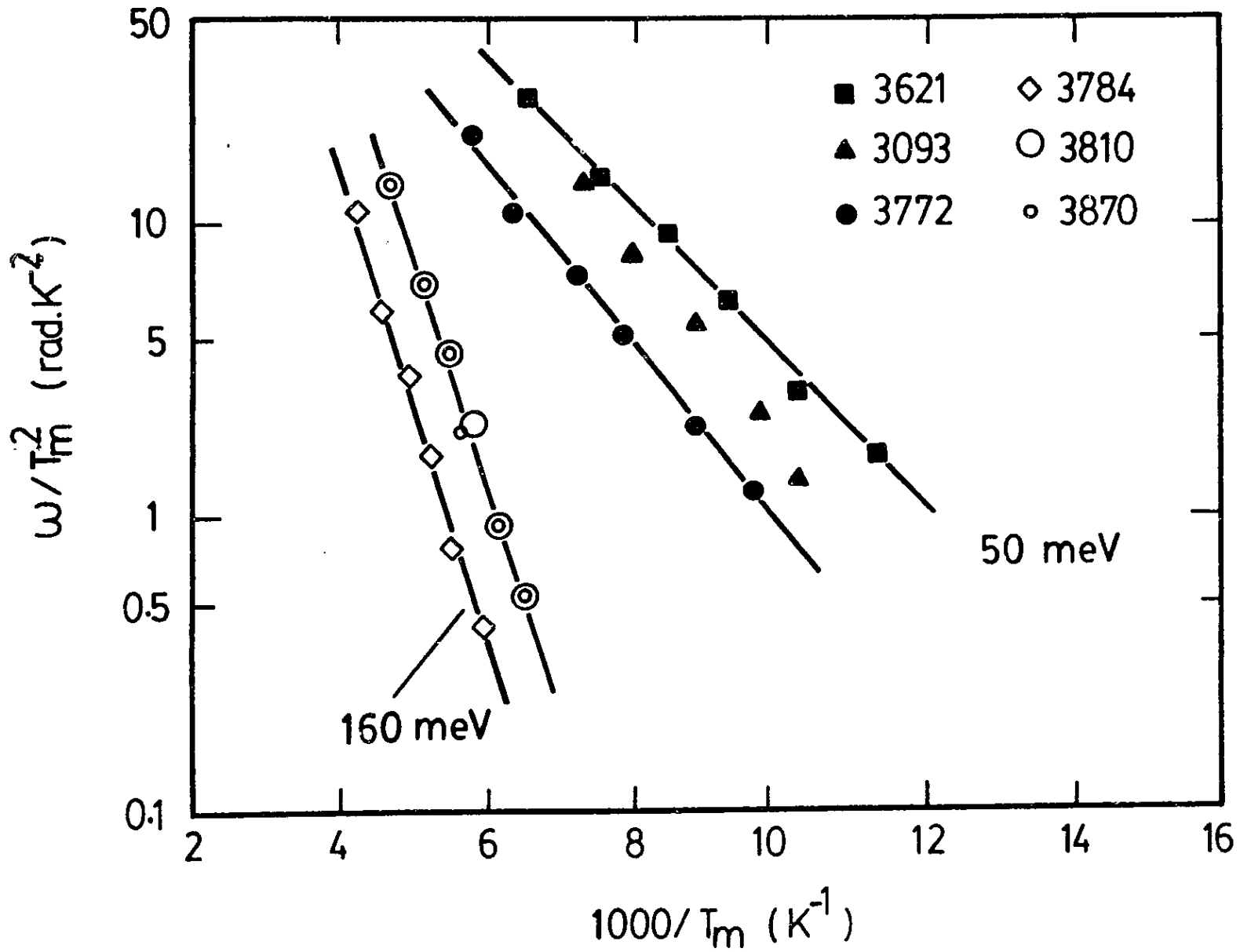


Fig. 8.9 Plots of ω/T_m^2 vs. $1/T$ for six CdS/CuInSe₂ devices. Slope of the lines gives the energy value of the deep level.

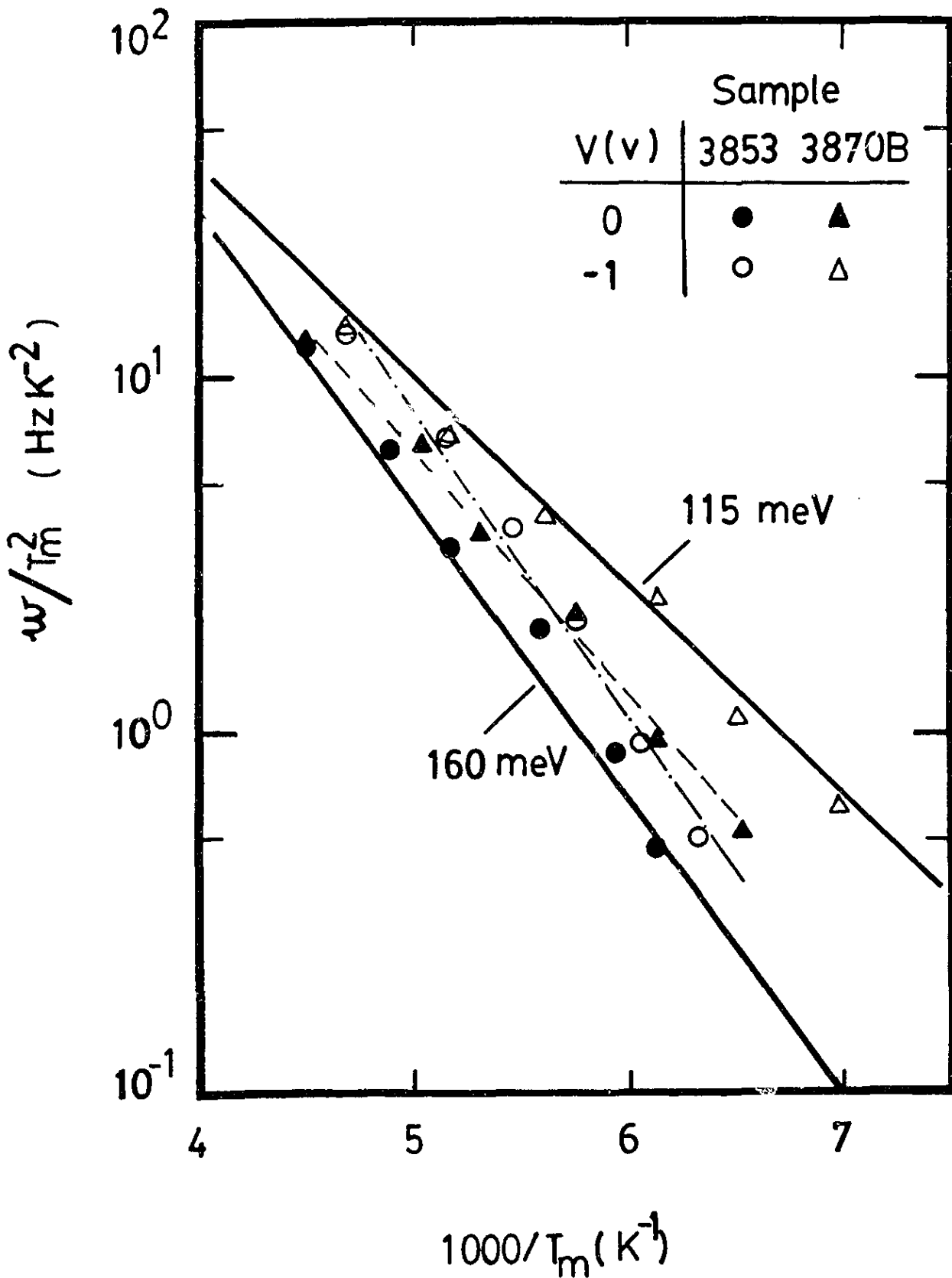


Fig. 8.10 Results of ω/T_m^2 vs. $1/T$ for samples No. 3853 and No. 3870, obtained both with and without the reverse bias. Slightly different energy values were obtained for the deep levels.

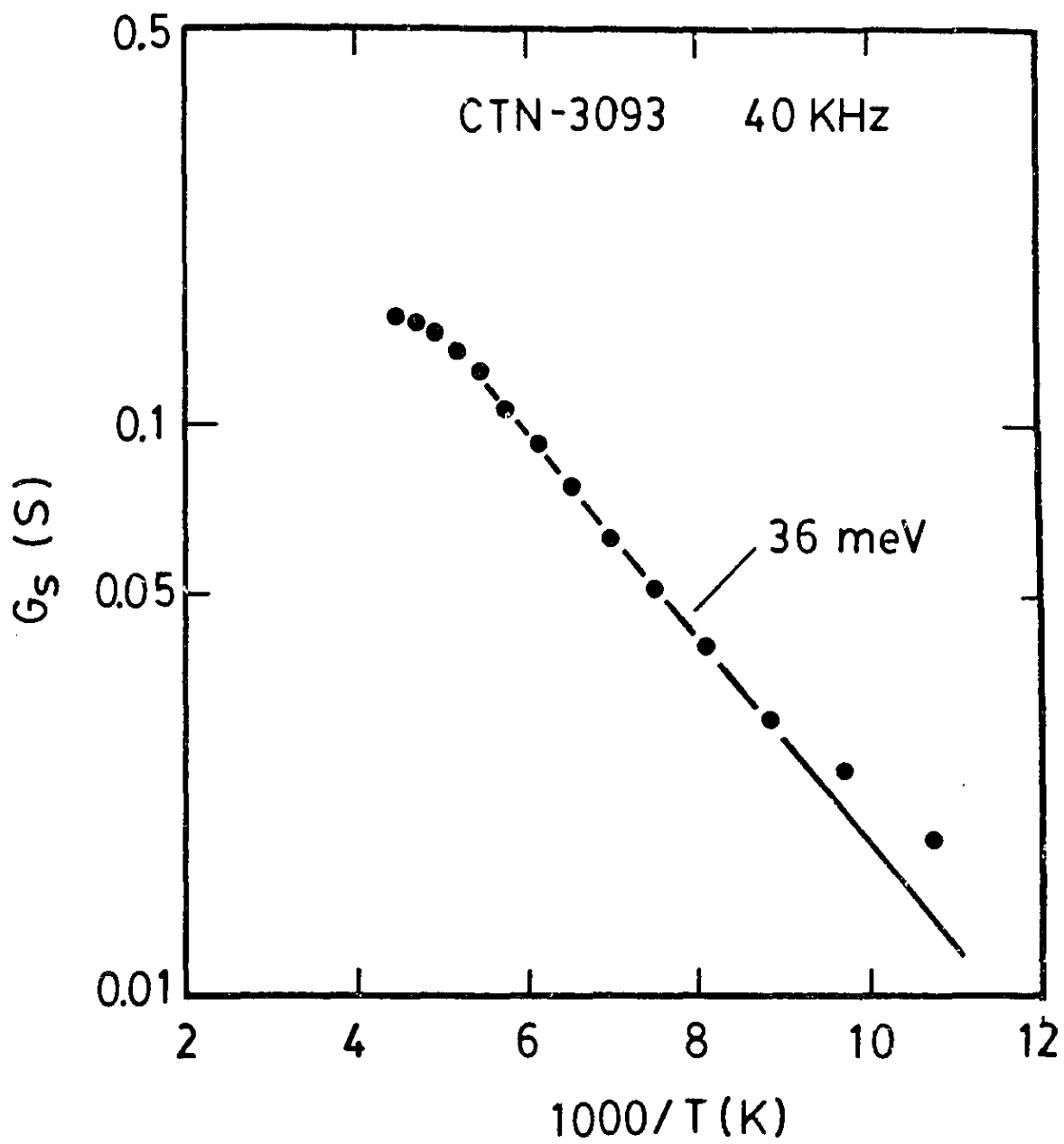


Fig. 8.11 A plot of G_S vs $1/T$ for the sample No. 3093, yielding shallow level of 36 meV. The value is smaller than that obtained from figure 8.9.

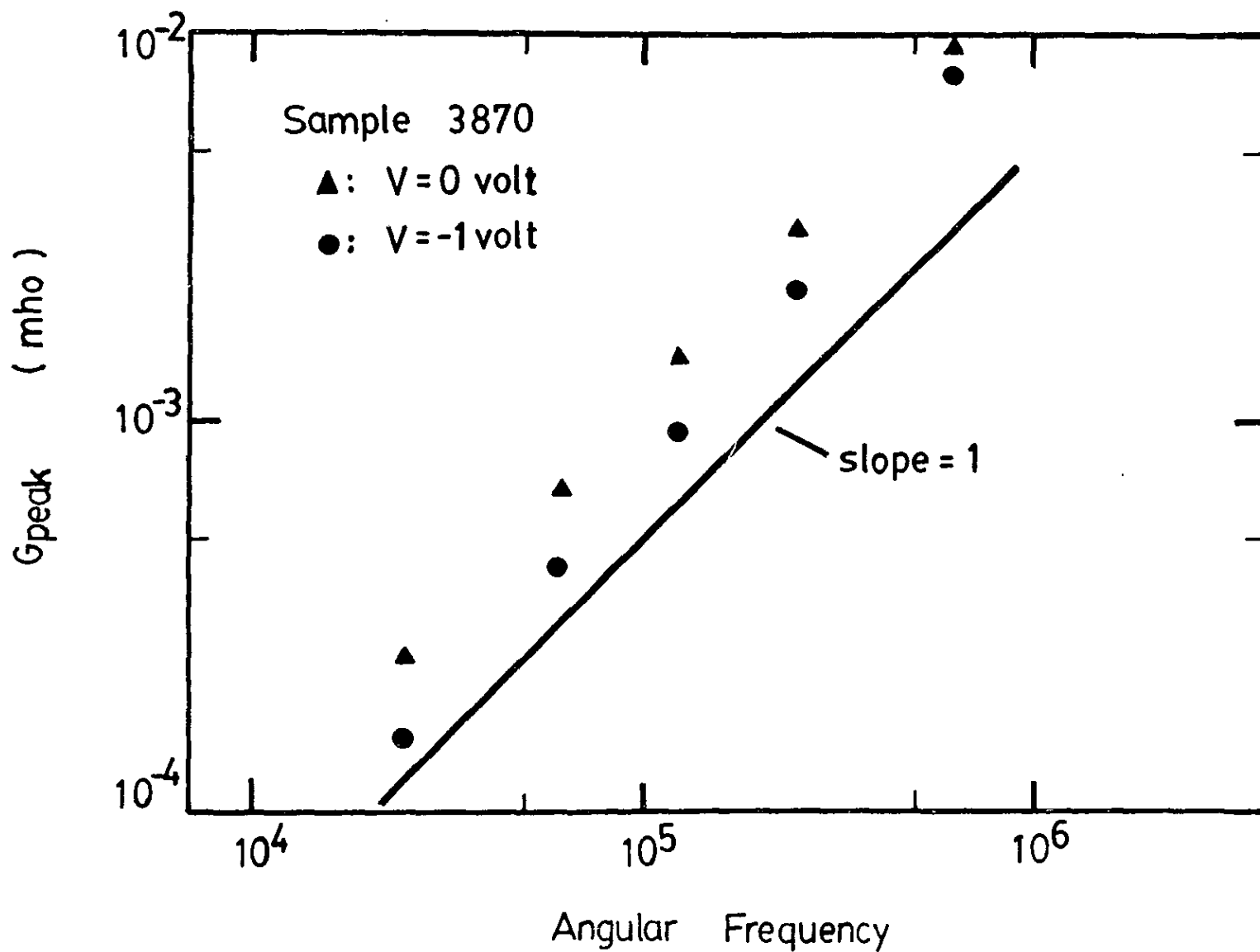


Fig. 8.12 A plot of G_{peak} vs. for the device No. 3870 showing a linear variation with the slope close to unity.

Chapter 9 DISCUSSION AND CONCLUSIONS

In order to simplify the procedure and to lower the cost for the fabrication of the CuInSe_2 -based solar cells, a one-step electrodeposition process has been developed in our laboratory to prepare thin films of CuInSe_2 . Using this method, uniform CuInSe_2 films with a thickness of 1-4 μm were deposited on both Mo and Mo/glass substrates. The electrodeposited CuInSe_2 films were found to be polycrystalline with a single phase and the preferred 112 orientation perpendicular to the substrate. Compositional uniformity of the films was found to be satisfactory for device applications. Because the adhesion on the CuInSe_2 films to the substrates was very good, separation of good quality films from the substrates was difficult. Therefore, electronic parameters were not measured for the CuInSe_2 films using the standard Hall effect measurements. Although some of the n-type samples were successfully separated from the substrates, reliable Hall effect results were still not obtained due to the large density of pin holes produced during the separation.

Effects of vacuum heat treatment on the electrodeposited CuInSe_2 films were studied. X-ray results revealed a strong relationship between crystalline quality of the CuInSe_2 samples and the treatment temperatures. The crystalline quality of the films was improved significantly as the temperature was increased, with a critical temperature value of about 300°C. However, heat treatment at a temperature above 400°C produced films

with multiphases. The diffraction intensity of the second phase became stronger as the temperature was increased further. Results also showed that composition of the films was affected by the heat treatment. However, if the treatment temperature was not too high, the Cu/In ratio in the treated films was essentially the same as that in the untreated ones. Therefore, the metal ratio in the final films could be predetermined during the deposition experiments.

Al/CuInSe₂ Schottky junctions made with the electrodeposited CuInSe₂ films showed a dominant recombination process for the junction current. The apparent diffusion potential for those devices was small (0.3 ± 0.06 V), suggesting the presence of interface states with a high density in the devices. The frequency-dependent dispersion effect in the C-V characteristics of the Schottky junctions was first assumed to be due to the enhanced interface states. The possibility of the effect to be due to deep traps was excluded in the present devices because no frequency dispersion was observed in the C^{-2} versus V curves for the CdS/CuInSe₂ cells fabricated on the same CuInSe₂ film. Since the apparent diffusion potential was essentially independent of measurement frequencies, it was further assumed that the interface states in the Al/CuInSe₂ Schottky junctions had characteristics which were different from that for the ones in the CdS/CuInSe₂ heterojunctions. However, the proposed large density of interface states alone could not interpret the frequency-dependent variation of the slope of the C^{-2} -V curves for the Al/CuInSe₂ Schottky junctions. Another possible explanation for

the dispersion effect in the C-V curves is the elemental interdiffusion which affected the density of deep level in the CuInSe_2 surface. In the Al/CuInSe_2 devices, the density of deep traps is large and these are responsible for the dispersion in the C-V curves. During the post-fabrication air heat treatment of the CdS/CuInSe_2 cells, an interdiffusion occurred and this caused a decrease in the density of the deep levels in the CuInSe_2 film. With the low defect density, the dispersion effect is negligible and can not be observed in the CdS/CuInSe_2 cells. However, in order to obtain a complete understanding of the two kinds of devices, further investigation using other methods, like deep level transient spectroscopy must be carried out.

The carrier concentration in the CuInSe_2 films of the Schottky junctions was found to increase after the 200°C air treatment, which was believed to be due to the diffusion of oxygen. This change was opposite to the change in the heterojunctions after a similar air heat treatment. Therefore, one should be careful when using the results obtained from the Schottky junctions to optimize the solar cell fabrication procedure using the electrodeposited CuInSe_2 films. Only the information obtained before any treatment reflects real properties of the CuInSe_2 films. After the heat treatment, the apparent diffusion potential was increased. This could be due to the formation of an interfacial layer.

Cells of CdS/CuInSe_2 with single layer CdS and CuInSe_2 were made on two different substrates: molybdenum plates and molybdenum coated glass plates. Photovoltaic effects were readily ob-

tained for the cells on the Mo/glass substrates. However, an air heat treatment (at 200 °C) had to be carried out for the cells on the Mo plates in order to produce strong photovoltaic effects. The air heat treatment was also found to improve the performance of the cells on the Mo/glass substrates. The treatment resulted in a decrease in the carrier concentration of the CuInSe₂ films, which is interpreted as a result of elemental inter-diffusion during the treatment. It was also observed that the change of concentration in the region near the physical junction was smaller, indicating an oxygen compensation effect during the air heat treatment. The short circuit current in the CdS/CuInSe₂ cells was observed to be affected by the composition of the CuInSe₂ films. An indium to copper ratio of 1.1 was found to give the best results for the single-layer cell structure. The fitting results for room temperature I-V characteristics of the cells showed that recombination current was about one order of magnitude larger than the saturation current. From the saturation current, a barrier height of about 0.64 V was obtained. This value was close to the diffusion potential value obtained from the C-V characteristics.

From the fitting results given in Tables 5.1 and 7.1, curves of $I_r/T^{3/2}$ versus $1000/T$ were obtained for a Schottky junction (No. 3824) and a heterojunction (No. 3784) (see Fig. 9.1). From the slopes of the lines in Fig. 9.1, the activation energy values for the recombination current can be obtained according to the equation:

$$I_r = T^{3/2} \exp[-E_a/2kT]^{9.1} \quad (9.1)$$

Here I_r is the pre-exponential term in the second term of equation (5.1). It is seen that the E_a value obtained for the Schottky junction is about 0.9 eV, which is close to the reported band gap value for the crystalline CuInSe_2 . The results thus allow one to conclude that the dominant current in the Schottky junction is the space charge recombination in CuInSe_2 side. For the heterojunction device, the activation energy is about 0.66 eV, suggesting that the interface recombination process is dominant in the recombination current of the heterojunction device.

The intercepts of the C^{-2} -V curves for the cells were frequency-dependent. This effect suggested that the interface states presented in the CdS/CuInSe_2 cells have a wide range of response time constants. In addition to the above, the C-V results were also affected by external illumination. Under the illumination, the C^{-2} -V curves shifted to a more negative voltage region, giving a smaller voltage intercept value. These results suggested the presence of interface states with a high concentration. Under AM1 illumination condition, the density of the light induced interface states was estimated to be about $5 \times 10^{12} \text{ cm}^{-2}$ for a 5% cell. This value, which is large enough to cause a large interface recombination component in the junction current, was believed to be smaller than the total density of the interface states. The effects of deep levels on the illuminated C-V were also observed. The slope of C_L^{-2} -V curves was slightly smaller than that for the non-illuminated C^{-2} -V curves. The charged deep level density under AM1 illumination was estimated for one of the

cell to be less than one third of the dark effective carrier concentration.

The electrically active energy states in the electrodeposited CuInSe_2 films were investigated using the admittance spectroscopy technique. In such experiments, the admittance of the CdS/CuInSe_2 devices at different frequencies was measured in the temperature range from 80 K to 300 K. Conductance peaks were observed for all of the devices studied and the devices were classified into two groups according to the location of the conductance peaks. For the first group, conductance peaks occurred in the range from 100 K to 140 K for frequencies ranging from 4 kHz to 40 kHz. The activation energy value for these devices was about 50 meV. The second group of samples showed conductance peaks in a much higher temperature range (180 K to 220 K) and an activation energy of about 160 meV was obtained for those samples. The difference in the activation energy was found to be related to the metal ratio in the CuInSe_2 films. The In/Cu ratio was about 1.1 for the first group of devices (energy 50 meV) and was 1.25 for the second one (energy 160 meV).

From the results obtained in this thesis, it is clear that the electronic quality of the electrodeposited CuInSe_2 thin films is appropriate for photovoltaic device fabrication. However, in the present cells studied, the resistivities of the CdS and the CuInSe_2 films were too low to form a wider depletion region. In addition to the above, the open circuit voltage of the cells was relatively small due to the presence of interface states and defects in the CuInSe_2 films. Due to the large leakage current

and the relatively large series resistance, the fill factor of the devices was also limited. All of the above mentioned problems are the basic problems of the single layer CdS/CuInSe₂ cell structure.

In order to improve the performance of the cells, new device structures must be adopted. For instance, double layer CdS and CuInSe₂ (with high resistivity CdS and CuInSe₂ layers adjacent to each other) can be used to increase the I_{sc} and FF values. If high resistivity CdZnS film is used, the lattice mismatch can be reduced and the density of the interface states will decrease. An additional increase in the short circuit current can be obtained if the low resistivity top CdS layer (E_g=2.4 eV) is replaced by a low resistivity ZnO films (E_g=3.3 eV). The defects in the CuInSe₂ films can be reduced by a more careful treatment of the substrates or by increasing the thickness of the Mo films. The cell results in the present work also showed that it is important to achieve uniform properties in the deposited CdS films.

From the results obtained in this thesis, it can be stated that solar cells made with thin films of CuInSe₂ deposited using the electrodeposition method have a very encouraging future especially for large scale photovoltaic applications. The price of the cells can be very low if large area cells are fabricated using this method of low energy consumption and high material utilization. By adopting better cell structures, the conversion efficiency is expected to approach that of the vacuum deposited cells. A lot of work has to be done, however, before this target can be achieved.

Finally, main contributions of this thesis are summarized as follows:

The first contribution of the work is on the successful development of a chemical deposition process for the preparation of ternary compound semiconductor CuInSe_2 . The conditions were established for the deposition of good quality CuInSe_2 thin films with controlled composition. The second contribution is on the investigation of effects of a vacuum annealing on the crystallinity and the composition of the electrodeposited CuInSe_2 films. The third contribution is on the participation in the study of I-V, C-V characteristics of the Al/(p) CuInSe_2 Schottky junctions. The fourth contribution is on the fabrication of CdS/CuInSe_2 solar cells on the electrodeposited CuInSe_2 films with an active area conversion efficiency up to 5.6%. The fifth contribution is on the investigation of effect of post-fabrication air-treatment on the performance of the cells and variation of space charge concentration in the electrodeposited CuInSe_2 films with the air heat treatment. The sixth contribution is on the investigation of the current transport mechanism in the CdS/CuInSe_2 cells. This includes studies of interface states and deep levels in the CuInSe_2 cells by illuminated C-V measurements. The last contribution is on the identification of energy levels in the electrodeposited CuInSe_2 films by admittance spectroscopy measurements. This includes the observation of the relationship between the energy level(s) and the metal ratio in the electrodeposited CuInSe_2 films.

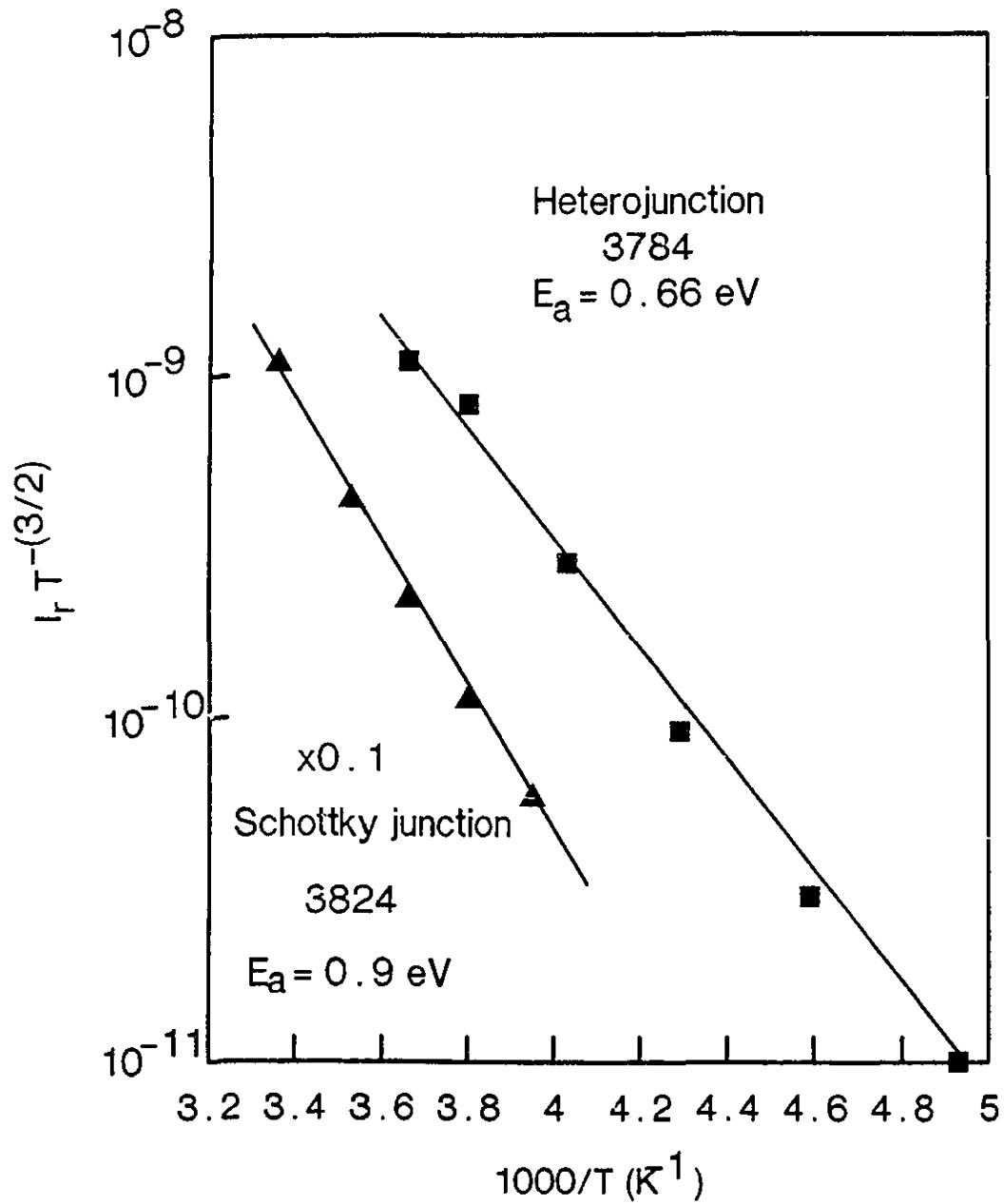


Fig. 9.1 Plots of $I_r/T^{3/2}$ versus $1000/T$ for a Schottky junction and a heterojunction.

REFERENCES

- 1.1 W. R. Moomaw, Proc. of 21th IEEE Photovoltaic Specialists Conf., Florida, 9 (1990).
- 1.2 M. A. Green, Proc. of 21th IEEE Photovoltaic Specialists Conf., Florida, 9 (1990).
- 1.3 D.M. Chapin, C. S. Fuller and G.L.Pearson, J.Appl. Phys. 25, 676 (1954).
- 1.4 J. Parkes, R. D. Tomlinson and M. J. Hampshire, J. Appl. Cryst., 6, 414 (1973).
- 1.5 K. L. Chopra and S. R. Das, Thin Film Solar Cells, Plenum Press, New York and London (1983).
- 1.6 K. Mitchell, C. Eberspacher, J. Ermer and D. Pier, Proc. of 20th IEEE Photovoltaic Specialists Conf., 1384 (1988).
- 1.7 R. P. Gale, R. W. McClelland, B. D. Dingle, J.V. Gormley, R.M. Burgess, N. P. Kim, R. A. Mickelsen and B. J. Stanbery, Proc. of 21th IEEE Photovoltaic Specialists Conf., Florida, 53 (1990).
- 1.8 R. A. Mickelsen and W. S. Chen, Proc. of 16th IEEE Photovoltaic Specialists Conf., 781 (1982).
- 1.9 R. K. Ahrenkiel, L. L. Kazmerski, R.J. Matson, C. Osterwald, T. P. Massopust, R. A. Mickelsen and W. S. Chen, Appl. Phys. Lett., 43, 658 (1983).
- 1.10 A.Hermann, K. Zweibel and R. Mitchell, Proc. of 17th IEEE Photovoltaic Specialists Conf., Orlando, 910 (1984).
- 1.11 W.E.Devaney, R. A. Mickelsen and W. S. Chen, Proc. of 18th IEEE Photovoltaic Specialists Conf., Las Vegas, 1733 (1985).
- 1.12 J. H. Ermer, R. B. Love, A. K. Khannan, S. C. Lewis and F. Cohen, Proc. of 18th IEEE Photovoltaic Specialists Conf., Las Vegas, 1655 (1985).
- 1.13 J. Piekoszewski, J. J. Loferski, R. Beaulieu, J. Beall, B. Roessler and J. Shewchun, Solar Energy Materials, 2, 363 (1980).

- 1.14 J. A. Thornton, D. G. Cornog, R. B. Hall, S. P. Shea and J. D. Meakin, Proc. of 17th IEEE Photovoltaic Specialists Conf., Orlando, 781 (1984).
- 1.15 T. C. Lommasson, H. Talich, J. D. Meakin and J. A. Thornton, Proc. of 19th IEEE Photovoltaic Specialists Conf., 1285 (1987).
- 1.16 V. K. Kapur, B. M. Basol and E.S. Tseng, Solar Cells, 21, 65 (1987).
- 1.17 R. D. Varrin, Jr., S. Verma, R. W. Birkmire, B. E. McCandless and T. W. F. Russell, Proc. of 21th IEEE Photovoltaic Specialists Conf., Florida, 529 (1990).
- 1.18 B. M. Basol and V. K. Kapur, Proc. of 21th IEEE Photovoltaic Specialists Conf., Florida, 546 (1990).
- 1.19 C. W. Bates, M. Uekita, K. F. Nelson, C. Abernathy and J.B. Mooney, Proc. 16th IEEE Photovoltaic Specialists Conf., 1427 (1982).
- 1.20 M. S. Tomar and F. J. Garcia, Thin Solid Films, 90, 419 (1982).
- 1.21 I. Shih and C. X. Qiu, Proc. 19th IEEE Photovoltaic Specialists Conf., New Orleans, 1291 (1987).
- 1.22 S. Wagner, J. L. Shay and H. M. Kasper, J. Phys. (France), 36, C-3 101 (1975).
- 1.23 T. Irie, S. Endo and S. Kimura, Jpn. J. Appl. Phys., 18, 1303 (1979).
- 2.1 A. M. Hermann, L. Fabick, K. Zweibel and R. Hardy, Proc. 16th IEEE Photovoltaic Specialists Conf., 840 (1982).
- 2.2 H. J. Hovel, Solar Cells, in R. K. Willardson and A. C. Beer, Eds., Semiconductors and Semimetals, Vol. 11, Academic, New York, 1975; "Photovoltaic Materials and Devices for terrestrial Applications," IEEE Tech. Dig. Int. Electron Device Meet., 1979, p. 3.
- 2.3 M. B. Prince, J. Appl. Phys., 26, 534 (1955).
- 2.4 J. J. Loferski, J. Appl. Phys., 27, 777 (1956).
- 2.5 H. J. Hovel, "Semiconductor and Semimetal," Vol. 2, "Solar Cells," Academic Press (1975).
- 3.1 M. P. R. Panicker, M. Knaster and F. A. Kroger, J. Electro

- chem. Soc., 125, 556 (1987).
- 3.2 D. Elwell, R. S. Peigelson and M. M. Simkins, J. Crystal Growth, 51, 171 (1981).
 - 3.3 R. N. Bhattacharya, J. Electrochem. Soc., 130, 2040 (1983).
 - 3.4 G. Hodes and D. Cahen, Solar Cells, 16, 245 (1986).
 - 3.5 R. N. Bhattacharya and K. Rajeshwar, Solar Cells, 16, 237 (1986).
 - 3.6 I. Shih, C. X. Qiu, S. K. Zhang and J. K. Chen, Material Lett., 3, 226 (1985).
 - 3.7 I. Shih and C. X. Qiu, Material Lett., 3, 446 (1985).
 - 3.8 C. X. Qiu and I. Shih, Can. J. Phys., 65, 1011 (1987).
 - 3.9 R. Garg, J.C Garg and A.C. Rastogi, Proc. 21th IEEE Photo voltaic Conference, 1990, p. 471.
 - 3.10 L. Thouin, S. Rouquette-Sanchez and J. Vedel, Proc. 10th European Photovoltaic Solar Energy Conference, 1991.
 - 3.11 R. A. Mickelsen and W. S. Chen, Appl. Phys. Lett., 36, 371 (1980).
 - 3.12 S. Isomura, H. Kaneko and S. Tomioka, Japan. J. Appl. Phys., 19, 23 (1980).
 - 3.13 L. L. Kazmerski, F. R. White and . K. Morgan, Appl. Phys. Lett., 22, 268 (1976).
 - 3.14 R. Noufi, R. Axton, D. Cahen and S. K. Deb, Proc. 17th IEEE Photovoltaic Specialists Conf., Florida, 927 (1984).
 - 4.1 W. E. Devaney, R. A. Mickelsen and W. S. Chen, Proc. 18th IEEE Photovoltaic Specialists Conf., Las Vegas, 1733 (1985).
 - 4.2 R. A. Mickelsen and W. S. Chen, Proc. 15th IEEE Photovoltaic Specialists Conf., 800 (1981).
 - 5.1 P. Robinson and J. I. B. Wilson, Inst. Phys. Conf. Ser. No. 35 , 229 (1975).
 - 5.2 N. Yalcin, I. S. Al-Saffer, and R. T. Tomlinson, J. Appl. Phys., 52, 5857 (1981).
 - 5.3 J. J. B. Prasad, D. Krishna Rao, D. Sridevi, J. Majhi, K. V. Reddy and J. sobhanadri, Solid-State Electron., 28, 1251

(1985).

- 5.4 F. Leccabue, D. Seuret and O. Vigil, Appl. Phys. Lett., 46, 853 (1985).
- 5.5 C. L. Chan and I. Shih, J. Appl. Phys., 67, 6544 (1990).
- 5.6 I. Shih, C. X. Qiu, S. N. Qiu and J. F. Haung, J. Appl. Phys., 63, 439 (1988).
- 5.7 A. B. McLean, I. M. Dharmadasa and R. H. Williams, Semicond. Sci. Technol., 1, 137 (1986).
- 6.1 W. E. Devaney, R. A. Mickelsen and W. S. Chen, Proc. of 18th IEEE Photovoltaic Specialists Conf., Las Vegas, 1733 (1985).
- 6.2 K. L. Chopra and S. R. Das, "Thin Film Solar Cells", Plenum Press, New York, 1983.
- 6.3 W. L. Choi, L. S. Yip and I. Shih, J. of The Canadian Ceramic Society, 58, 56 (1989).
- 6.4 N. Romeo, G. Sberveglieri and L. Tavricone, Thin Solid Films, 55, 413 (1978).
- 6.5 I. Shih, C. X. Qiu, S. N. Qiu and W. L. Choi, J. Canadian Ceramics Society, 56, 67 (1987).
- 7.1 J. L. Shay, S. Wagner and H. M. Kasper, Appl. Phys. Lett., 27, 89 (1975).
- 7.2 R. P. Potter, Solar Cells, 16, 521 (1986).
- 7.3 C. Goradia and M. Ghalla-Goradia, Solar Cells, 16, 611 (1986).
- 7.4 L. C. Isett, Appl. Phys. Lett., 43, 577 (1983).
- 7.5 R. K. Ahrenkiel, Solar Cells, 16, 549 (1986).
- 7.6 J. P. Donnelly and A. G. Milnes, IEEE Trans. Electron Devices, ED-14, 63 (1967).
- 7.7 H. Tavakolian and J. R. Sites, Proc. 18th IEEE Photovoltaic Specialists Conf., Las Vegas, 1065 (1985).
- 7.8 C. L. Chan and I. Shih, J. Appl. Phys., 67, 6544 (1990).
- 8.1 D. V. Lang, J. Appl. Phys., 45, 3023 (1974).
- 8.2 R. A. Mickelsen, W. S. Chen, Y. R. Hsiao and V. E. Lowe,

- IEEE Trans. Electron Devices, ED31, 542 (1984).
- 8.3 C. T. Sah, W. W. Chan, H. S. Fu and J. W. Walker, Appl. Phys. Lett., 20, 193, (1972).
- 8.4 D. L. Losee, Appl. Phys. Lett., 21, 54 (1972).
- 8.5 D. L. Losee, J. Appl. Phys., 46, 2204 (1975).
- 8.6 J. L. Pautrat and B. Katircioglu, N. Magnea, D. Bensahel, J. C. Pfister and L. Revoil, Solid-State Electronics, 23, 1159 (1980).
- 8.7 Y. Tokuda and A. Usami, J. Appl. Phys., 48, 1668 (1977).
- 8.8 X. P. Gao, J. Zhou and C. C. Hsu, Chinese J. Semiconductors, 7, 346 (1986).
- 8.9 A. Kobayashi and T. Mori, J. Appl. Phys., 18, 345 (1979).
- 8.10 L. C. Isett and P. K. Raychaudhuri, J. Appl. Phys., 55, 3605 (1984).
- 8.11 H. J. Hoffman and H. Reisser, Phys. Stat. Sol., (a)51, K171 (1979).
- 8.12 L. B. Fabick and K. L. Eskenas, Proc. 18th IEEE Photovoltaic Specialists Conf., Las Vegas, 754 (1985).
- 8.13 R. Vaidhyanathan, R. Noufi, T. Datta, R. C. Powell and S. K. Deb, Proc. 18th IEEE Photovoltaic Specialists Conf., Las Vegas, 1054 (1985).
- 8.14 E. C. Demetriou and A. Rothwarf, 19th IEEE Photovoltaic Specialists Conf., New Orleans, 764 (1987).
- 8.15 G. L. Miller, D. V. Lang and L. C. Kimerling, Annu. Rev. Matter. Sci., 1, 377 (1977).
- 9.1 I. Shih and C. X. Qiu, Electronics Lett., 21, 350 (1985).